Forschungsbericht 2010-37

Flexible Aircraft Modelling for Flight Loads Analysis of Wake Vortex Encounters

Tobias Mauermann

Institute of Aeroelasticity
Göttingen

DLR
Deutsches Zentrum
für Luft- und Raumfahrt e.V.
in der Helmholtz-Gemeinschaft

DLR

Herausgeber
Deutsches Zentrum
für Luft- und Raumfahrt e.V.
Bibliotheks- und
Informationswesen
D-51170 Köln
Porz-Warnheide
Linder Höhe
D-51147 Köln

Telefon (0 22 03) 6 01-31 01
Telefax (0 22 03) 6 01-47 47

ISSN 1434-8454

Flexible Aircraft Modelling for Flight Loads Analysis of Wake Vortex Encounters

Tobias Mauermann

Institute of Aeroelasticity
Göttingen

190	Seiten
95	Bilder
32	Tabellen
141	Literaturstellen

Für Sirkka und Lovisa

Flexible Aircraft Modelling for Flight Loads Analysis of Wake Vortex Encounters

Von der Fakultät für Maschinenbau
der Technischen Universität Carolo-Wilhelmina zu Braunschweig

zur Erlangung der Würde

einer Doktor-Ingenieurin oder eines Doktor-Ingenieurs (Dr.-Ing.)

genehmigte Dissertation

von: Herr Dipl.-Ing. Tobias Mauermann
aus (Geburtsort): Altenerding

eingereicht am: 15. Juni 2010
mündliche Prüfung am: 9. Dezember 2010

Referentinnen oder Referenten:
Prof. Dr.-Ing. L. Tichy
Prof. Dr.-Ing. R. Radespiel

2011

Abstract

The main objective of this thesis is the development of a novel approach to the integral modelling of flexible aircraft. As an exemplary application, the model is to be applied to the flight loads analysis of a large transport category aircraft encountering a wake vortex. The focus is on the aerodynamic and aeroelastic model, which should satisfy several requirements from industrial practice: straight-forward model generation, consideration of existing model components and a trade-off between computational efficiency and physical accuracy.

The aerodynamic model consists of two parts, a database describing the distributed, non-linear steady aerodynamic load on the quasi-flexible aircraft and an unsteady, incompressible, potential-based vortex ring method formulated in the time domain. The governing equations of the numerical method are derived for lifting surfaces and non-lifting bodies, followed by the linearised formulation in state space form and special cases for quasi-steady and harmonic motion. To improve the accuracy of the unsteady vortex lattice method, a correction method using steady reference data is proposed. Additionally, an order reduction based on balanced realization of wake sub-models is outlined. Finally, an incremental formulation of the numerical method is derived and cast into the typical notation used for rational function approximation (RFA), thereby allowing the direct use in existing aeroelastic analysis tools.

It follows the description of the structure and mass models and the non-linear equations of motion of the flexible aircraft. This is supplemented by the equations of structural loads and a presentation of options to obtain linearized equations of motion.

To interconnect the aerodynamic and reduced-order structural models, a coupling method based on beam interpolation elements and orthogonal rigid lever arms is derived. The method is able to map forces and displacement on all 6 degrees of freedom, conserves virtual work and can be set up in a highly automatized way.

The application of the aircraft model is demonstrated for the flight load analysis of a large transport aircraft encountering a wake vortex. The influence of the relative wake vortex position on component structural loads is analysed. By comparison of different modelling approaches, the importance of combining flight dynamics, structural dynamics and unsteady aerodynamics for flight loads considerations is worked out.

The major contribution of this thesis is the comprehensive presentation of a low-speed integral model of the flexible aircraft, useful for flight physical analysis in the time and frequency domain. The model satisfies industrial process requirements and contrary to customary approaches is directly established in the time domain.

Zusammenfassung

Ziel dieser Arbeit ist die Entwicklung eines neuartigen, integralen Berechnungsmodells des frei fliegenden, elastischen Flugzeugs und dessen beispielhafte Anwendung auf die Bestimmung von Strukturlasten, die auf ein großes Transportflugzeug während des Durchfliegens einer Wirbelschleppe einwirken. Der Schwerpunkt der Arbeit liegt auf der aerodynamischen und aeroelastischen Modellierung, wobei speziell die aus der industriellen Praxis motivierten Anforderungen nach einfacher Modellgenerierung, Berücksichtigung vorliegender Modellelemente und einem ausgewogenen Verhältnis von numerischer Leistungsfähigkeit zu physikalischer Genauigkeit berücksichtigt werden.

Das zweiteilige aerodynamische Modell umfasst eine datenbankbasierte Komponente zur Beschreibung der verteilten, nicht-linearen, stationären Luftkräfte am quasi-flexiblen Flugzeug sowie ein instationäres, auf inkompressibler Potentialtheorie im Zeitbereich basierendes Wirbelringverfahren. Die das numerische Aerodynamikverfahren beschreibenden Gleichungen werden für Tragflächen und Verdrängungskörper hergeleitet und daraus die linearisierte Formulierung in Zustandsform bestimmt. Davon ausgehend werden die Spezialfälle für quasi-stationäre Strömungszustände und harmonisch schwingende Bewegung abgeleitet. Zur Genauigkeitsverbesserung wird eine Methodik zur Korrektur mit stationären Referenzdaten vorgestellt und ein Ordnungsreduktionsverfahren basierend auf Balanced Realization für einzelne Nachlaufstreifen eingeführt. Schließlich wird eine inkrementelle Formulierung des Verfahrens abgeleitet und in die für rationale Funktionsapproximation von Luftkräften übliche Notation gebracht. Es folgt die Darstellung des Struktur- und Massenmodells sowie der nichtlinearen Bewegungsgleichungen des flexiblen Flugzeugs. Ergänzt wird dies um die Bestimmungsgleichung für Strukturlasten sowie die Beschreibung von Möglichkeiten, linearisierte Formen der Bewegungsgleichungen zu erhalten. Zur aeroelastischen Ankopplung des aerodynamischen Modells an das kondensierte Strukturmodell wird ein Kopplungsverfahren mit finiten Interpolationsbalkenelementen und orthogonal projizierten starren Hebelarmen hergeleitet. Das Verfahren transportiert Verformungen und Kräfte aller sechs Freiheitsgrade bei Erhaltung der virtuellen Arbeit und erlaubt das weitgehend automatisierte Verknüpfen der Teilmodelle. Anhand des Durchfliegens einer Wirbelschleppe wird die Anwendung des Gesamtmodells auf die Berechnung von Strukturlasten eines großen Verkehrsflugzeugs demonstriert. Es wird gezeigt, in welcher Weise die Relativposition von Flugbahn und Wirbelschleppe die Lasten an den einzelnen Flugzeugstrukturkomponenten beeinflusst. Durch Vergleich verschiedener Modellierungsansätze wird die Relevanz der kombinierten Betrachtung von Flugmechanik, Strukturdynamik und instationärer Aerodynamik zur Lastenberechnung herausgearbeitet.

Der Beitrag dieser Arbeit liegt in der umfassenden Darstellung eines für niedrige Machzahlen gültigen integralen Flugzeugmodells für flugphysikalische Anwendungen im Zeit- und im Frequenzbereich, welches industriellen Anforderungen gerecht wird und entgegen üblicher Vorgehensweise direkt im Zeitbereich aufgestellt wird.

Danksagung

Diese Arbeit wurde durch die gemeinschaftliche Förderung des DLR Instituts für Aeroelastik in Göttingen und der Abteilung Loads & Aeroelastics der Airbus Operations GmbH in Hamburg ermöglicht.

Mein Dank gilt zunächst Herrn Prof. Dr.-Ing. L. Tichy vom DLR Institut für Aeroelastik in Göttingen und Herrn Prof. Dr.-Ing. R. Radespiel vom Institut für Strömungsmechanik der Technischen Universität Braunschweig für die Übernahme des Referats. Ihre Offenheit und ihr Interesse, sich mit industriell motivierten Fragestellungen auseinanderzusetzten und kritisch mit mir zu diskutieren, waren sehr hilfreich bei der Ausrichtung und Umgrenzung dieser Arbeit. Herrn Prof. Dr.-Ing. P. Horst vom Institut für Flugzeugbau und Leichtbau der Technischen Universität Braunschweig danke ich dafür, den Vorsitz der Promotionskommission übernommen zu haben.

Für die engagierte Betreuung dieser Arbeit seitens Airbus in Hamburg bedanke ich mich herzlich bei Herrn Dr.-Ing. J. Schuler, der mir das Themengebiet der Integralen Flugzeugmodellierung näher brachte. Unsere fachlichen Diskussionen und Fortschrittsbesprechungen halfen mir, den roten Faden und die Zielsetzungen dieser Arbeit nicht aus den Augen zu verlieren. Meinen Hamburger Kollegen Herrn Dr.-Ing. C. Reschke und Herrn W. Weigold bin ich für viele interessante und technisch erhellende Gespräche dankbar.

Am DLR Institut für Aeroelastik in Göttingen betreute mich Herr Dr.-Ing. F. Kiessling, der mir während der Entstehung dieser Arbeit stets seine unschätzbar wertvolle fachliche Unterstützung anbot und durch sein praktisch enzyklopädisches Wissen auf dem Gebiet der Aeroelastik ein großartiger Lehrer war. Insbesondere danke ich ihm für die Zuversicht, die er in den Abschluss dieser Arbeit gesetzt hat. Meine Göttinger Kollegen Herrn J. Schwochow und Herrn J. Neumann waren mir in vielen technischen Diskussionen zu aeroelastischen Themen und CFD eine große Hilfe. Frau U. Fürst danke ich für Ihren mustergültigen IT-Support, gelegentlich bis nach Hamburg.

Abschliessender Dank gilt meinen Eltern Gudrun und Lutz und meiner Ehefrau Sirkka mit meiner Tochter Lovisa. Ohne sie wäre diese Arbeit nicht entstanden.

Tobias Mauermann

Hamburg, im Juni 2011

Contents

List of Figures

List of Tables

Nomenclature

Latin Letters

A	Panel area	
a	Relative airfoil attachment position	
A_0	Aerodynamic stiffness matrix	
A_1	Aerodynamic damping matrix	
A_2	Aerodynamic inertia matrix	
A	Aerodynamic influence coefficient matrix (bound rings)	
$\boldsymbol{a}_y, \boldsymbol{a}_z$	Vectors of shape function scaling factors)	
b	Semi-chord and span	m
B	Aerodynamic influence coefficient matrix (wake)	
C	Shape function coefficient matrix	
c	Relative flap hinge position	
C_H	Hinge moment coefficient	
$C(k)$	Theodorsen function	
C_L	Lift coefficient	
C_M	Pitching moment coefficient	
c_p	Pressure coefficient	
D	Aerodynamic lag matrix	
$\boldsymbol{d}$	Downwash vector	
Δt	Time step size	
$\frac{D()}{Dt}$	Total derivative	
Δz_{V}	Wake vortex vertical offset	
E_0	Lag state matrix (airfoil state)	
E_1	Lag state matrix (airfoil state derivative)	
$\boldsymbol{f}$	Body forces exerted on the fluid	$\mathrm{m/s^2}$
$\boldsymbol{f}_{\mathrm{D}}$	Panel induced drag vector	
F_h	Vertical aerodynamic force	N
$\boldsymbol{f}_{\mathrm{S}}$	Panel steady force vector	
G_{Ag}	Global aero-structure interconnection matrix	
h	Vertical coordinate and altitude	m
I_α	Rotational inertia of the airfoil	$\mathrm{kg\,m^2}$
I_δ	Rotational inertia of the flap	$\mathrm{kg\,m^2}$
i_h	Horizontal stabilizer setting	
J_{B}	Inertia tensor	
K	Stiffness matrix	
k	Reduced Frequency $\omega c/V$	

K_α	Torsional spring stiffness	Nm/rad
K_c	Control matrix	
K_δ	Torsional flap spring stiffness	Nm/rad
K_h	Tension spring stiffness	N/m
l_A	Aerodynamic Mean Chord (AMC)	m
$\boldsymbol{L}_\mathrm{g}$	Vector of structural loads	
l_H	Lever arm of the horizontal tail	m
M	Mass matrix	
$\boldsymbol{m}$	Panel moment vector about centroid	
m	Total mass	kg
M_α	Aerodynamic moment about airfoil attachment	Nm
M_δ	Aerodynamic moment about flap hinge	Nm
$\boldsymbol{n}$	Panel normal vector	
n_z	Vertical load factor	
P	Permutation matrix	
p	Fluid pressure	N/m^2
p	Rate of roll	rad/s
$\boldsymbol{P}_\mathrm{A}$	Vector of aerodynamic forces	
$\boldsymbol{P}_\mathrm{g}$	Vector of structural forces	
p_∞	Freestream pressure	
$\tilde{p}$	Vector of aerodynamic forces	
$\boldsymbol{p}_y, \boldsymbol{p}_z$	Strip load vectors)	
$\boldsymbol{Q}$	Vector of generalized forces	
q	Rate of pitch	rad/s
q_∞	Dynamic pressure	N/m^2
R	Lag state matrix	
r	Rate of yaw	rad/s
R_BG	Transformation matrix for rates (body axis to geodetic)	
$\boldsymbol{r}_\mathrm{G}$	Aircraft position vector	
S	Strip summation matrix	
S_1	*Kutta-Joukowski* load matrix	
S_2	Load matrix for total derivative of potential	
S_α	Static moment of the airfoil	kg m
S_δ	Static moment of the flap	kg m
$S(k)$	Sears function	
T	Transformation matrix	
T_B	Matrix for total body circulation	
T_BG	Transformation matrix (geodetic to body axis)	
T_P	Bound circulation transport matrix	
T_W	Wake transport matrix	
$\boldsymbol{u}$	Control vector	
$\boldsymbol{u}_\mathrm{A}$	Vector of panel displacement	
$\boldsymbol{u}_\mathrm{G}$	Vector of panel gust velocity	
$\boldsymbol{u}_\mathrm{g}$	Vector of structural deformation	
$\boldsymbol{V}$	Velocity	m/s
$\boldsymbol{V}_\mathrm{B}$	Vector of body axis velocities u, v, w	
$\boldsymbol{v}_\mathrm{E}$	Velocity due to structural deformation	

$\boldsymbol{v}_\mathrm{G}$	Local atmospheric disturbance velocity	
V_∞	Freestream velocity	
$\boldsymbol{V}_\mathrm{kin}$	Velocity of the moving frame of reference	
$\boldsymbol{v}_\mathrm{R}$	Velocity due to rigid body motion	
$\boldsymbol{v}_\mathrm{S}$	Total velocity of the body surface	
V_θ	Wake vortex tangential velocity	
$\boldsymbol{w}$	Relative fluid velocity perceived from the moving frame of reference	
$\bar{\boldsymbol{w}}$	Panel velocity jump vector	
w_G	Vertical gust velocity	m/s
$\boldsymbol{x}$	State vector	
$\boldsymbol{x}_A$	Vector of lag states	

Greek Letters

α	Angle of attack	rad
$\dot{\alpha}$	Rate of incidence	rad/s
δ	Flap deflection	rad
δ_{ij}	Kronecker product	
ϵ	Downwash angle	rad
$\boldsymbol{\eta}$	Vector of modal generalized coordinates	
Γ	Vortex ring circulation	
γ	Vortex sheet strength	
Γ_eff	Effective circulation vector	
$\mathbf{\Gamma}_\mathrm{P}$	Bound circulation vector	
γ_V	Wake vortex elevation	
$\mathbf{\Gamma}_\mathrm{W}$	Wake circulation vector	
Λ	Aspect ratio b^2/S	
λ	Eigenvalue	
$\boldsymbol{\omega}_\mathrm{B}$	Vector of body angular rates p, q, r	
$\boldsymbol{\mathit{\Phi}}$	Matrix of Eigenvectors	
$\phi(\tau)$	Wagner function	
$\mathbf{\Phi}$	Eigenvector	
$\boldsymbol{\varphi}$	Vector of panel rotations	
$\mathbf{\Pi}_{ij}$	Stress tensor	$\mathrm{N/m^2}$
$\psi(\tau)$	Küssner function	
Ψ_V	Wake vortex azimuth	
ρ	Density of the air	$\mathrm{kg/m^2}$
τ	Non-dimensional time $2tV/c$	
$\boldsymbol{\tau}_{ij}$	Viscous stress tensor	$\mathrm{N/m^2}$
$\boldsymbol{\tau}_1$	First panel tangential vector	
$\boldsymbol{\tau}_2$	Second panel tangential vector	
$\mathbf{\Theta}$	Vector of Euler angles ϕ, θ, ψ	
ξ	Non-dimensional position $2x/c$	
ζ_i	Modal damping factor	

List of Acronyms

AIC	aerodynamic influence coefficient
CFD	computational fluid dynamics
DLM	doublet lattice method
EFCS	electronic flight control system
HVLM	harmonic vortex lattice method
HQ	handling qualities
HSV	Hankel singular values
IAM	integral aircraft model
LTI	linear time-invariant
RFA	rational function approximation
RMM	residual model method
SVD	singular value decomposition
UVLM	unsteady vortex lattice method
VLM	vortex lattice method
WVE	wake vortex encounter
RANS	Reynolds-averaged Navier-Stokes

1 Introduction

In the early 1950ies, the development of the Boeing B-47 Stratojet bomber depicted in Fig. 1.1 marked a turning point for the engineering fields of flight dynamics and aeroelasticity. Because of its new thin, high-aspect-ratio swept wings with underslung engines and a slender, long fuselage, the need to consider aeroelastic effects in the design process assumed critical importance. The relatively low frequency of the structural modes reduced the frequency separation between the flight dynamic modes and the structural vibrations and caused a coupled dynamic response of the aircraft to external disturbances such as control surface input or gust. New experimental techniques for wind tunnel flutter analysis (such as the one by Kinnaman [65]) had to be conceived that took into account the flexibility of the entire aircraft including the ability to undergo rigid body motion. Also the method of analyzing dynamic response to control surface excitation was revisited by Cole et al. [22] to confirm the validity of the quasi-static aeroelastic approach traditionally applied in flight dynamic analysis. The assumption of quasi-static aeroelastic behavior presumes that the change of aerodynamic loading occurs so slowly that the aircraft structure is always in static equilibrium, or, in other words, the aerodynamic forces do not excite structural vibrations [35]. Taken from Cole's report is Fig. 1.2, which compares the pitching velocity frequency response to elevator deflection at the center of gravity obtained from flight test with a rigid and quasi-static aircraft model. Two important conclusion could be drawn from this diagram: first, the assumption of a rigid aircraft is invalid even at low frequencies. Second, the quasi-static assumption begins to fail once the excitation frequency approaches that of the structural modes around 5 radians per second. In a follow-up report, Cole and Holleman [21] presented results obtained by a dynamic response model including some wing and fuselage structural modes which confirmed better agreement with flight test for excitation above the frequency of the short-period mode.

Certification requirements for transport category aircraft today reflect these early findings as illustrated by the following quotations from the flight loads relevant parts of the European Certification Specifications for Large Aeroplanes (CS-25, Subpart C: Structure):

§25.301 Loads "If deflections under load would significantly change the distribution of external or internal loads, this redistribution must be taken into account."

§25.305 Strength and Deformation "Where structural flexibility is such that any rate of load application likely to occur in the operating conditions might produce transient stresses appreciably higher than those corresponding to static loads, the effects of this rate of application must be considered."

§25.341 Gust and Turbulence Loads "Loads on each part of the structure must be determined by dynamic analysis. The analysis must take into account unsteady

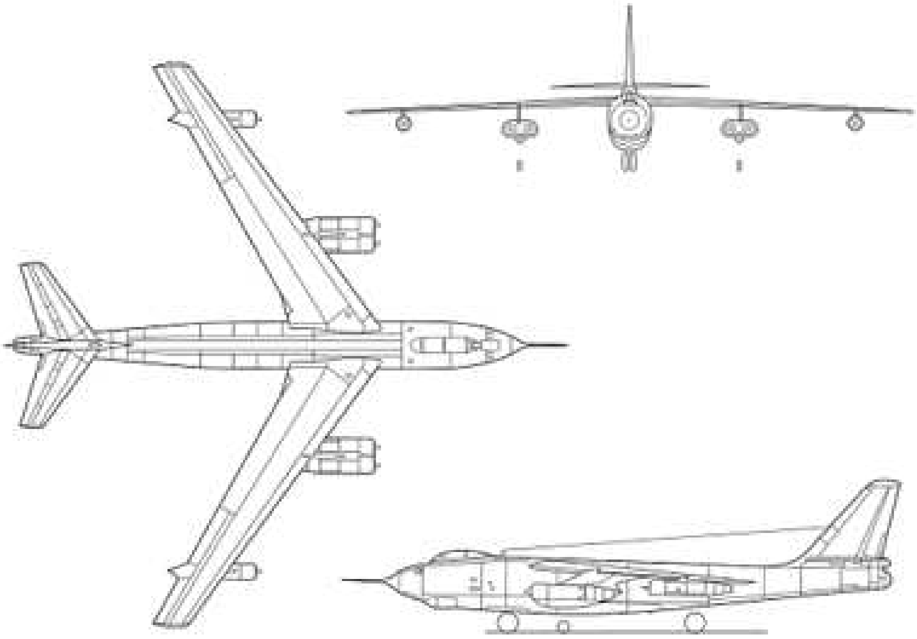

Figure 1.1: Boeing B-47 Stratojet

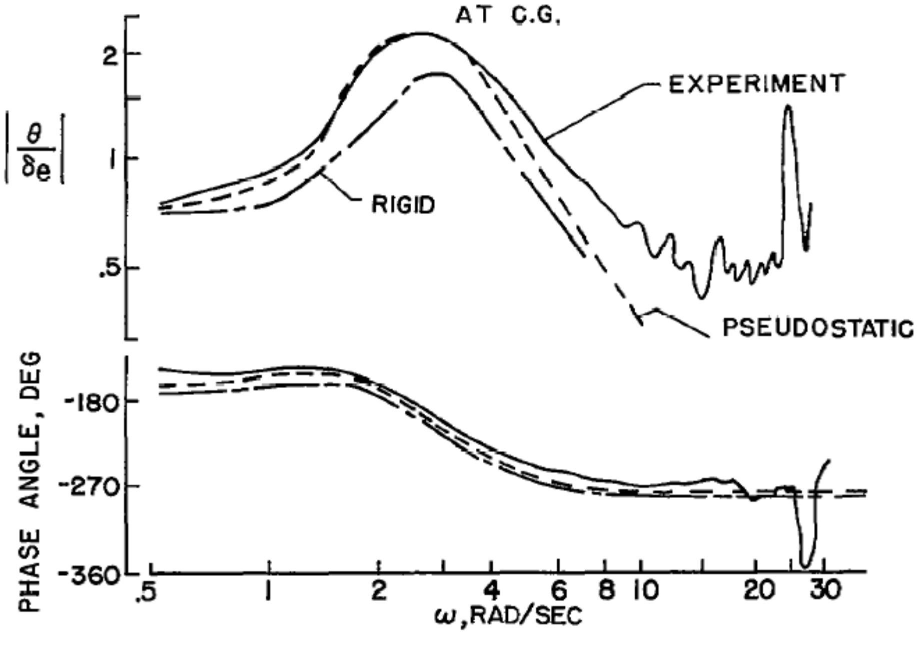

Figure 1.2: Frequency response of pitching velocity at CG due to elevator deflection of the Boeing B-47 (from Cole et al. [22])

aerodynamic characteristics and all significant structural degrees of freedom including rigid body motion."

§25.473 Landing Load Conditions "The method of analysis of airplane and landing gear loads must take into account at least the following elements:

1. Landing gear dynamic characteristics
2. Spin-up and springback
3. Rigid body response
4. Structural dynamic response of the airframe, if significant."

The respective aviation regulations have lead the transport aircraft manufacturer's design office to establish different types of aircraft models used in the task of design loads analysis. Design maneuver loads analysis typically relies on non-linear rigid body simulation models similar to the ones used for handling quality assessment and piloted simulation. The models use a database of steady, non-linear aerodynamic loads with quasi-static aeroelastic corrections to reflect the elastic behavior of the airframe. It is assumed that the electronic flight control system (EFCS) is designed to prevent the pilot from exciting structural modes, for instance by means of structural filters, and therefore the quasi-static aeroelastic assumption is valid. Gust and turbulence loads and loads due to oscillatory control surface failures are determined with incremental linearized, dynamic aircraft models including unsteady, linearized aerodynamics where it is assumed that the perturbation of the rigid body motion is only small. The analysis is typically performed in the frequency domain and requires a linearization of the flight control system. Due to the complex kinematics of the landing gear, ground loads are typically obtained by non-linear multi-body simulations, often including structural modes and neglecting the aerodynamic loads. By postulating that the different types of design loads will not be imposed on the aircraft simultaneously, the total envelope of design loads can be found from merging the envelopes of the three analyses.

This segregated approach to design loads analysis, even though proven, bears the likelihood of physical inconsistency, requires to some extend data redundancy and demands expertise for building the various types of models. Therefore, from both a physics and business point of view, it is preferable to develop a so called integral aircraft model (IAM) capable of simultaneously fulfilling the requirements of all fields of design load analysis. With this IAM, the traditional specific loads models could not only be consistently derived, but additional tasks could be performed:

1. design and validation of non-linear flight control laws, especially in regard of structural mode control and load alleviation functions
2. loads analysis for combined maneuver and gust or turbulence
3. assessment of flexible aircraft handling qualities in piloted simulation
4. assessment of the loads aspects of special upset conditions as for instance aircraft wake vortex encounter (WVE)

The global objective of this thesis is the development of an IAM for the last application, the flight loads analysis of WVEs. In the following literature review, previous work in the field of integral modelling with a focus on the aerodynamic model is summarized. Also modelling approaches typically used for wake vortex encounter studies are reviewed. Then the objectives and contributions of this work are presented, followed by the outline of the overall structure of this document.

1.1 Previous Work

1.1.1 Unsteady Aerodynamic Models for Simulation

In order to simulate arbitrarily maneuvering aircraft taking into account unsteady aerodynamic effects, a time-domain representation of the aerodynamic forces is required. There exist *indirect* and *direct* methods, the former constructing the time response from existing solutions for oscillatory, step or impulse type of motion and the latter directly solving the time-dependent governing equations of the flow field.

From the indirect methods, the use of the *indicial function* concept to model linear and linearized unsteady aerodynamics dates back to the first half of the 20th century. By way of convolution, the aerodynamic response to arbitrary motion is aggregated from the response due to a series of step inputs. For a two-dimensional airfoil in inviscid, incompressible flow, the work by Wagner [130] and Küssner [72] describing the transient aerodynamic load due to step change in angle of attack and step vertical gust, respectively, laid the foundation for this approach. The incompressible, inviscid two-dimensional case of an isolated airfoil was treated by von Kármán and Sears [129], Söhngen [114] and Garrick [39]. Jones [59] extended the approach to wings of finite aspect ratio. Klein [67] derived indicial functions for the downwash at a horizontal tail and Klein and Noderer [68] investigated the impact of unsteady aerodynamics on the longitudinal motion of an aircraft. A review of the incompressible two- and three-dimensional approach for inviscid flow is given by Cicala [19]. Mazelsky and Drischler [87], Lomax et al. [81] and Tobak [123] analyzed unsteady inviscid subsonic and supersonic aerodynamics of airfoils, small aspect ratio wings and wing-tail combinations. Indicial functions for two-dimensional, viscous incompressible flow were obtained by Brar et al. [9] using computational fluid dynamics (CFD). Alternatively, Guendel [46] demonstrates that the response to arbitrary motion can be constructed from the convolution of *impulse response functions*. The response to displacement and velocity impulse input was obtained from a time-stepping panel method. The *Laplace inversion integral* was used by Edwards et al. [31] to simulate the subsonic and supersonic inviscid behavior of an airfoil with flap.

Time domain models based on the *rational function approximation (RFA)* of frequency-domain aerodynamic forces have been obtained in several ways and were compared by Smith et al. [113]. There exists a vast number of options for calculation of these harmonic aerodynamic forces. Thin airfoil solutions were found for the incompressible case by Küssner and Schwarz [75] and for the compressible case by Küssner [73] and Wille [134]. For lifting surfaces in inviscid, subsonic flow, the doublet lattice method (DLM) by Albano and Rodden [1] and kernel function approaches like the one by Laschka [78] have the widest use in industry. The effect of airfoil thickness in two-dimensional, unsteady, incompressible potential flow was considered by Giesing [44] applying a surface panel method and also allowing for the interaction of multiple bodies.

For the transsonic flow regime, time-linearized methods based on potential flow like the Transonic Doublet Lattice method by Lu and Voss [84] or based on the Euler equations like the approach by Ni and Sisto [96] can directly give computationally competitive solutions.

When transforming the Laplace approximations of frequency-domain aerodynamic forces into the time-domain, the resulting number of states characterizing the aerodynamic lag behavior depends on the order of the approximating function. Roger [105] approximated the generalized forces with one set of denominator poles common to each generalized coordinate. To reduce the number of required lag states, Vepa [127] introduced the matrix form of the Padé approximation. Karpel [63] developed the so called Minimum State Method that iteratively approximates the generalized forces with a set of denominator poles common to all generalized coordinates. Dinu et al. [27] recently obtained approximations based on Chebyshev polynomials and showed its superiority in terms of accuracy, computational cost and system order compared to the matrix Padé approximations. Zrenner [141] derived *transfer functions* between the quasi-steady aerodynamic load from a lifting line method and the unsteady load from the doublet lattice method. The transfer functions were then converted to equivalent filter functions in the time domain. Mönnich [92] derived filter functions for the delay effect of downwash on the horizontal tail for longitudinal aircraft motion based on a lifting surface method combined with a starting vortex model.

Turning to the direct methods, *surface panel methods* (based on Green's theorem) using combinations of source and doublet panels have widely been used to solve the problem of unsteady potential flow. For two-dimensional incompressible flow, Basu and Hancock [6] computed the time history of flow around an airfoil due to a step change in angle of attack, sharp-edged gust and harmonic oscillation. Arbitrary unsteady motion in two-dimensional subsonic flow was analyzed by Long and Watts [82]. Maskew and Rao [86] applied a modified time-domain version of the commercial panel code VSAERO to the incompressible analysis of helicopter rotor blades undergoing a pitching motion. The code used constant doublet and source panels on the wing surface and linear doublet panels in the free wake. Using a similar approach but with a rigid wake, Ruiz-Calavera [107] analyzed the unsteady behavior of wings. van Staveren [125] applied the same method using a rigid wake to analyze the gust and turbulence response of a business jet configuration. Willis et al. [135] developed a formulation representing the far-field wake as vortex particles and implemented a pre-corrected FFT-solver and a fast multipole tree algorithm to accelerate the free wake computation. Eller [33] developed an unsteady panel method using triangular panels and a computationally efficient separation of near and far field. The time-domain formulation of the unsteady boundary value problem for subsonic potential flow is presented in the exhaustive review by Morino [93].

By far the most frequently applied direct method is the *unsteady vortex lattice method (UVLM)* for incompressible potential flow. Konstadinopoulos et al. [71] applied the method to study delta wings with leading edge separation and small aspect ratio rectangular wings with tip separation undergoing prescribed motion. Strganac [116] used the method in a closely coupled aeroelastic analysis of a rigid wing with elastic support and an elastic wing below and above the critical flutter speed. Kinnas et al. [66] used the method to simulate the unsteady behavior of ducted propellers. Ye [137] also applied the method to delta wings with leading edge separation and introduced a multi-step method for the wake relaxation to improve the accuracy of the wake position. Ramsey [99] introduced a de-singularized version of the Biot-Savart law to study the free wake of moving hydrofoils, instability of shear layers aerodynamics of sails.

The UVLM was applied to thick wings by Karkehabadi [60, 61] and in the following used for active control of a high aspect ratio flexible wing by Hall [48]. Preidikman [98] employed the method to investigate flutter of bridges and of a business aircraft wing. Cattarius [17] applied the method to the analysis of store flutter on a fighter wing where the store body was also modelled using a vortex lattice. Wang [132] studied stability of formation flight and simulated a free to roll flexible wing of high aspect ratio. Gologan and Schneider [45] presented a continuous-time matrix formulation of the UVLM using a fixed wake and applied it to the aeroelastic response simulation of a regional transport aircraft. A discrete-time matrix formulation using a fixed wake was presented by Hall [49] and served as the reference model for Eigen-decomposition based reduced order models. Another particular field of application for the UVLM is the study of flapping flight, see for instance the implementation of Fritz and Long [38] using a decaying wake model or the optimization effort to maximize flapping performance by Ito [56]. An excellent step by step description of the method appearing as a reference in most of the aforementioned publications can be found in the textbook by Katz and Plotkin [64]. A version of the vortex lattice method valid for purely oscillatory motion was derived by Laha [76] assuming a fixed wake. An attempt to introduce the effect of compressibility by means of a simple Prandtl-Glauert transformation contained in the Biot-Savart law was presented by Szymendera [117].

All aforementioned direct methods fail in the transonic flow regime where the appearance of shocks leads to unsteady effects not captured by the linearized potential flow equations. Alternative approaches must be applied that require an significantly higher computational effort due to the need to discretize the entire flow field rather than the wetted surface only. At the lower end of that computation scale, still solving the potential flow equations in a reduced form, transonic small disturbance methods as the one applied by Ballhaus and Goorjian [5] can be found and are able to capture harmonic shock movement ("Type A" according to Tijedeman [122]) for small motion amplitudes. Alternatively, the full potential equations can be solved at higher computational cost, see for instance Isogai [55].

At the upper end for the practical analysis of full aircraft configurations in the time domain are methods solving the Euler equations or Reynolds-averaged Navier-Stokes (RANS) equations, commonly referred to as *computational fluid dynamics (CFD)* methods. Farhat et al. [36] presented a three-field approach (structure, dynamic mesh and fluid) for the simulation of the pull-up maneuver of a generic fighter aircraft based on the solution of the Euler flow equations. Geuzaine et al. [43] applied a similar method to aeroelastic response calculations of an F-16 fighter aircraft in steady and accelerated flight as well as under high vertical load factor and compared their results against flight test. Henke [52] reported on aeroelastic simulations of the LANN wing and full aircraft configuration coupling an Euler code with boundary layer to a modal structural model and compared the results to experimental data and flight test. Steady state maneuver solutions for flexible fighter type aircraft using CFD were also reported by van Gelder et al. [124] and Raveh et al. [100] both solving the Euler equations. The rolling motion of a flexible delta wing mounted on a sting was simulated by Einarsson and Neumann [32] using a coupled RANS, structural dynamics and flight mechanics model.

1.1.2 Integral Flexible Aircraft Models

The equations of motion of the flexible, free-flying aircraft have been derived by numerous authors. By using various levels of simplifying assumptions, a more or less compact formulation can be obtained. Milne [91] and De Veubeke [26] both presented general developments of the equation of motions without treating in detail the aerodynamic forces. Youssef et al. [138] studied an integral inertially coupled model ignoring aerodynamics. Assuming constant angular body rates, Eigenvalues for the system were determined and the impact of angular rate on the stability behavior was quantified. Owing to its simplicity, aerodynamic strip theory allows closed-form solution of the flexible aircraft equation of motion as demonstrated by Waszak and Schmidt [133], Ro and Barlow [103] and Meirovitch and Tuzcu [90]. Siepenkötter and Alles [112] made use of this closed-form solution to study the non-linear stability behavior. As examples of more complex aerodynamic models, Drela [29] and Gologan and Schneider [45] applied unsteady lifting line theory and the UVLM, respectively, to their IAM. In the latter publication, the time derivative of the bound circulation was forgotten in the calculation of unsteady aerodynamic forces. Eller [33] developed a time domain aerodynamic surface panel method to link to the flexible aircraft equations of motion.

A large number of publications is dedicated to the idea of supplementing existing models by the effect of structural dynamics and their resulting aerodynamic loads. Thereby it must be distinguished between supplementing flight dynamic models for the rigid aircraft and models where quasi-static aeroelastic corrections are already included. For the former case, Buttrill et al. [15], Schuler [111], Hanel [50] and Damveld [24] developed add-on aeroelastic models relying on unsteady aerodynamic forces obtained from RFA of frequency domain generalized forces. For the latter case, care must be taken no to double account for the quasi-static effect and therefore a split of the aeroelastic model into quasi-static and incremental dynamic contributions must be performed. A splitting method based on spectral decomposition was proposed by König and Schuler [70] employing again RFAs. An alternative approach, referred to as the residual model method, was applied by Dykman and Rodden [30] using quasi-steady vortex lattice aerodynamics and by Lavretsky [79] and Winther et al. [136] using the p-transform of flutter point aerodynamic solutions. Looye [83] extended the approach to proper treatment of aerodynamic lag-states and Reschke [102] was the first to use a quasi-steady aerodynamic distribution model rather than total aircraft coefficients for coupling the rigid body motion and modal equations of motion.

1.1.3 Wake Vortex Encounters

Typically, aircraft wake vortex encounters are simulated using steady aerodynamic approaches like strip theory (Vicroy and Nguyen [128]), lifting surface (Kloidt [69]), vortex lattice (Lampe et al. [77]) or surface panel methods (Walden and van Dam [131]), that provide aerodynamic increments to existing flight dynamics simulation models. It is assumed that the incremental aerodynamic forces induced by the wake are not altered by aeroelastic effects, i.e. that the aircraft does not deform under the incremental load. Unsteady aerodynamic effects and wake deformation were considered by Karkehabadi [62] who applied the unsteady vortex lattice method with wake rollup to two aircraft passing each other on prescribed trajectories. The adequacy to use the vortex lattice method (VLM) for wake vortex effects was validated by Rossow [106]. Compared to flying quality and controllability studies, publications investigating the aspect of aircraft flight loads during WVE are only very few in number. The engineering study by Brown [13] used a simplified aircraft model restricted to lateral motion and employing the Wagner indicial function to model the unsteady aerodynamic behavior. The paper by Luber [85] presents analytical predictions and flight test results of the dynamic loads and accelerations of a fighter aircraft during aerial refueling and air combat but offers little insight in the employed model.

1.2 Objectives and Document Structure

The goal of this thesis is the development of a novel approach to the integral modelling of flexible aircraft. The model should enable the combined flight loads analysis of aircraft maneuvers and atmospheric disturbances, both for large amplitude motion in the time domain and small disturbance and stability analysis in the frequency domain. This requires proper representation of both rigid body motion and structural dynamic behavior of the aircraft, not only in terms of equation of motion, but also in terms of aerodynamic forces distributed over the aircraft. The aerodynamic model must cover the non-linear, quasi-steady aerodynamic effects stemming from the low frequency rigid body motion as well as unsteady, transient aerodynamic loading induced by structural vibration and atmospheric gust. A well-balanced trade off between accuracy and computational performance must be chosen in order to permit large scale parametric studies and use in iterative optimization processes. Also establishing the model must require a low effort and must be automatized to a large degree for the purpose of low process lead time and quick integration into parametric design processes. After the model has been developed, its usefulness is to be demonstrated in a suitable scenario relevant to flight loads analysis.

To reach these objectives, several model components are addressed in this thesis. In the first part of Chapter 2, the non-linear, quasi-steady aerodynamic model is described. It builds on an aerodynamic database that is queried by the flight state vector of the aircraft and yields the aerodynamic load distributions over the entire aircraft. In order to map the strip loads to a set of discrete aerodynamic forces on a surface reference grid, a mapping procedure conserving the total sum of forces an moments is established. In the second and major part of Chapter 2, the unsteady aerodynamic model is derived. Rather than starting from the customary frequency-domain based aerodynamic forces and moving to the time domain by RFA, the incompressible, potential-based unsteady vortex lattice method directly in the time domain is chosen here. The governing equations are derived leading to a discrete time stepping method applicable to both lifting surfaces and non-lifting bodies. In addition, a linearized formulation in continuous time state space form is consistently developed. This includes a solution of the singularity problem for non-lifting bodies when only vortex loops are used as singularity elements. Special cases for quasi-steady and steady flow are derived next. Based on the linearized formulation of the UVLM, the frequency domain harmonic vortex lattice method (HVLM) is derived. It permits aeroelastic stability analysis and additionally can serve as a means to optimize the wake discretization of the UVLM by direct comparison with the wake-less frequency-domain DLM. The next part is dedicated to a proposal how to correct the UVLM with steady aerodynamic reference data from wind tunnel or other high fidelity data sources to increase the accuracy and applicability of the method. To decrease the model size and increase the computational performance of the state space formulation of the UVLM, a order reduction of the wake states by way of balanced reduction applied to the wake panel strips is presented. Finally, numerical examples illustrating the influence of wake discretization and approaches for rate of incidence modelling are provided.

Chapter 3 contains the description of the reduced order mass and structural model.

The equations of motion for the flexible aircraft and equations of load with the underlying assumptions are presented. After that, alternative ways to obtain linearized small disturbance formulations from the linear modal equations of motion or the non-linear equations of motion are laid out.

The aeroelastic model integration, that is the connection of structural and aerodynamic models, is described in Chapter 4. To introduce the discrete aerodynamic forces from the two aerodynamic model parts into the aircraft structure and in turn translate the elastic deformation into deformation of the aerodynamic grid, an interconnection method based on finite interpolation elements is developed. The method is capable of interconnecting all 6 degrees of freedom on the aerodynamic and structural nodes and is particularly suited for reduced order structural models. In the second part of Chapter 4, model integration options depending on the desired application are presented.

The application of the flexible aircraft loads model is demonstrated in Chapter 5 using the example of wake vortex encounter. After introducing the wake model of a super category transport aircraft, a flight loads study for different encounter scenarii of a heavy category aircraft is presented. A variety of aircraft models with increasing complexity are compared in terms of structural loads and acceleration results and conclusions with respect to the adequacy of the models are drawn.

The final Chapter 6 summarizes the contributions of this thesis and proposes next steps recommendable for future research and improvement of the presented model.

1.3 A Motivational Example

This section introduces the residual model method (RMM) as a tool to consistently combine steady and unsteady aeroelastic data from different sources. Using the popular example of the typical aeroelastic section, the RMM is derived and its applicability to the simulation of flexible aircraft is deduced.

1.3.1 Aeroelastic System

Consider a NACA 1608 airfoil with a flap located at 75% of the profile chord which is part of the aeroelastic system depicted in Fig. 1.3. The system is modellized by a tension spring with stiffness K_h constraining the motion along the vertical coordinate h, a torsional spring with stiffness K_α constraining the pitching motion α of the complete airfoil and a torsional spring with stiffness K_δ constraining the flap deflection δ. Structural damping of the system is not considered. The structural state of the system can be fully described by the vector of generalized coordinates $\boldsymbol{x} = \{h, \alpha, \delta\}^{\mathrm{T}}$. The relative position a of the elastic axis (positive when the elastic axis is aft of midchord) and the relative position c of the flap hinge (positive when the flap hinge is aft of midchord) are given as fractions of the semi-chord length of the airfoil b. Defining the system control vector $\boldsymbol{u} = \{\alpha_c, \delta_c\}^{\mathrm{T}}$ with commanded incidence α_c and flap angle δ_c, the linear equation of motion of the system reads

$$\mathsf{M}\ddot{\boldsymbol{x}} + \mathsf{K}\boldsymbol{x} = \boldsymbol{p} + \mathsf{K}_c\boldsymbol{u} \tag{1.3.1}$$

where M is the structural mass matrix

$$\mathsf{M} = \begin{bmatrix} m & S_\alpha & S_\delta \\ S_\alpha & I_\alpha & I_\delta + b(c-a)S_\delta \\ S_\delta & I_\delta + b(c-a)S_\delta & I_\delta \end{bmatrix}$$

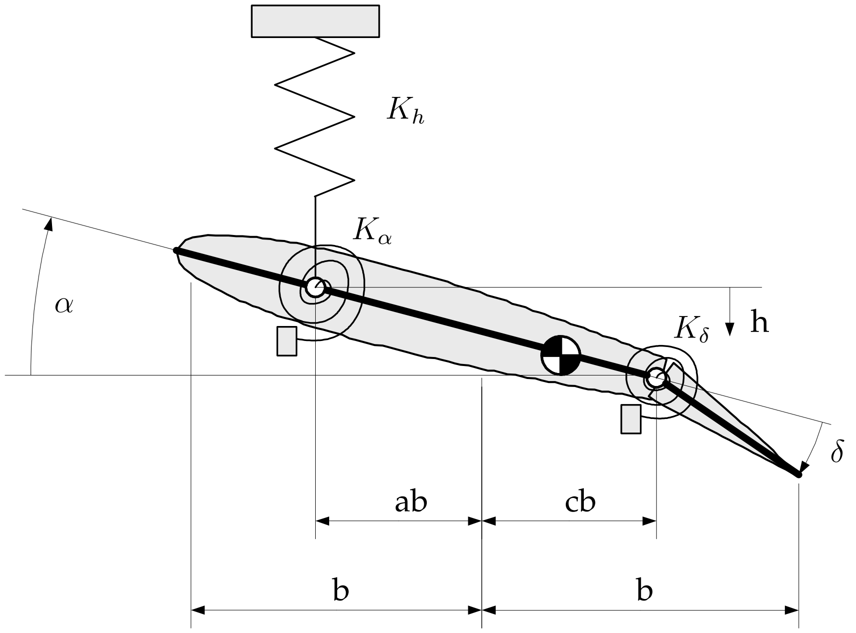

Figure 1.3: Aeroelastic System of an Airfoil with Flap

and m is the mass of the complete airfoil, I_α and S_α are the moment of inertia and the static moment of the complete airfoil with respect to the elastic axis and I_δ and S_δ are the moment of inertia and the static moment of the flap with respect to the flap hinge. The structural stiffness matrix K and control matrix K_c are defined as

$$K = \begin{bmatrix} K_h & 0 & 0 \\ 0 & K_\alpha & 0 \\ 0 & 0 & K_\delta \end{bmatrix}, K_c = \begin{bmatrix} 0 & 0 \\ K_\alpha & 0 \\ 0 & K_\delta \end{bmatrix}$$

as a function of the aforementioned spring stiffnesses. The vector of aerodynamic forces and moments with respect to the elastic axis and the flap hinge, $\boldsymbol{p} = \{F_h, M_\alpha, M_\delta\}^{\mathrm{T}}$, is obtained by transformation of the vector of non-dimensional aerodynamic coefficients $\tilde{\boldsymbol{p}} = \{C_L, C_{M25}, C_H\}^{\mathrm{T}}$

$$\boldsymbol{p} = q_\infty T_{\mathrm{EA}} \tilde{\boldsymbol{p}}$$

where q_∞ is the dynamic pressure and T_{EA} is the transformation matrix

$$T_{\mathrm{EA}} = \begin{bmatrix} 2b & 0 & 0 \\ 2(\frac{1}{2} + a)b^2 & 4b^2 & 0 \\ 0 & 0 & 4b^2 \end{bmatrix}$$

depending on geometric values only. All non-dimensional aerodynamic coefficients

$$C_L = \frac{F}{2q_\infty b}$$
$$C_{M25} = \frac{M_{25}}{4q_\infty b^2}$$
$$C_H = \frac{M_H}{4q_\infty b^2}$$

are referenced to the full chord length $2b$ of the profile.

1.3.2 Non-Linear Steady Aerodynamic Data

In this example, steady non-linear aerodynamic data for the airfoil is obtained using a surface panel method coupled to a boundary layer solver[1] at incompressible, viscous flow conditions described by a Mach number of $M = 0$ and a Reynolds number of $Re = 1.10^6$. For comparison, also inviscid results neglecting the boundary layer are computed. Polars are acquired for both the clean profile and with upward and downward flap deflection as depicted in Fig. 1.4.

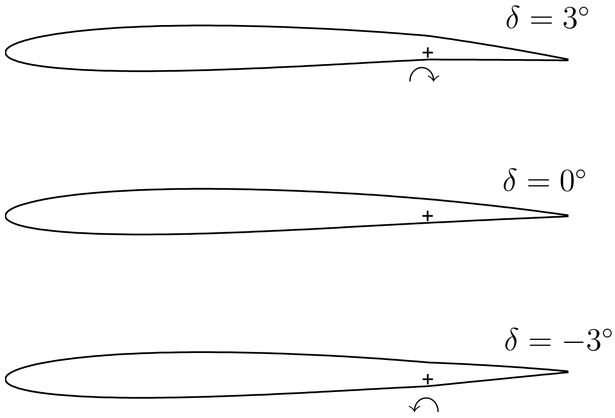

Figure 1.4: NACA 1608 Airfoil with Flap

In a post-processing step, the incremental effect of flap deflection δ is separated from the effect of angle of attack α, so the profile lift coefficient C_L, pitching moment coefficient with respect to 25% chord C_{M25} and flap hinge moment coeffcicient C_H formally can be written as:

$$\tilde{\boldsymbol{p}}^{\mathrm{NL}}(\alpha,\delta) = \begin{Bmatrix} C_L \\ C_{M25} \\ C_H \end{Bmatrix}_{\alpha,\delta=0} + \begin{Bmatrix} \Delta C_L \\ \Delta C_{M25} \\ \Delta C_H \end{Bmatrix}_{\alpha,\delta} \tag{1.3.2}$$

In the following, this precomputed aerodynamic forces are denoted by the superscript *"NL"* .

In Fig. 1.5, the lift and pitching moment coefficient of the profile without flap deflection are plotted as a function of angle of attack (black line) and compared to results neglecting viscosity (red line). For large positive and negative values of angle of attack, the non-linear influence of flow separation becomes apparent, in particular in terms of the pitching moment. In Fig. 1.6, the incremental lift and moment coefficient due to flap deflection δ are depicted. Again, flow separation leads to a strong dependency of flap efficiency on angle of attack in the viscous case. Finally in Fig. 1.7, the hinge moment coefficient of the flap as a function of angle of attack and flap angle is shown.

1.3.3 Linear Unsteady Aerodynamic Model

Because of the potentially rapid motion of the system, a theoretical unsteady aerodynamic method (in the following denoted by the superscript *"US"*) valid for incompressible, inviscid flow can be used instead of the steady non-linear database. The

---

[1] for a description of XFOIL see http://rafael.mit.edu/xfoil

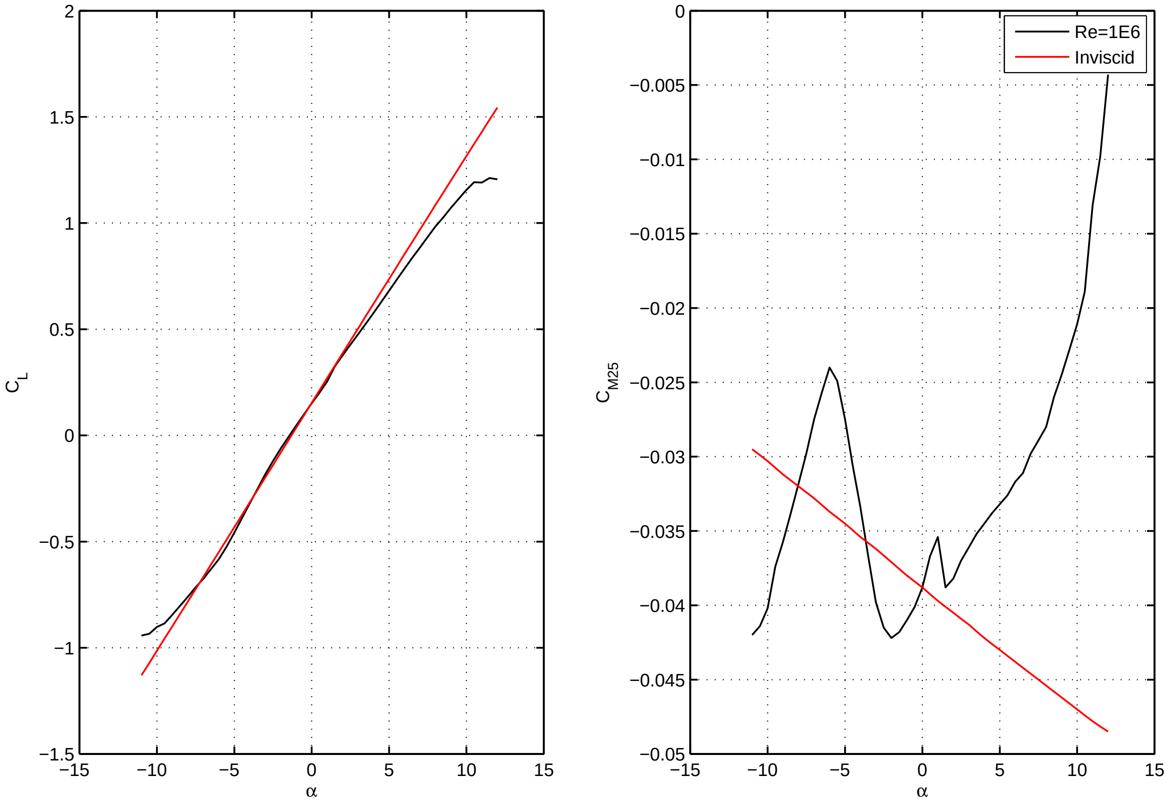

Figure 1.5: Airfoil Lift and Pitching Moment (Incidence Effect)

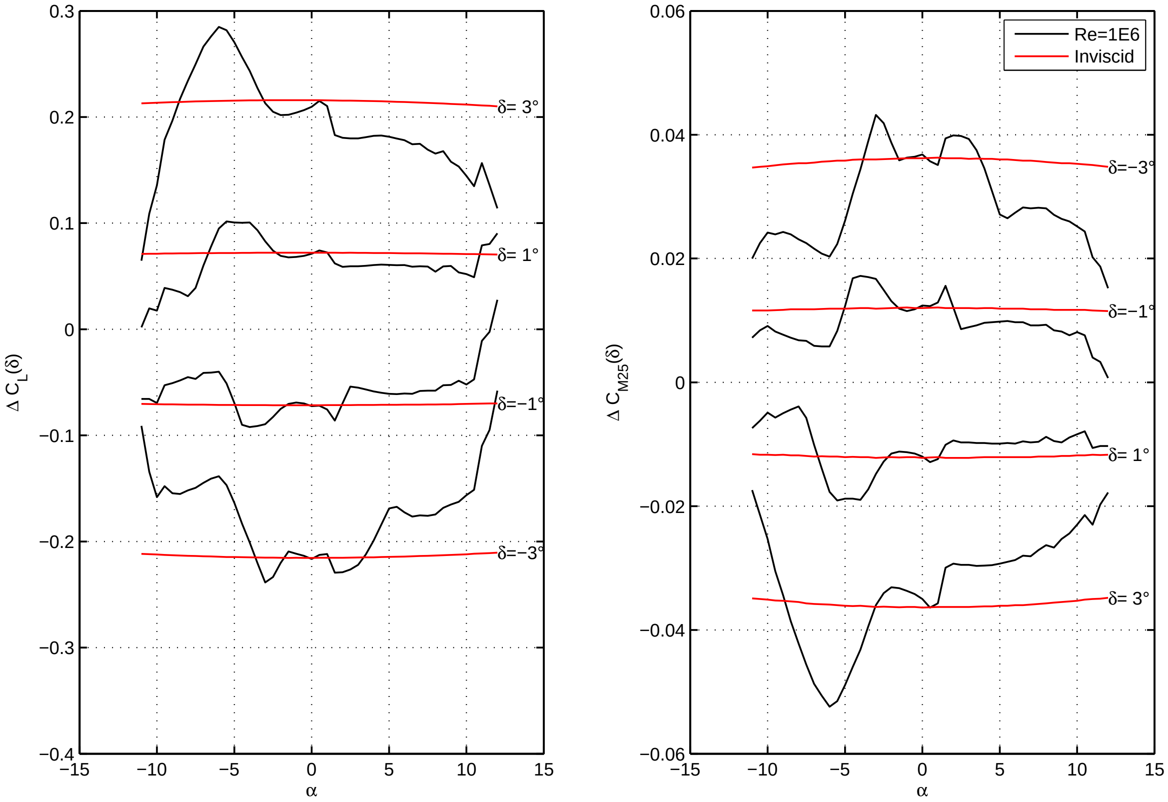

Figure 1.6: Incremental Lift and Pitching Moment due to Flap Deflection

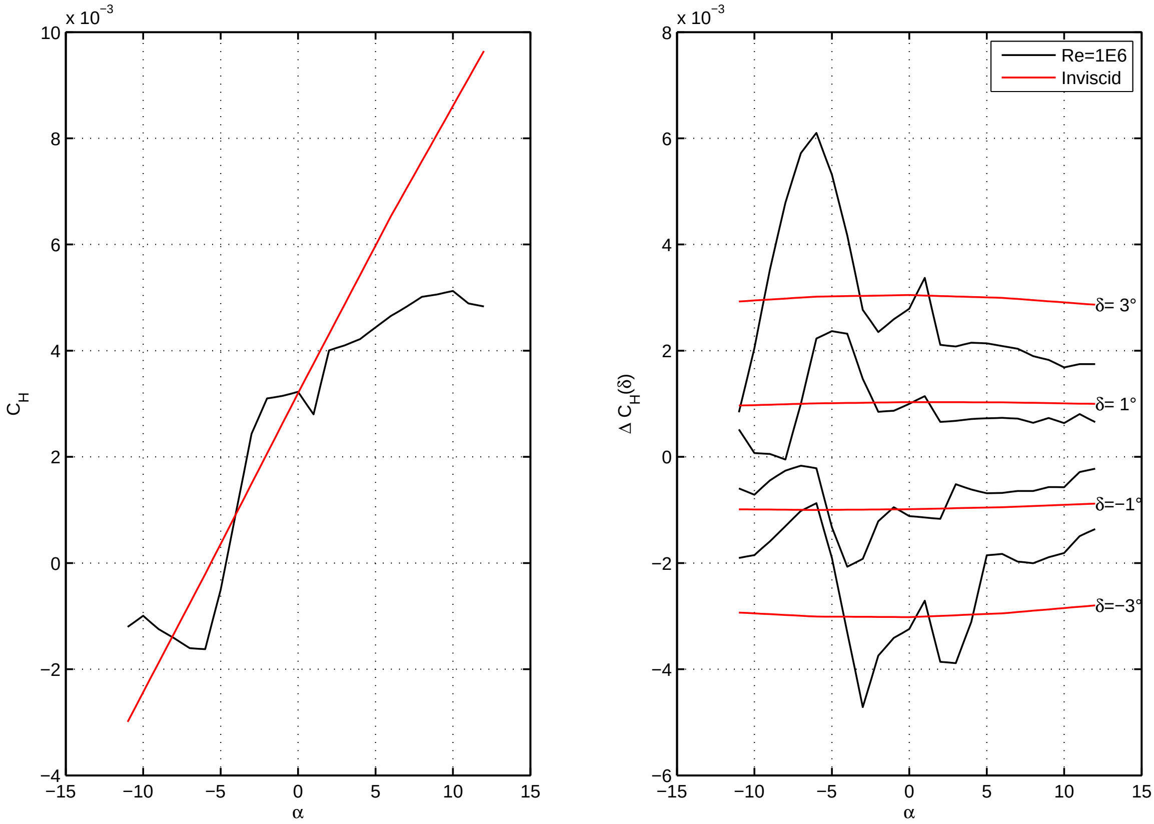

Figure 1.7: Airfoil Hinge Moment and Incremental Hinge Moment due to Flap Deflection

method represents the airfoil with flap by a chain of flat plates and thus neglects the airfoil thickness and camber, for details see Küssner and Göllnitz [74]. Adopting the notation typically employed for rational function approximation of frequency domain aerodynamic forces, this linear model can be written as a first order differential equation system for the aerodynamic lag states and an output equation yielding the aerodynamic coefficients

$$\begin{aligned} \dot{\boldsymbol{x}}_A &= E_0\boldsymbol{x} + E_1\dot{\boldsymbol{x}} + R\,\boldsymbol{x}_A \\ \tilde{\boldsymbol{p}}^{\mathrm{US}} &= \begin{Bmatrix} C_L \\ C_{M25} \\ C_H \end{Bmatrix}^{\mathrm{US}} = A_0\boldsymbol{x} + A_1\dot{\boldsymbol{x}} + A_2\ddot{\boldsymbol{x}} + D\,\boldsymbol{x}_A \end{aligned} \tag{1.3.3}$$

Here $\boldsymbol{x}_A$ is the vector of aerodynamic lag states and E_0, E_1 and R are the lag state system matrices characterizing the influence of the airfoil wake. The aerodynamic coefficient output is computed using the aerodynamic inertia A_2, damping A_1, stiffness A_0 and lag state D matrices. A quasi-steady version of the aerodynamic model (in the following denoted by the superscript *"QS"*) neglecting the aerodynamic mass effect and transient lag effect can be derived by letting $\dot{\boldsymbol{x}}_A = \ddot{\boldsymbol{x}} = 0$:

$$\tilde{\boldsymbol{p}}^{\mathrm{QS}} = \begin{Bmatrix} C_L \\ C_{M25} \\ C_H \end{Bmatrix}^{\mathrm{QS}} = \left(A_0 - DR^{-1}E_0\right)\boldsymbol{x} + \left(A_1 - DR^{-1}E_1\right)\dot{\boldsymbol{x}} \tag{1.3.4}$$

If the aeroelastic system is excited at low frequency, the accuracy of this type of model is typically sufficient.

1.3.4 Static Analysis using Non-Linear Steady Aerodynamic Data

As a first step we would like to study the static aeroelastic behavior of the system using the steady non-linear aerodynamic data presented above. Due to the interaction of the structural flexibility and the aerodynamic loading, the steady state response of the airfoil will deviate from the commanded incidence and flap angle and consequently its aerodynamic effectiveness will be different from the rigid case. Neglecting the transient response of the system to the control input, i.e. assuming steady state $\ddot{\boldsymbol{x}} = 0$, we can solve for the state vector in static equilibrium for a given control input $\boldsymbol{u}$:

$$\mathsf{K}\boldsymbol{x} = q_\infty \mathsf{T}_{\mathrm{EA}}\tilde{\boldsymbol{p}}^{\mathrm{NL}} + \mathsf{K}_c\boldsymbol{u} \tag{1.3.5}$$

Because the aerodynamic loading $\tilde{\boldsymbol{p}}^{\mathrm{NL}}$ is a tabulated, non-linear function of the state variables α and δ, this equation must be solved iteratively. The resulting aerodynamic forces in static aeroelastic equilibrium can be stored in reference to the commanded input parameters to yield a new database that can be regarded as an "elastified" or quasi-flexible version of the aerodynamic data (in the following denoted by the superscript *"QF"*). This introduces dynamic pressure as an additional independent parameter and therefore the aerodynamic model equation becomes

$$\tilde{\boldsymbol{p}}^{\mathrm{NL,QF}}(\alpha_c, \delta_c, q_\infty) = \left\{ \begin{array}{c} C_L \\ C_{M25} \\ C_H \end{array} \right\}_{\alpha_c, \delta_c = 0, q_\infty} + \left\{ \begin{array}{c} \Delta C_L \\ \Delta C_{M25} \\ \Delta C_H \end{array} \right\}_{\alpha_c, \delta_c, q_\infty} \tag{1.3.6}$$

In Figs. 1.8-1.10, the variation of airfoil lift, pitching moment and flap hinge moment with dynamic pressure is shown, where the location of the elastic axis has been chosen to be $a = -0.6$. For this position of the elastic axis, the effect of flexibility is both a reduction of aerodynamic efficiency as well as a shift of the non-linearities with respect to angle of attack. For the flexible hinge moment, this is a result of the rotation of the complete airfoil about the elastic axis in combination with the elastic deformation of the flap.

1.3.5 Static and Dynamic Analysis using the Linear Aerodynamic Model

We now turn to the static and dynamic analysis of the aeroelastic system employing the linear aerodynamic model. Three types of equation of motion for the aeroelastic system can be constructed depending on the choice of structural and aerodynamic model, where the aerodynamic coefficients have been defined as output quantities $\boldsymbol{y}$:

Model A is taking into account both the ability of the system to vibrate and unsteady aerodynamic forces according to Eq. (1.3.3) and can be written as

$$\begin{aligned} \mathsf{M}\ddot{\boldsymbol{x}} + \mathsf{K}\boldsymbol{x} &= q_\infty \mathsf{T}_{\mathrm{EA}} \left(\mathsf{A}_0\boldsymbol{x} + \mathsf{A}_1\dot{\boldsymbol{x}} + \mathsf{A}_2\ddot{\boldsymbol{x}} + \mathsf{D}\,\boldsymbol{x}_A \right) + \mathsf{K}_c\boldsymbol{u} \\ \dot{\boldsymbol{x}}_A &= \mathsf{E}_0\boldsymbol{x} + \mathsf{E}_1\dot{\boldsymbol{x}} + \mathsf{R}\,\boldsymbol{x}_A \\ \boldsymbol{y} &= \mathsf{A}_0\boldsymbol{x} + \mathsf{A}_1\dot{\boldsymbol{x}} + \mathsf{A}_2\ddot{\boldsymbol{x}} + \mathsf{D}\,\boldsymbol{x}_A \end{aligned} \tag{1.3.7}$$

Model B considers the vibrational behavior of the system but considers only quasi-

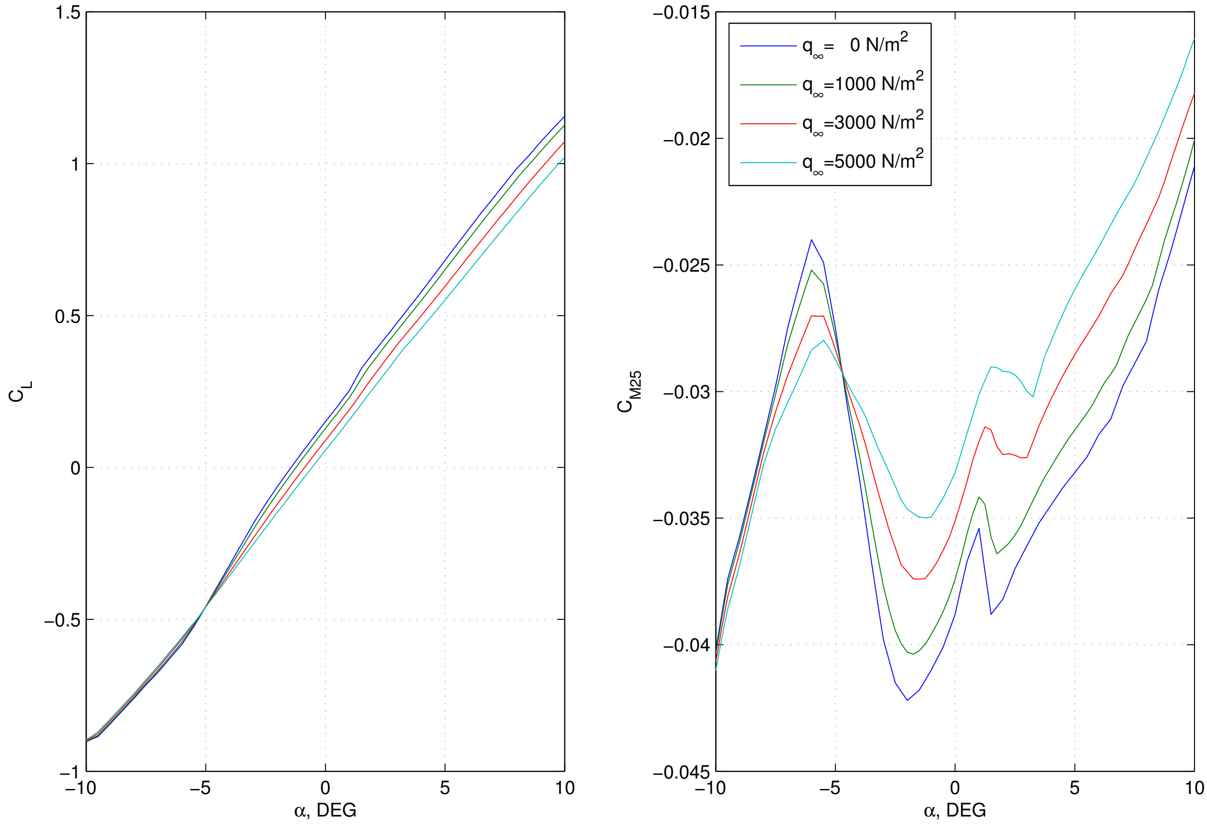

Figure 1.8: Flexible Airfoil Lift and Pitching Moment (Incidence Effect)

steady aerodynamic effects according to Eq. (1.3.4):

$$\begin{aligned} M\ddot{\boldsymbol{x}} + K\boldsymbol{x} &= q_\infty T_{\mathrm{EA}}\left[\left(A_0 - DR^{-1}E_0\right)\boldsymbol{x} + \left(A_1 - DR^{-1}E_1\right)\dot{\boldsymbol{x}}\right] + K_c\boldsymbol{u} \\ \boldsymbol{y} &= \left(A_0 - DR^{-1}E_0\right)\boldsymbol{x} + \left(A_1 - DR^{-1}E_1\right)\dot{\boldsymbol{x}} \end{aligned} \tag{1.3.8}$$

Model C is the steady-state solution obtained from Model A by letting $\ddot{\boldsymbol{x}} = \dot{\boldsymbol{x}} = \dot{\boldsymbol{x}}_A = 0$ and thus considers only the steady structural and aerodynamic behavior of the system.

$$\begin{aligned} \boldsymbol{x} &= \left[K - q_\infty T_{\mathrm{EA}}(A_0 - DR^{-1}E_0)\right]^{-1} K_c\boldsymbol{u} \\ \boldsymbol{y} &= \left(A_0 - DR^{-1}E_0\right)\boldsymbol{x} \end{aligned} \tag{1.3.9}$$

The output of these three models will be increasingly dissimilar the higher the frequency content of the input signal.

1.3.6 Comparison of the System Response

To illustrate the impact of modelling assumptions on the response of the aeroelastic system, simulations of a ramp input for angle of attack combined with a doublet input for flap angle are carried out. The results in terms of the state variables are compared in Fig. 1.11 also including the non-linear static results from section 1.3.4 denoted as Model D. Several important observations can be made. First, the flap doublet excites the system to vibrate at reduced frequencies where unsteady aerodynamic effects can be observed and therefore Model A and Model B yield different transients, mainly for the heave coordinate and the flap angle. Second, the results of Model C can be seen as

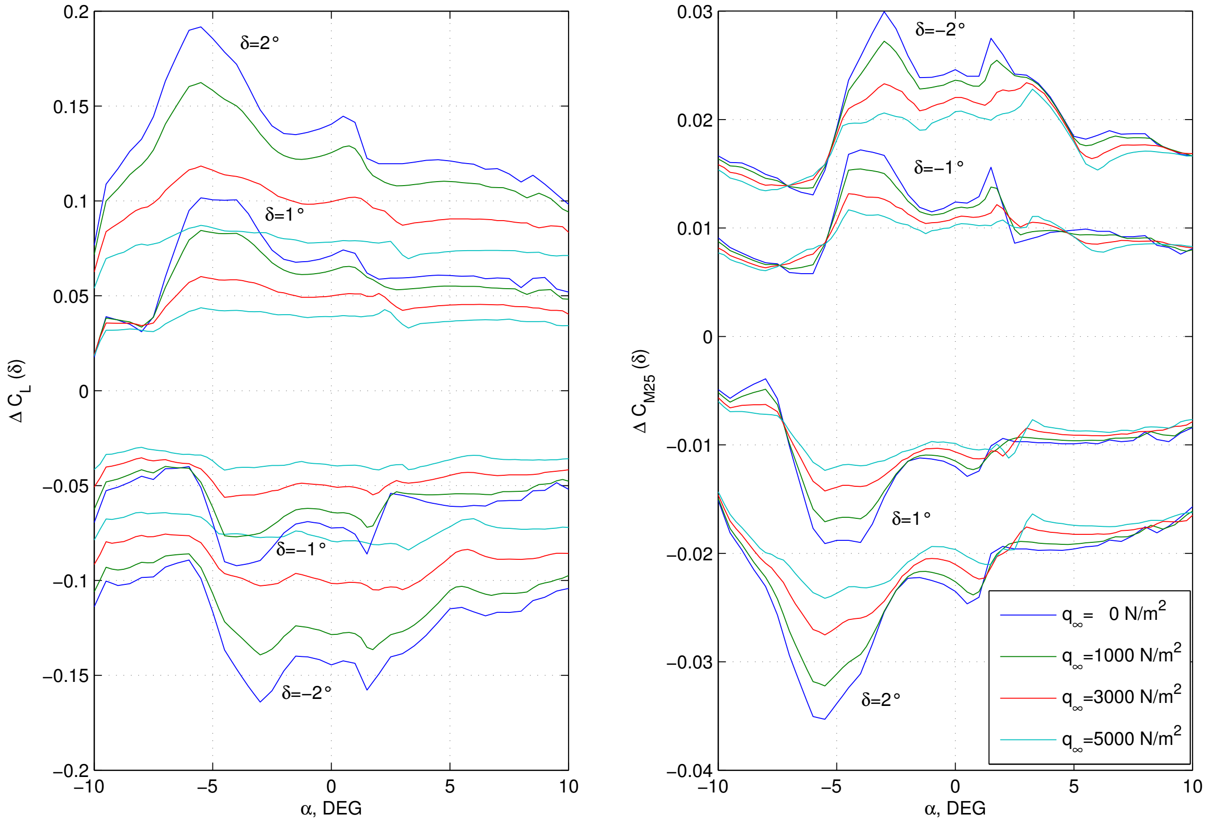

Figure 1.9: Flexible Incremental Lift and Pitching Moment due to Flap Deflection

the mean value about which the oscillations predicted by Model A and B occur. Nevertheless, due to the simplifying assumptions of the unsteady aerodynamic method, this mean value does not match the results from Model D which include the effects of thickness, camber and viscosity. Looking at the transient aerodynamic loads acting on the aeroelastic systems as shown in Fig. 1.12, we can observe the same characteristics and it can be concluded that for a reliable sizing of the tension and torsion springs it is desirable to combine the characteristics of Model A and Model D, i.e. modulate the dynamic behavior of Model A onto the static behavior of Model D. In the following section, modelling approaches to achieve this will be outlined.

1.3.7 The Residual Model Method

The most straightforward approach to combine the two aerodynamic data sources would be to simply remove the steady aerodynamic contribution Eq. (1.3.9) from the unsteady model Eq. (1.3.7) and add the contribution of the rigid non-linear database Eq. (1.3.2). This coupling based on rigid aerodynamic data however is not the direction in which we would like to proceed here. Rather we would like to make use of the non-linear aerodynamic data *including* the static aeroelastic correction from Eq. (1.3.6) and superimpose only the incremental dynamic contribution coming from aeroelastic model of Eq. (1.3.7). To avoid double accounting of the static aeroelastic effect, the overlap between the models must be removed before adding their outputs. To this end we postulate

The static behavior of the aeroelastic system is equivalent to the quasi-flexible cor-

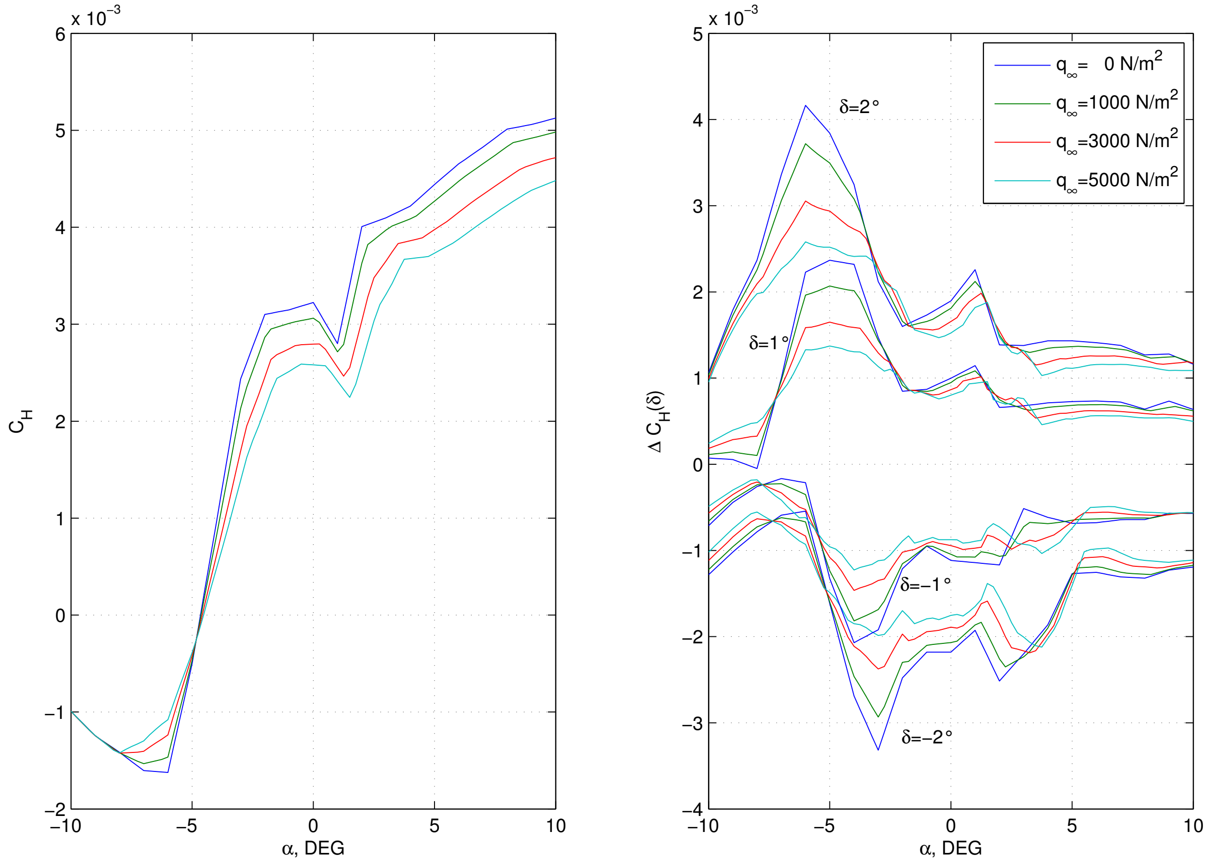

Figure 1.10: Flexible Airfoil Hinge Moment and Incremental Hinge Moment due to Flap Deflection

rection contained in the non-linear aerodynamic database.

and combine Eqn. (1.3.7) and (1.3.9) to produce an incremental dynamic output:

$$\begin{aligned} M\ddot{\boldsymbol{x}} + K\boldsymbol{x} &= q_\infty T_{\text{EA}} \left(A_0\boldsymbol{x} + A_1\dot{\boldsymbol{x}} + A_2\ddot{\boldsymbol{x}} + D\,\boldsymbol{x}_A\right) + K_c\boldsymbol{u} \\ \dot{\boldsymbol{x}}_A &= E_0\boldsymbol{x} + E_1\dot{\boldsymbol{x}} + R\,\boldsymbol{x}_A \\ \boldsymbol{x}_0 &= \left[K - q_\infty T_{\text{EA}}(A_0 - DR^{-1}E_0)\right]^{-1} K_c\boldsymbol{u} \\ \boldsymbol{y} &= A_0\left(\boldsymbol{x} - \boldsymbol{x}_0\right) + A_1\dot{\boldsymbol{x}} + A_2\ddot{\boldsymbol{x}} + D\,\boldsymbol{x}_A \end{aligned} \tag{1.3.10}$$

This model yields the aeroelastically corrected aerodynamic forces without the static aeroelastic contribution, an approach referred to as residual model method (RMM).

Even though not too apparent in the case of the simple example given, there are several good reasons for this approach:

1. The static aeroelastic correction can be based on a different structural model than the one underlying the dynamic aeroelastic model. For instance the static correction can be based on a highly detailed structural model in physical coordinates whereas the dynamic model can be limited to a low number of important dynamic modes unable to accurately capture the static behavior.

2. The computationally expensive iteration to obtain the non-linear static aeroelastic correction can be performed once as a pre-process.

3. Both models can be individually adapted to match experimental data. For instance the static model can be adapted to match flight test or can be the result of

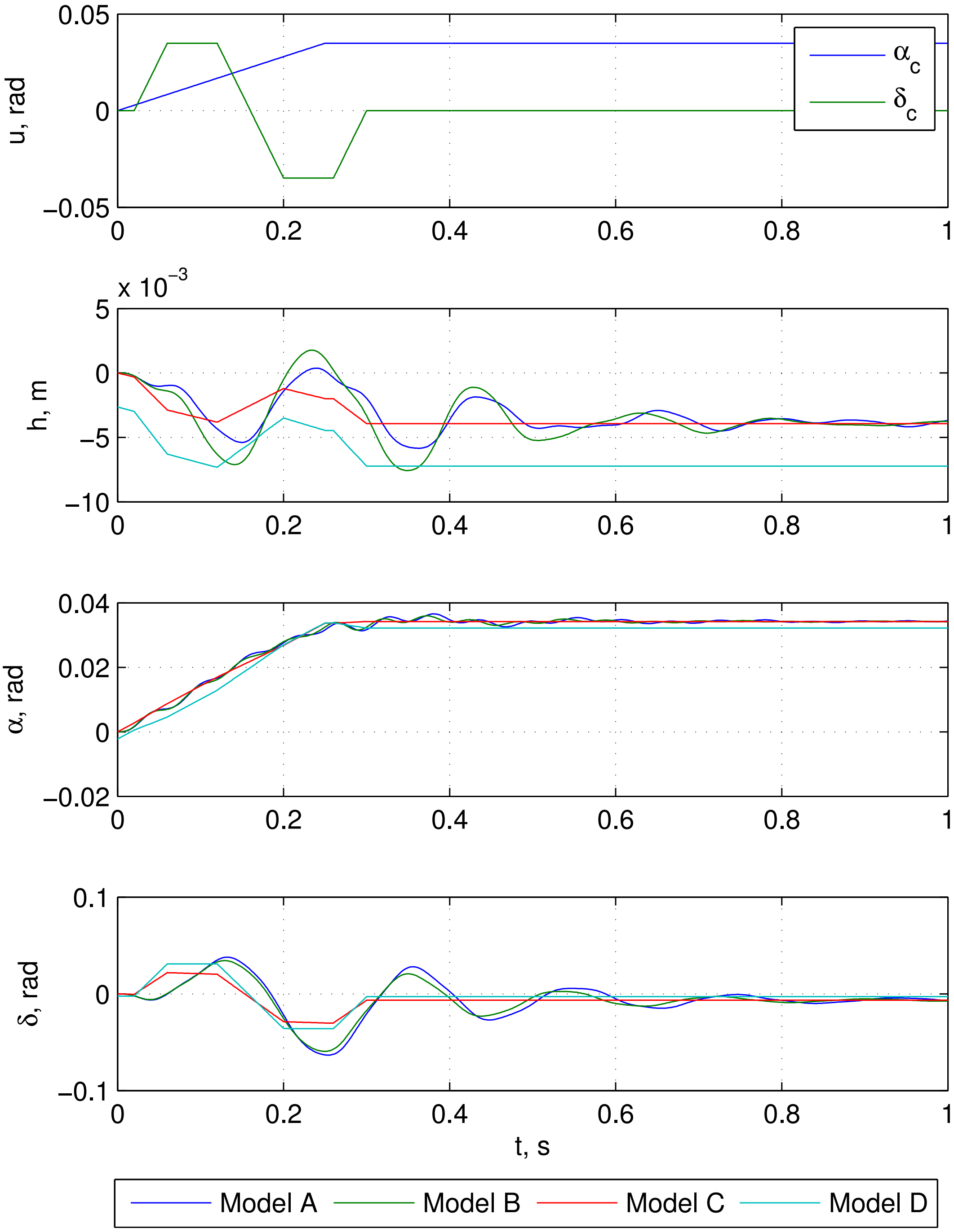

Figure 1.11: Response of different aeroelastic models

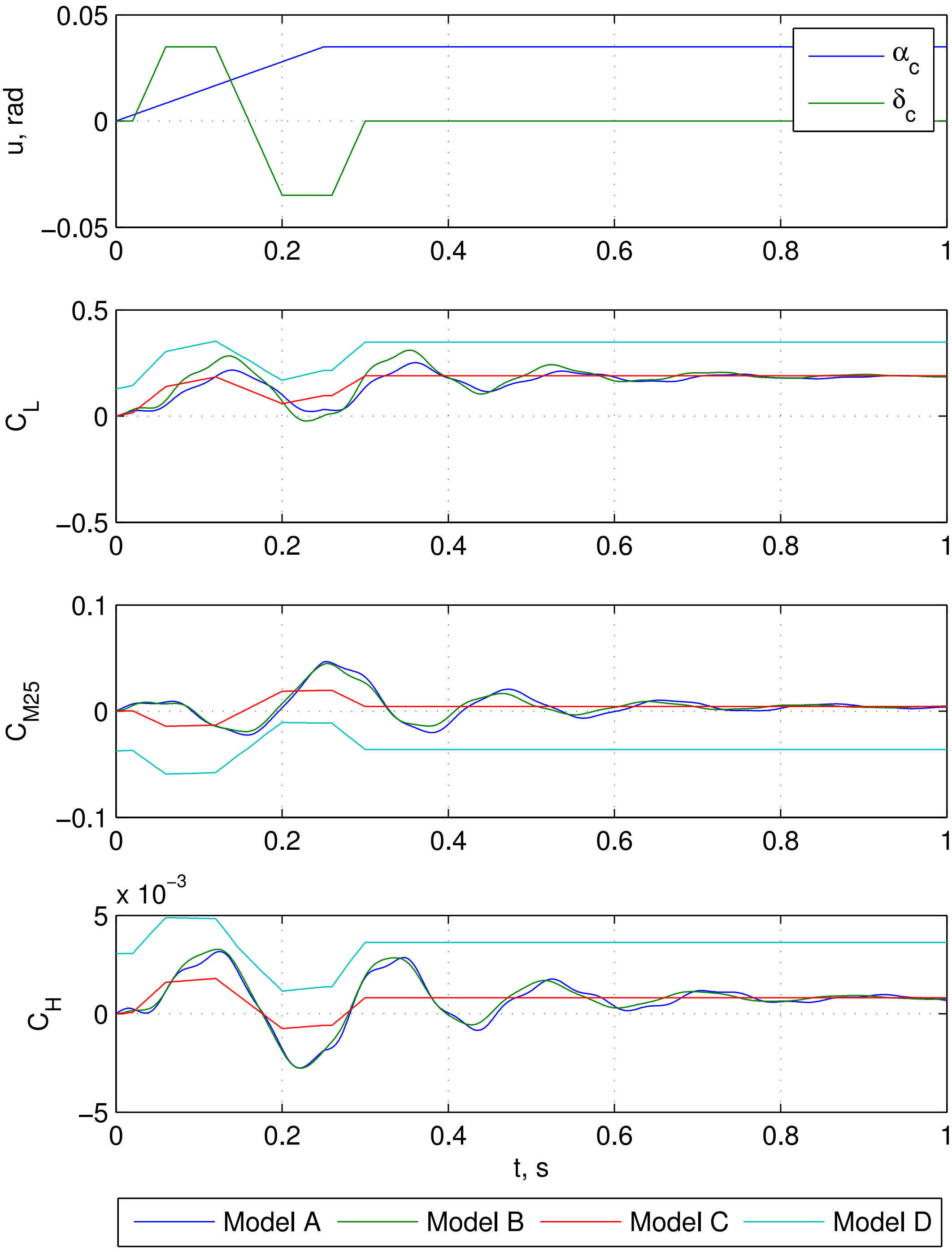

Figure 1.12: Transient Aerodynamic Loads of the Aeroelastic Models

a wind tunnel measurement with a flexible model. The dynamic model can be adapted to match ground vibration tests.

4. The dynamic incremental model can be treated as a simple add-on to an existing static analysis process.

The benefit of the approach for the aerodynamic loads of the typical section become obvious in Fig. 1.13. Shown are the aerodynamic pitching moment correlated to the aerodynamic lift for the input described in Section 1.3.6 and the convex hull of the correlation typically used to determine the sizing cases of the structure. From the comparison of Model A and Model C the importance of the dynamic structural and unsteady aerodynamic behavior for the given system excitation becomes evident. However due to the missing effects of thickness, camber and viscosity, the envelopes are shifted relative to the one from Model D. Application of the RMM pastes the incremental dynamic aeroelastic behavior of Model A onto the loads from the non-linear static Model D and yields a result that combines the advantages of Model A and Model D.

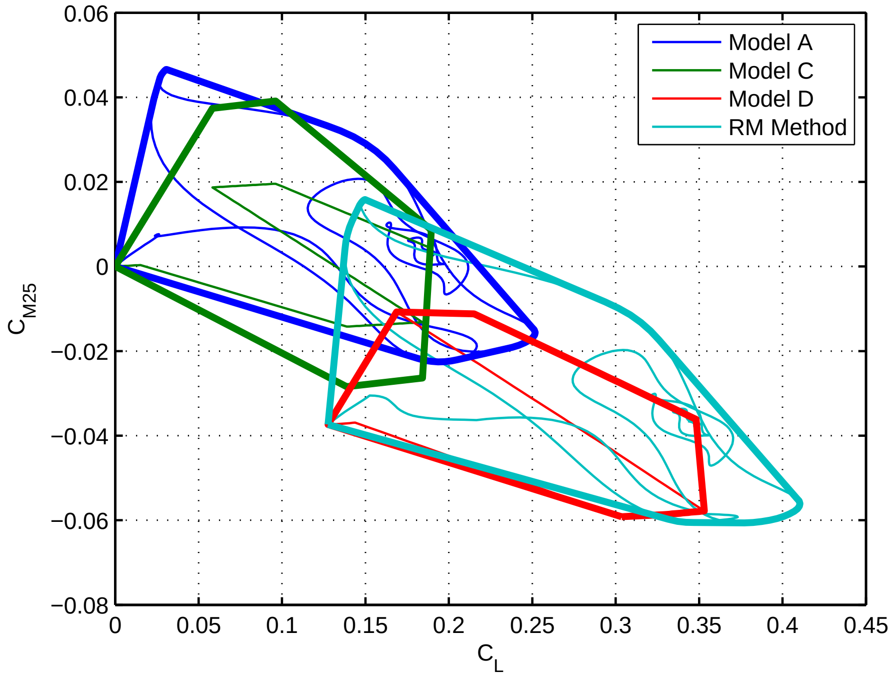

Figure 1.13: Comparison of Correlated Aerodynamic Loads

This thesis shall provide the model constituents necessary to apply the outlined coupling method to a full aircraft configuration with the aim to improve the time domain computation of flight loads when both large amplitude quasi-static effects and unsteady dynamic effects must be considered simultaneously.

2 Aerodynamic Models

The simulation of aircraft in flight requires the knowledge of the external forces acting on the body, of which the aerodynamic forces are of paramount importance. At the heart of every simulation platform lies an aerodynamic database, that feeds the differential equations of motion with the momentary aerodynamic forces and moments according to the aircraft state. Typically, during maneuvering of transport category aircraft the aircraft states change slow enough for the airflow to adjust to it instantaneously. Therefore the quasi-steady approximation of the aerodynamics is justified, e.g. the momentary flow field does not depend on the history of the aircraft motion. Once the aircraft experiences aerodynamic disturbances that have higher frequency content or that are of discrete nature as it is the case for atmospheric gust or rapid control surface actuation, unsteady aerodynamic effects appear and require additional modelling.

In this Chapter, the aerodynamic building blocks of the simulation model for combined maneuver and gust are described. In Section 2.1, an overview of the provided legacy database for quasi-steady aerodynamics is given and necessary extensions for the coupling with a structural model are outlined. The description of the numerical unsteady aerodynamic model follows in Section 2.2, where the derivation of the governing equations, the solution method and numerical examples are presented.

2.1 Quasi-steady Aerodynamic Database

During the design cycle of a new aircraft, aerodynamic properties of the airframe geometry are obtained from several sources. In the early stage, when the geometry definition is not yet frozen, semi-empirical methods and simple numerical methods help to establish the design concept. Once a limited number of promising configurations has been short-listed, more costly numerical analysis, for instance computational fluid dynamics (CFD), and early wind tunnel campaigns can be initiated. After the design freeze, the aerodynamic view on the design is successively elaborated by more extensive numerical and experimental data acquisition and finally confirmed by flight test. The means to share the bulk of aerodynamic design information with the engineering community is typically an increasingly detailed database, into which new data from the aforementioned sources must be continuously integrated in a consistent manner. The database describes the aerodynamic loading of the aircraft as a function of numerous parameters that can be categorized as follows:

1. parameters describing the motion of the aircraft: for example angle of attack, rate of rotation about one of the body axes or control surface deflections,
2. parameters describing the flight regime: for example Mach number or if the aircraft is in ground effect,

3. parameters describing the aircraft configuration: for example the setting of slats and flaps or the state of the landing gear.

To reduce the amount of stored data and to provide a continuous description of the aerodynamic behavior, analytical functions of the category 1 parameters are typically fitted to the raw data. The analytical models are then stored for a carpet of discrete parameter values from categories 2 and 3, as for these analytical descriptions are not required or would be too complex to establish. The availability of analytical models also facilitates the understanding of the physical behavior of the aircraft and additionally permits the systematic alteration of the aerodynamic characteristics. For instance, at an early stage of the development cycle, the aerodynamic data can be based on the scaled analytical model of a previous aircraft design (provided the aerodynamic characteristics are expected to be similar). The analytical model is also helpful for the consistent update of the database once new aerodynamic data is available and for the identification of key aerodynamic parameters during flight test.

The aerodynamic data set required for flight loads analysis largely exceeds the amount of data for pure aircraft response simulation, e.g. handling qualities (HQ) assessment or pilot training. The latter focusses on an accurate representation of the non-linear behavior of the total aircraft and usually only distinguishes between wing-fuselage-pod (WFP) and empennage contributions to the overall aerodynamic load. In a wind tunnel, this type of data can be obtained by using separate balances for the entire model and the empennage or by differential measurement with and without tail surfaces. Typical wind tunnel models in high lift and cruise configuration are shown in Fig. 2.1. Flight load analysis, however, requires the knowledge of the aerodynamic load distribution over the airframe in order to quantify the loads critical for sizing of the structural components. The data acquisition in a wind tunnel must be performed by measuring both, pressure distributions on the aircraft surface and total aircraft and empennage loads for data harmonization. Typically this imposes limitations on the level of complexity of the analytical aerodynamic model due to the fact that consistency must be maintained down to the level of sub-components as slats and flaps. Take for instance a typical total aircraft lift curve C_L over angle of attack α as depicted in Fig. 2.2. Up to the onset of stall at α_1 the lift curve slope is approximately constant, e.g. lift is a linear function of angle of attack. Beyond α_1, the lift curve exhibits a non-linear behavior as indicated by the dashed-dotted line and reaches its maximum $(C_L)_{max}$ at


(a) High Lift Configuration (b) Cruise Configuration

Figure 2.1: Wind Tunnel Models (Source: DLR)

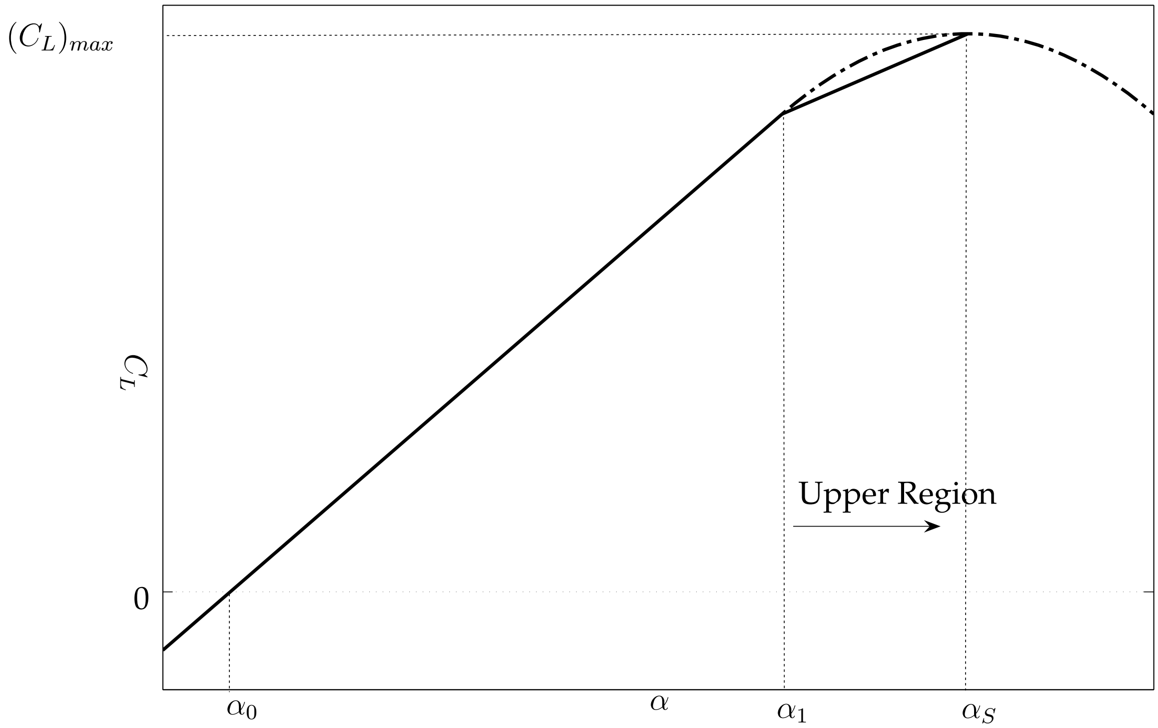

Figure 2.2: Piecewise Linear Incidence Model

α_s. Rather than attempting to retain the exact non-linear lift curve, the aerodynamic model for loads analysis establishes a piecewise linear lift curve model able to capture the onset of stall at α_1 and the maximum lift at α_s. This implies that only one consistent set of component distributions needs to be derived for each region rather than storing the full set of load distributions for numerous angles of attack. Depending on the stall behavior of the given aircraft, the number of linear regions can vary. The stall breakpoint α_1 must be carefully chosen to ensure that the sectional stall behavior on the wing is adequately retained. To this end, the stall onset of a mid-wing station can be taken as the reference.

In the following section, some examples of analytical model assumptions are presented.

2.1.1 Examples of Modelling Assumptions

The starting point for the development of modelling assumptions is the Taylor series expansion of the aerodynamic loads with respect to the parameters of interest. Some aerodynamic effects on the aircraft can be modelled as a function of a single parameter only, effectively using only the first order term of the expansion. As an example, loads due to incidence can be described by the following piecewise linear formulation

$$\begin{aligned}
C_{i,\alpha} &= \frac{\partial C_i}{\partial \alpha}(\alpha - \alpha_0) + \Delta C_{i,\alpha}^{\text{upper}} \\
\Delta C_{i,\alpha}^{\text{upper}} &= \begin{cases} \left(\frac{\partial C_i}{\partial \alpha}\right)^{\text{upper}} (\alpha - \alpha_1) & \text{for} \quad \alpha > \alpha_1 \\ 0 & \text{for} \quad \alpha \le \alpha_1 \end{cases} \\
&\text{with} \quad i = x, y, z, l, m, n
\end{aligned}$$

where α_0 is the incidence for zero lift and α_1 is the incidence of stall onset. Other effects, for example incremental loads due to sideslip angle β, must be modelled using two parameters and thus require also some of the second order terms of the Taylor series expansion

$$\begin{aligned}\Delta C_{i,\beta} &= \left(\frac{\partial C_i}{\partial \beta} + \frac{\partial C_i}{\partial \beta \partial \alpha}(\alpha - \alpha_0)\right)\beta \\ &\text{with} \quad i = x, y, z, l, m, n\end{aligned}$$

The non-linear behavior of some aerodynamic effects would require additional higher order terms to be retained and it is often easier to partially tabulate the data in favor of a complex analytical model. As an example, incremental loads due to aileron deflection δ_a are modelled as

$$\begin{aligned}\Delta C_{i,\delta_a} &= \Delta C_{i0}|_{\delta_a} + \left.\frac{\partial C_i(\delta_a)}{\partial \alpha}\right|_{\delta_a}(\alpha - \alpha_0) \\ &\text{with} \quad i = x, y, z, l, m, n\end{aligned}$$

and consequently use an analytical model for the incidence effect and table-lookup for the deflection effect.

2.1.2 Quasi-Steady Approximation

In addition to steady state information, the aerodynamic database used here contains loads for rotational rates about the body axes, also referred to as aerodynamic damping loads, and rate of incidence. To illustrate the difference between these effects, three aircraft motions with zero rate of pitch, zero rate of incidence and combined rate of pitch and incidence, respectively, are depicted in Fig. 2.3. Acceleration about the vertical body axis, e.g. rate of angle of attack, is an unsteady aerodynamic effect that in general requires a transfer function model. As pointed out by Etkin [34], the conventional derivatives fail to give an accurate value of the instantaneous forces, because they are independent of the history of the motion. However, for transport category aircraft the time scale for rigid body motion is typically large and the flow field is changing slowly. Therefore it is adequate to approximate rate of incidence effects using a non-linear lag-in-downwash model as described by Etkin and Reid [35]

$$\begin{aligned}\Delta C_{i,\dot\alpha} &= \frac{\partial C_i}{\partial \dot\alpha}\,\dot\alpha = -\frac{\partial C_i^{HTP}}{\partial \alpha}\left.\left(\frac{d\epsilon}{d\alpha}\right)\right|_{\alpha}\frac{l_H}{V}\,\dot\alpha \\ &\text{with} \quad i = x, y, z, l, m, n\end{aligned}$$

with the underlying assumption, that the downwash at the tail ϵ does not immediately react to a change of angle of attack on the wing. The delay is characterized by the time a fluid particle on the wing requires to convect to the horizontal tail $\Delta t = \frac{l_H}{V}$, where l_H is the lever arm of the horizontal tail, typically taken as the distance between the quarter chord points of the aerodynamic mean chords, and V is the flight speed. In other words, the tail downwash $\epsilon(t)$ corresponds to a wing incidence $\alpha(t - \Delta t)$. This approximation considers the contribution of the horizontal tail only, the sidewash effect on the vertical tail and the unsteady wing lift are neglected.

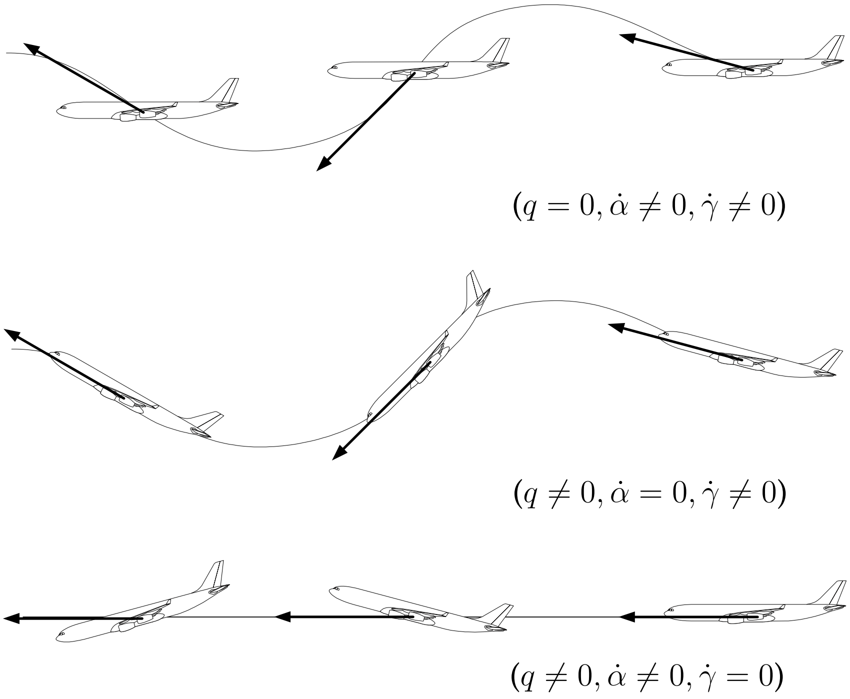

Figure 2.3: Significance of Rate of Pitch and Rate of Incidence (after Etkin and Reid [35], Moulder et al. [94])

2.1.3 Static Aeroelastic Considerations

Structural flexibility causes the aircraft to deform under aerodynamic load which in turn affects the aerodynamic characteristics. Because it is not feasible to acquire the full set of aerodynamic data for multiple aircraft shapes, typically the shape of the aircraft in cruise condition with a representative mass distribution is determined and data production is performed for that reference shape only. The resulting database for the rigid aircraft then requires additional aeroelastic corrections for deviations of mass distribution, flight condition and load factors from the reference condition. The correction terms are typically derived by linear aeroelastic methods and significantly increase the size of the database. In Fig. 2.4, the actual wing shape of a transport aircraft during flight test is shown in comparison to the corresponding correction model. An

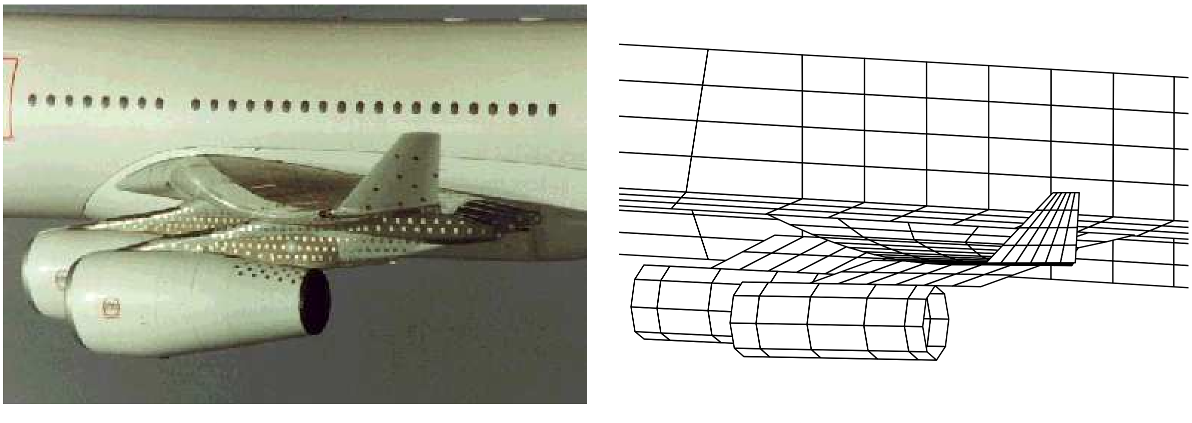

(a) Flight Measurement (b) Correction Model

Figure 2.4: Aeroelastic Deformation

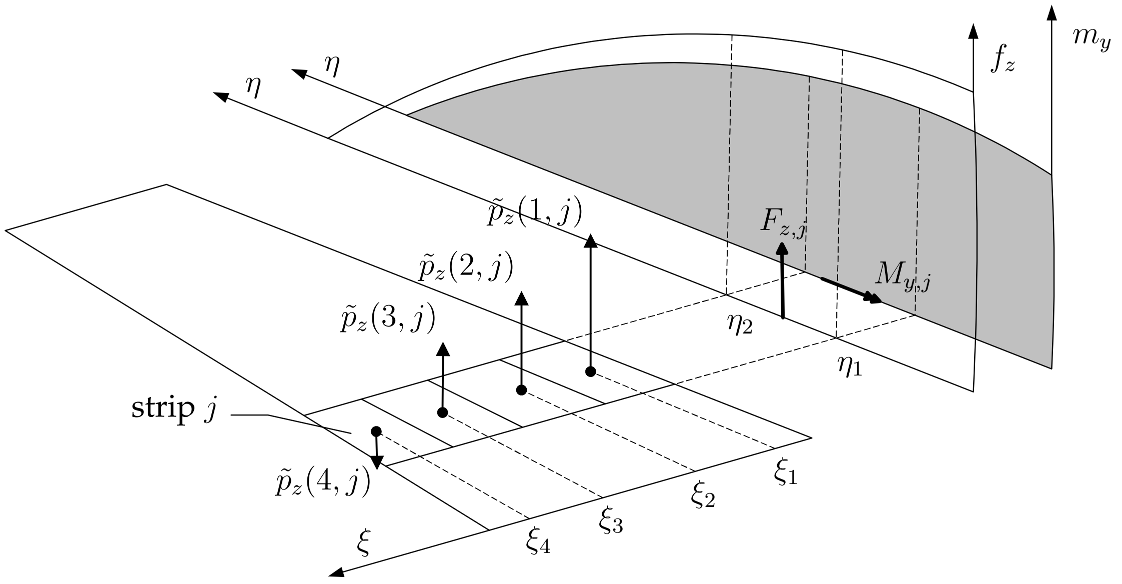

Figure 2.5: Mapping to the Reference Grid

exception is the modelling of the angle of attack at the horizontal tail α_r, that already includes a term due to the vertical load factor n_z

$$\alpha_r = \alpha + i_h - \left.\frac{\partial\epsilon}{\partial\alpha}\right|_{\alpha} \alpha - \frac{\partial\epsilon}{\partial n_z} n_z$$

and captures the change of downwash angle ϵ due to the distortion of the wing.

2.1.4 Mapping of Load Distributions

The aerodynamic loads contained in the database are stored as distributed sectional forces and moments. To ensure consistency of the load transfer into the structural model, a mapping of the one-dimensional distributions onto a two-dimensional aerodynamic reference grid must be performed. The mapping procedure translates the sectional forces and moments into discrete forces acting on the panels of the reference grid as depicted in Fig. 2.5. Integrating the lift and moment distributions between the boundaries of a chordwise strip of the reference grid yields a strip load vector $\boldsymbol{p} = \{F_x, F_y, F_z, M_x, M_y, M_z\}^{\mathrm{T}}$, that must be matched by the total load and moment resulting from the discrete panels forces on the strip . Because the number of panels per strip N_{C} is typically more than 6, there are more unknowns than constraint equations and an assumption has to be made how the forces are distributed in the chordwise direction. To this end, the first two *Birnbaum-Ackermann* normal distributions as described by Schlichting and Truckenbrodt [109] are selected as shape functions and are shown in Fig. 2.6. They represent the pressure distribution on an inclined flat plate and parabolically cambered thin airfoil, respectively, and are seen as a simple, yet physical choice. In a first step, the mapping procedure is applied to the z- and y-components of the load. An equation system for N_{S} strips with the shape function scaling factors as unknowns is set up

$$\boldsymbol{p}_z = \mathsf{SC}\boldsymbol{a}_z \tag{2.1.1a}$$

$$\boldsymbol{p}_y = \mathsf{SC}\boldsymbol{a}_y \tag{2.1.1b}$$

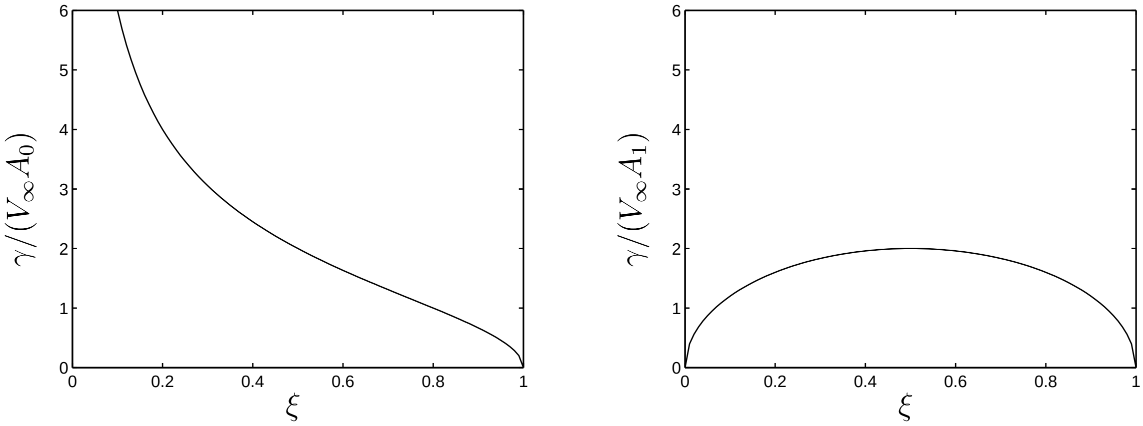

(a) Inclined Flat Plate (b) Parabolical Thin Airfoil

Figure 2.6: Load Distributions according to Birnbaum-Ackermann

where $\boldsymbol{p}_z$ and $\boldsymbol{p}_y$ are the strip load vectors

$$\boldsymbol{p}_z = \begin{Bmatrix} F_{z,1} \\ -M_{y,1} \\ \vdots \\ F_{z,N_\mathrm{S}} \\ -M_{y,N_\mathrm{S}} \end{Bmatrix}, \quad \boldsymbol{p}_y = \begin{Bmatrix} F_{y,1} \\ M_{z,1} \\ \vdots \\ F_{y,N_\mathrm{S}} \\ M_{z,N_\mathrm{S}} \end{Bmatrix},$$

stemming from the stripwise integration of the load and moment distributions coming from the database. The strip summation matrix S

$$S = \begin{bmatrix} S_1 & 0 & \dots & 0 \\ 0 & S_2 & \dots & 0 \\ \vdots & \vdots & \ddots & \vdots \\ 0 & 0 & \dots & S_{N_\mathrm{S}} \end{bmatrix} \quad \text{with} \quad S_j = \begin{bmatrix} 1 & \dots & 1 \\ \Delta l(1,j) & \dots & \Delta l(N_\mathrm{C}(j),j) \end{bmatrix},$$

sums up the panel forces in one strip and computes the strip moment with respect to its leading edge using the panel lever arms Δl. The shape function coefficient matrix C

$$C = \begin{bmatrix} C_1 & 0 & \dots & 0 \\ 0 & C_2 & \dots & 0 \\ \vdots & \vdots & \ddots & \vdots \\ 0 & 0 & \dots & C_{N_\mathrm{S}} \end{bmatrix} \quad \text{with} \quad C_j = \begin{bmatrix} C_0(1,j) & C_1(1,j) \\ \vdots & \vdots \\ C_0(N_\mathrm{C}(j),j) & C_1(N_\mathrm{C}(j),j) \end{bmatrix}$$

contains the values of the shape functions. The weighted coefficients of the first and second *Birnbaum-Ackermann* normal distributions are

$$\begin{aligned} C_0(i,j) &= 2\,\frac{\Delta c(i,j)}{c(j)}\sqrt{\frac{1-\xi(i,j)}{\xi(i,j)}} \\ C_1(i,j) &= 4\,\frac{\Delta c(i,j)}{c(j)}\sqrt{\xi(i,j)(1-\xi(i,j))} \end{aligned}$$

respectively, where $\frac{\Delta c}{c}$ is the relative panel chord and ξ is the non-dimensional chordwise coordinate of the panel centroid. Finally $\boldsymbol{a}_z$ and $\boldsymbol{a}_y$ are the vectors

$$\boldsymbol{a}_z = \begin{Bmatrix} a_{z0,1} \\ a_{z1,1} \\ \vdots \\ a_{z0,N_\mathrm{S}} \\ a_{z1,N_\mathrm{S}} \end{Bmatrix}, \qquad \boldsymbol{a}_y = \begin{Bmatrix} a_{y0,1} \\ a_{y1,1} \\ \vdots \\ a_{y0,N_\mathrm{S}} \\ a_{y1,N_\mathrm{S}} \end{Bmatrix}$$

with respectively $2N_\mathrm{S}$ unknown scaling factors. The force components $\tilde{p}_z$ and $\tilde{p}_y$ of a panel i in strip j are then computed from

$$\begin{aligned} \tilde{p}_z(i,j) &= \{C_0(i,j) \quad C_1(i,j)\} \begin{Bmatrix} a_{z0,j} \\ a_{z1,j} \end{Bmatrix} \\ \tilde{p}_y(i,j) &= \{C_0(i,j) \quad C_1(i,j)\} \begin{Bmatrix} a_{y0,j} \\ a_{y1,j} \end{Bmatrix} \end{aligned}$$

In a second step, the x-component of the panel forces $\tilde{p}_x$ is found by distributing the x-component of the strip load proportional to the magnitude of the mapped forces from step 1. This purely empirical assumption is chosen for convenience. For a panel i in strip j this can be written as

$$\tilde{p}_x(i,j) = \frac{\sqrt{\tilde{p}_y(i,j)^2 + \tilde{p}_z(i,j)^2}}{\sum_{i=1}^{N_\mathrm{c}(j)} \sqrt{\tilde{p}_y(i,j)^2 + \tilde{p}_z(i,j)^2}} \quad F_{x,j}.$$

The resulting mapped discrete forces are finally sorted into the overall vector of aerodynamic panel loads $\boldsymbol{P}_\mathrm{A}^\mathrm{NL}$ of length $6N_\mathrm{P}$ with all aerodynamic moments about the panel centroids set to zero:

$$\boldsymbol{P}_\mathrm{A}^\mathrm{NL} = \begin{Bmatrix} \tilde{\boldsymbol{p}}_1 \\ \vdots \\ \tilde{\boldsymbol{p}}_{N_\mathrm{P}} \end{Bmatrix} \quad \text{with} \quad \tilde{\boldsymbol{p}}_i = \begin{Bmatrix} \tilde{p}_x \\ \tilde{p}_y \\ \tilde{p}_z \\ 0 \\ 0 \\ 0 \end{Bmatrix} \tag{2.1.2}$$

To illustrate this procedure, Fig. 2.7 depicts the mapping of the aerodynamic loading of a typical transport aircraft wing. In Fig. 2.7(a), the database output of distributed force f_z and moment m_y versus the non-dimensional spanwise coordinate $\eta = 2y/b$ is plotted. By stripwise integration, the strip forces F_z and moments M_y as shown in Fig. 2.7(b) are obtained. The solution of Eq. (2.1.1) yields the shape function parameters for incidence a_{z0} and camber a_{z1} drawn in Fig. 2.7(c), that lead to the discrete forces on the reference grid in Fig. 2.7(d).

2.1.5 Implementation

The implementation of the aerodynamic database into SIMULINK consists of three modules as depicted in Fig. 2.8. For a given aircraft state, the aerodynamic component module (ACM) outputs the contributions of the aircraft components (wing, fuselage etc.) to the total forces and moments. In addition, every component contribution is further split up into aerodynamic effects. Also control surface hinge moments and

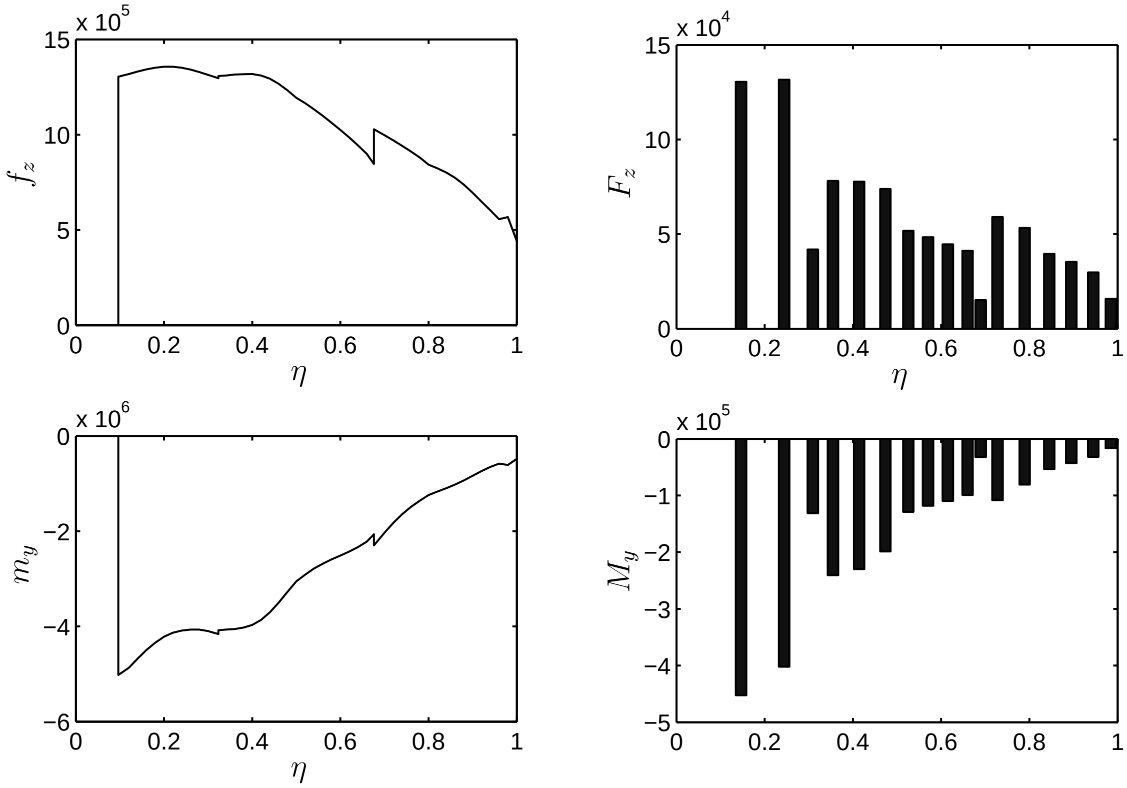

(a) Distributed Loads

(b) Integrated Loads on Reference Strips

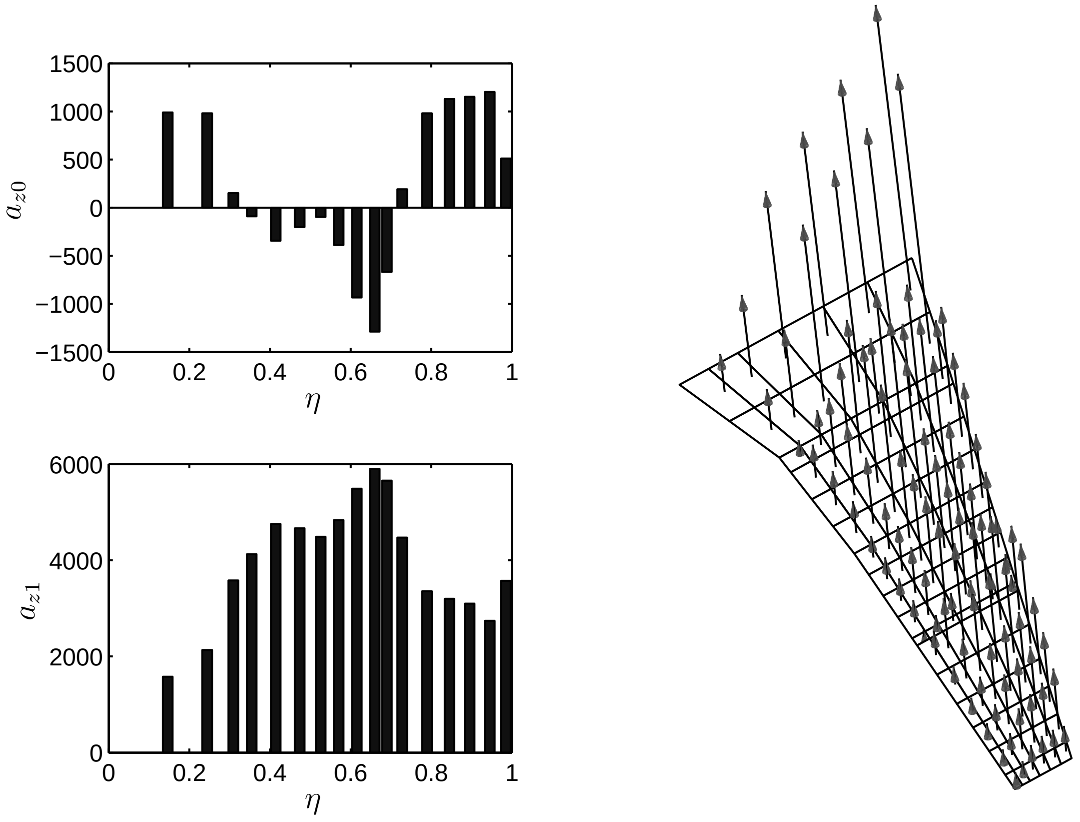

(c) Shape Function Scaling Parameters

(d) Mapped Loads on Reference Grid

Figure 2.7: Example of Mapping Procedure for a Wing

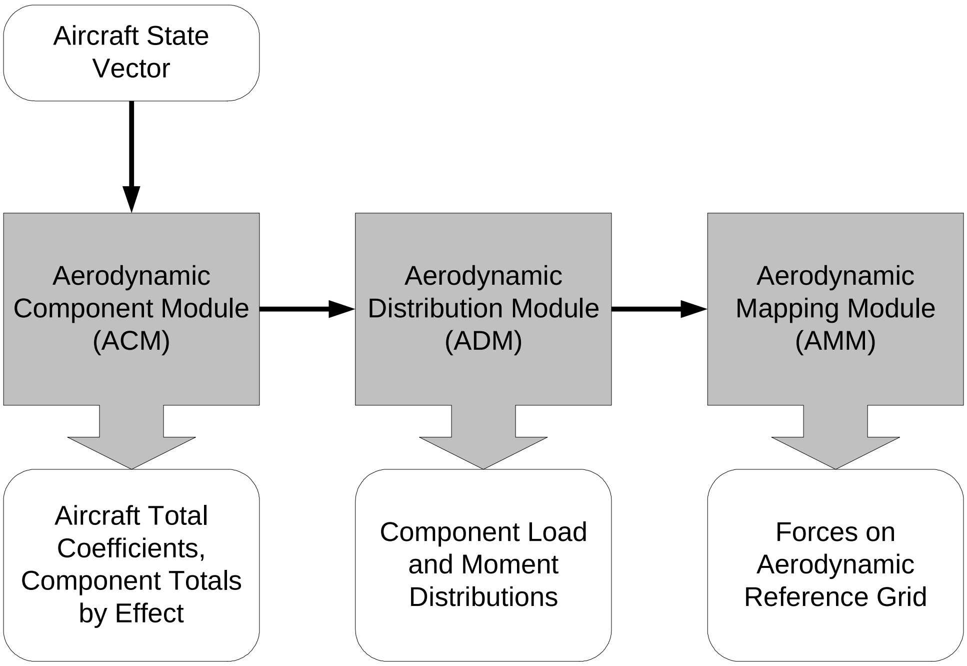

Figure 2.8: Implementation of the Aerodynamic Database

normal forces are provided. The output of the ACM is input to the aerodynamic distribution module (ADM) which assembles the resulting aircraft load and moment distribution by scaling component unit distributions. Both, ACM and ADM are production legacy codes written in FORTRAN and are ported to SIMULINK using *MEX-Functions* in conjunction with *M-S-Functions*[1]. The aerodynamic mapping module (AMM) that performs the mapping procedure outlined above is as well realized as an *M-S-Function*.

---

[1] see The Mathworks [120, 121] for details

2.2 Unsteady Aerodynamic Model

Multi-point aerodynamic models that take into account the local inflow at the main aircraft components in conjunction with constant aerodynamic derivatives, can be an efficient tool to analyze rigid aircraft response to atmospheric turbulence (Brockhaus [12], van Staveren [125]). For the analysis of flexible aircraft, this approach is unsatisfactory because the unsteady interaction of structural vibrations with the air flow cannot be modelled without a representation of the local aerodynamic loads. Therefore, a distributed unsteady aerodynamic model in the time domain is necessary to supplement or replace the quasi-steady aerodynamic database described above. In the following, an unsteady aerodynamic model for incompressible potential flow is derived, based on a time-stepping procedure. To enhance the applicability of the model, linearized versions in the time and frequency domain are derived together with correction and order reduction methods.

2.2.1 Governing Equations

Conservation of Mass

The continuity equation results from the application of the law of conservation of mass to an infinitesimal control volume fixed in space (Eulerian approach). It relates the rate of change of mass in the control volume to the mass flux across its boundaries and yields the following equation

$$\frac{\mathrm{D}\rho}{\mathrm{D}t} + \rho(\boldsymbol{\nabla} \cdot \boldsymbol{V}) = 0 \tag{2.2.1}$$

where ρ is the density of the fluid, t is the time and $\boldsymbol{V}$ is the vector of local fluid velocity. Here the substantial or total derivative

$$\frac{\mathrm{D}(\quad)}{\mathrm{D}t} = \frac{\partial(\quad)}{\partial t} + \boldsymbol{V} \cdot \boldsymbol{\nabla}(\quad) \tag{2.2.2}$$

has been used, that combines the local and convective time rate of change.

Conservation of Momentum

Application of Newton's Second Law to an infinitesimal control volume fixed in space yields the momentum equation

$$\rho\frac{\mathrm{D}\boldsymbol{V}}{\mathrm{D}t} = \rho\boldsymbol{f} + \boldsymbol{\nabla} \cdot \mathit{\Pi}_{ij} \tag{2.2.3}$$

where $\boldsymbol{f}$ is the vector of body forces per unit volume and $\mathit{\Pi}_{ij}$ is the stress tensor. The equation relates the rate of change of momentum in the control volume and the momentum flux across its boundaries to the body forces and surface forces exerted on the fluid in the control volume. Its validity is not limited to continuum flows, but as we seek a model for subsonic air flow, we now make the following

Assumption 1 (Newtonian Fluid) *If air is treated as a continuum, there exists a linear relationship between stress and the rates of strain at some point in the fluid.*

In this case, the stress tensor can be separated into contributions from pressure and viscosity (see Tannehill et al. [119]), respectively, which yields

$$\Pi_{ij} = -p\,\delta_{ij} + \boldsymbol{\tau}_{ij} \tag{2.2.4}$$

with the Kronecker product δ_{ij}, fluid pressure p and the viscous stress tensor τ_{ij}. By substituting Eq. (2.2.4) into the momentum equation Eq. (2.2.3), one obtains the *Navier-Stokes* equation

$$\rho\frac{\mathrm{D}\boldsymbol{V}}{\mathrm{D}t} = \rho\boldsymbol{f} - \boldsymbol{\nabla}p + \boldsymbol{\nabla}\cdot\boldsymbol{\tau}_{ij} \tag{2.2.5}$$

which is the momentum equation for a viscous, compressible Newtonian fluid. The numerical solution of these equations for engineering applications today is computationally not feasible and even solution of the *Reynolds-averaged Navier-Stokes (RANS)* equations, a time averaged version of the Navier-Stokes equations, is very expensive - the typical order of magnitude for the flow solution around a full aircraft configuration is several hours per flight point. The rapid estimation of unsteady aerodynamic loads therefore requires further simplifying assumptions as follows:

Assumption 2 (Body Forces) *For air, the influence of body forces, most commonly the gravitational force, is small compared to pressure and viscous stress:*

$$\boldsymbol{f} \approx \boldsymbol{0}$$

Assumption 3 (Viscosity) *For high Reynolds number, viscous effects are confined to the thin boundary layer on the aircraft surface and the outer flow can be computed neglecting viscosity. Therefore the viscous part of the stress tensor vanishes*

$$\boldsymbol{\tau}_{ij} \approx \boldsymbol{0}$$

By these assumptions, Eq. (2.2.5) becomes

$$\frac{\mathrm{D}\boldsymbol{V}}{\mathrm{D}t} + \frac{1}{\rho}\boldsymbol{\nabla}p = 0, \tag{2.2.6}$$

which is the inviscid momentum equation without body forces also known as the *Euler*-equation. A further simplification is possible if the fluid particles do not rotate about their axes:

Assumption 4 (Vorticity) *The flow field is irrotational and therefore vorticity vanishes*

$$\boldsymbol{\nabla}\times\boldsymbol{V} = 0$$

As a result, velocity can be expressed as the gradient of a scalar velocity potential

$$\boldsymbol{V} = \boldsymbol{\nabla}\phi$$

This assumption is valid if there are no shocks in the flow field and the rotational flow is only contained in the boundary layer. Expanding the total derivative of the local fluid velocity in Eq. (2.2.6), the total acceleration of a fluid particle can be written as

$$\begin{aligned} \frac{\mathrm{D}\boldsymbol{V}}{\mathrm{D}t} &= \frac{\partial \boldsymbol{V}}{\partial t} + \boldsymbol{V} \cdot \boldsymbol{\nabla} \boldsymbol{V} = \\ &= \frac{\partial \boldsymbol{V}}{\partial t} + \frac{1}{2} \boldsymbol{\nabla} \left(\boldsymbol{V} \cdot \boldsymbol{V} \right) - \underbrace{\boldsymbol{V} \times \left(\boldsymbol{\nabla} \times \boldsymbol{V} \right)}_{=0} \end{aligned} \tag{2.2.7}$$

where the last term vanishes due to Assumption 4. By substituting this result back into the *Euler*-equation Eq. (2.2.6)

$$\frac{\partial \boldsymbol{V}}{\partial t} + \frac{1}{2} \boldsymbol{\nabla} \left(\boldsymbol{V} \cdot \boldsymbol{V} \right) + \frac{1}{\rho} \boldsymbol{\nabla} p = 0,$$

rearranging, and using the definition of the velocity potential, we obtain

$$\boldsymbol{\nabla} \left(\frac{\partial \phi}{\partial t} + \frac{1}{2} \left(\boldsymbol{V} \cdot \boldsymbol{V} \right) + \int \frac{\mathrm{d}p}{\rho} \right) = 0.$$

The integral of this expression is referred to as the unsteady, compressible *Bernoulli*-equation in terms of the local time derivative

$$\frac{\partial \phi}{\partial t} + \frac{1}{2} \left(\boldsymbol{V} \cdot \boldsymbol{V} \right) + \int \frac{\mathrm{d}p}{\rho} = 0 \tag{2.2.8}$$

or alternatively

$$\frac{\mathrm{D}\phi}{\mathrm{D}t} - \frac{1}{2} \left(\boldsymbol{V} \cdot \boldsymbol{V} \right) + \int \frac{\mathrm{d}p}{\rho} = 0 \tag{2.2.9}$$

in terms of the total derivative of the velocity potential. If we limit ourselves to low flight Mach numbers, we can make the final

Assumption 5 (Compressibility) *The fluid is incompressible and therefore density is constant*

$$\rho = \mathrm{const.}$$

and by performing the integration from the undisturbed fluid to an arbitrary point in the flow field, we obtain from Eq. (2.2.9) the pressure coefficient for unsteady, incompressible potential flow

$$c_p = \frac{p - p_\infty}{\frac{1}{2} \rho_\infty V_\infty^2} = -\frac{2}{V_\infty^2} \frac{\mathrm{D}\phi}{\mathrm{D}t} + \frac{\boldsymbol{V} \cdot \boldsymbol{V}}{V_\infty^2} \tag{2.2.10}$$

in terms of the total derivative of the velocity potential. To obtain the governing equation for the velocity potential, Assumptions 4 and 5 are applied to the continuity equation Eq. (2.2.1), yielding *Laplace's* equation

$$\boldsymbol{\nabla} \cdot \boldsymbol{V} = \boldsymbol{\nabla} \cdot \boldsymbol{\nabla} \phi = \boldsymbol{\nabla}^2 \phi = 0 \tag{2.2.11}$$

for incompressible, potential flow. Even though the time derivative no longer appears in Eq. (2.2.11), *Laplace's* equation is valid for both steady and unsteady flows.

Transformation to moving coordinates

The derivation so far was based on an Eulerian point of view, e.g. a stationary frame of reference. For the analysis of maneuvering aircraft, it is more convenient to transform the governing equations to a frame of reference attached to the body moving with velocity $\boldsymbol{V}_{\text{kin}}$. The local velocity vector $\boldsymbol{V}$ can be written as

$$\boldsymbol{\nabla}\phi = \boldsymbol{V} = \boldsymbol{V}_{\text{kin}} + \boldsymbol{w}$$

where $\boldsymbol{w}$ is the relative fluid velocity perceived from the moving frame of reference. The total derivative of the potential in the moving frame becomes

$$\frac{\mathrm{D}\phi}{\mathrm{D}t} = \frac{\partial\phi}{\partial t} + \boldsymbol{w}\cdot\boldsymbol{\nabla}\phi = \frac{\partial\phi}{\partial t} + \boldsymbol{w}\cdot(\boldsymbol{V}_{\text{kin}} + \boldsymbol{w})$$

and consequently the pressure equation Eq. (2.2.10) becomes

$$c_p = -\frac{2}{V_\infty^2}\frac{\partial\phi}{\partial t} + \frac{\boldsymbol{V}_{\text{kin}}\cdot\boldsymbol{V}_{\text{kin}}}{V_\infty^2} - \frac{\boldsymbol{w}\cdot\boldsymbol{w}}{V_\infty^2} \tag{2.2.12}$$

As will be shown later, it is also convenient to retain the formulation in terms of the total derivative

$$c_p = -\frac{2}{V_\infty^2}\frac{\mathrm{D}\phi}{\mathrm{D}t} + \frac{(\boldsymbol{V}_{\text{kin}} + \boldsymbol{w})\cdot(\boldsymbol{V}_{\text{kin}} + \boldsymbol{w})}{V_\infty^2}. \tag{2.2.13}$$

The continuity equation Eq. (2.2.11) is invariant to transformations of the frame of reference and therefore also holds in the moving frame.

2.2.2 Unsteady Vortex Lattice Method

Laplace's equation is an elliptical partial differential equation resulting in a boundary value problem. It can be solved by distributing elementary solutions on the problem boundaries and determining their appropriate strength in such a way that the following boundary conditions are fulfilled.

Boundary Conditions

On the body surface, the boundary condition of zero normal flow must be satisfied, e.g. the body surface must become a stream surface. In terms of the unknown potential ϕ this can be stated as

$$(\boldsymbol{\nabla}\phi + \boldsymbol{v}_{\text{S}} + \boldsymbol{v}_{\text{G}})\cdot\boldsymbol{n} = 0 \tag{2.2.14}$$

where $\boldsymbol{v}_{\text{S}}$ is the total velocity of the body surface relative to the fluid at rest, $\boldsymbol{v}_{\text{G}}$ is the local atmospheric disturbance velocity and $\boldsymbol{n}$ is the surface normal vector, all values perceived in the moving coordinate frame. The total velocity of the body $\boldsymbol{v}_{\text{S}}$ is

$$\boldsymbol{v}_{\text{S}} = \boldsymbol{v}_{\text{R}} + \boldsymbol{v}_{\text{E}}$$

where $\boldsymbol{v}_{\text{R}}$ is the velocity due to rigid body motion and $\boldsymbol{v}_{\text{E}}$ is the velocity due to structural deformation.

The second boundary condition requires that fluid disturbances caused by the moving body diminish in far distance from the body. In the body axis frame this can be stated as

$$\lim_{|\boldsymbol{r}|\to\infty}\boldsymbol{\nabla}\phi = 0 \tag{2.2.15}$$

where $\boldsymbol{r}$ is the position vector of an arbitrary point. Because the first boundary condition affects the normal derivative of the potential and specifies the flow outside of the body immerged in the fluid, the problem is called the *Neumann* exterior problem.

Solution by Vortex Ring Elements

The potential vortex is an elementary solution to *Laplace's* equation and is used by classical lifting line, lifting surface and vortex lattice methods (see any textbook on fundamental aerodynamics, for instance Anderson [2] or Katz and Plotkin [64]). In this thesis, the unsteady version of the vortex lattice method is applied, using vortex ring elements instead of horseshoe vortices. In the steady case, vortex rings are equivalent to horseshoe vortices but offer the possibility to also model non-planar lifting surfaces and bodies by placing the rings on the camber surface or the body surface, respectively. This choice of singularity element satisfies the *Helmholtz* vortex theorems that state

> **Theorem 1 (Helmholtz)** *The strength of a vortex filament is constant along its length.*
>
> **Theorem 2 (Helmholtz)** *A vortex filament cannot end in a fluid. It must extend to the boundaries of the fluid or form a closed path.*

As shown in Fig. 2.9(a), the lifting surfaces are divided into a regular grid of N_{P} quadrilateral panels and vortex ring elements are placed between the quarter chord lines of streamwise adjacent panels. As shown in Fig. 2.9(b), body surfaces are also discretized with a regular grid of triangular panels at the body apexes and quadrilateral panels away from it and vortex rings are placed on the edges of the panels. On the triangular panels, the vortex rings consist of only three filaments.

For lifting surfaces, the surface boundary condition Eq. (2.2.14) is enforced at panel collocation points located at the intersection of the three-quarter chord line and the panel center line. As pointed out by James [57], this placement of singularity and collocation point satisfies the two-dimensional *Kutta* condition and yields the exact lift and moment results for a flat plate. On bodies, the collocation point is located at the panel centroid.

Time dependence of the problem is introduced by the motion of the body axis frame and the according change of the boundary conditions. Additionally, by way of

> **Theorem 3 (Kelvin)** *The time rate of change of circulation around a closed curve consisting of the same fluid elements is zero.*

a wake will be generated behind the lifting surfaces. In terms of the total derivative of the circulation this can be stated as

$$\frac{\mathrm{D}}{\mathrm{D}t}\left(\Gamma_{\mathrm{P,total}} + \Gamma_{\mathrm{W,total}}\right) = 0$$

which implies that any change of the bound circulation $\Gamma_{\mathrm{P,total}}$ effects a change of circulation in the wake $\Gamma_{\mathrm{W,total}}$. Therefore in the time stepping procedure, after each solution

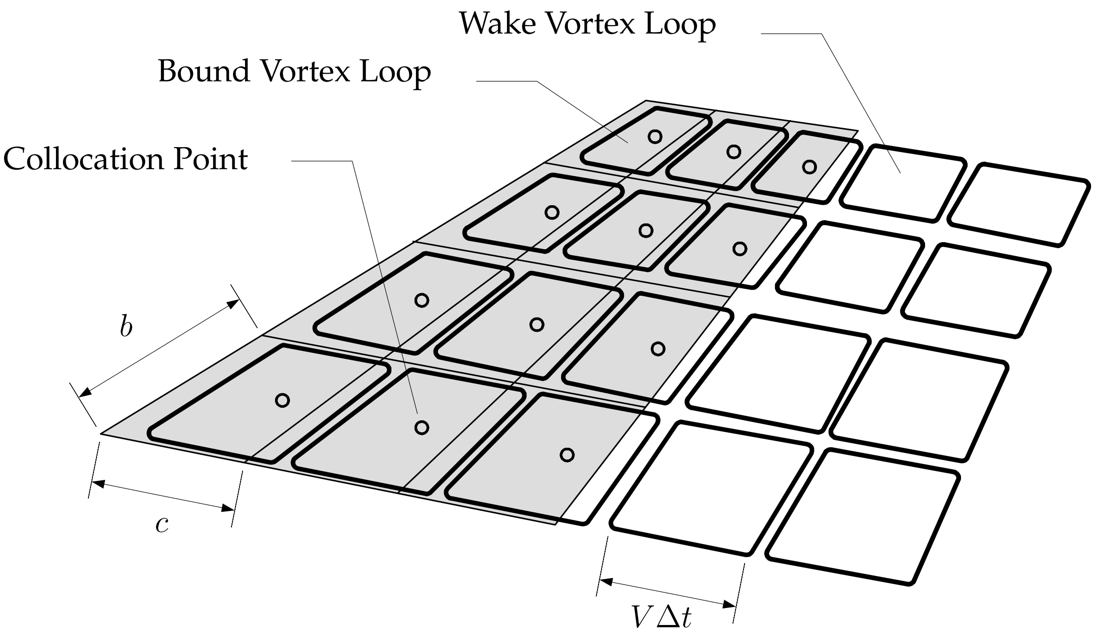

(a) Lifting Surfaces

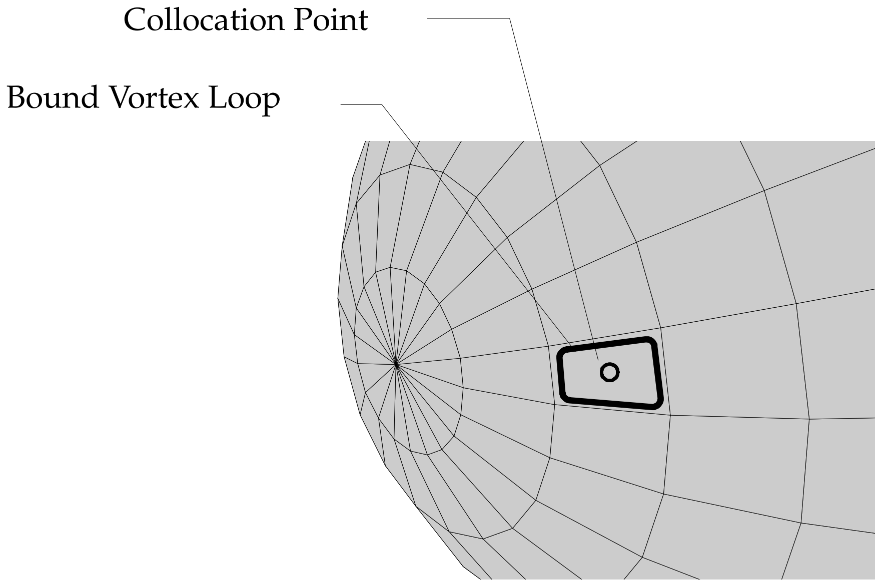

(b) Bodies

Figure 2.9: Discretization with Vortex Ring Elements

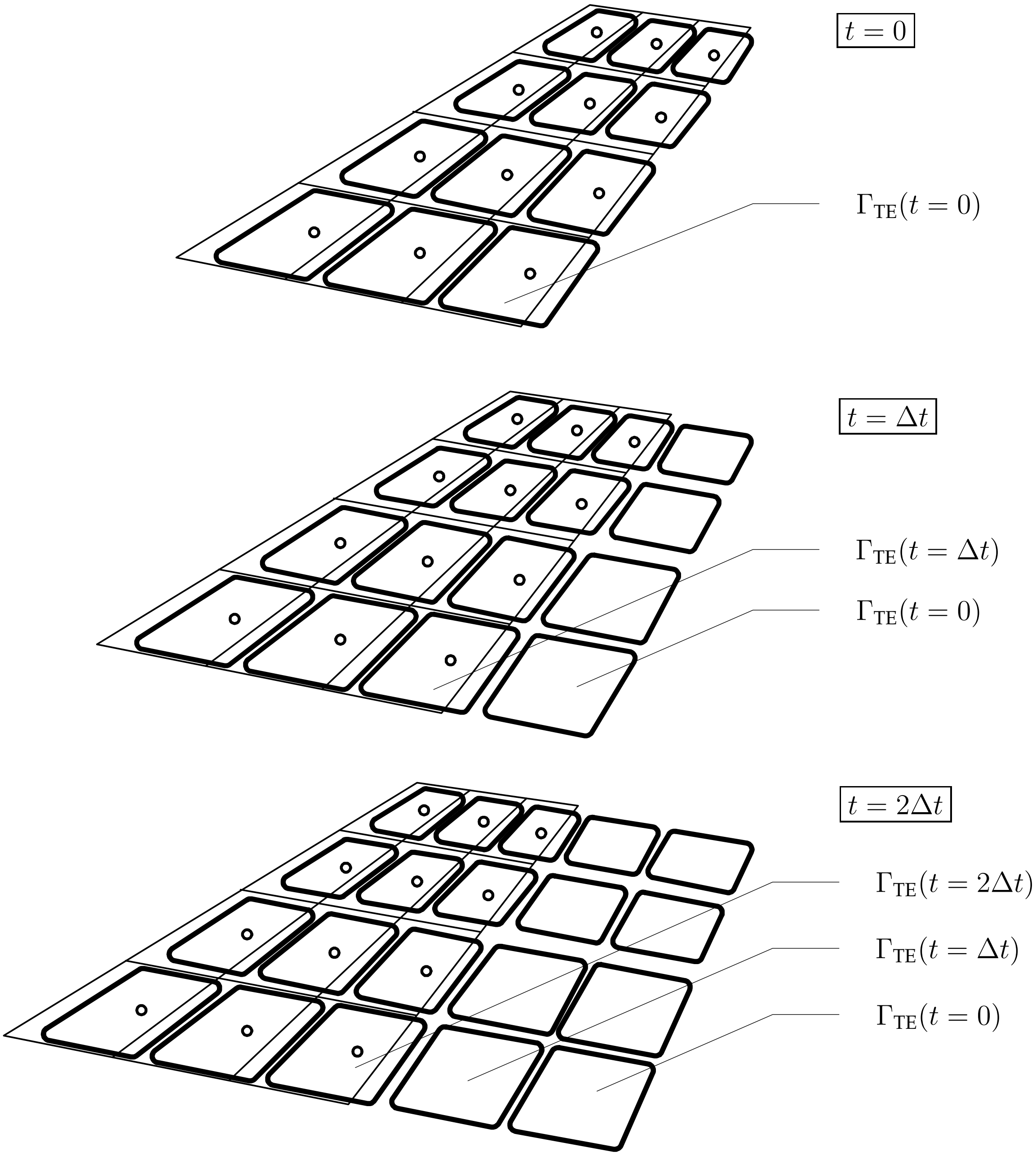

Figure 2.10: Wake Development

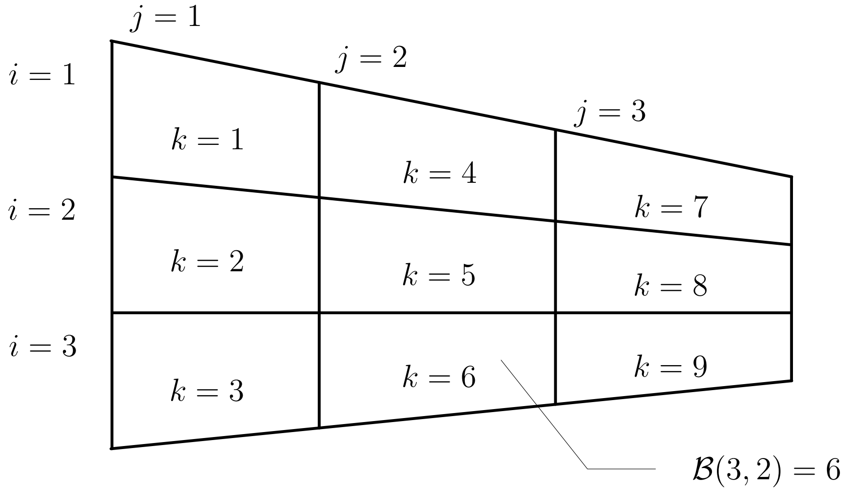

Figure 2.11: Example of Panel Indexing

step the position of the lifting surfaces in the earth fixed reference frame is updated and a column of new wake panels is released from the trailing edge, see Fig. 2.10. The circulation of each newly released wake panel is set equal to the circulation of the trailing edge panel it was released from and therefore the *Kelvin*-condition is automatically satisfied. During the first solution step, when no wake panels have yet been shed, the spanwise downstream vortex segments of the panels next to trailing edge form the starting vortex. Bodies are assumed to generate no lift by maintaining zero total circulation and therefore do not require wake modelling.

To facilitate the following derivation, each panel is identified by an index pair (i, j), where j and i describe the panel strip number and the position in that strip counting from the leading edge, respectively. The total number of strips is denoted by N_S and the number of panels per strip is given by the vector $\boldsymbol{N}_\text{C}$. If the panel position in a strip is not relevant, the panel can alternatively be identified by the single index k that results from the bijective mapping $\mathcal{B}(i, j) \rightarrow k$. As an example, Fig. 2.11 shows a typical panel arrangement with 3 strips and 3 panels per strip where $N_\text{S} = 3$, $\boldsymbol{N}_\text{C} = \{3, 3, 3\}^\text{T}$ and $\mathcal{B}(3, 2) = 6$.

Panel Properties

The geometric properties of a panel are width b and chord length c as shown in Fig. 2.12. Normal vector $\boldsymbol{n}$ and surface area A are obtained by the cross product of the diagonal vectors

$$\begin{aligned}\boldsymbol{n} &= \frac{\boldsymbol{r}_{\text{d},1} \times \boldsymbol{r}_{\text{d},2}}{|\boldsymbol{r}_{\text{d},1} \times \boldsymbol{r}_{\text{d},2}|} \\ A &= \frac{1}{2}|\boldsymbol{r}_{\text{d},1} \times \boldsymbol{r}_{\text{d},2}|\end{aligned}$$

The panel coordinate system is located at the panel centroid with the first tangential vector $\boldsymbol{\tau}_1$ passing through the midpoint beetween the two downstream corner points and the second tangential vector $\boldsymbol{\tau}_2$ forming a right-handed coordinate system with $\boldsymbol{n}$ and $\boldsymbol{\tau}_1$.

To model the flexibility of the aircraft, 6 degrees of freedom relative to the moving frame of reference are defined at the panel center: three translations $\boldsymbol{u} = \{u_x, u_y, u_z\}^\text{T}$

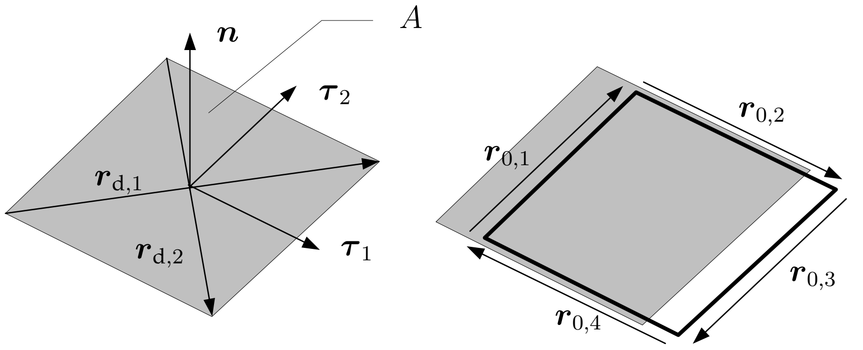

(a) Area, Local Coordinates and Filaments

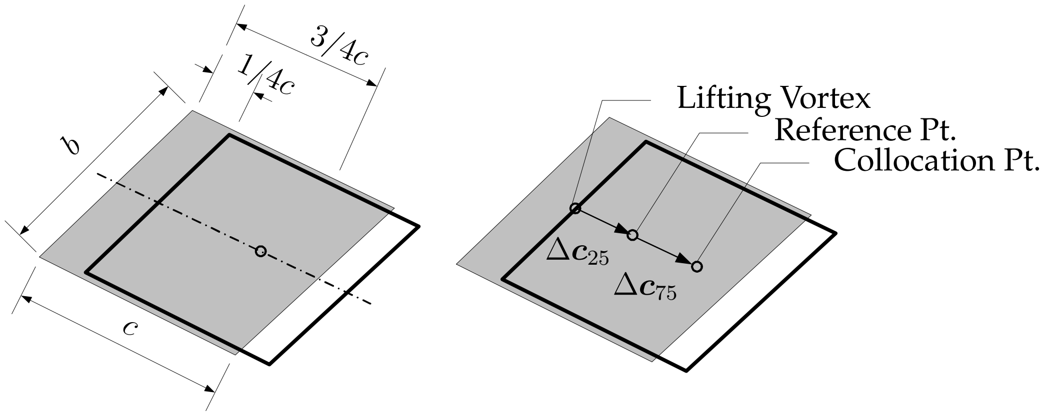

(b) Lifting Surface Panel Geometry

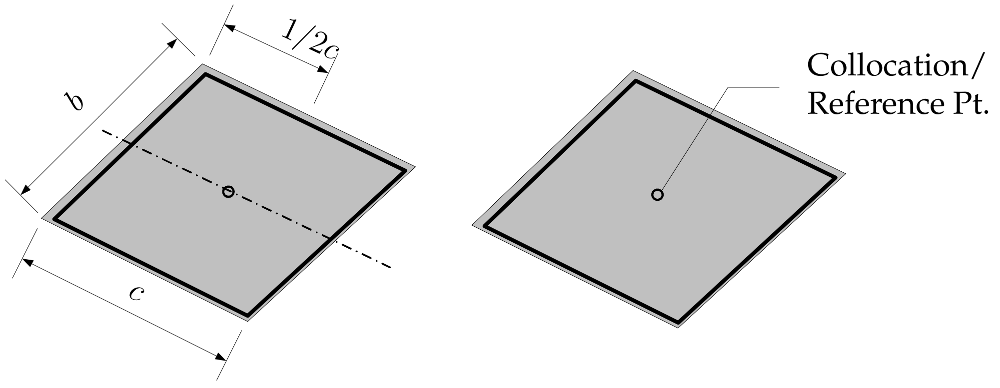

(c) Body Panel Geometry

Figure 2.12: Panel Properties

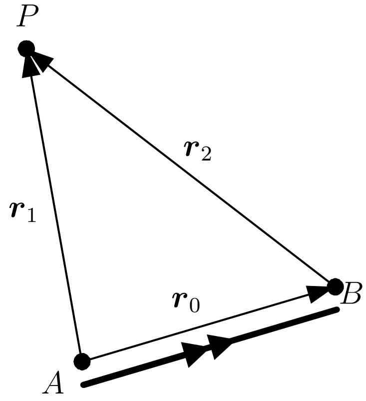

Figure 2.13: Induction by a Vortex Filament

and three rotations $\boldsymbol{\varphi} = \{\varphi_x, \varphi_y, \varphi_z\}^{\mathrm{T}}$. In terms of these panel freedoms, the velocity of the collocation point due to rate of structural deformation becomes

$$\boldsymbol{v}_{\mathrm{E}} = \begin{cases} \dot{\boldsymbol{u}} + \dot{\boldsymbol{\varphi}} \times \Delta \boldsymbol{c}_{75} & \text{on lifting surfaces} \\ \dot{\boldsymbol{u}} & \text{on bodies} \end{cases}$$

where $\Delta \boldsymbol{c}_{75} = \{\Delta c_{75,x}, \Delta c_{75,y}, \Delta c_{75,z}\}^{\mathrm{T}}$ is the offset vector from the panel center to the collocation point, see Fig. 2.12. The deformation dependent normal vector $\boldsymbol{n}_{\mathrm{E}}$ becomes

$$\boldsymbol{n}_{\mathrm{E}} = \boldsymbol{n} + \boldsymbol{\varphi} \times \boldsymbol{n}$$

and the total downwash at the collocation point in terms of the velocity of the moving frame $\boldsymbol{v}_{\mathrm{R}}$, atmospheric disturbance $\boldsymbol{v}_{\mathrm{G}}$ and the panel center degrees of freedom is

$$d = \begin{cases} (\boldsymbol{v}_{\mathrm{R}} + \dot{\boldsymbol{u}} + \dot{\boldsymbol{\varphi}} \times \Delta \boldsymbol{c}_{75} + \boldsymbol{v}_{\mathrm{G}}) \cdot (\boldsymbol{n} + \boldsymbol{\varphi} \times \boldsymbol{n}) & \text{on lifting surfaces} \\ (\boldsymbol{v}_{\mathrm{R}} + \dot{\boldsymbol{u}} + \boldsymbol{v}_{\mathrm{G}}) \cdot (\boldsymbol{n} + \boldsymbol{\varphi} \times \boldsymbol{n}) & \text{on bodies} \end{cases} \tag{2.2.16}$$

The only assumption made in this formulation is that rotational deformations in the moving frame are small.

Biot-Savart Law

The *Biot-Savart* law describes the velocity induced by a finite length vortex filament. With the geometric quantities shown in Fig. 2.13, the induced velocity $\boldsymbol{v}_{\text{ind}}$ at an arbitrary point P due to a vortex filament with end points A and B and circulatory strength Γ is

$$\boldsymbol{v}_{\text{ind}} = \frac{\Gamma}{4\pi} \frac{\boldsymbol{r}_1 \times \boldsymbol{r}_2}{|\boldsymbol{r}_1 \times \boldsymbol{r}_2|^2 + \delta^2 |\boldsymbol{r}_0|^2} \left(\boldsymbol{r}_0 \cdot \frac{\boldsymbol{r}_1}{|\boldsymbol{r}_1|} - \boldsymbol{r}_0 \cdot \frac{\boldsymbol{r}_2}{|\boldsymbol{r}_2|} \right) \tag{2.2.17}$$

This formulation employs the desingularization parameter δ introduced by Ramsey [99] in order to damp excessive induced velocities in close proximity to the vortex filaments. Situations, where $\boldsymbol{r}_1$ and $\boldsymbol{r}_2$ are co-linear and therefore $|\boldsymbol{r}_1 \times \boldsymbol{r}_2|^2 \to 0$, can occur when modelling full aircraft configurations or during roll-up of a flexible wake. Inspection of the *Biot-Savart* reveals that the use of potential vortex elements automatically fulfills the farfield boundary condition of Eq. (2.2.15) because

$$\lim_{|\boldsymbol{r}_1|,|\boldsymbol{r}_2| \to \infty} \boldsymbol{v}_{\text{ind}} = \boldsymbol{0}$$

and therefore the induced velocity vanishes far away from the vortex singularity. To obtain the induced velocity of an entire vortex ring, Eq. (2.2.17) is evaluated for all segments of the ring.

Influence Coefficients and Solution

The potential flow solution is obtained by the method of collocation, e.g. the surface boundary condition Eq. (2.2.14) must exactly be fulfilled at the control point of all lifting surface and body panels. It results a simultaneous set of N_P equations

$$(\boldsymbol{\nabla}\phi + \boldsymbol{v}_\mathrm{R} + \boldsymbol{v}_\mathrm{E} + \boldsymbol{v}_\mathrm{G})_k \cdot \boldsymbol{n}_k = 0 \quad \text{with} \quad k = 1 \dots N_\mathrm{P} \tag{2.2.18}$$

where $\boldsymbol{\nabla}\phi_k \cdot \boldsymbol{n}_k$ is the induced normalwash at panel k due to all singularities in the flow field. This normalwash can be expressed in terms of the velocity influence coefficients of the N_P bound vortex ring elements a_{kl} and of the N_W wake vortex ring elements b_{kl}

$$\boldsymbol{\nabla}\phi_k \cdot \boldsymbol{n}_k = \sum_{j=1}^{N_\mathrm{P}} a_{kj}\Gamma_{\mathrm{P},j} + \sum_{j=1}^{N_\mathrm{W}} b_{kj}\Gamma_{\mathrm{W},j} \tag{2.2.19}$$

with bound vortex ring circulation $\Gamma_{\mathrm{P},j}$ and wake vortex ring circulation $\Gamma_{\mathrm{W},j}$. The velocity influence coefficient a_{kj} represents the normalwash induced by vortex ring j at collocation point k and is obtained by summing up the contributions of the four ring segments

$$a_{kj} = \boldsymbol{n}_k \cdot \sum_{m=1}^{4} \boldsymbol{v}_{kj,m}(\Gamma_{\mathrm{P},j} = 1)$$

assuming unit circulation. The influence coefficients b_{kl} of the wake vortex ring elements are computed in the same way. If bodies are modelled, additional equations arise from the requirement, that the sum of vortex ring circulations on every body is zero. Denoting the number of panels on a body with N_PB, this can be written as

$$\sum_{j=1}^{N_\mathrm{PB}} \Gamma_{\mathrm{P},j} = 0 \tag{2.2.20}$$

The set of linear equations Eqns. (2.2.18) and (2.2.20) can be rearranged and cast into matrix notation

$$A\boldsymbol{\Gamma}_\mathrm{P} = -\boldsymbol{d} - B\boldsymbol{\Gamma}_\mathrm{W} \tag{2.2.21a}$$

$$T_\mathrm{B}\boldsymbol{\Gamma}_\mathrm{P} = \boldsymbol{0} \tag{2.2.21b}$$

where

$$A = \begin{bmatrix} a_{11} & a_{12} & \dots & a_{1N_\mathrm{P}} \\ \vdots & \vdots & \ddots & \vdots \\ a_{N_\mathrm{P}1} & a_{N_\mathrm{P}2} & \dots & a_{N_\mathrm{P}N_\mathrm{P}} \end{bmatrix}$$

is the aerodynamic influence matrix (AIC) of the bound vortex ring elements,

$$\boldsymbol{\Gamma}_\mathrm{P} = \begin{Bmatrix} \Gamma_{\mathrm{P},1} \\ \vdots \\ \Gamma_{\mathrm{P},N_\mathrm{P}} \end{Bmatrix}$$

is the vector of circulation strength of the bound vortex rings,

$$\boldsymbol{d} = \begin{Bmatrix} (\boldsymbol{v}_\mathrm{S} + \boldsymbol{v}_\mathrm{G})_1 \cdot \boldsymbol{n}_1 \\ \vdots \\ (\boldsymbol{v}_\mathrm{S} + \boldsymbol{v}_\mathrm{G})_{N_\mathrm{P}} \cdot \boldsymbol{n}_{N_\mathrm{P}} \end{Bmatrix}$$

is the vector of normalwashes at the collocation points due to rigid body motion, structural elasticity and atmospheric disturbance,

$$\mathsf{B} = \begin{bmatrix} b_{11} & b_{12} & \dots & b_{1N_W} \\ \vdots & \vdots & \ddots & \vdots \\ b_{N_\mathrm{P}1} & b_{N_\mathrm{P}2} & \dots & b_{N_\mathrm{P}N_\mathrm{W}} \end{bmatrix}$$

is the aerodynamic influence matrix of the vortex rings in the wake,

$$\boldsymbol{\Gamma}_\mathrm{W} = \begin{Bmatrix} \Gamma_{\mathrm{W},1} \\ \vdots \\ \Gamma_{\mathrm{W},N_\mathrm{W}} \end{Bmatrix}$$

is the vector of circulation strength of the vortex rings in the wake and

$$\mathsf{T}_{\mathrm{B},ij} = \begin{cases} 1 & \text{if panel } j \text{ is located on body } i \\ 0 & \text{if panel } j \text{ is not located on body } i \end{cases}$$

is a selection matrix with one row for each of the N_B bodies. Assuming that downwash $\boldsymbol{d}$ and wake circulation $\boldsymbol{\Gamma}_\mathrm{W}$ are known, the equation system (2.2.21) provides $N_\mathrm{P} + N_\mathrm{B}$ equations for N_P unknowns and therefore is overdetermined if $N_\mathrm{B} > 0$. To solve for $\boldsymbol{\Gamma}_\mathrm{P}$, the problem could be made determined by deleting one of the equations from (2.2.21a). In that case, the boundary condition of zero-normal flow would be violated on one arbitrarily chosen panel yielding unphysical results (see Katz and Plotkin [64], page 288). On the other hand, deleting one of Eqns. (2.2.21b) will yield a singular AIC matrix A because placing only vortex elements on a closed body does not constitute a unique solution to the *Laplace* equation. Therefore, in this thesis all $N_\mathrm{P} + N_\mathrm{B}$ equations are retained and a solution minimizing the error norm is determined as follows. First, Eqns. (2.2.21) are combined into one matrix equation

$$\tilde{\mathsf{A}}\boldsymbol{x} = \boldsymbol{b}$$

and the orthogonal-triangular decomposition (QR) of $\tilde{\mathsf{A}}$ is calculated

$$\tilde{\mathsf{A}} = \mathsf{QR} = \begin{bmatrix} \mathsf{Q}_1 & \mathsf{Q}_2 \end{bmatrix} \begin{bmatrix} \mathsf{R}_1 \\ \mathsf{0} \end{bmatrix} = \mathsf{Q}_1\mathsf{R}_1$$

such that Q is a orthonormal square matrix of size $(N_\mathrm{P} + N_\mathrm{B})$ and R is upper triangular with size $(N_\mathrm{P}+N_\mathrm{B})\times N_\mathrm{P}$. The matrix partitioning reflects the fact that the bottom $(m-n)$ rows of an upper $(m \times n)$ triangular matrix consist entirely of zeros. The solution minimizing $||\tilde{\mathsf{A}}\boldsymbol{x} - \boldsymbol{b}||$ is then computed by solving the back substitution problem

$$\boldsymbol{x} = \mathsf{R}_1^{-1}\mathsf{Q}_1^\mathrm{T}\boldsymbol{b}$$

Consequently, the unknown bound circulation is found to be

$$\boldsymbol{\Gamma}_\mathrm{P} = \mathsf{A}^{-1}\left(-\boldsymbol{d} - \mathsf{B}\boldsymbol{\Gamma}_\mathrm{W}\right) \tag{2.2.22}$$

if only lifting surfaces are modelled and

$$\boldsymbol{\Gamma}_{\mathrm{P}} = R_1^{-1} Q_1^{\mathrm{T}} \left(\begin{Bmatrix} -\boldsymbol{d} \\ \boldsymbol{0} \end{Bmatrix} - \begin{bmatrix} B \\ 0 \end{bmatrix} \boldsymbol{\Gamma}_{\mathrm{W}} \right) \tag{2.2.23}$$

if also bodies are modelled. For a fixed bound vortex ring layout, A^{-1} or respectively $R_1^{-1} Q_1^{\mathrm{T}}$ only need to be computed once. For the sake of legibility of the following sections, only the notation for the lifting surface case is presented. The reader should have no problem with adapting it to the additional equation and approximate matrix inversion required for bodies.

Wake Model

Depending on how the wake elements are treated after leaving the trailing edges, three different wake models can be distinguished:

1. **Prescribed wake** (Fig. 2.14(a)): The wake loops leave the trailing edge in the direction of the chordwise surface tangent and form a flat vortex sheet with a fixed geometry independent of the motion of the lifting surfaces. This has the advantage, that the influence coefficients B of the wake only need to be computed once. If a large number of wake panels is used, e.g. the wake is not truncated after a number of time steps, then a very large, fully populated matrix will result.
2. **Rigid wake** (Fig. 2.14(b)): The most recent column of wake loops always connects the current position of the trailing edge with the position of the trailing edge during the previous time step. This orientation remains fixed in inertial space over time. This option is costly because every time step the influence of the wake elements on the lifting surfaces must be computed.
3. **Free wake with rollup** (Fig. 2.14(c)): Similar to the rigid wake, the shed wake rings are placed on the surface traced by the trailing edge. Rather than remaining at their initial location, the wake rings are free to move with the local stream velocity, effectively yielding a force free wake. This is the most costly option because in addition to the induction on the lifting surfaces the induced velocity among all wake elements must be determined.

Interaction of Wake with Bodies and Surfaces

When modelling full aircraft configurations, significant effort must be put in the definition of the wake behavior relative to neighboring lifting surfaces and bodies. For rigid or free wake analysis, this implies monitoring the position of all wake rings relative to the configuration and defining rules to avoid wake pass-through and piercing of the surfaces and bodies. A systematic treatment of the topic has been presented by He et al. [51]. In the present analysis, a prescribed wake model is used and therefore only the position of the wake relative to the other lifting surfaces and bodies must be defined a priori. Of particular interest is the inboard part of the wing wake relative to the fuselage as shown in Fig. 2.15(a). The black part of the wake results from extruding the trailing edges in the direction of flight. However, this leads to a strong streamwise vortex passing by close to the fuselage surface and causing unphysically high induced velocities. To avoid this, the inboard wing wake boundary should be attached to the

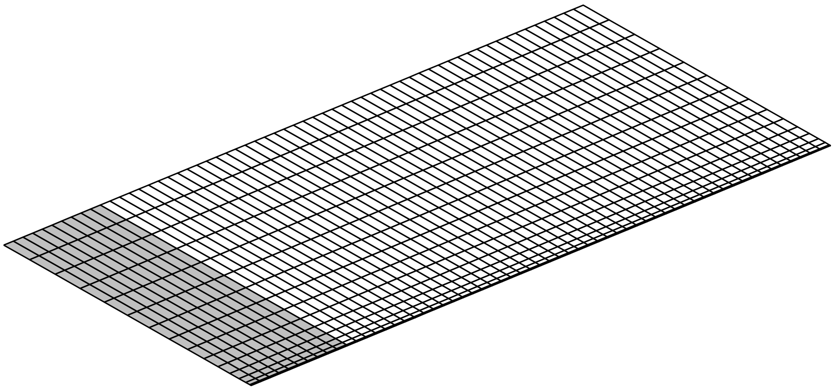

(a) Prescribed

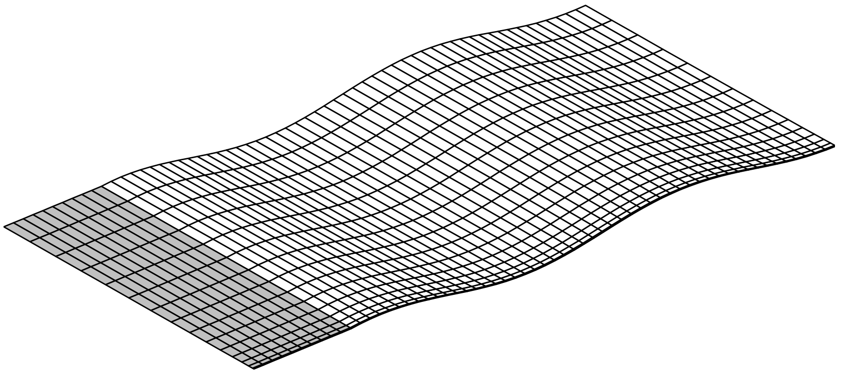

(b) Rigid

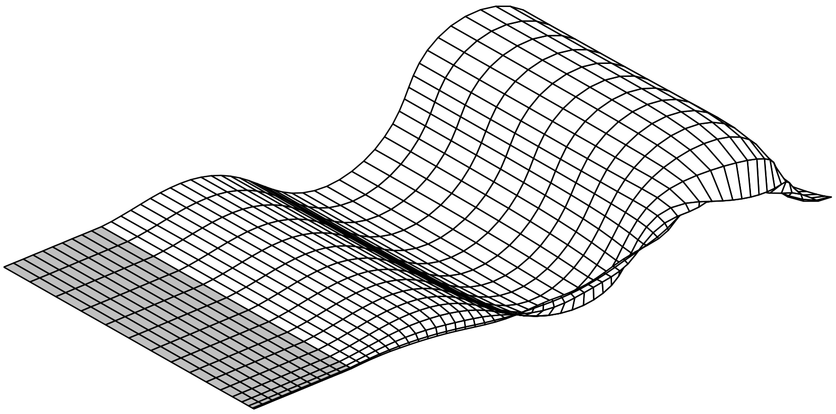

(c) Free

Figure 2.14: Types of Wake Models

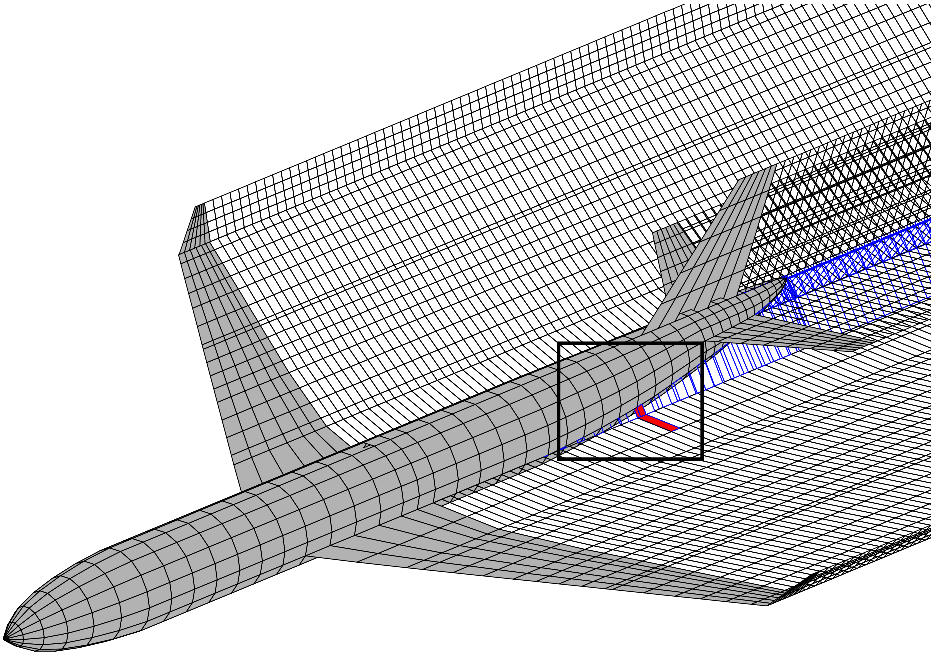

(a) Overview

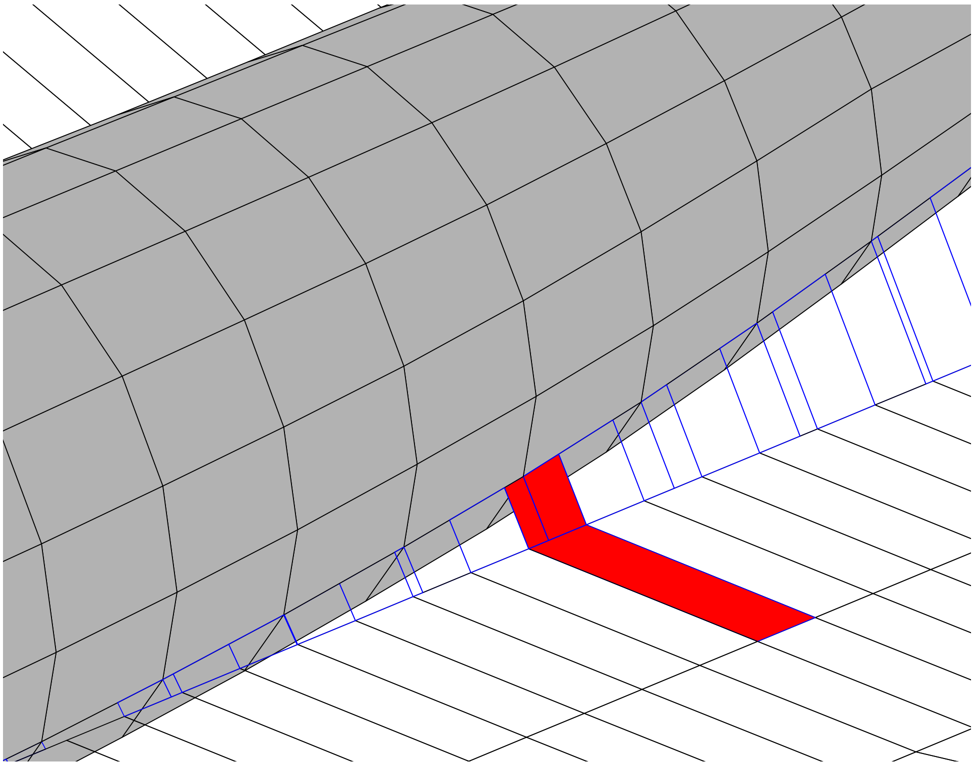

(b) Detail

Figure 2.15: Wake-Body Attachment

fuselage surface and follow the panel boundaries there (the task of defining this attachment is frequently called “wake stitching”). Insertion of a filler wake between wing wake and fuselage as depicted in blue in Fig. 2.15(a) yields the desired effect. Typically the streamwise discretization of the wake does not match the streamwise panel spacing on the fuselage and therefore the filler wake needs a discretization which is union of the two in order to follow the fuselage panel boundary. As shown in the detail of Fig. 2.15(b), this leads to series of filler panels inheriting the circulation from one wing wake panel (the red area signifies panels of identical circulation) and because the interior vortex segments cancel each other out, this is equivalent to a three dimensional vortex polygon.

Aerodynamic Loads and Induced Drag

Once Eq. (2.2.22) or respectively Eq. (2.2.23) yield the unknown bound circulation $\boldsymbol{\Gamma}_\mathrm{P}$, the resulting aerodynamic loads can be computed by applying the unsteady *Bernoulli* equation Eq. (2.2.12). The differential pressure coefficient across lifting surfaces is obtained by application to the upper and lower sides

$$\begin{aligned}\Delta c_p = (c_p)_\mathrm{l} - (c_p)_\mathrm{u} = -\frac{2}{V_\infty^2}\left(\left(\frac{\mathrm{D}\phi}{\mathrm{D}t}\right)_\mathrm{l} - \left(\frac{\mathrm{D}\phi}{\mathrm{D}t}\right)_\mathrm{u}\right)\\ + \frac{(\boldsymbol{V}_\mathrm{kin} + \boldsymbol{w}_\mathrm{l}) \cdot (\boldsymbol{V}_\mathrm{kin} + \boldsymbol{w}_\mathrm{l})}{V_\infty^2} - \frac{(\boldsymbol{V}_\mathrm{kin} + \boldsymbol{w}_\mathrm{u}) \cdot (\boldsymbol{V}_\mathrm{kin} + \boldsymbol{w}_\mathrm{u})}{V_\infty^2}.\end{aligned} \tag{2.2.24}$$

The aerodynamic panel force is then acting in the normal direction of the panel

$$\boldsymbol{f}/q_\infty = (\Delta c_p\, A)\, \boldsymbol{n} \tag{2.2.25}$$

and has a component in the direction of the free stream, implying aerodynamic drag. Because the leading edge suction force cannot be resolved with the vortex lattice method, this induced drag is overestimated. To overcome this deficiency, only the unsteady part of the *Bernoulli* equation, that is the term with the total derivative of the potential, is retained on lifting surfaces. The remainder of Eq. (2.2.24) is replaced by the three-dimensional *Kutta-Joukowski* theorem for vortex lift that yields the steady force vector $\boldsymbol{f}_\mathrm{S}$ normal to the panel inflow

$$\boldsymbol{f}_\mathrm{S}/q_\infty = \frac{2}{V_\infty}\,\Gamma_\mathrm{eff}\,(\boldsymbol{v}_\mathrm{R} + \boldsymbol{v}_\mathrm{E} + \boldsymbol{v}_\mathrm{G}) \times \boldsymbol{r}_0 \tag{2.2.26}$$

where $\boldsymbol{r}_0$ is the vector of the lifting vortex on the quarter chord line. The effective circulation Γ_eff of the lifting vortices is dependent on whether the bound vortex ring element is located on the leading edge or not, see Fig. 2.16. Introducing the permutation matrix P, the effective circulation can be written in terms of the vortex loop circulations

$$\boldsymbol{\Gamma}_\mathrm{eff} = \mathsf{P}\,\boldsymbol{\Gamma}_\mathrm{P}.$$

Induced drag is determined separately from

$$\boldsymbol{f}_\mathrm{D}/q_\infty = \frac{2}{V_\infty}\,\Gamma_\mathrm{eff}\,\boldsymbol{v}_\mathrm{ind}^* \times \boldsymbol{r}_0 \tag{2.2.27}$$

where $\boldsymbol{v}_\mathrm{ind}^*$ is the velocity induced by the streamwise segments of the bound vortex rings and all segments of the vortex rings in the wake. Expressed as a tensor product, this induced velocity for drag becomes

$$\boldsymbol{v}_\mathrm{ind}^* = (\mathsf{A}_\mathrm{u}\boldsymbol{\Gamma}_\mathrm{P} + \mathsf{B}_\mathrm{u}\boldsymbol{\Gamma}_\mathrm{W})\boldsymbol{i}^\mathrm{T} + (\mathsf{A}_\mathrm{v}\boldsymbol{\Gamma}_\mathrm{P} + \mathsf{B}_\mathrm{v}\boldsymbol{\Gamma}_\mathrm{W})\boldsymbol{j}^\mathrm{T} + (\mathsf{A}_\mathrm{w}\boldsymbol{\Gamma}_\mathrm{P} + \mathsf{B}_\mathrm{w}\boldsymbol{\Gamma}_\mathrm{W})\boldsymbol{k}^\mathrm{T}$$

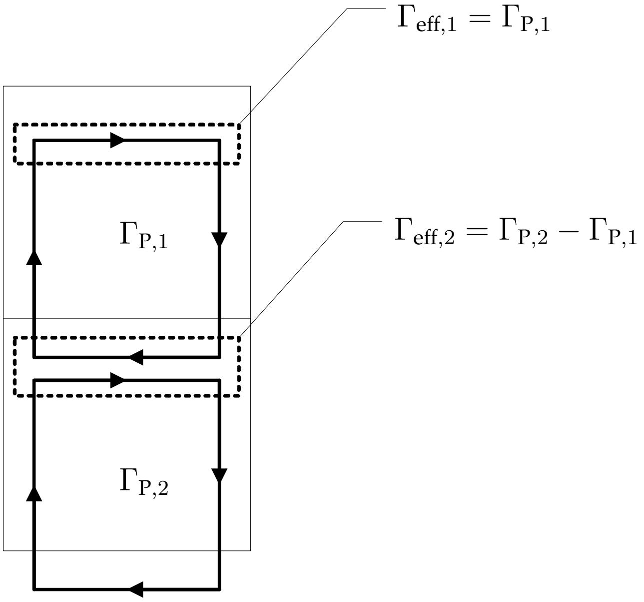

Figure 2.16: Effective circulation of the lifting vortex

where $A_{\text{u,v,w}}$ and $B_{\text{u,v,w}}$ are the bound and wake influence matrices, respectively, for the velocity components in the direction of the base vectors $\boldsymbol{i}, \boldsymbol{j}, \boldsymbol{k}$. Clearly, the induced drag is a quadratic function of the bound vortex loop circulation.

For the computation of pressure coefficients on body panels, the *Kutta-Joukowski* theorem for vortex lift is unsuitable. Instead, the steady part of the pressure is computed using the total velocity in panel coordinates

$$c_p = 1 - \frac{(\boldsymbol{V}_{\text{kin}} + \boldsymbol{w}) \cdot (\boldsymbol{V}_{\text{kin}} + \boldsymbol{w})}{V_\infty^2} \tag{2.2.28}$$

$$\boldsymbol{w} = \boldsymbol{w}_{\text{ind}} + \bar{\boldsymbol{w}} \tag{2.2.29}$$

where $\boldsymbol{w}_{\text{ind}}$ is the velocity induced by all other vortex rings and $\bar{\boldsymbol{w}}$ is the tangential velocity jump, that the vortex ring induces on itself. All velocities here are resolved in the direction of the panel coordinate system. The tangential velocity jump across a vortex sheet is related to its vortex sheet strength γ by (see [64])

$$\Delta u = \frac{\gamma}{2}$$

and must be determined for both tangential directions $\boldsymbol{\tau}_1$ and $\boldsymbol{\tau}_2$ separately by applying the following procedure (see also van Staveren [125]). First, a second order polynomial is fitted to the panel circulation Γ of the target panel and two neighboring panels along the arc length s connecting the panel centroids:

$$\Gamma(s) = a_2 s^2 + a_1 s + a_0$$

Then, the vortex sheet strength in the direction of the arc length s is determined by differentiating the polynomial to obtain

$$\gamma = \frac{\partial \Gamma(s)}{\partial s} = 2a_2 s + a_1$$

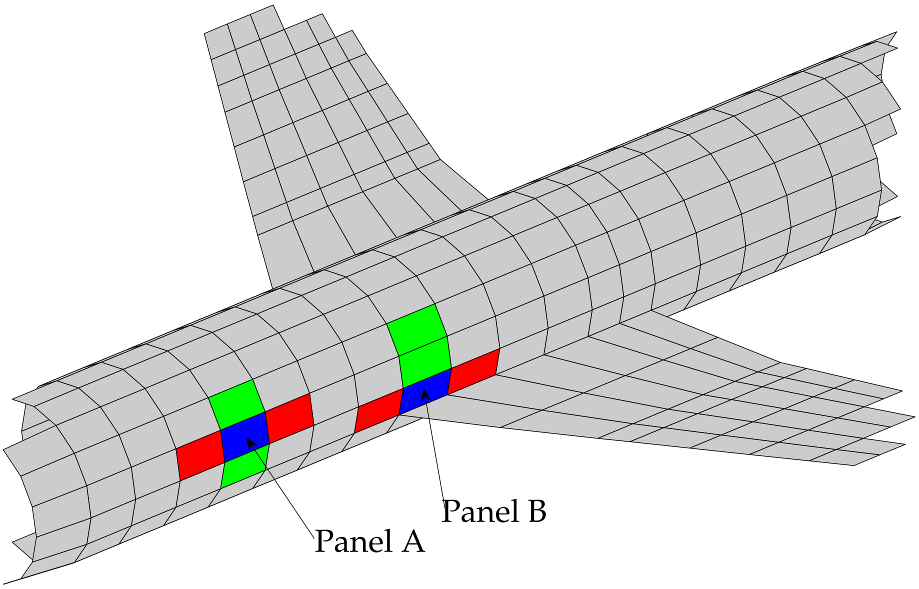

Figure 2.17: Determination of Body Vortex Sheet Strength

Finally, the veclocity jump in the tangential directions becomes

$$\bar{\boldsymbol{w}} = \frac{1}{2}\begin{Bmatrix} 2a_2s + a_1 \\ 2b_2s + b_2 \\ 0 \end{Bmatrix} \tag{2.2.30}$$

where the letters a and b have been chosen for the polynomial coefficients in the $\boldsymbol{\tau}_1$ and $\boldsymbol{\tau}_2$ direction, respectively, and the normal direction does not experience the discontinuity in velocity. The coordinate s must be set to the value of the target panel centroid.

Care must be taken not to form the polynomial across discontinuities as wakes or lifting surfaces attached to the body. In these cases, two neighboring panels on one side of the target panel are chosen. As illustration, Fig. 2.17 depicts two different target panels in blue. In order to determine the cirumferential vortex sheet strength on panel A, a regulare central difference approach using the green panels is applied whereas on panel B, the wing intersecting the body requires the forming of an one-sided difference. For the streamwise vortex sheet strength, in both cases a central difference using the red panels can be applied.

Total Derivative of the Potential

The total derivative of the potential in Eq. (2.2.13) represents the rate of change of the potential following a point on the lifting surfaces moving through the fluid. The velocity-based formulation of the problem Eq. (2.2.14) does not yield the potential on the lifting surfaces and bodies but the singularity strength and requires only velocity influence coefficients. In order to avoid the introduction of additional potential influence coefficients only for the determination of the total derivative of the potential, an indirect approach is chosen according to Cebeci et al. [18]. As shown in Fig. 2.18, the disturbance velocity field is integrated in two steps, first along a straight line from far away upstream to the apex of the body or leading edge of the lifting surface, then from that point to the panel control point along the body contour or the upper or lower side

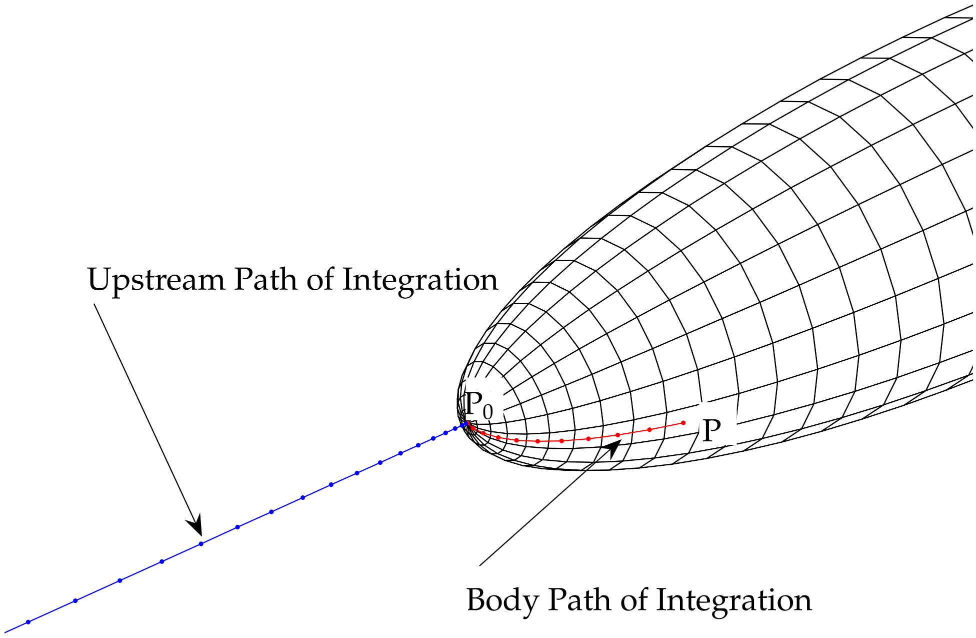

Figure 2.18: Determination of Velocity Potential

of the lifting surface, respectively. Only the velocity induced by the singularities is taken into account and on bodies the self-induction term according to Eq. (2.2.30) must be included:

$$\phi_{\mathrm{P}} = \phi_{\mathrm{P}_0} + (\phi_{\mathrm{P}} - \phi_{\mathrm{P}_0}) = \int_{\infty}^{\mathrm{P}_0} \boldsymbol{w}_{\mathrm{ind}} \mathrm{d}\boldsymbol{s} + \int_{\mathrm{P}_0}^{\mathrm{P}} (\boldsymbol{w}_{\mathrm{ind}} + \bar{\boldsymbol{w}}) \mathrm{d}\boldsymbol{s}$$

Because of the quadratic decline of induced velocity with distance from the body, the upstream integration is only carried out along a straight line extending ten body lengths upstream. On the line, a number of control points are distributed in cosine spacing and the trapezoidal rule is applied to determine the integral value. For lifting surfaces where the instantaneous local potential jump

$$\Delta\phi_{\mathrm{P}} = \phi_{\mathrm{P_u}} - \phi_{\mathrm{P_l}}$$

between the lower and upper surface is sought, the freestream integral cancels out and given a vortex sheet strength γ, the velocity potential jump is obtained by integration from the leading edge to a point just above and below the sheet

$$\Delta\phi_{\mathrm{P}} = \int_{\mathrm{P}_0}^{\mathrm{P_u}} \frac{\gamma}{2} \mathrm{d}s - \int_{\mathrm{P}_0}^{\mathrm{P_l}} -\frac{\gamma}{2} \mathrm{d}s = \int_{\mathrm{P}_0}^{\mathrm{P}} \gamma \mathrm{d}s$$

For the vortex ring model, the vortex sheet strength is constant for each panel and the integration reduces to a summation in the chordwise direction

$$\begin{aligned}\Delta\phi(i,j) &= \sum_{l=1}^{i} \gamma(l,j)\, c(l,j) = \\ &= \frac{\Gamma_{\mathrm{P}}(1,j)}{c(1,j)}\, c(1,j) + \sum_{l=2}^{i} \frac{\Gamma_{\mathrm{P}}(l,j) - \Gamma_{\mathrm{P}}(l-1,j)}{c(l,j)}\, c(l,j) = \Gamma_{\mathrm{P}}(i,j).\end{aligned}$$

Therefore the potential jump over a vortex ring element in the lifting surfaces is given by the ring circulation itself and its total derivative reduces to the simple time derivative of the vortex ring circulation because we look at the circulation in the moving frame of reference. Using finite differences in time with a discrete time step denoted by superscript n, the first order backward expression for the time derivative is

$$\left(\frac{\mathrm{D}\Delta\phi_{\mathrm{P}}}{\mathrm{D}t}\right)^{n} \approx \frac{\Gamma_{\mathrm{P}}^{n}-\Gamma_{\mathrm{P}}^{n-1}}{\Delta t} \qquad \text{on lifting surfaces} \tag{2.2.31a}$$

$$\left(\frac{\mathrm{D}\phi_{\mathrm{P}}}{\mathrm{D}t}\right)^{n} \approx \frac{\phi_{\mathrm{P}}^{n}-\phi_{\mathrm{P}}^{n-1}}{\Delta t} \qquad \text{on bodies} \tag{2.2.31b}$$

and the second order backward expression is

$$\left(\frac{\mathrm{D}\Delta\phi_{\mathrm{P}}}{\mathrm{D}t}\right)^{n} \approx \frac{3\Gamma_{\mathrm{P}}^{n}-4\Gamma_{\mathrm{P}}^{n-1}+\Gamma_{\mathrm{P}}^{n-2}}{2\Delta t} \qquad \text{on lifting surfaces} \tag{2.2.32a}$$

$$\left(\frac{\mathrm{D}\phi_{\mathrm{P}}}{\mathrm{D}t}\right)^{n} \approx \frac{3\phi_{\mathrm{P}}^{n}-4\phi_{\mathrm{P}}^{n-1}+\phi_{\mathrm{P}}^{n-2}}{2\Delta t} \qquad \text{on bodies} \tag{2.2.32b}$$

where Δt is the time step size. With Eqn. (2.2.25), the load on a panel due to the time rate of change of the potential becomes

$$\boldsymbol{f}_{\mathrm{U}}/q_{\infty} = \begin{cases} -\frac{2A}{V_{\infty}^{2}}\left(\frac{\mathrm{D}\Delta\phi_{\mathrm{P}}}{\mathrm{D}t}\right)\boldsymbol{n} & \text{on lifting surfaces} \\ -\frac{2A}{V_{\infty}^{2}}\left(\frac{\mathrm{D}\phi_{\mathrm{P}}}{\mathrm{D}t}\right)\boldsymbol{n} & \text{on bodies} \end{cases} \tag{2.2.33}$$

The total unsteady force $\boldsymbol{f}$ on a vortex ring panel is the sum of Eqn. (2.2.26), (2.2.27) and (2.2.33)

$$\boldsymbol{f}/q_{\infty} \;=\; \left(\boldsymbol{f}_{\mathrm{S}}+\boldsymbol{f}_{\mathrm{D}}+\boldsymbol{f}_{\mathrm{U}}\right)/q_{\infty} \tag{2.2.34}$$

Due to the mixed formulation on lifting surfaces, the force resulting from the first two terms act at the center of the quarter-chord line of the panel, whereas the force from the third term acts at the panel center. On body panels, all forces act at the panel center. The total unsteady panel moment $\boldsymbol{m}$ with respect to the panel center is therefore

$$\boldsymbol{m}/q_{\infty} = \begin{cases} \left(\boldsymbol{f}_{\mathrm{S}}+\boldsymbol{f}_{\mathrm{D}}\right)/q_{\infty}\times\Delta\boldsymbol{c}_{25} & \text{on lifting surfaces} \\ \boldsymbol{0} & \text{on bodies} \end{cases} \tag{2.2.35}$$

where $\Delta\boldsymbol{c}_{25} = \{\Delta c_{25,x}, \Delta c_{25,y}, \Delta c_{25,z}\}^{\mathrm{T}}$ is the offset vector from the center of the quarter chord line to the panel center, see Fig. 2.12.

A summary of the solution process using the unsteady vortex lattice method is given in Fig. 2.19. First, the downwash due to rigid body motion, elastic deformation and gust is determined according to Eq. (2.2.16). Then the downwash induced by the wake is computed and the linear equations system Eq. (2.2.21) is solved. After that, the aerodynamic panel loads result from Eqn. (2.2.34) and (2.2.35). Finally, the position of the body frame of reference is updated, new wake panels are released and if necessary the wake is deformed according to the local flow velocities. This procedure is repeated for the desired number of time steps.

2.2.3 Linearized Formulation

A linearized formulation of the unsteady vortex lattice method permits a closed form solution when the following simplifying assumptions are made:

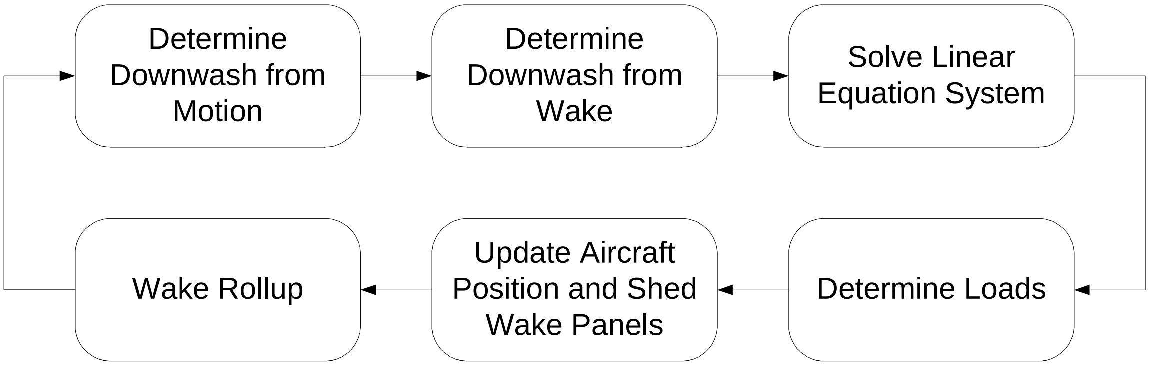

Figure 2.19: Solution Steps of the Unsteady Vortex Lattice Method

1. The shape of the wake is prescribed and therefore the wake influence coefficient matrix B is constant.
2. The body fixed frame of reference is moving in the direction of the positive x-axis with constant velocity V_∞.
3. Induced drag is neglected.

Linearized Downwash

If we assume small perturbations of the panel degrees of freedom $\boldsymbol{u}$ and $\boldsymbol{\varphi}$ about the steady flow $\boldsymbol{v}_\mathrm{R} = \{V_\infty, 0, 0\}^\mathrm{T}$ and the reference geometry with normal vectors $\boldsymbol{n} = \{n_x, n_y, n_z\}^\mathrm{T}$, we obtain from Eq. (2.2.16) the linearized downwash perturbation of a panel

$$\delta d = \begin{cases} \boldsymbol{v}_\mathrm{R} \cdot (\boldsymbol{\varphi} \times \boldsymbol{n}) + (\boldsymbol{v}_\mathrm{G} + \dot{\boldsymbol{u}} + \dot{\boldsymbol{\varphi}} \times \Delta \boldsymbol{c}_{75}) \cdot \boldsymbol{n} & \text{on lifting surfaces} \\ \boldsymbol{v}_\mathrm{R} \cdot (\boldsymbol{\varphi} \times \boldsymbol{n}) + (\boldsymbol{v}_\mathrm{G} + \dot{\boldsymbol{u}}) \cdot \boldsymbol{n} & \text{on bodies} \end{cases}$$

Expressed in matrix notation, the perturbed downwash vector $\delta \boldsymbol{d}$ becomes

$$\delta \boldsymbol{d} = D_1 \boldsymbol{u}_\mathrm{A} + D_2 \dot{\boldsymbol{u}}_\mathrm{A} + D_3 \boldsymbol{u}_\mathrm{G} \tag{2.2.36}$$

where D_1, D_2 and D_3 are the downwash matrices due to panel displacement, panel velocity and atmospheric disturbance and the vectors $\boldsymbol{u}_\mathrm{A}, \dot{\boldsymbol{u}}_\mathrm{A}$ and $\boldsymbol{u}_\mathrm{G}$ are the panel vectors of displacement, velocity and atmospheric disturbance, respectively. Details of the construction of the individual terms can be found in Appendix B.1.

Linearized Loads

Assuming that all inflow velocities not related to the rigid body motion are small, e.g. $|\boldsymbol{v}_\mathrm{E}|, |\boldsymbol{v}_\mathrm{G}|, |\boldsymbol{v}^*_\mathrm{ind}| \ll V_\infty$, the expression for the panel forces and moments on lifting surfaces defined by Eqn. (2.2.34) and (2.2.35) simplifies to the matrix equation

$$\boldsymbol{f}_\mathrm{A}/q_\infty = S_1 P\, \boldsymbol{\Gamma}_\mathrm{P} + S_2\, \dot{\boldsymbol{\Gamma}}_\mathrm{P} \tag{2.2.37}$$

where S_1 is the *Kutta-Joukowski* load matrix, P is the permutation matrix to determine the effective circulation as outlined above and S_2 is the load matrix for the total derivative of the potential. Details of the construction of the individual terms can be found in Appendix B.2. On body panels, the linearized expression is significantly more complicated because linearization of Eq. (2.2.29) yields for the steady part of the perturbed pressure coefficient

$$\delta c_p = 2\frac{(\boldsymbol{V}_{\mathrm{kin}} + \boldsymbol{w})\,(\delta\boldsymbol{V}_{\mathrm{kin}} + \delta\boldsymbol{w})}{V_\infty^2}.$$

This implies that the steady state about which the small perturbations occur is coupled with the linearized incremental unsteady solution. Provided that a steady state solution is available, the matrix equation for the steady part of the perturbed body panel load can be written as

$$(\boldsymbol{f}_{\mathrm{A}}/q_\infty)_{\mathrm{steady}} = S_2 S_{\mathrm{V}}\left(\delta\boldsymbol{d}_\tau + (G + A_\tau)\,\boldsymbol{\Gamma}_{\mathrm{P}} + B_\tau\boldsymbol{\Gamma}_{\mathrm{W}}\right) \tag{2.2.38}$$

where S_2 has been introduced above, S_{V} is the panel velocity matrix of the steady state, G is the circulation gradient matrix and A_τ and B_τ are the tangential velocity aerodynamic influence matrices of bound vorticity and wake, respectively. The perturbed tangential velocity at the body panels $\delta\boldsymbol{d}_\tau$ is determined from

$$\delta\boldsymbol{d}_\tau = D_{1\tau}\boldsymbol{u}_{\mathrm{A}} + D_{2\tau}\dot{\boldsymbol{u}}_{\mathrm{A}} + D_{3\tau}\boldsymbol{u}_{\mathrm{G}} \tag{2.2.39}$$

where $D_{1\tau}$, $D_{2\tau}$ and $D_{3\tau}$ are the tangential disturbance matrices due to panel displacement, panel velocity and atmospherice disturbance, repsectively. Details of the construction of the individual terms can be found in Appendix B.3.

The pressure coefficient due to the time derivative of the potential can be written as

$$(\boldsymbol{f}_{\mathrm{A}}/q_\infty)_{\mathrm{unsteady}} = S_2\left((I_{0\mathrm{P}} + I_{\mathrm{P}}\,(G + A_\tau))\,\dot{\boldsymbol{\Gamma}}_{\mathrm{P}} + (I_{0\mathrm{W}} + I_{\mathrm{P}}B_\tau)\,\dot{\boldsymbol{\Gamma}}_{\mathrm{W}}\right) \tag{2.2.40}$$

where $I_{0\mathrm{P}}$ and $I_{0\mathrm{W}}$ are the upstream potential integration matrices for bound vorticity and wake and I_{P} is the body contour integration matrix. Again, the details of the construction of the individual terms can be found in Appendix B.3.

Wake Transition Matrix

When following the body fixed frame and using a prescribed wake of fixed temporal or respective spatial extend, the convection of circulation at every time step can be split into two parts. The fist part is the transfer of the trailing edge circulation on lifting surfaces into the wake. If we denote an arbitrary discrete time step by the superscript n, the wake panel adjacent to a trailing edge in strip j will contain the circulation of its bound trailing edge neighbor from the previous time step $n-1$

$$\Gamma_{\mathrm{W}}^{n}(1,j) = \Gamma_{\mathrm{P}}^{n-1}(\boldsymbol{N}_{\mathrm{C}}(j),j) \tag{2.2.41}$$

The second part of the convection occurs in the wake, where a wake panel in strip j will contain the circulation of the its upstream neighbor from the previous time step $n-1$. Recursively using Eq. (2.2.41), this can be written as

$$\Gamma_{\mathrm{W}}^{n}(i,j) = \Gamma_{\mathrm{W}}^{n-1}(i-1,j) = \Gamma_{\mathrm{P}}^{n-i}(\boldsymbol{N}_{\mathrm{C}}(j),j) \tag{2.2.42}$$

and shows, that at time step n, the circulation value at wake element (i,j) can be related to the trailing edge circulation at time step $n-i$. Defining the transport matrices T_{P} and T_{W}, Eqn. (2.2.41) and (2.2.42) can be cast in matrix notation

$$\boldsymbol{\Gamma}_{\mathrm{W}}^{n} = T_{\mathrm{P}}\boldsymbol{\Gamma}_{\mathrm{P}}^{n-1} + T_{\mathrm{W}}\boldsymbol{\Gamma}_{\mathrm{W}}^{n-1} \tag{2.2.43}$$

where T_{P} is of size $(N_{\mathrm{W}} \times N_{\mathrm{P}})$ and T_{W} is of size $(N_{\mathrm{W}} \times N_{\mathrm{W}})$. This equation relates the wake circulation to the bound circulation.

State Space Equation for the Wake

To obtain a state space expression for the wake circulation, we must eliminate $\mathbf{\Gamma}_\mathrm{P}$ from the wake transport equation. Using Eq. (2.2.22), the expression for the bound circulation at time step $(n-1)$ becomes

$$\mathbf{\Gamma}_\mathrm{P}^{n-1} = A^{-1}\left(-\boldsymbol{d}^{n-1} - B\mathbf{\Gamma}_\mathrm{W}^{n-1}\right)$$

and can be substituted into Eq. (2.2.43) yielding

$$\mathbf{\Gamma}_\mathrm{W}^{n} = \left(T_\mathrm{W} - T_\mathrm{P}A^{-1}B\right)\mathbf{\Gamma}_\mathrm{W}^{n-1} - T_\mathrm{P}A^{-1}\boldsymbol{d}^{n-1} \tag{2.2.44}$$

This is the discrete time state space description of the wake circulation. To obtain a continuous time equivalent of the state space system, an approximate time integration scheme must be chosen. To illustrate integration alternatives, Eq. (2.2.44) is written in terms of the z-transform, the discrete-time counterpart to the Laplace transform (for details see for instance the textbook by Franklin et al. [37]). The operator z acts as a forward shift in time by one time step and therefore

$$z\mathbf{\Gamma}_\mathrm{W} = \left(T_\mathrm{W} - T_\mathrm{P}A^{-1}B\right)\mathbf{\Gamma}_\mathrm{W} - T_\mathrm{P}A^{-1}\boldsymbol{d}$$

Depending on how the continuous frequency variable s of the Laplace transform is approximated, three variants of time integration can be identified

$$s \approx \begin{cases} \frac{z-1}{\Delta t} & \text{forward rectangular} \\ \frac{1}{z}\frac{z-1}{z} & \text{backward rectangular} \\ \frac{2}{\Delta t}\frac{z-1}{z+1} & \text{bilinear} \end{cases}$$

The time step size is determined by the streamwise discretization of the prescribed wake and the steady flight velocity $\Delta t = \Delta x / V_\infty$. Choosing for simplicity the forward rectangular (Euler) integration, the Laplace domain approximation of the wake state space equation becomes

$$s\mathbf{\Gamma}_\mathrm{W} = \frac{1}{\Delta t}\left(T_\mathrm{W} - T_\mathrm{P}A^{-1}B - I\right)\mathbf{\Gamma}_\mathrm{W} - \frac{1}{\Delta t}T_\mathrm{P}A^{-1}\boldsymbol{d}$$

and by inverse Laplace transformation, the continuous time domain version

$$\dot{\mathbf{\Gamma}}_\mathrm{W} \approx \frac{1}{\Delta t}\left(T_\mathrm{W} - T_\mathrm{P}A^{-1}B - I\right)\mathbf{\Gamma}_\mathrm{W} - \frac{1}{\Delta t}T_\mathrm{P}A^{-1}\boldsymbol{d}$$

is obtained. Application of any of the other two integration methods requires the additional inversion of the bracketed term in front of $\mathbf{\Gamma}_\mathrm{W}$ and yields a continuous time domain system with the time derivative of the downwash as an extra input parameter. In typical state space notation, the wake equation can be written as

$$\dot{\mathbf{\Gamma}}_\mathrm{W} = \bar{A}\mathbf{\Gamma}_\mathrm{W} + \bar{B}_1\boldsymbol{d} + \bar{B}_2\dot{\boldsymbol{d}} \tag{2.2.45}$$

with the state matrix

$$\bar{A} = \frac{1}{\Delta t}\left(T_\mathrm{W} - T_\mathrm{P}A^{-1}B - I\right),$$

and the input matrices

$$\begin{aligned} \bar{B}_1 &= -\frac{1}{\Delta t}T_\mathrm{P}A^{-1} \\ \bar{B}_2 &= 0 \end{aligned}$$

The tabulated coefficients for the other two integration methods can be found in Appendix B.4. Because the sparse structure of matrix $\bar{A}$ is only preserved in the case of forward rectangular integration, this approach is applied in the following. Then because $\bar{B}_2 = 0$, the subscript of $\bar{B}_1$ is dropped and the notation $\bar{B}$ is used instead.

Output Equation

The output equation of the state space system must provide the panel loads according to Eqns. (2.2.37), (2.2.38) and (2.2.40). To obtain an expression for the time rate of change of the bound circulation $\dot{\boldsymbol{\Gamma}}_\mathrm{P}$, we take the time derivative of Eq. (2.2.22) and substitute Eq. (2.2.45) to find

$$\dot{\boldsymbol{\Gamma}}_\mathrm{P} \quad = \quad -A^{-1}\left(\dot{\boldsymbol{d}} + B\left(\bar{A}\boldsymbol{\Gamma}_\mathrm{W} + \bar{B}\boldsymbol{d}\right)\right). \tag{2.2.46}$$

For lifting surfaces, substitution of this equation together with Eq. (2.2.22) into Eq. (2.2.37) yields the desired output equation for the state space system

$$\boldsymbol{f}_\mathrm{A}/q_\infty = \bar{C}\boldsymbol{\Gamma}_\mathrm{W} + \bar{D}_1\boldsymbol{d} + \bar{D}_2\dot{\boldsymbol{d}} \tag{2.2.47}$$

with the output matrix

$$\bar{C} \quad = \quad -S_1PA^{-1}B - S_2A^{-1}B\bar{A}$$

the feedthrough matrix for downwash

$$\bar{D}_1 \quad = \quad -S_1PA^{-1} - S_2A^{-1}B\bar{B}_1$$

and the feedthrough matrix for the rate of downwash

$$\bar{D}_2 \quad = \quad -S_2A^{-1} - S_2A^{-1}B\bar{B}_2$$

For body panels, substitution of Eqn. (2.2.45) and (2.2.46) in Eq. (2.2.38) in combination with Eq. (2.2.40) yields the output equation

$$\boldsymbol{f}_\mathrm{A}/q_\infty = \bar{C}\boldsymbol{\Gamma}_\mathrm{W} + \bar{D}_1\boldsymbol{d} + \bar{D}_2\dot{\boldsymbol{d}} + \bar{D}_3\delta\boldsymbol{d}_\tau \tag{2.2.48}$$

with the output matrix

$$\begin{aligned}\bar{C} = -S_2\big[&S_\mathrm{V}\left(G + A_\tau\right)A^{-1}B - S_\mathrm{V}B_\tau \\ &+ \left(I_{0\mathrm{P}} + I_\mathrm{P}\left(G + A_\tau\right)\right)A^{-1}B\bar{A} - \left(I_{0\mathrm{W}} + I_\mathrm{P}B_\tau\right)\bar{A}\big],\end{aligned}$$

the feedthrough matrix for downwash

$$\bar{D}_1 = -S_2\left[S_\mathrm{V}\left(G + A_\tau\right)A^{-1} + \left(I_{0\mathrm{P}} + I_\mathrm{P}\left(G + A_\tau\right)\right)A^{-1}B\bar{B}_1 - \left(I_{0\mathrm{W}} + I_\mathrm{P}B_\tau\right)\bar{B}_1\right],$$

the feedthrough matrix for rate of downwash

$$\bar{D}_2 = -S_2\left(I_{0\mathrm{P}} + I_\mathrm{P}\left(G + A_\tau\right)\right)A^{-1}\left(I + B\bar{B}_2\right) + \left(I_{0\mathrm{W}} + I_\mathrm{P}B_\tau\right)\bar{B}_2$$

and the feedthrough matrix for the tangential disturbance velocity

$$\bar{D}_3 = S_2S_\mathrm{V}.$$

Aeroelastic Degrees of Freedom

The state space form of the unsteady vortex lattice method can now be formulated in terms of the typical aeroelastic input vectors for the panel degrees of freedom $\bar{\boldsymbol{u}}_\text{A}$

$$\bar{\boldsymbol{u}}_\text{A} = \begin{Bmatrix} \boldsymbol{u}_\text{A} \\ \dot{\boldsymbol{u}}_\text{A} \\ \ddot{\boldsymbol{u}}_\text{A} \end{Bmatrix}$$

and gust $\bar{\boldsymbol{u}}_\text{G}$

$$\bar{\boldsymbol{u}}_\text{G} = \begin{Bmatrix} \boldsymbol{u}_\text{G} \\ \dot{\boldsymbol{u}}_\text{G} \end{Bmatrix} .$$

Taking the time derivative of the linearized downwash Eq. (2.2.36), the matrix equation for the rate of linearized downwash becomes

$$\delta\dot{\boldsymbol{d}} = D_1\dot{\boldsymbol{u}}_\text{A} + D_2\ddot{\boldsymbol{u}}_\text{A} + D_3\dot{\boldsymbol{u}}_\text{G}. \tag{2.2.49}$$

For a more compact matrix notation, define the total downwash matrices for panel freedoms D_A and gust D_G

$$D_\text{A} = \begin{bmatrix} D_1 & D_2 & 0 \end{bmatrix} , \qquad D_\text{G} = \begin{bmatrix} D_3 & 0 \end{bmatrix} ,$$

the rate of downwash matrices for panel degree of freedoms R_A and gust R_G

$$R_\text{A} = \begin{bmatrix} 0 & D_1 & D_2 \end{bmatrix} , \qquad R_\text{G} = \begin{bmatrix} 0 & D_3 \end{bmatrix} ,$$

and total tangential velocity disturbance

$$D_{\tau\text{A}} = \begin{bmatrix} D_{1\tau} & D_{2\tau} & 0 \end{bmatrix} , \qquad D_{\tau\text{G}} = \begin{bmatrix} D_{3\tau} & 0 \end{bmatrix} ,$$

to obtain the state space and output equations in terms of panel degrees of freedom

$$\begin{aligned} \dot{\boldsymbol{\Gamma}}_\text{W} &= \bar{A}\boldsymbol{\Gamma}_\text{W} + \left(\bar{B}_1 D_\text{A} + \bar{B}_2 R_\text{A}\right)\bar{\boldsymbol{u}}_\text{A} + \left(\bar{B}_1 D_\text{G} + \bar{B}_2 R_\text{G}\right)\bar{\boldsymbol{u}}_\text{G} \\ \boldsymbol{f}_\text{A}/q_\infty &= \begin{cases} \bar{C}\boldsymbol{\Gamma}_\text{W} + \left(\bar{D}_1 D_\text{A} + \bar{D}_2 R_\text{A}\right)\bar{\boldsymbol{u}}_\text{A} + \left(\bar{D}_1 D_\text{G} + \bar{D}_2 R_\text{G}\right)\bar{\boldsymbol{u}}_\text{G} \\ \bar{C}\boldsymbol{\Gamma}_\text{W} + \left(\bar{D}_1 D_\text{A} + \bar{D}_2 R_\text{A} + \bar{D}_3 D_{\tau\text{A}}\right)\bar{\boldsymbol{u}}_\text{A} + \left(\bar{D}_1 D_\text{G} + \bar{D}_2 R_\text{G} + \bar{D}_3 D_{\tau\text{G}}\right)\bar{\boldsymbol{u}}_\text{G} \end{cases} \end{aligned} \tag{2.2.50}$$

2.2.4 Steady and Quasi-Steady Formulations

For the aeroelastic model integration, two special cases of the unsteady vortex lattice method are required in addition to the unsteady formulation. The first is the case of steady flow, when effectively the fluid has an infinite amount of time to adjust to the steady motion and shape of the aircraft. The amount of circulation shed into the wake becomes constant over time and the wake does not exhibit a streamwise gradient of circulation. Unless the accurate shape of the steady wake is of interest (e.g. in a free wake analysis), this implies that the wake discretization can be reduced to one wake vortex ring element per trailing edge panel. This single row of wake vortex ring is extended far downstream in order to remove the influence of the starting vortex and to emulate semi-infinite trailing vortices. As shown in Fig. 2.20, the vortex ring discretization becomes fully equivalent to horseshoe vortices. In order to fulfill the steady *Kutta*-condition of zero circulation on the trailing edge, the circulation of the wake panels must be identical to the trailing edge panel they are attached to. The columns of the

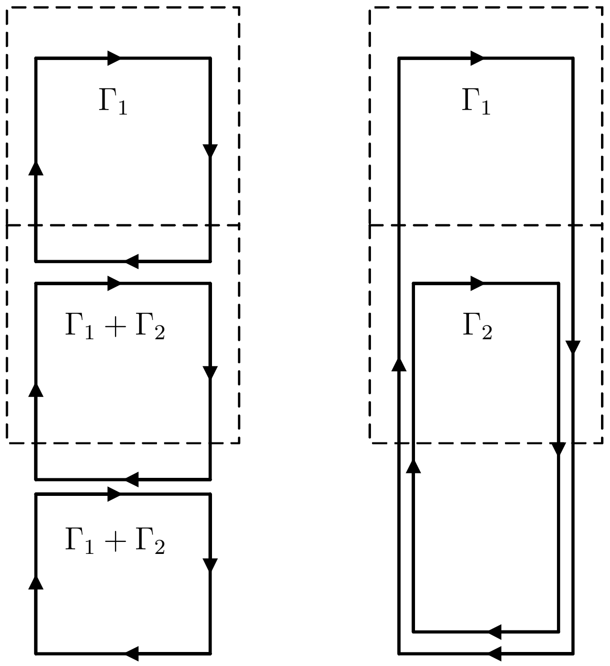

Figure 2.20: Equivalency of Vortex Loops and Horseshoe Vortices

wake influence matrix B can therefore be added to the respective column of the bound influence matrix A, yielding a combined steady state influence matrix A_S. The solution for the bound circulation according to Eq. (2.2.22) simplifies to

$$\boldsymbol{\Gamma}_\mathrm{P} = A_\mathrm{S}^{-1}\left(-\boldsymbol{d}\right)$$

and the aerodynamic loads are the sum of the *Kutta-Joukowski* vortex lift and the induced drag

$$\boldsymbol{f}/q_\infty = \left(\boldsymbol{f}_\mathrm{S} + \boldsymbol{f}_\mathrm{D}\right)/q_\infty .$$

The linearized formulation for steady state conditions is obtained from the state space formulation by first setting the wake gradient $\dot{\boldsymbol{\Gamma}}_\mathrm{W}$ and rate of downwash $\dot{\boldsymbol{d}}$ in Eq. (2.2.45) to zero. The resulting wake circulation

$$\boldsymbol{\Gamma}_\mathrm{W} = -\bar{A}^{-1}\bar{B}\boldsymbol{d} \tag{2.2.51}$$

is substituted in the output equation Eq. (2.2.47) or Eq. (2.2.48) and, setting the rate of downwash $\dot{\boldsymbol{d}}$ to zero, we obtain the steady load

$$\boldsymbol{f}_\mathrm{A}/q_\infty = \begin{cases} \left(-\bar{C}\bar{A}^{-1}\bar{B} + \bar{D}_1\right)\boldsymbol{d} \\ \left(-\bar{C}\bar{A}^{-1}\bar{B} + \bar{D}_1\right)\boldsymbol{d} + \bar{D}_3\delta\boldsymbol{d}_\tau \end{cases} \tag{2.2.52}$$

This derivation does not require the additional computation of a steady state wake matrix and provides the consistent limit value of the linearized unsteady formulation for constant downwash as time approaches infinity.

The second special case that needs to be addressed is so called quasi-steady flow. When downwash is changing at a constant rate, also the amount of circulation shed into the wake changes at a constant rate and the wake exhibits a constant streamwise circulation gradient. Using this approach, the time delay of downwash at the empennage of a full aircraft configuration can be modelled as follows. Analogous to Section 2.1.2, the

0	*0*
0	Wing → Tail

(a) Matrix $A_\mathrm{S}^{W\rightarrow T}$

Tail → Wing	Wing
Tail	*0*

(b) Matrix $A_\mathrm{S}^{W\nrightarrow T}$

Figure 2.21: Partitions of the Modified Influence Matrices

lever arm of the horizontal tail is l_H and the characteristic convection time from wing to tail is $\Delta t = l_\mathrm{H}/V_\infty$. For a given rate of downwash $\dot{\boldsymbol{d}}$, the induced velocities at the empennage at time t are caused by the bound circulation $\boldsymbol{\Gamma}_\mathrm{P}^*$ at time $t - \Delta t$

$$\boldsymbol{\Gamma}_\mathrm{P}^* \quad = \quad A_\mathrm{S}^{-1}\left(-\boldsymbol{d}^*\right)$$

where $\boldsymbol{d}^*$ is the rate-corrected downwash

$$\boldsymbol{d}^* \quad = \quad \boldsymbol{d} - \frac{l_\mathrm{H}}{V_\infty}\,\dot{\boldsymbol{d}}.$$

The induced normalwash on the tail can be expressed with the induction influence matrix $A_\mathrm{S}^{W\rightarrow T}$, where all influence coefficients are zero except those describing the induction from the wing on the tail. The actual bound circulation is then found from

$$A_\mathrm{S}^{W\nrightarrow T}\boldsymbol{\Gamma}_\mathrm{P} + A_\mathrm{S}^{W\rightarrow T}\boldsymbol{\Gamma}_\mathrm{P}^* = -\boldsymbol{d} \tag{2.2.53}$$

where $A_\mathrm{S}^{W\nrightarrow T}$ is the influence matrix without interference from the wing onto the tail. For clarification, Fig. 2.21 graphically shows the partitions for the modified matrices. Once the bound circulation is known, the aerodynamic loads are determined as outlined for the steady case.

The linearized formulation for quasi-steady conditions is alternatively obtained from the state space formulation by first taking the time derivative of Eq. (2.2.45) and requiring $\ddot{\boldsymbol{\Gamma}}_\mathrm{W} = \boldsymbol{0}$. The resulting wake gradient

$$\dot{\boldsymbol{\Gamma}}_\mathrm{W} = -\bar{A}^{-1}\bar{B}\dot{\boldsymbol{d}}$$

is substituted back into Eq. (2.2.45) to yield the wake circulation

$$\boldsymbol{\Gamma}_\mathrm{W} = -\bar{A}^{-1}\left(\bar{A}^{-1}\bar{B}\right)\dot{\boldsymbol{d}} - \bar{A}^{-1}\bar{B}\boldsymbol{d}$$

Then the output equations Eq. (2.2.47) or (2.2.48) yield the quasi-steady loads

$$\boldsymbol{f}_\mathrm{A}/q_\infty = \begin{cases} \left(-\bar{C}\bar{A}^{-1}\bar{B} + \bar{D}_1\right)\boldsymbol{d} + \left(-\bar{C}\bar{A}^{-1}\left(\bar{A}^{-1}\bar{B}\right) + \bar{D}_2\right)\dot{\boldsymbol{d}} \\ \left(-\bar{C}\bar{A}^{-1}\bar{B} + \bar{D}_1\right)\boldsymbol{d} + \left(-\bar{C}\bar{A}^{-1}\left(\bar{A}^{-1}\bar{B}\right) + \bar{D}_2\right)\dot{\boldsymbol{d}} + \bar{D}_\tau\delta\boldsymbol{d}_\tau \end{cases} \tag{2.2.54}$$

2.2.5 Incremental Formulation and Analogy to Rational Function Approximation

The state space formulation of the unsteady vortex lattice method (UVLM) given by the state equation Eq. (2.2.45) and output equation Eq. (2.2.47) has been derived in terms of the total wake circulation $\mathbf{\Gamma}_{\mathrm{W}}$ and in the case of a steady state input leads to a non-zero final value of the state vector. For some applications it is helpful to reformulate the system in terms of the incremental unsteady contribution of the wake only, leading to a system that in response to a steady state disturbance returns to zero final state. To this end, the wake circulation is split into the steady state $\mathbf{\Gamma}_{\mathrm{W,s}}$ and unsteady $\mathbf{\Gamma}_{\mathrm{W,s}}$ contributions

$$\begin{aligned} \mathbf{\Gamma}_{\mathrm{W}} &= \mathbf{\Gamma}_{\mathrm{W,s}} + \mathbf{\Gamma}_{\mathrm{W,u}} \\ \dot{\mathbf{\Gamma}}_{\mathrm{W}} &= \dot{\mathbf{\Gamma}}_{\mathrm{W,s}} + \dot{\mathbf{\Gamma}}_{\mathrm{W,u}} \end{aligned}$$

where $\mathbf{\Gamma}_{\mathrm{W,s}}$ and $\dot{\mathbf{\Gamma}}_{\mathrm{W,s}}$ are given by Eq. (2.2.51) and by its time derivative, respectively:

$$\begin{aligned} \mathbf{\Gamma}_{\mathrm{W,s}} &= -\bar{A}^{-1}\bar{B}\boldsymbol{d} \\ \dot{\mathbf{\Gamma}}_{\mathrm{W,s}} &= -\bar{A}^{-1}\bar{B}\dot{\boldsymbol{d}} \end{aligned}$$

The latter term is the rate of change of the wake circulation if for every instant in time steady flow is assumed. Inserting these expressions in the original state space formulation and rearranging yields the state space equation in terms of the unsteady wake only

$$\begin{aligned} \dot{\mathbf{\Gamma}}_{\mathrm{W,u}} &= \bar{A}\mathbf{\Gamma}_{\mathrm{W,u}} + \bar{A}^{-1}\bar{B}\dot{\boldsymbol{d}} \\ \boldsymbol{f}_{\mathrm{A}}/q_\infty &= \bar{C}\mathbf{\Gamma}_{\mathrm{W,u}} + (\bar{D}_1 - \bar{C}\bar{A}^{-1}\bar{B})\boldsymbol{d} + \bar{D}_2\dot{\boldsymbol{d}} \end{aligned}$$

or written in terms of panel degrees of freedom instead of downwash

$$\begin{aligned} \dot{\mathbf{\Gamma}}_{\mathrm{W,u}} &= \bar{A}\mathbf{\Gamma}_{\mathrm{W,u}} + \bar{A}^{-1}\bar{B}D_1\dot{\boldsymbol{u}}_{\mathrm{A}} + \bar{A}^{-1}\bar{B}D_2\ddot{\boldsymbol{u}}_{\mathrm{A}} \\ \boldsymbol{f}_{\mathrm{A}}/q_\infty &= \bar{C}\mathbf{\Gamma}_{\mathrm{W,u}} + (\bar{D}_1 - \bar{C}\bar{A}^{-1}\bar{B})D_1\boldsymbol{u}_{\mathrm{A}} + \left[(\bar{D}_1 - \bar{C}\bar{A}^{-1}\bar{B})D_2 + \bar{D}_2D_1\right]\dot{\boldsymbol{u}}_{\mathrm{A}} + \bar{D}_2D_2\ddot{\boldsymbol{u}}_{\mathrm{A}} \end{aligned}$$

Adopting the typical notation used for rational function approximation (RFA) this incremental formulation becomes

$$\begin{aligned} \dot{\boldsymbol{x}}_{\mathrm{A}} &= R\boldsymbol{x}_{\mathrm{A}} + E_1\dot{\boldsymbol{u}}_{\mathrm{A}} + E_2\ddot{\boldsymbol{u}}_{\mathrm{A}} \qquad (2.2.55) \\ \boldsymbol{f}_{\mathrm{A}}/q_\infty &= A_0\boldsymbol{u}_{\mathrm{A}} + A_1\dot{\boldsymbol{u}}_{\mathrm{A}} + A_2\ddot{\boldsymbol{u}}_{\mathrm{A}} + D\boldsymbol{x}_{\mathrm{A}} \end{aligned}$$

where the individual terms can be identified by comparison of coefficients. Clearly the unsteady wake contribution is equivalent to the lag states used in the RFA. These lag states are only driven by the velocity and acceleration of the aerodynamic panels and decay once the system approaches steady state. Therefore, in contrast to the absolute wake formulation, the steady state aerodynamic loading is simply obtained by letting $\boldsymbol{x}_{\mathrm{A}} = \dot{\boldsymbol{u}}_{\mathrm{A}} = \ddot{\boldsymbol{u}}_{\mathrm{A}} = \mathbf{0}$.

2.2.6 Harmonic Formulations

For frequency domain analysis, it is useful to obtain the unsteady aerodynamic loads for a harmonic variation of the downwash

$$\boldsymbol{d} = \bar{\boldsymbol{d}}_0\mathrm{e}^{\mathrm{i}\omega t}$$

where $\bar{\boldsymbol{d}}_0$ is the complex downwash amplitude and ω is the oscillatory frequency. In the following, this approach is referred to as harmonic vortex lattice method (HVLM). One possible approach is the *Laplace* transformation of the state space system Eqn. (2.2.45) and (2.2.47) or (2.2.48) that yields the transfer function

$$\mathcal{L}\left\{\boldsymbol{f}_\mathrm{A}/q_\infty\right\} = \begin{cases} \bar{C}\left(s\,I-\bar{A}\right)^{-1}\boldsymbol{\Gamma}_\mathrm{W}(t_0)+\left(\bar{C}\left(s\,I-\bar{A}\right)^{-1}\bar{B}+\bar{D}_1+s\,\bar{D}_2\right)\boldsymbol{d}(s) \\ \bar{C}\left(s\,I-\bar{A}\right)^{-1}\boldsymbol{\Gamma}_\mathrm{W}(t_0)+\left(\bar{C}\left(s\,I-\bar{A}\right)^{-1}\bar{B}+\bar{D}_1+s\,\bar{D}_2\right)\boldsymbol{d}(s)+ \\ +\bar{D}_3\delta\boldsymbol{d}_\tau(s). \end{cases}$$

Setting $s=\mathrm{i}\omega$, the complex unsteady load amplitude becomes $\bar{\boldsymbol{f}}_\mathrm{A0}$

$$\bar{\boldsymbol{f}}_\mathrm{A0}/q_\infty = \begin{cases} \left(\bar{C}\left(\mathrm{i}\omega\,I-\bar{A}\right)^{-1}\bar{B}+\bar{D}_1+\mathrm{i}\omega\,\bar{D}_2\right)\bar{\boldsymbol{d}}_0 \\ \left(\bar{C}\left(\mathrm{i}\omega\,I-\bar{A}\right)^{-1}\bar{B}+\bar{D}_1+\mathrm{i}\omega\,\bar{D}_2\right)\bar{\boldsymbol{d}}_0+\bar{D}_3\delta\bar{\boldsymbol{d}}_\tau \end{cases}$$

if the initial wake circulation $\boldsymbol{\Gamma}_\mathrm{W}(t_0)$ is zero. The computation of the resolvent $\left(\mathrm{i}\omega\,I-\bar{A}\right)^{-1}$ is required for every new oscillatory frequency and renders this approach computationally very costly.

A more efficient procedure based on a direct frequency domain approach is therefore suggested as follows. From the differential equation for the wake circulation Eqn. (2.2.45) and the expression for the bound circulation Eqn. (2.2.22) it follows, that these quantities will also be harmonic functions if downwash is harmonic

$$\begin{aligned} \boldsymbol{\Gamma}_\mathrm{P} &= \bar{\boldsymbol{\Gamma}}_\mathrm{P0}\mathrm{e}^{\mathrm{i}\omega t} \\ \boldsymbol{\Gamma}_\mathrm{W} &= \bar{\boldsymbol{\Gamma}}_\mathrm{W0}\mathrm{e}^{\mathrm{i}\omega t} \end{aligned}$$

where $\bar{\boldsymbol{\Gamma}}_\mathrm{P0}$ and $\bar{\boldsymbol{\Gamma}}_\mathrm{W0}$ are the complex amplitudes of the bound and wake ciculation, respectively. The wake transport relations can therefore be reformulated in terms of the exponential function. The transfer of the trailing edge circulation Eq. (2.2.41) into the wake becomes

$$\bar{\Gamma}_\mathrm{W0}(1,j)\,\mathrm{e}^{\mathrm{i}\omega t}=\bar{\Gamma}_\mathrm{P0}(\boldsymbol{N}_\mathrm{CP}(j),j)\,\mathrm{e}^{\mathrm{i}\omega(t-\Delta t)}$$

whereas the downstream transport of the wake circulation Eq. (2.2.42) becomes

$$\bar{\Gamma}_\mathrm{W0}(i,j)\,\mathrm{e}^{\mathrm{i}\omega t}=\bar{\Gamma}_\mathrm{W0}(i,j-1)\mathrm{e}^{\mathrm{i}\omega(t-\Delta t)}=\bar{\Gamma}_\mathrm{P0}(\boldsymbol{N}_\mathrm{CP}(j),j)\mathrm{e}^{\mathrm{i}\omega(t-i\Delta t)}.$$

With these harmonic transport relations, the wake circulation can be fully expressed in terms of the complex bound circulation amplitude $\bar{\boldsymbol{\Gamma}}_\mathrm{P0}$ at the trailing edge delayed by complex lag terms. The matrix equation Eq. (2.2.21) can be rewritten to yield

$$A\bar{\boldsymbol{\Gamma}}_\mathrm{P0}\mathrm{e}^{\mathrm{i}\omega t}=-\bar{\boldsymbol{d}}_0\mathrm{e}^{\mathrm{i}\omega t}-BL\bar{\boldsymbol{\Gamma}}_\mathrm{P0}\mathrm{e}^{\mathrm{i}\omega t}$$

where the complex delay matrix L has been introduced. The size of L is $(N_\mathrm{W}\times N_\mathrm{P})$ and the lag terms elements using *Euler's* notation are

$$L_{kl} = \mathrm{e}^{-\mathrm{i}\omega j\Delta t}=\cos(\omega j\Delta t)-\mathrm{i}\sin(\omega j\Delta t)$$

where k is the linear index of the wake panel, l is the linear index of the trailing edge panel connected to the strip of wake panel k, and j is the number of time steps wake panel k is downstream of the trailing edge. Using the linearized downwash matrices from Eq. (2.2.36), this can be written as

$$(A+BL)\bar{\boldsymbol{\Gamma}}_\mathrm{P0}\mathrm{e}^{\mathrm{i}\omega t}=-\left(\left(D_1+\mathrm{i}\omega D_2\right)\bar{\boldsymbol{u}}_\mathrm{A0}+D_2\bar{\boldsymbol{u}}_\mathrm{G0}\right)\mathrm{e}^{\mathrm{i}\omega t} \qquad (2.2.56)$$

where $\bar{\boldsymbol{u}}_{\mathrm{A}0}$ is the complex amplitude of panel freedoms and $\bar{\boldsymbol{d}}_{\mathrm{G}0}$ is the complex gust amplitude. With Eq. (2.2.37), the unsteady complex loads amplitude $\bar{\boldsymbol{f}}_{\mathrm{A}0}$ becomes

$$\left(\bar{\boldsymbol{f}}_{\mathrm{A}0}/q_\infty\right)\mathrm{e}^{\mathrm{i}\omega t} = \begin{cases} \left(S_1 P + \mathrm{i}\omega S_2\right)\bar{\boldsymbol{\Gamma}}_{\mathrm{P}0}\mathrm{e}^{\mathrm{i}\omega t} \\ S_2 S_{\mathrm{V}}\left(\delta\bar{\boldsymbol{d}}_{\tau 0} + \left(G + A_\tau + B_\tau L\right)\bar{\boldsymbol{\Gamma}}_{\mathrm{P}0}\right)\mathrm{e}^{\mathrm{i}\omega t} + \\ +\mathrm{i}\omega S_2\left(I_{0\mathrm{P}} + I_{\mathrm{P}}\left(G + A_\tau\right) + \left(I_{0\mathrm{W}} + I_{\mathrm{P}} B_\tau\right) L\right)\bar{\boldsymbol{\Gamma}}_{\mathrm{P}0}\mathrm{e}^{\mathrm{i}\omega t} \end{cases}$$

and it is tempting to directly substitute the solution of Eq. (2.2.56). However, to avoid the inversion of $(A + BL)$ for every new oscillatory frequency, the following efficient solution procedure can be applied. First, the matrix equation Eq. (2.2.56) is partitioned into bound vortex panels not on the trailing edge (partition 1) and on the trailing edge (partition 2)

$$\begin{bmatrix} C_{11} & C_{12} \\ C_{21} & C_{22} \end{bmatrix} \begin{Bmatrix} \bar{\boldsymbol{\Gamma}}_{\mathrm{P}0,1} \\ \bar{\boldsymbol{\Gamma}}_{\mathrm{P}0,2} \end{Bmatrix} = - \begin{Bmatrix} \bar{\boldsymbol{d}}_{0,1} \\ \bar{\boldsymbol{d}}_{0,2} \end{Bmatrix}$$

where $(A + BL)$ has been abbreviated by C and the downwash has been lumped in the expression $\bar{\boldsymbol{d}}_0$. First, solving for the circulation of the trailing edge vortex ring elements yields

$$\bar{\boldsymbol{\Gamma}}_{\mathrm{P}0,2} \quad = \quad \left(C_{22} - C_{21} C_{11}^{-1} C_{12}\right)^{-1}\left(-\bar{\boldsymbol{d}}_{0,2} + C_{21} C_{11}^{-1}\bar{\boldsymbol{d}}_{0,1}\right)$$

and the circulation for the remaining bound vortex ring elements is then found to be

$$\bar{\boldsymbol{\Gamma}}_{\mathrm{P}0,1} = C_{11}^{-1}\left(-\bar{\boldsymbol{d}}_{0,1} - C_{12}\bar{\boldsymbol{\Gamma}}_{\mathrm{P}0,2}\right).$$

Because only the panels on the trailing edge are affected by the delay matrix L, the partitions C_{11} and C_{21} are independent of the oscillatory frequency and partition C_{11}, that is typically the largest partition of C, needs to be inverted only once. Also by separating the wake influence coefficient matrix B from the delay matrix L, the influence coefficients of the wake need to be computed only once, which is seen to be a big advantage over the approach outlined by Laha [76].

Having the harmonic formulation available also offers as a side effect a systematic means to optimize the discretization of the wake for time domain application. All that is needed in addition is the availability of the industry standard doublet lattice method (DLM), a frequency domain surface panel method based on the acceleration potential which requires only discretization of the lifting surfaces and no wake definition (see Albano and Rodden [1]). The DLM is applied to the same surface panel discretization as the HVLM, obtaining harmonic solutions for a set of downwash modes at various oscillatory frequencies. The wake discretization of the HVLM, in particular the streamwise spacing and positioning of the first row of vortex loops relative to the trailing edge, can then be adjusted until a good match with the acceleration potential results is achieved. This approach will be demonstrated in the next section.

2.2.7 Numerical Examples

In this section, numerical examples of the computational methods outlined above are presented and studies of the adjustable key parameters are given. As a test case, the wing-tail configuration depicted in Fig. 2.22 is derived from the geometry of a typical high capacity transport category aircraft. The computational grid is generated for a symmetric half model valid for the analysis of longitudinal motion. In addition to the grid of vortex ring elements, a grid with identical geometry and discretization is created for the DLM for validation and reference purposes.

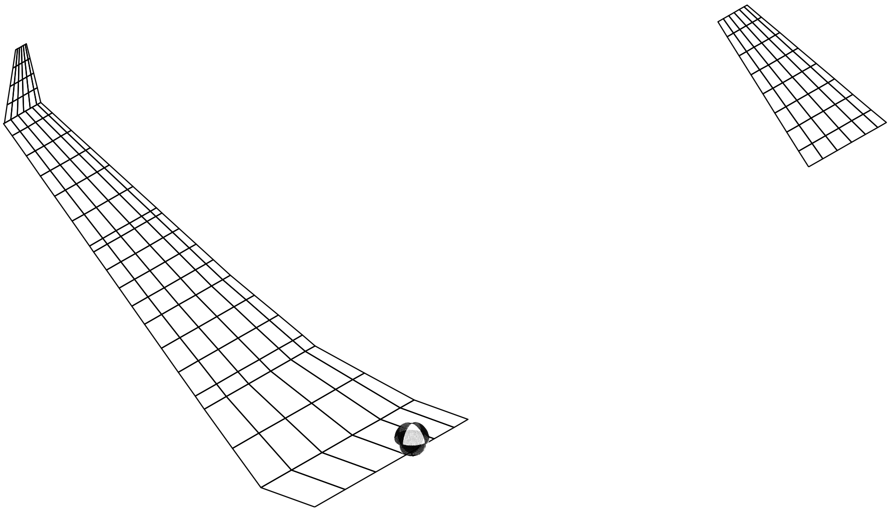

Figure 2.22: Wing Tail Configuration for Parametric Studies

Wake Modelling

When discretizing the wake, several adjustable parameters have an immediate impact on the result and the problem size. In order to find the optimal values, parameter studies are performed with the harmonic formulation from Section 2.2.6 and the results are compared with the DLM results.

As a first fundamental validation step, the results of the vortex lattice method (VLM) and DLM are compared in the steady case, e.g. for reduced frequency $k = 0.0$ with the length of the wake set to more than 5 wing spans. The spanwise local load $c_l \frac{l}{l_g}$ and local pitching moment $c_m \frac{l}{l_g}$ distributions on the wing and horizontal tail are shown in Fig. 2.23 and show excellent agreement. The first wake parameter studied is the non-dimensional time step size $\tau = \Delta t \frac{V}{c}$, which is varied between the values 0.12 and 0.012. This range is equivalent to a spatial discretization between 100% and 10% of the chord length of the most inboard panel on the trailing edge of the horizontal tail surface. In Figs. 2.24 and 2.25, the complex spanwise local load $c_l \frac{l}{l_g}$ and local pitching moment $c_m \frac{l}{l_g}$ distributions on the wing and horizontal tail are compared for a heaving motion of the aircraft at reduced frequency $k = 1.0$, respectively. The length of the wake was fixed to more than 5 wing spans. Clearly, the results are sensitive to the choice of time step size and only average convergence can be observed with decreasing time step size. For the smallest step size, the agreement with the DLM result is good with light deviations on the inboard part of the lifting surfaces. To overcome the poor convergence behavior with other means than the computationally expensive reduction of time step size, Daughaday and Piziali [25] proposed a method that uses continuous vorticity distributions close to the trailing edges and discrete vortex filaments in the farfield wake (see also Johnson [58]). However, an improved accuracy is only obtained if the required polynomial fit of the bound circulation includes both past and future values. For purely harmonic motion this imposes no difficulty, whereas for non-periodic motion a predictor-corrector approach is required, which complicates the time-integration significantly. Alternatively, linear doublet panels could be used for the wake, see Ruiz-Calavera [107] and Geissler [41], but the higher-order doublet panels

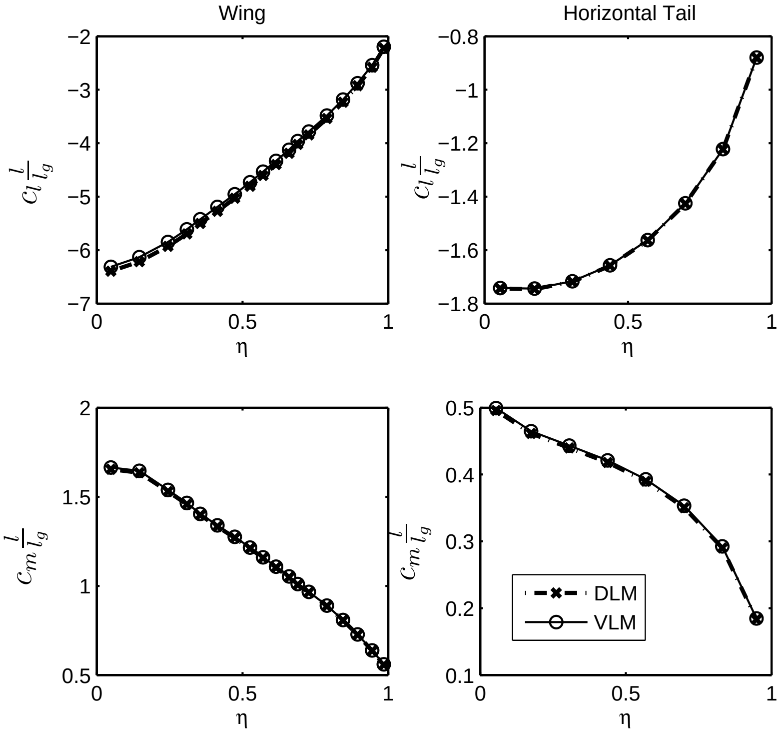

Figure 2.23: Comparison of Wing and Horizontal Tail Load due to Pitch for $k = 0.0$

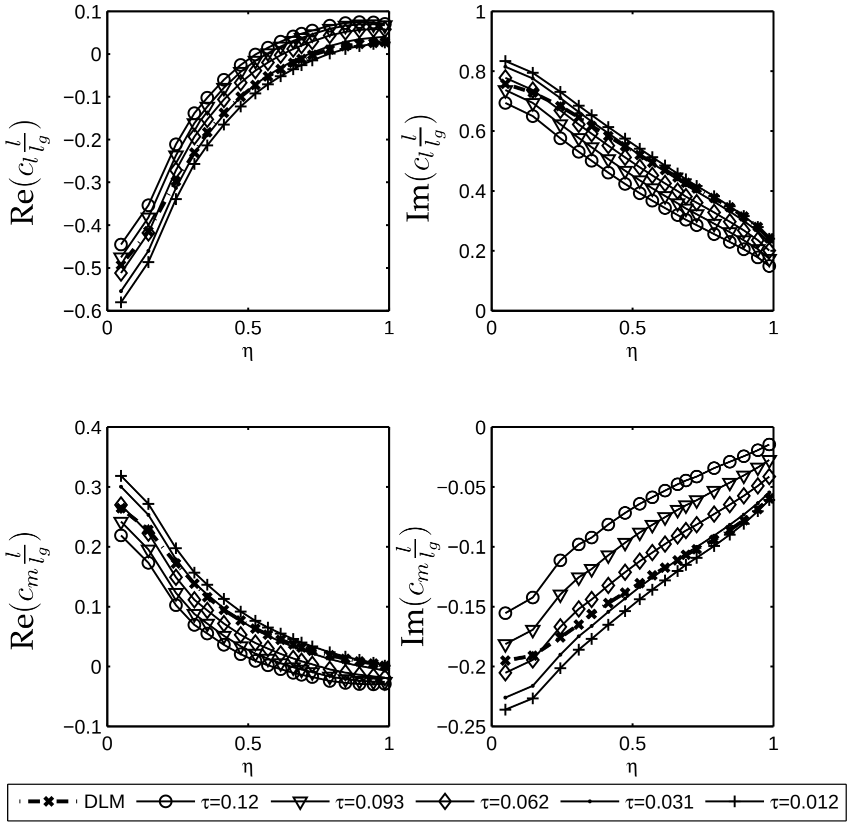

Figure 2.24: Influence of time step size on unsteady wing loads for heaving motion $k = 1.0$

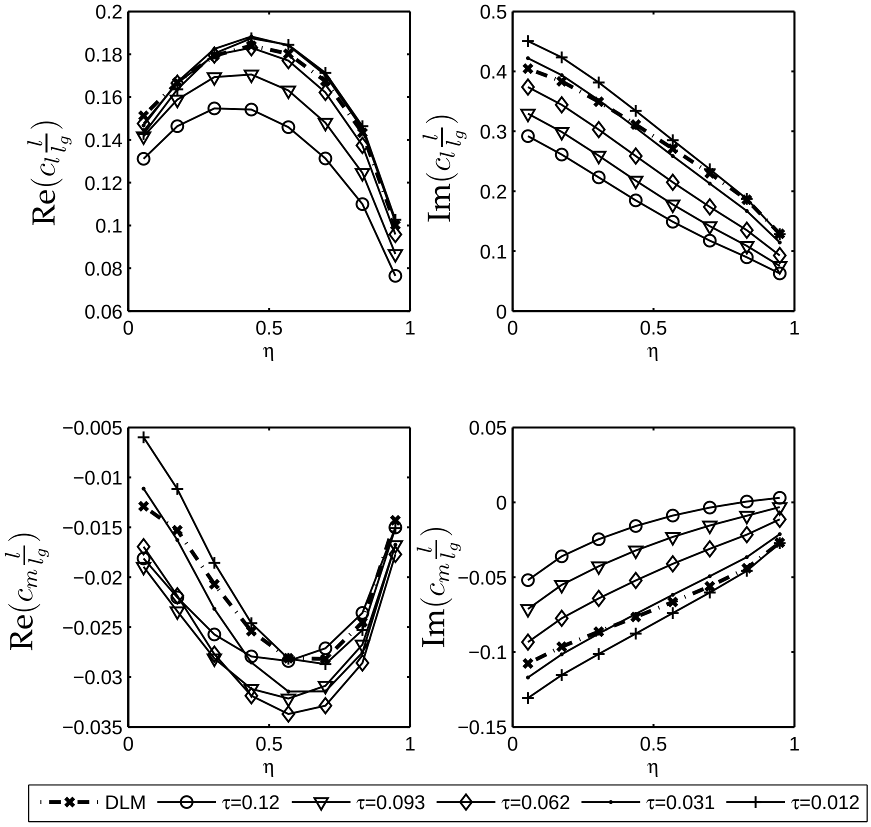

Figure 2.25: Influence of time step on unsteady tail loads for heaving motion $k = 1$

are very complex to evaluate and are not merited by the simplicity of the UVLM.

Instead, a simple but very efficient modification of the UVLM to improve the wake accuracy is the shift of the wake system closer to the trailing edge (see Katz and Plotkin [64]). In Fig. 2.26, the complex wing loading for a pitching motion at reduced frequency $k = 1$ is shown for varying offsets of the first transverse vortices from the trailing edge. An offset $\Delta c = 0$ means that the vortices are placed at the position of the trailing edge during the previous time step, whereas an offset $\Delta c > 0$ indicates a relative shift closer to the new position of the trailing edge. It can be inferred that shifting the wake closer to the trailing edge by about 30% of the distance covered during on time step yields the best agreement with the DLM result.

A further parameter of interest is the required length of the wake. Contrary to helicopter aerodynamics where the rotor wake always remains close to the rotor blades, the wake of a transport category aircraft is left behind the aircraft. From the Biot-Savart Law Eq. 2.2.17 it becomes apparent, that the wake influence decays quadratically with the geometric distance and therefore rapidly becomes irrelevant for the aircraft aerodynamics. In Fig. 2.27, the impact of relative wake length $\lambda = \frac{2l}{b}$ on the complex aerodynamic tail load for a heaving motion at reduced frequency $k = 1$ is illustrated. It can be inferred, that for a wake length larger than 2.7 half-spans the results are converged.

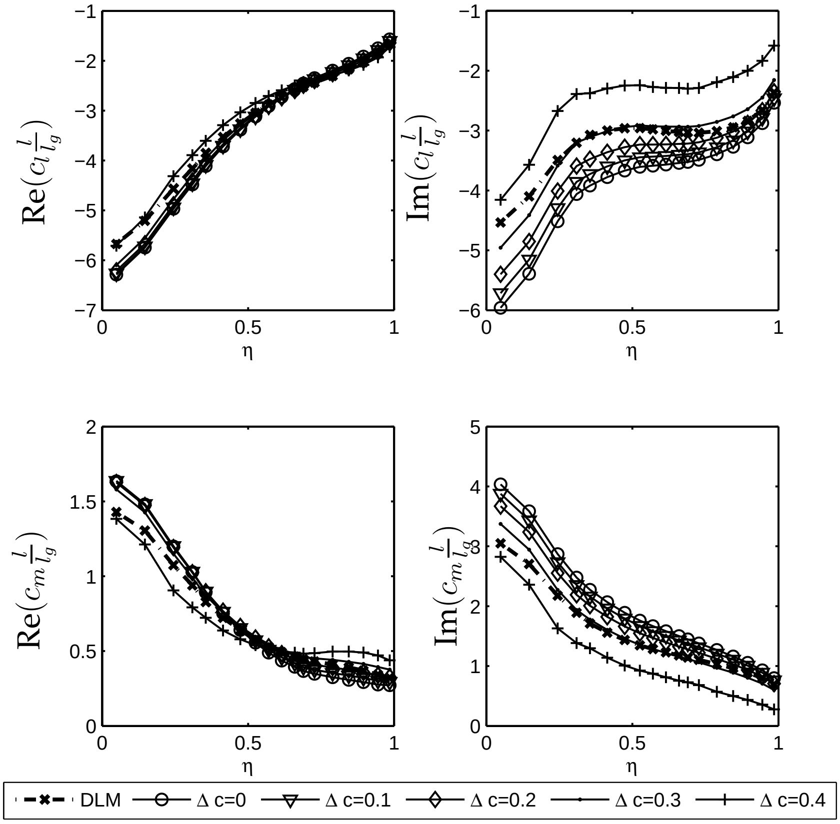

Figure 2.26: Influence of trailing edge vortex position on unsteady wing loads for pitching motion $k = 1$

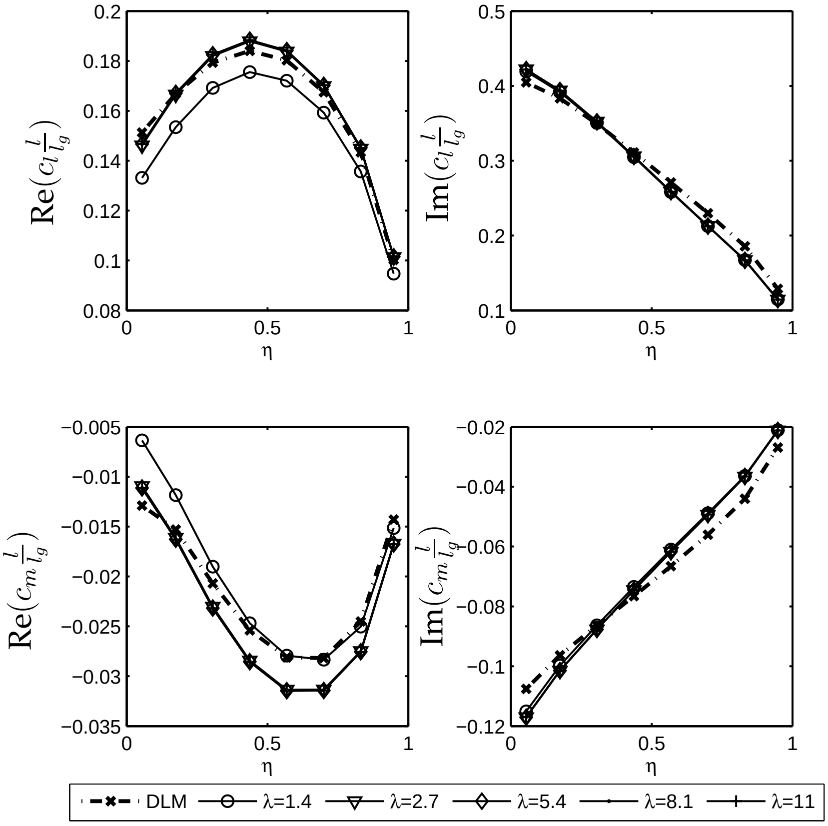

Figure 2.27: Influence of relative wake length $\lambda = \frac{2l}{b}$ on unsteady tail loads for heaving motion $k = 1$

Constant Rate of Incidence Modelling

To investigate the reliability of the quasi-steady formulations, the wing-tail combination undergoing a linear increase in angle of attack is examined. As a reference, the motion is simulated with the unsteady formulation and compared to the lag-in-downwash and constant-wake-gradient formulations. In a addition, the stability derivatives $\frac{\partial C_L}{\partial \dot{\alpha}}$ and $\frac{\partial C_M}{\partial \dot{\alpha}}$ are estimated from the generalized harmonic aerodynamic loads due to heave at very low reduced frequency as outlined by Rodden and Giesing [104]

$$C_{L,\dot{\alpha}} = -\frac{\Re(Q_{zz})\, c}{h_0^2\, S\, k^2} \tag{2.2.57}$$

$$C_{M,\dot{\alpha}} = -\frac{\Re(Q_{\theta z})}{\theta_0\, h_0\, S\, k^2} \tag{2.2.58}$$

with the complex generalized vertical force due to heave Q_{zz}, the complex generalized pitching moment due to heave $Q_{\theta z}$, the generalized heave amplitude h_0 and the generalized pitch amplitude θ_0. This approach should be very similar to the constant-wake-gradient formulation, because for very low reduced frequency the wave length becomes very large and consequently the slope of the streamwise circulation is approximately linear in the near-field. In Fig. 2.28, the various lift and moment results are plotted over non-dimensional time $\tau = t\,\frac{V}{c}$. The simulation values are obtained by subtracting the steady lift and moment due to incidence from the instantaneous lift and moment and dividing by the constant rate of incidence. After an initial transient, during which the starting vortex is travelling from the wing to the horizontal tail, the lift and moment results of the first-order approximations are in very good agreement with the simulation, except the estimated $C_{L,\dot{\alpha}}$ value from the harmonic aerodynamic analysis that appears to be too low. The results from the lag-in-downwash formulation could be further improved by adapting the lever arm of the horizontal tail.

Validation with Reference Solutions

In Appendix A, the UVLM and HVLM formulations presented above are validated by comparison to analytical solutions and published results obtained from similar numerical methods.

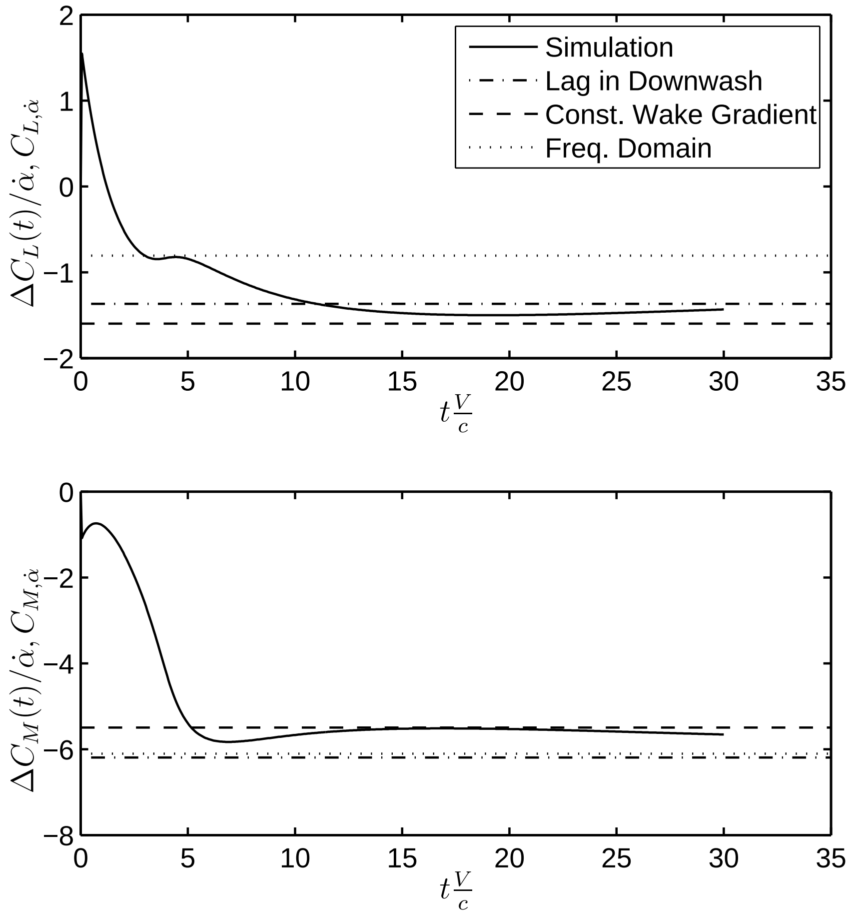

Figure 2.28: Comparison of Rate of Incidence Models

2.3 Steady Correction of the UVLM by External Data

The UVLM method was derived based on the assumption of incompressible potential flow which theoretically limits its applicability to Mach numbers roughly below $M \leq 0.3$. Also the effects of thickness and viscosity cannot be captured. However as will be shown in this section, the quality and range of applicability of the model can be improved by correction with high-fidelity steady state aerodynamic data obtained from wind tunnel tests or CFD. The method used here is derived from the least-squares algorithm by Brink-Spalink and Bruns [11] and permits the simultaneous correction for multiple aerodynamic effects.

2.3.1 Formulation of the Correction Problem

Given the steady state aerodynamic influence coefficient (AIC) matrix

$$Q = \left(-\bar{C}\bar{A}^{-1}\bar{B} + \bar{D}_1\right)$$

that relates panel downwash to panel forces (see Eq. (2.2.52)), we seek a fully populated correction matrix ΔQ with minimal weighted norm satisfying the equation

$$\begin{aligned} [\boldsymbol{p}_1^c\, \boldsymbol{p}_2^c\, \dots\, \boldsymbol{p}_n^c] &= S\,(Q + \Delta Q)\,[\boldsymbol{d}_1^c\, \boldsymbol{d}_2^c\, \dots\, \boldsymbol{d}_n^c] \\ ||\Delta Q./W|| &\to \min \\ W &= |Q|^{\frac{1}{2}} \end{aligned}$$

where $\boldsymbol{p}_i^c$ are the target aerodynamic quantities of the aerodynamic effects to be matched, S is a summation matrix computing the target quantities from panel forces and $\boldsymbol{d}_i^c$ are the downwash vectors related to the target aerodynamic effects. The weighting matrix W is typically chosen to be the absolute value of the uncorrected AIC matrix elements which results in correction values proportional to the magnitude of the original AIC elements. From the incremental AIC matrix correction, a fully populated downwash correction matrix F^c can be derived

$$F^c = Q^{-1}\,(Q + \Delta Q)$$

yielding the corrected UVLM state space model

$$\begin{aligned} \dot{\boldsymbol{\Gamma}}_{\mathrm{W}} &= \bar{A}\boldsymbol{\Gamma}_{\mathrm{W}} + \tilde{B}\boldsymbol{d} \\ \boldsymbol{f}_{\mathrm{A}}/q_\infty &= \bar{C}\boldsymbol{\Gamma}_{\mathrm{W}} + \tilde{D}_1\boldsymbol{d} + \tilde{D}_2\dot{\boldsymbol{d}} \end{aligned}$$

where

$$\begin{aligned} \tilde{B} &= -\frac{1}{\Delta t} T_{\mathrm{P}} A^{-1} F^c \\ \tilde{D}_1 &= -S_1 P A^{-1} F^c + \frac{1}{\Delta t} S_2 A^{-1} B T_{\mathrm{P}} A^{-1} \\ \tilde{D}_2 &= -S_2 A^{-1} F^c \end{aligned}$$

The appearance of the correction matrix in the term $\tilde{D}_2$ illustrates that the correction with steady state results also affects the unsteady behavior.

2.3.2 Application

The AMP transport aircraft wing studied by Zingel [140] is chosen to test the credibility of the correction method presented above. To obtain steady and unsteady aerodynamic reference results, the CFD code TAU from the German Aerospace Center DLR is employed. The inviscid version of the code used here solves the unsteady Euler fluid equations of motion by a multi-grid method. Both local and global time-stepping schemes on structured and unstructured meshes are available. Details of the TAU code can be found in the technical specification [28]. Based on the structured surface grid of the CFD mesh shown in Fig. 2.29(a), a vortex lattice grid is generated on the mean surface of the AMP wing and is depicted in Fig. 2.29(b). Steady state results are generated with TAU for a range of incidences $-3^\circ \leq \alpha \leq 3^\circ$ at Mach numbers M=0.2 and M=0.5. For this choice of parameters, the lift and moment coefficients as shown in Fig. 2.3.2 exhibit linear behavior. From the CFD surface pressures, spanwise lift and moment distributions and gradients with respect to incidence are derived in a post-processing step and used as the input to the correction procedure for the UVLM model. The target of the correction is to match the spanwise lift and moment coefficient due to incidence. After correction of the AIC, an inital downwash problem is solved to correct the downwash due to twist and camber $\boldsymbol{d}_0$ (see Eq. (2.2.36)) according to the target intercept value at $\alpha = 0$. The approach used is similar to the shape function mapping presented in section 2.1.4.

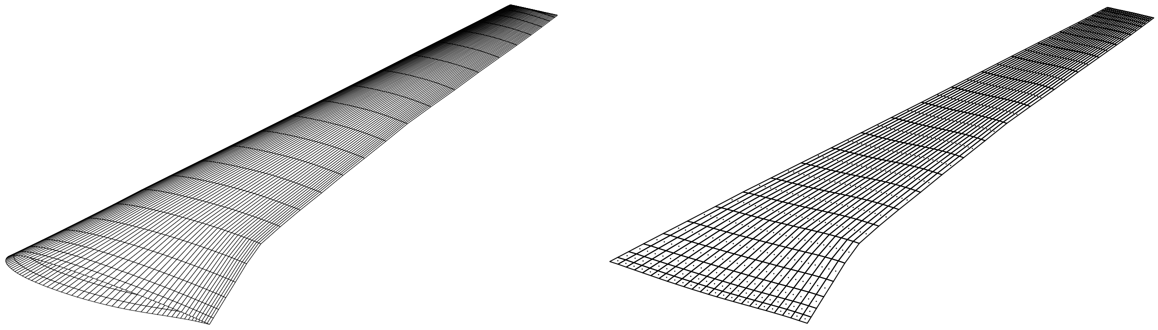

(a) CFD Surface Mesh (b) Mean Surface Vortex Lattice Grid

Figure 2.29: Numerical Grids of the AMP Wing

Unsteady simulations are performed with the TAU code at the same Mach numbers for heaving motion of the AMP wing at reduced frequency $k = 0.6$ and zero steady angle of attack. The amplitude of the heaving motion is set to achieve a maximum dynamic angle of attack of $\max\left(\left|\frac{\dot{h}}{V}\right|\right) = 3^\circ$. Results for one heaving cycle are extracted after the transient response to the motion has decayed and a harmonic flow field is established. In addition, a quasi-steady CFD solution using the steady polar is constructed based on the dynamic angle of attack.

The same heaving motion is then simulated using both the original and the corrected UVLM model as well as a quasi-steady VLM model. Local lift coefficient and local moment coefficient in three spanwise sections are compared for the six types of results and

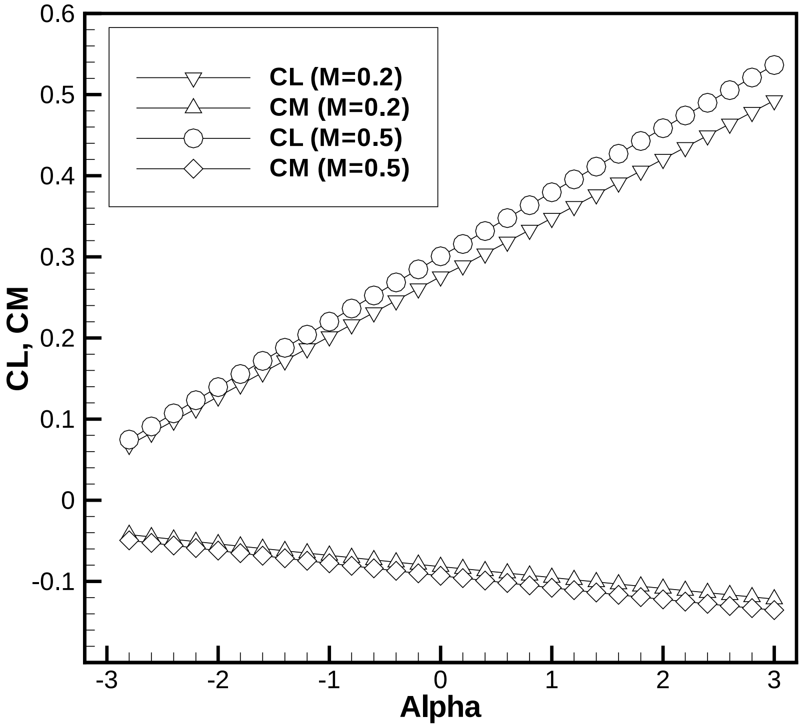

Figure 2.30: Lift and Moment Coefficient of the AMP Wing (M=0.2 and M=0.5)

are plotted as a function of generalized heaving coordinate in Fig. 2.3.2 for the Mach number $M = 0.2$. For this flight condition, effects of compressibility are low and the incompressible potential flow model should be able to yield good results. The perfect match of the quasi-steady results from VLM (dashed red line) and CFD (dashed green line) illustrates the successful correction process. The shift and scaling of the results relative to the uncorrected VLM (dashed black line) show that both intercept values and gradients are modified. Looking at the unsteady results it can be inferred that the steady correction also improves the unsteady behavior of the UVLM. Compared to the uncorrected UVLM (solid black line), the corrected UVLM (solid red line) result is affect in three characteristics of the lift and moment hysteresis loop: the loop is shifted to match the steady intercept value, the size of the minor axis is scaled to match the steady gradient and the loop is rotated due to the impact on the unsteady load term. The latter effect is very small. The agreement with the unsteady CFD results (solid green line) is appreciably good, with minor deviations of the inboard local pitching moment.

The same exercise is carried out at Mach number $M = 0.5$, where the effect of compressibility is not negligible. The six types of result are shown in Fig. 2.3.2. Even though the agreement with unsteady CFD is not as good as in the incompressible case, the results suggest that the applicability of the incompressible UVLM can be extended by correction with steady compressible data.

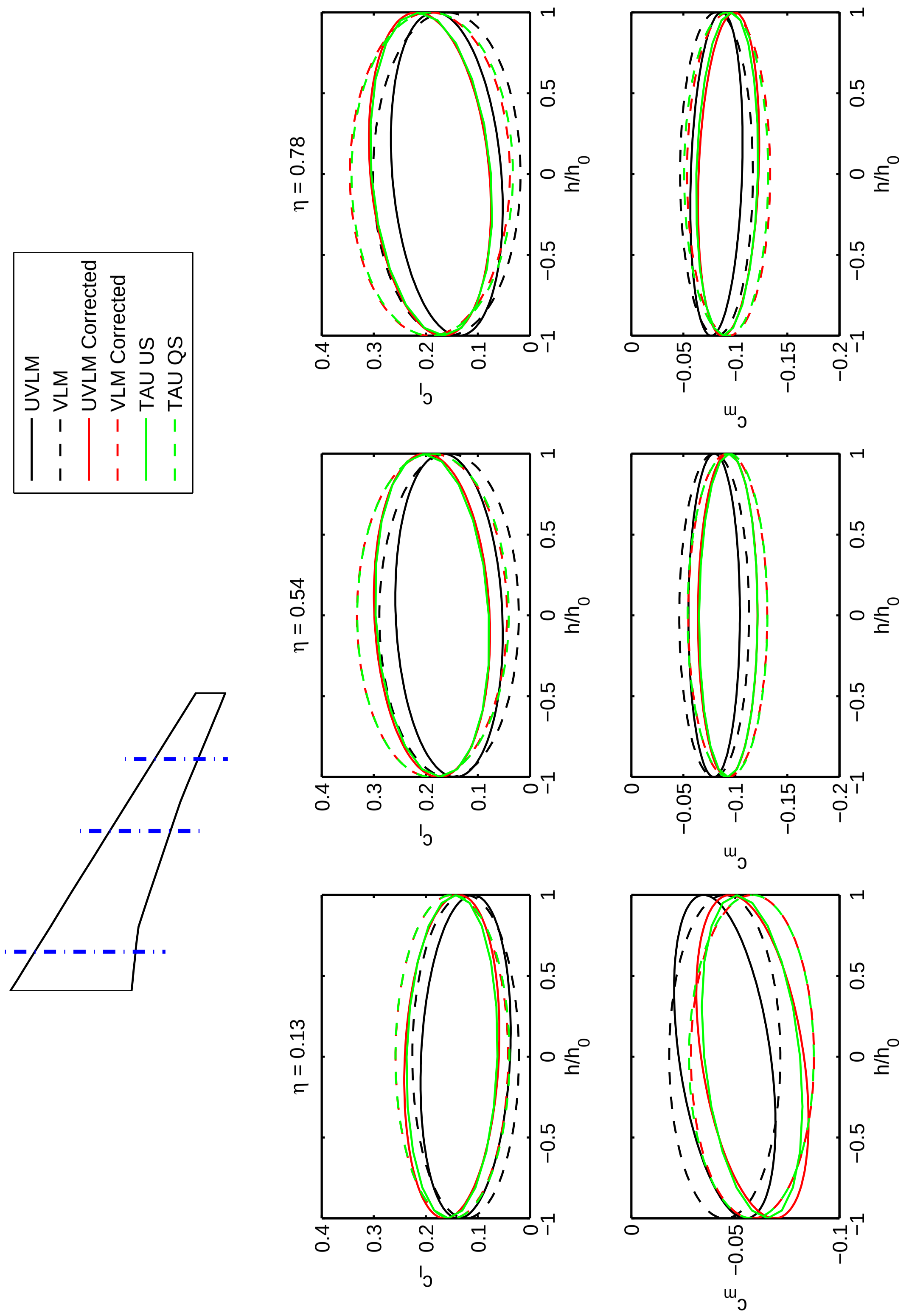

Figure 2.31: Comparison of Quasi-Steady and Unsteady Results for Heaving Motion of the AMP Wing ($k = 0.6,\ M = 0.2$)

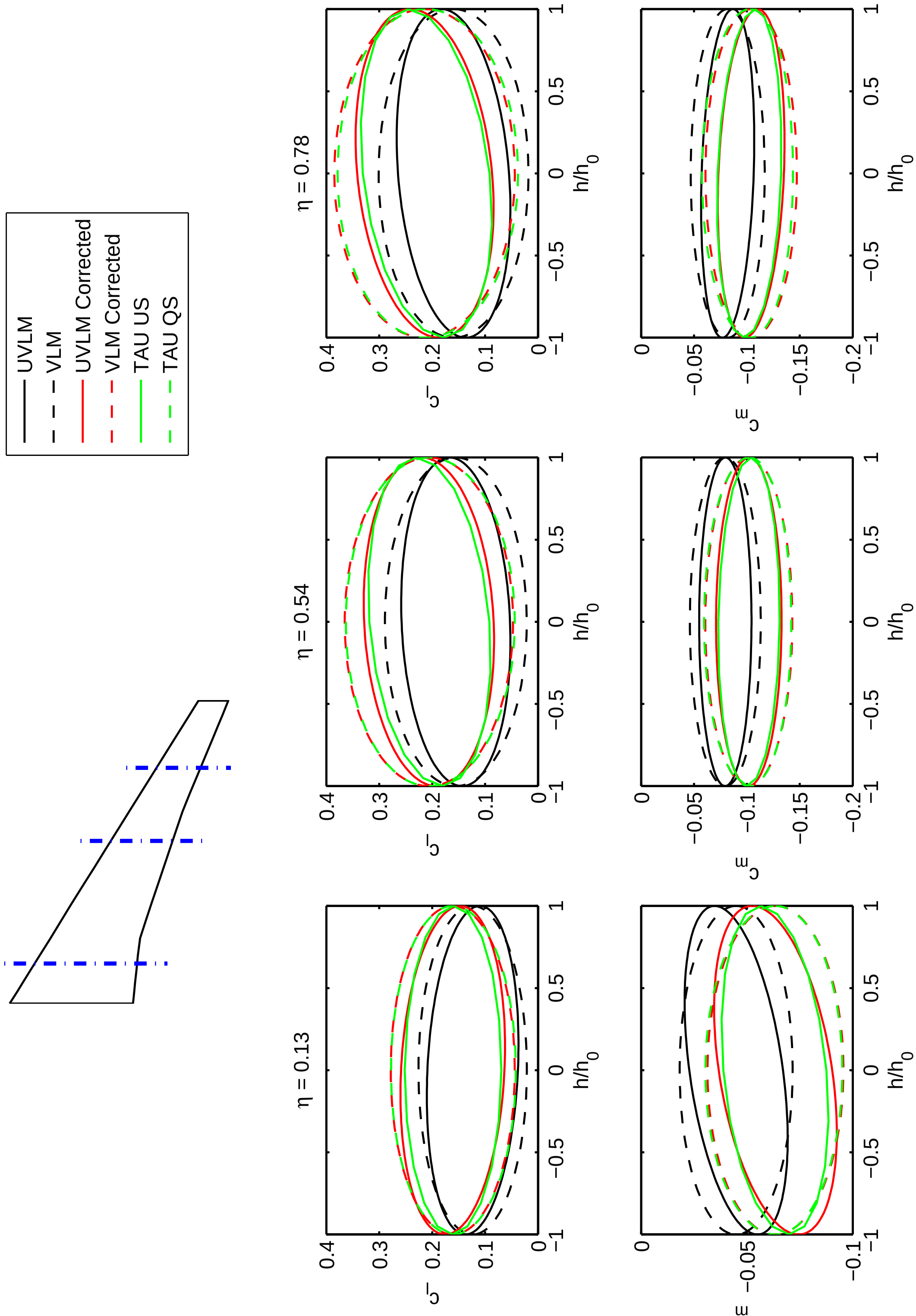

Figure 2.32: Comparison of Quasi-Steady and Unsteady Results for Heaving Motion of the AMP Wing ($k = 0.6,\ M = 0.5$)

2.4 Reduction of Model Order by Balanced Truncation

Compact unsteady aerodynamic models suitable for aeroservoelastic analysis and control law design are typically obtained by RFA of frequency domain AICs as for example the Minimum State method [63] or Roger's method [105]. However, one drawback of the RFA methods is that the approximation typically requires several parameters to be set by the engineer and therefore obtaining a good approximation can be tedious and is frequently correlated to experience. In particular, the approximation of large system matrices (e.g. right-generalized AIC matrices) can be cumbersome and repeated approximation with varying sets of fit parameters is computationally expensive.

On the other hand, the generation of time domain unsteady aerodynamic models using the UVLM is a straightforward procedure that requires less user input. However, due to the large number of required wake vortex loops, UVLM state space models are characterized by a high model order, however in conjunction with a sparse system matrix structure. It is therefore desirable to apply a model order reduction technique, both physics based and only requiring a limited amount of user interaction.

From an aeroelastician's point of view, standard Eigenvalue decomposition and subsequent modal truncation would be a natural choice for the reduction of dynamic model order. Unfortunately it has been shown by Rule et al. [108] that the Eigenvalues and Eigenvectors characterize the internal dynamics of the system and not the mapping of inputs to outputs. Thus, the quality of the truncated model is not uniformly related to the number of states retained and modal truncation solely based on the magnitude or damping of the Eigenvalues in most cases unsuccessful. This conclusion confirms this author's findings and to some extend contradicts the good results presented by Hall [49] and Tang et al. [118]. In [108], it has also been shown that applying balanced truncation, a method based on controllability and observability concepts from control theory, can lead to significantly better results. This method will subsequently be outlined and applied to the UVLM state space model.

2.4.1 Balanced Truncation

The general form of a linear time-invariant (LTI) system in state space form is:

$$\begin{Bmatrix} \dot{\boldsymbol{x}} \\ \boldsymbol{y} \end{Bmatrix} = \left[\begin{array}{c|c} A & B \\ \hline C & D \end{array}\right] \begin{Bmatrix} \boldsymbol{x} \\ \boldsymbol{u} \end{Bmatrix} \tag{2.4.1}$$

where $A \in \mathbb{R}^{n \times n}$, $B \in \mathbb{R}^{n \times p}$, $C \in \mathbb{R}^{q \times n}$, $D \in \mathbb{R}^{q \times p}$. For the UVLM model, the number of states n is large, whereas the number of inputs p and outputs q is typically $p, q \ll n$.

Balanced realization of a state space system is achieved by determining a similarity transform

$$\begin{Bmatrix} \dot{\overline{\boldsymbol{x}}} \\ \boldsymbol{y} \end{Bmatrix} = \left[\begin{array}{c|c} T^{-1}AT & T^{-1}B \\ \hline CT^{-1} & D \end{array}\right] \begin{Bmatrix} \overline{\boldsymbol{x}} \\ \boldsymbol{u} \end{Bmatrix} = \left[\begin{array}{c|c} \overline{A} & \overline{B} \\ \hline \overline{C} & D \end{array}\right] \begin{Bmatrix} \overline{\boldsymbol{x}} \\ \boldsymbol{u} \end{Bmatrix} \tag{2.4.2}$$

in such a way, that the controllablility Gramian P and observability Gramian Q of the balanced system become equal and diagonal:

$$\overline{P} = \overline{Q} = \Sigma = \begin{bmatrix} \sigma_1 & & & \\ & \sigma_2 & & \\ & & \ddots & \\ & & & \sigma_n \end{bmatrix} . \tag{2.4.3}$$

Here, σ denote the Hankel singular values (HSV) of the system, defined as the square root of the Eigenvalues of the matrix product PQ. Small HSV indicate weak contribution of a state to the system input-output behavior and therefore HSV are a useful indicator for order reduction. Note that a similarity transform preserves the Eigenvalues of a matrix and therefore the internal dynamics of the state space system remain unchanged. The Gramians are obtained from the solution of the two *Lyapunov* equations

$$AP + PA^{\mathrm{T}} + BB^{T} = 0 \tag{2.4.4}$$

$$A^{\mathrm{T}}Q + QA + C^{\mathrm{T}}C = 0 \tag{2.4.5}$$

and characterize the system in terms of energy. For a given initial state vector $\boldsymbol{x}_0$ and zero system input, the output energy of the system in response to the initial conditions is determined by the observability Gramian:

$$\int_0^\infty \left(\boldsymbol{y}^{\mathrm{T}}\boldsymbol{y}\right) dt = \boldsymbol{x}_0^{\mathrm{T}} Q \boldsymbol{x}_0.$$

Also, the minimal energy that must be input into the system to drive the states from zero initial value to the state $\boldsymbol{x}_0$ is determined by the controllability Gramian

$$\int_0^\infty \left(\boldsymbol{u}^{\mathrm{T}}\boldsymbol{u}\right) dt = \boldsymbol{x}_0^{\mathrm{T}} P^{-1} \boldsymbol{x}_0.$$

There exist several numerical approaches to determine the similarity transform T. Most straightforward is to compute the *LU* decomposition of the Gramians,

$$\begin{aligned} P &= P_L P_U \\ Q &= Q_L Q_U, \end{aligned}$$

then determine the singular value decomposition (SVD) of the matrix product $P_U Q_L$

$$P_U Q_L = USV^{\mathrm{T}}.$$

and finally obtain T from

$$T = S^{\frac{1}{2}} U^{\mathrm{T}} P_L^{-1} = S^{-\frac{1}{2}} V^{\mathrm{T}} Q_U.$$

States of the balanced system characterized by large HSV are therefore both well observable and controllable. If the system possesses unstable poles, additional intermediate steps are required (for details see for example Antoulas et al. [3]).

The order of the balanced system can then be reduced by truncation, i.e. consideration of those states only that correspond to HSV larger than a certain magnitude. To this end, the balanced system is partitioned in primary and secondary states

$$\begin{Bmatrix} \dot{\overline{\boldsymbol{x}}}_1 \\ \dot{\overline{\boldsymbol{x}}}_2 \\ \boldsymbol{y} \end{Bmatrix} = \left[\begin{array}{cc|c} \overline{A}_{11} & \overline{A}_{12} & \overline{B}_1 \\ \overline{A}_{21} & \overline{A}_{22} & \overline{B}_2 \\ \hline \overline{C}_1 & \overline{C}_2 & D \end{array}\right] \begin{Bmatrix} \overline{\boldsymbol{x}}_1 \\ \overline{\boldsymbol{x}}_2 \\ \boldsymbol{u} \end{Bmatrix} \tag{2.4.6}$$

and the secondary set is truncated to yield the reduced order model

$$\begin{Bmatrix} \dot{\overline{\boldsymbol{x}}}_1 \\ \boldsymbol{y} \end{Bmatrix} = \left[\begin{array}{c|c} \overline{A}_{11} & \overline{B}_1 \\ \hline \overline{C}_1 & D \end{array}\right] \begin{Bmatrix} \overline{\boldsymbol{x}}_1 \\ \boldsymbol{u} \end{Bmatrix} \tag{2.4.7}$$

Alternatively, a residualization neglecting the dynamic contribution of the secondary set of states can be performed yielding the statically equivalent reduced order system

$$\begin{Bmatrix} \dot{\bar{\boldsymbol{x}}}_1 \\ \boldsymbol{y} \end{Bmatrix} = \left[\begin{array}{c|c} \overline{A}_{11} - \overline{A}_{12}\overline{A}_{22}^{-1}\overline{A}_{21} & \overline{B}_1 - \overline{A}_{12}\overline{A}_{22}^{-1}\overline{B}_2 \\ \hline \overline{C}_1 - \overline{C}_2\overline{A}_{22}^{-1}\overline{A}_{21} & D - \overline{C}_2\overline{A}_{22}^{-1}\overline{B}_2 \end{array} \right] \begin{Bmatrix} \bar{\boldsymbol{x}}_1 \\ \boldsymbol{u} \end{Bmatrix} \tag{2.4.8}$$

The aforementioned direct approach is not feasible for large, sparse systems due to several reasons. First, the computation of the full system Gramians is computationally very expensive but required to determine the HSV. Second, the balancing transformation destroys the sparsity of the UVLM system matrices and therefore the balanced system demands extensive computer memory. Third, static condensation is only possible if the system has been fully balanced, i.e. $A \in \mathbb{R}^{n\times n}$ and $T \in \mathbb{R}^{n\times n}$. Therefore several numerical methods suitable for the approximate balanced truncation of large scale LTI systems have been conceived. They are based on low-rank approximations of the Gramians (low-rank square root method (LRSM) and dominant subspace projection model reduction (DSPMR), for details see Penzl [97]), direct solution for the Cross-Gramian PQ (for details see Antoulas et al. [3]) or approximation of the dominant Eigenspaces of the products PQ and QP (approximate implicit subspace iteration with alternating directions (AISIAD), for details see Vasilyev and White [126], Zhou and Sorensen [139]). None of these methods is entirely straight forward to implement and therefore an alternative method was developed, that applies balanced truncation for dense systems to lower order sub-models.

2.4.2 Balanced Truncation of Lower Order Sub-Models

The basic idea behind this approach is the determination of the balancing transformation matrix T_i and T_i^{-1} only for sub-models of the state space system followed by a transformation of the overall system with the concatenation of the truncated sub-model transformation matrices. For the UVLM, every sub-model consists of the states belonging to one wake column, i.e. all wake panels attached to one trailing edge panel. The order of the sub-model is therefore only the number of wake time steps chosen and not the product of number of trailing edge panels and wake time steps, permitting the application of dense system methods. After the similarity transform of the sub-model has been determined, it can then be truncated to the desired sub-model order and sorted into an overall transformation matrix.

2.4.3 Application

To validate the order reduction method, balanced realization is, as in section 2.3.2, applied to the UVLM state space model of the AMP wing. In Fig. 2.29(b), the discretization of the bound circulation with $n_s = 22$ spanwise and $n_c = 24$ chordwise panels is depicted. Not shown is the wake discretization with $n = 2200$ states corresponding to a wake length of 100 time steps. The model uses the $p = n_s n_c = 352$ panel downwashes as input and yields $q = 132$ strip loads as output. To assess the contribution of each state to the input-output behavior of the system, the complete set of HSV are computed, both for the full model and sub-model approach. In Fig. 2.33, the relative magnitudes σ_i/σ_1 of the first 100 HSV are plotted in semilogarithmic scale and their strong decay by more than three orders of magnitude for the full model and more than 30 orders of magnitude for the sub-models suggest that a significant reduction of model

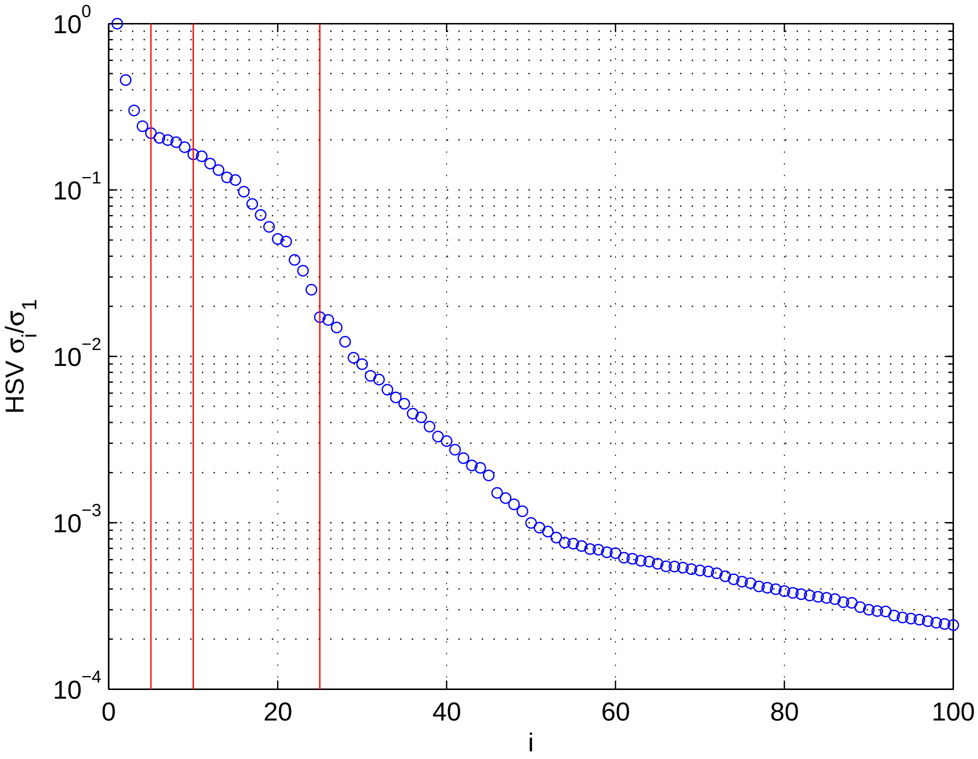

(a) Full Model

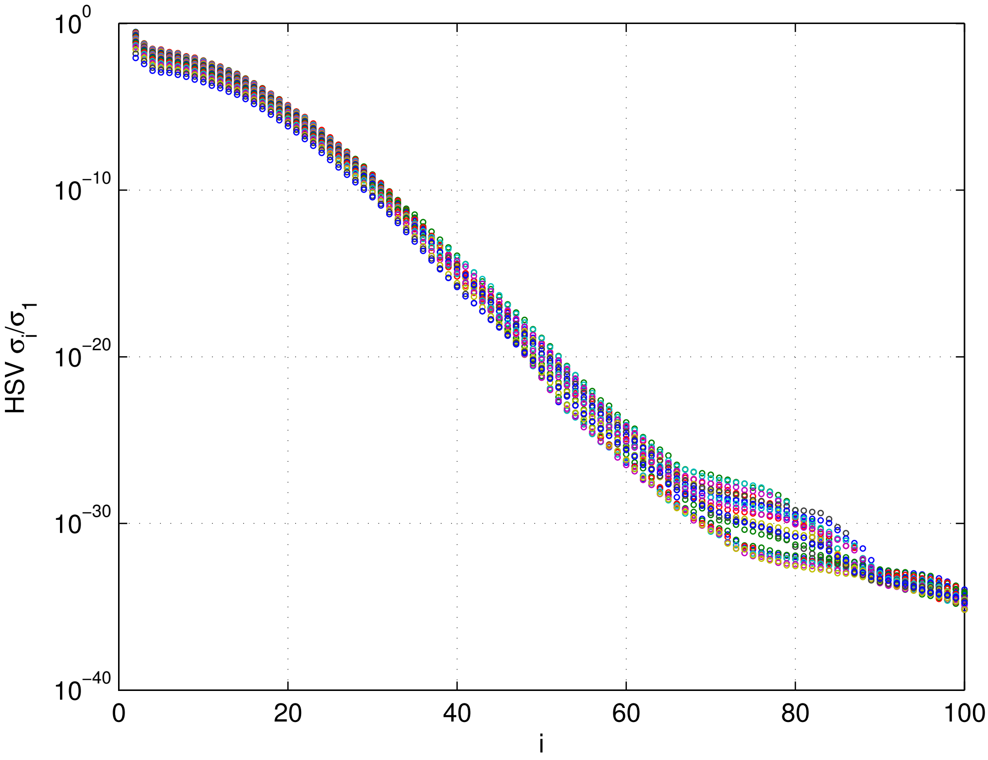

(b) Sub-Models

Figure 2.33: First 100 Hankel Singular Values of the AMP Model

order is possible. To shed light on the physical significance of the balanced states, the columns of the inverse transformation matrix T^{-1} can be examined. Whereas the states of the original system represent discrete circulation values in the wake, the balanced states can be thought of as weighting factors for distinct wake circulation modes. The first wake mode of the AMP wing corresponding to the first column of T^{-1} is depicted in Fig. 2.34 and, close to the trailing edge, exhibits a spanwise shape similar to the steady state bound circulation. The next three modes introduce spanwise oscillatory shapes with decreasing wave length. In the streamwise direction, all four modes decay rapidly.

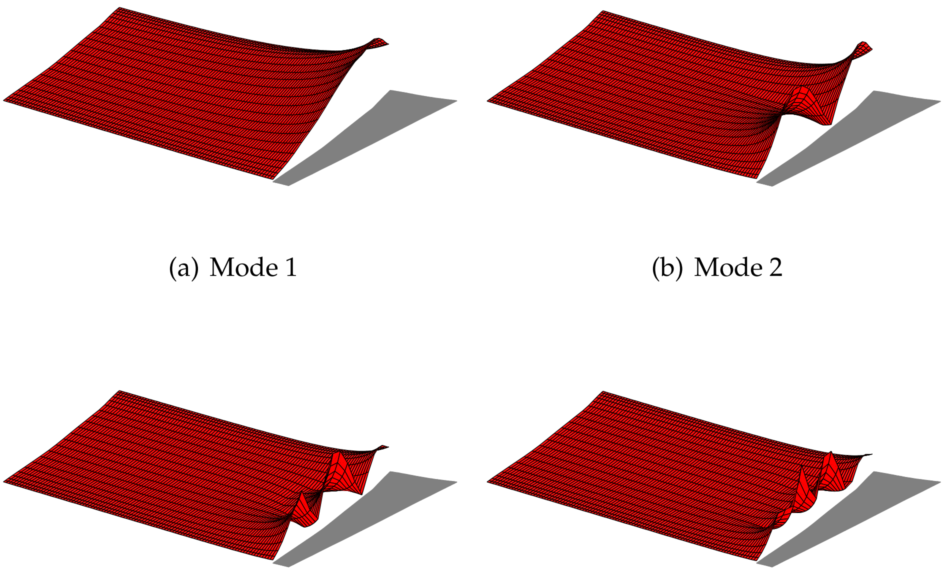
(a) Mode 1 (b) Mode 2

(c) Mode 3 (d) Mode 4

Figure 2.34: Wake Mode Shapes of the Total Balanced System

When applying sub-model balancing, i.e. separate balanced truncation of every wake column, wake modes as shown in Fig. 2.35 are obtained. The first sub-model wake mode is similar to the first balancing mode of the full model whereas the higher order modes introduce streamwise oscillatory shapes of decreasing wave length. Based on the kinks of the HSV plot, reduced model orders of 5, 10 and 25 are selected and truncation is performed on the balanced realization. The transfer functions of spanwise lift and moment due to heave, pitch and bending for a reduced frequency range up to $k = 2$ are compared to the full order model and depicted as Bode plots in Figs. 2.36-2.41.

The three types of motion have been selected to compare the influence of uniform, chordwise varying and spanwise varying downwash, respectively. Owing to the residualization, all reduced order models match the full order model at zero reduced frequency. The lift and moment at the inboard section ($\eta = 0.13$) are well matched even by the very low order models throughout the reduced frequency range. At the midwing ($\eta = 0.54$) and outboard sections ($\eta = 0.78$), the models of order 5 and 10 show deviations with increasing reduced frequency. Choosing a model order of 25 yields results indistinguishable from the reference model, which implies an order reduction by more than 98%. Baker et al. [4] proposed that this high degree of reduction was linked to

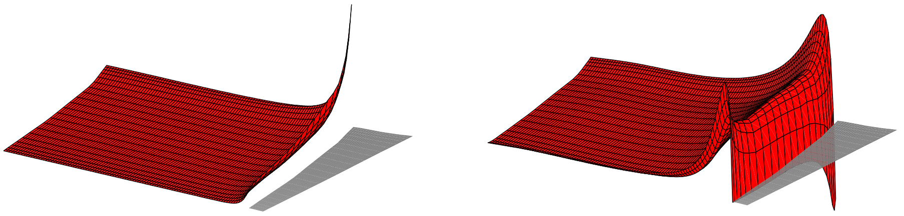

(a) Mode 1 (b) Mode 2

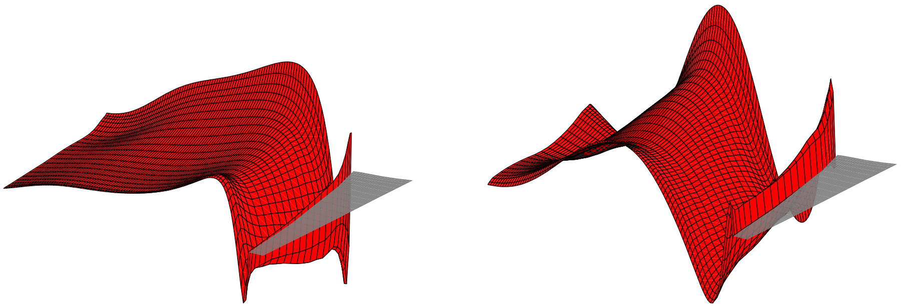

(c) Mode 3 (d) Mode 4

Figure 2.35: Wake Mode Shapes of of the Balanced Sub-Models

uniform spanwise downwash and therfore the relatively low importance of spanwise circulation modes. The results shown here suggest that a similar degree of reduction can also be achieved for spanwise variation of the downwash. The question arises how the process of order reduction can be automatized to some extend. One option could be, that the user specifies an error bound on the frequency response

$$
\begin{aligned}
\overline{e}(\omega) &= ||G(i\omega) - \overline{G}(i\omega)|| < tol \\
G(i\omega) &= \left(\boldsymbol{C}\left(i\omega I - A\right)^{-1}\boldsymbol{B} + \boldsymbol{D}\right)u \\
\overline{G}(i\omega) &= \left(\overline{\boldsymbol{C}}\left(i\omega I - \overline{A}\right)^{-1}\overline{\boldsymbol{B}} + \boldsymbol{D}\right)u
\end{aligned}
$$

and the system is successively truncated until the error bound is reached. Alternatively, the user could supply a minimum relative magnitude of HSV to be retained in the truncated system

$$\frac{\sigma_i}{\sigma_1} > tol.$$

In summary, balanced truncation is an effective means to reduce the problem size of the linearized UVLM in state space form and allows a physical interpretation of the retained wake modes. By successive application of the method to sub-models rather than directly to the full state space system, algorithms for dense matrix systems can still be applied without excessive memory requirements.

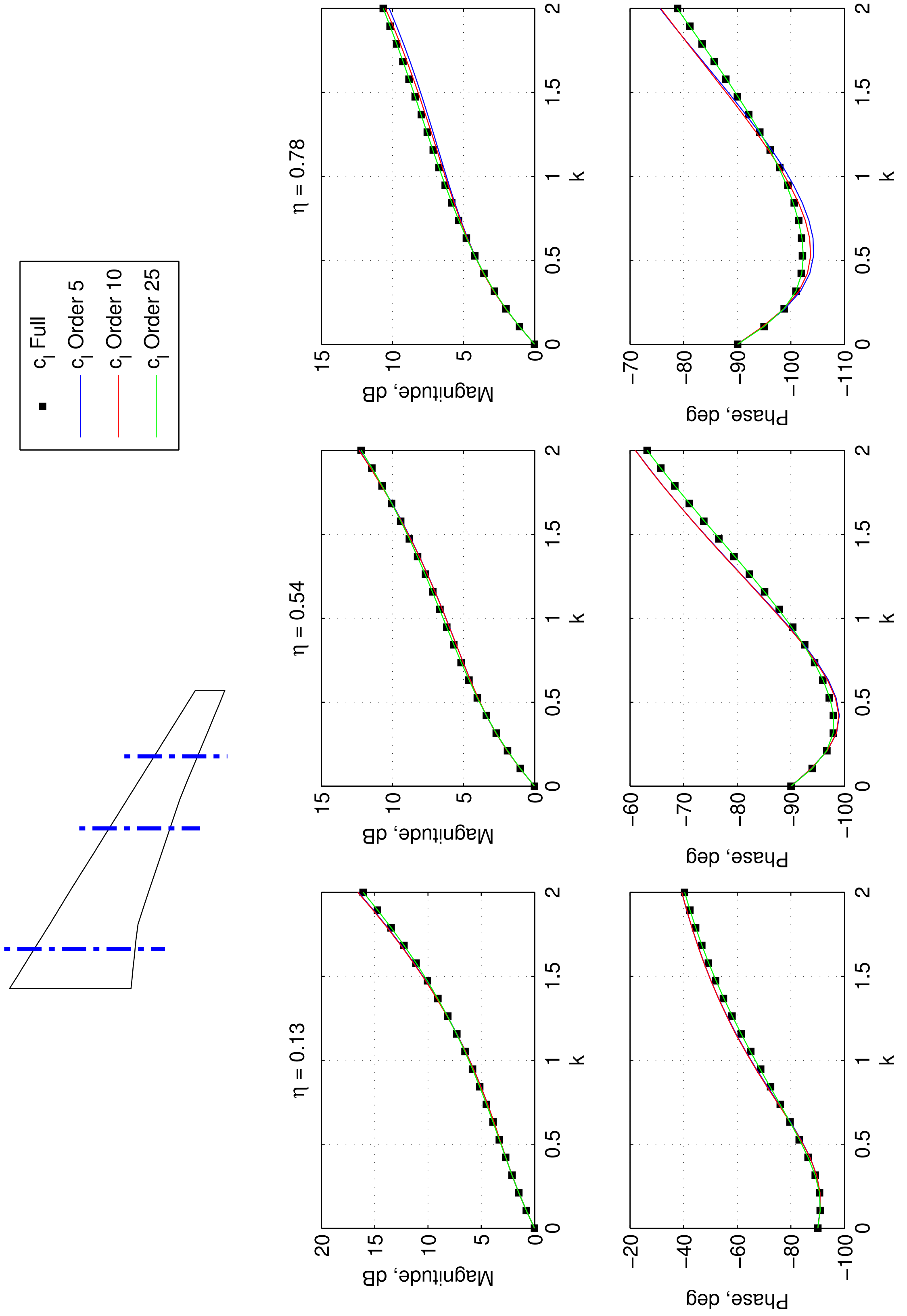

Figure 2.36: Reduced Order Models (Local Lift in Heaving Motion)

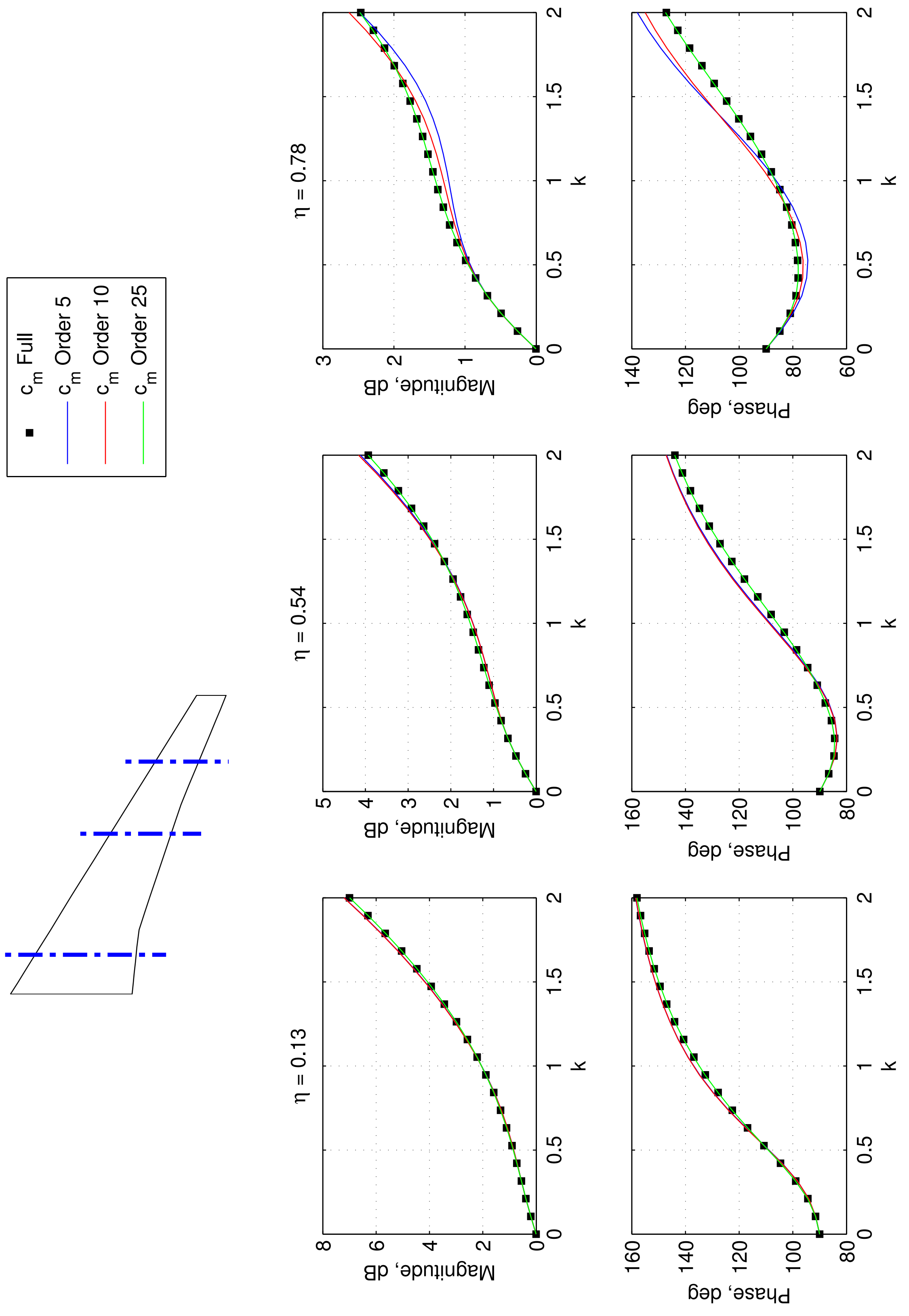

Figure 2.37: Reduced Order Models (Local Pitching Moment in Heaving Motion)

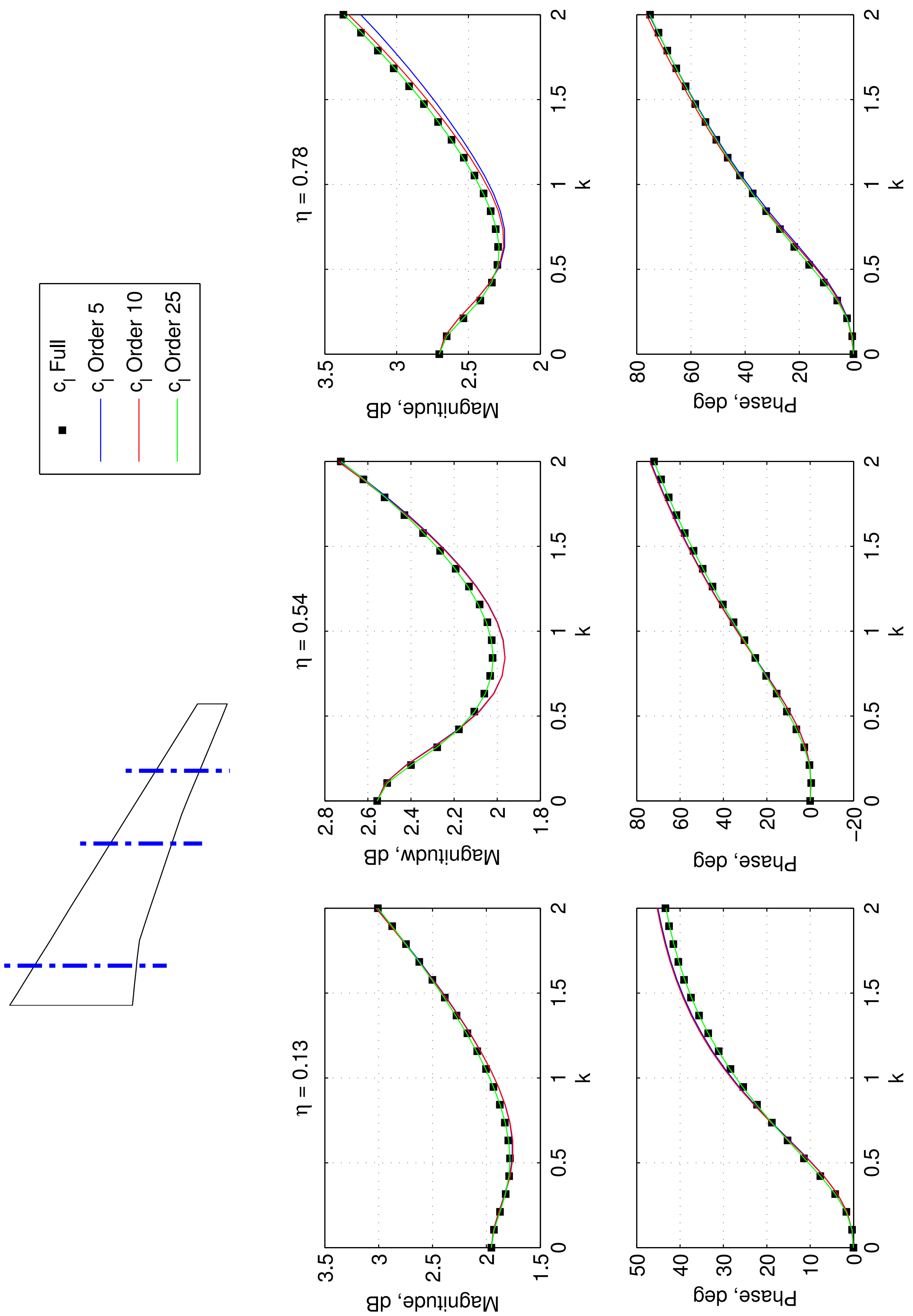

Figure 2.38: Reduced Order Models (Local Lift in Pitching Motion)

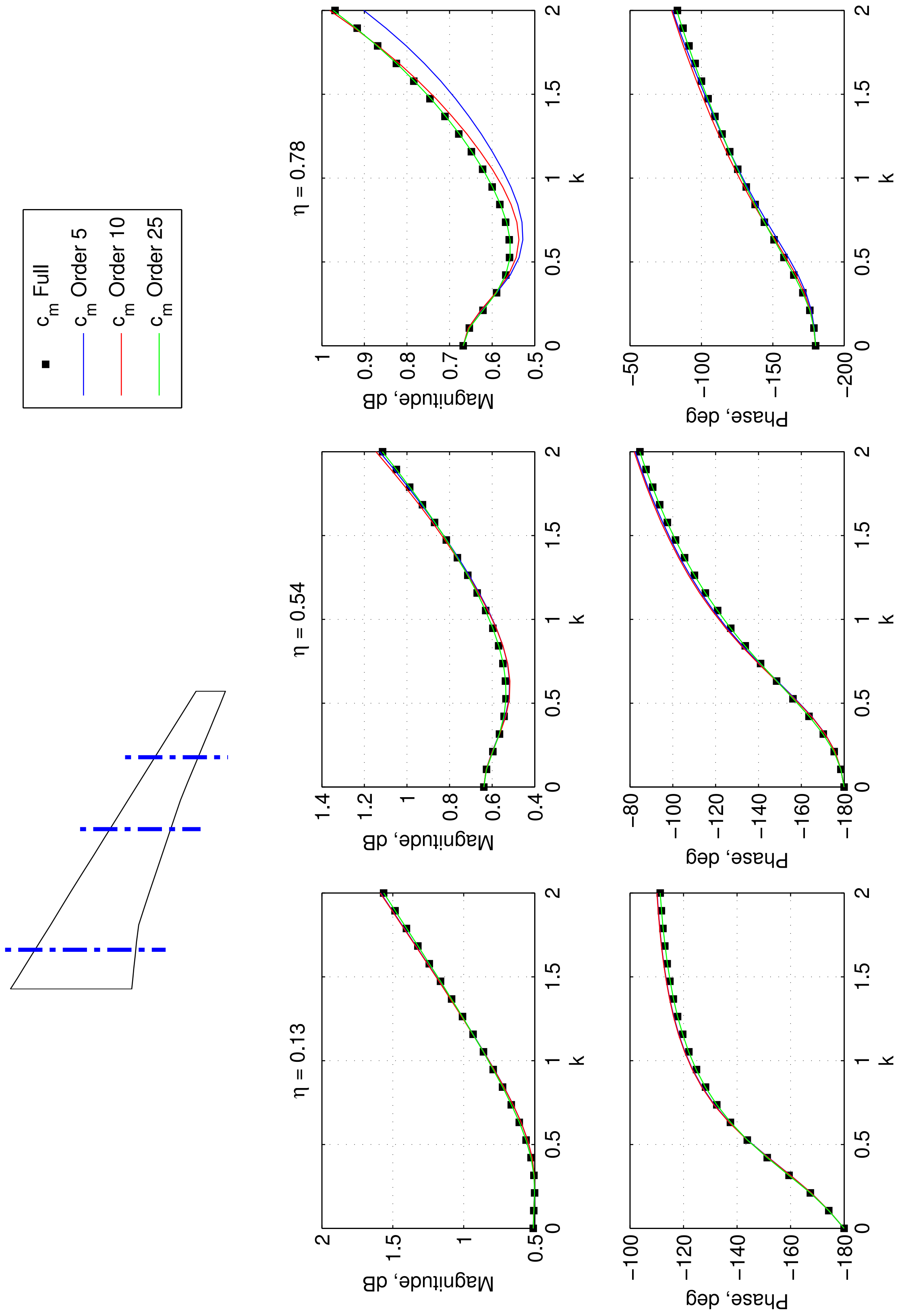

Figure 2.39: Reduced Order Models (Local Moment in Pitching Motion)

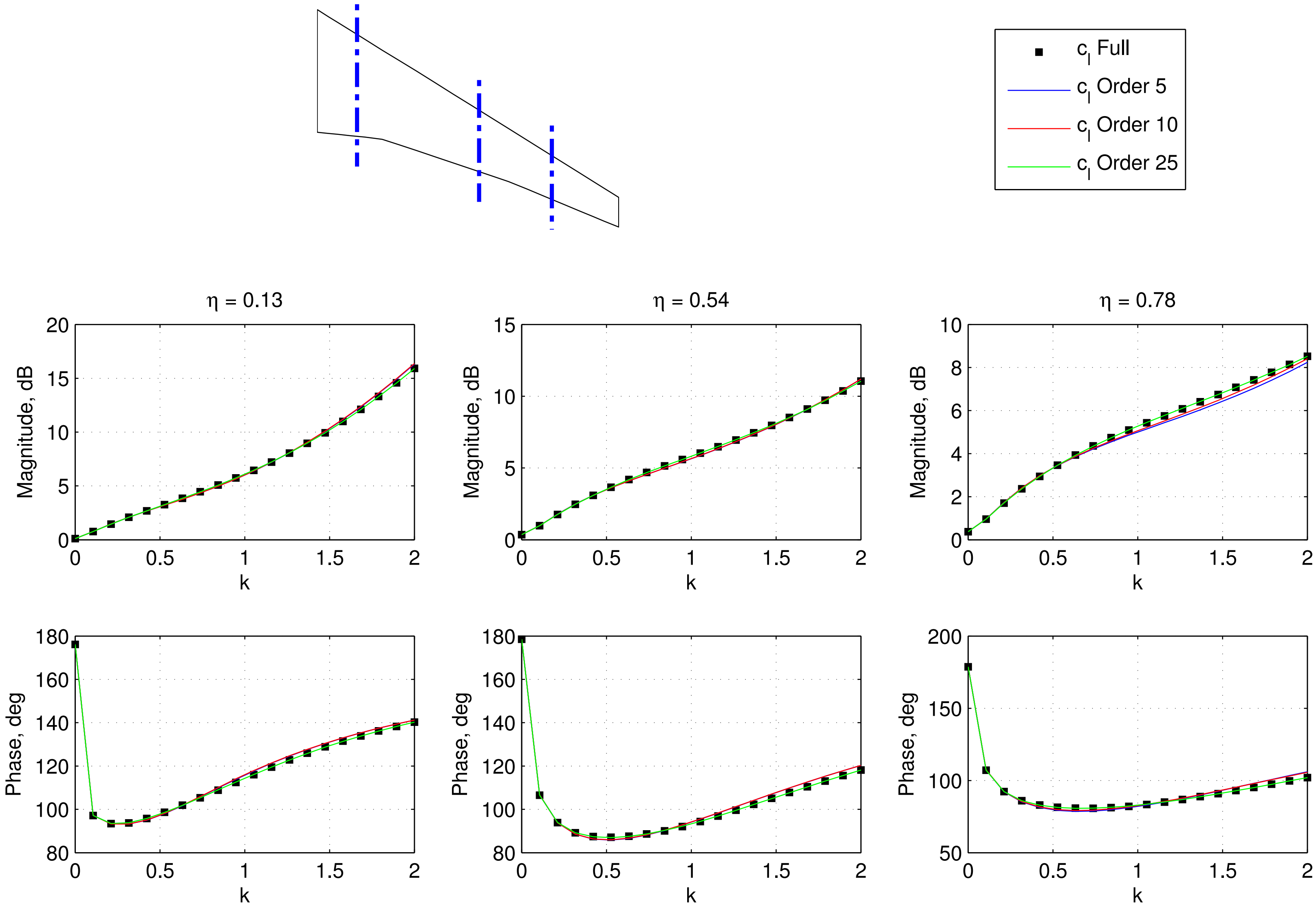

Figure 2.40: Reduced Order Models (Local Lift in Bending)

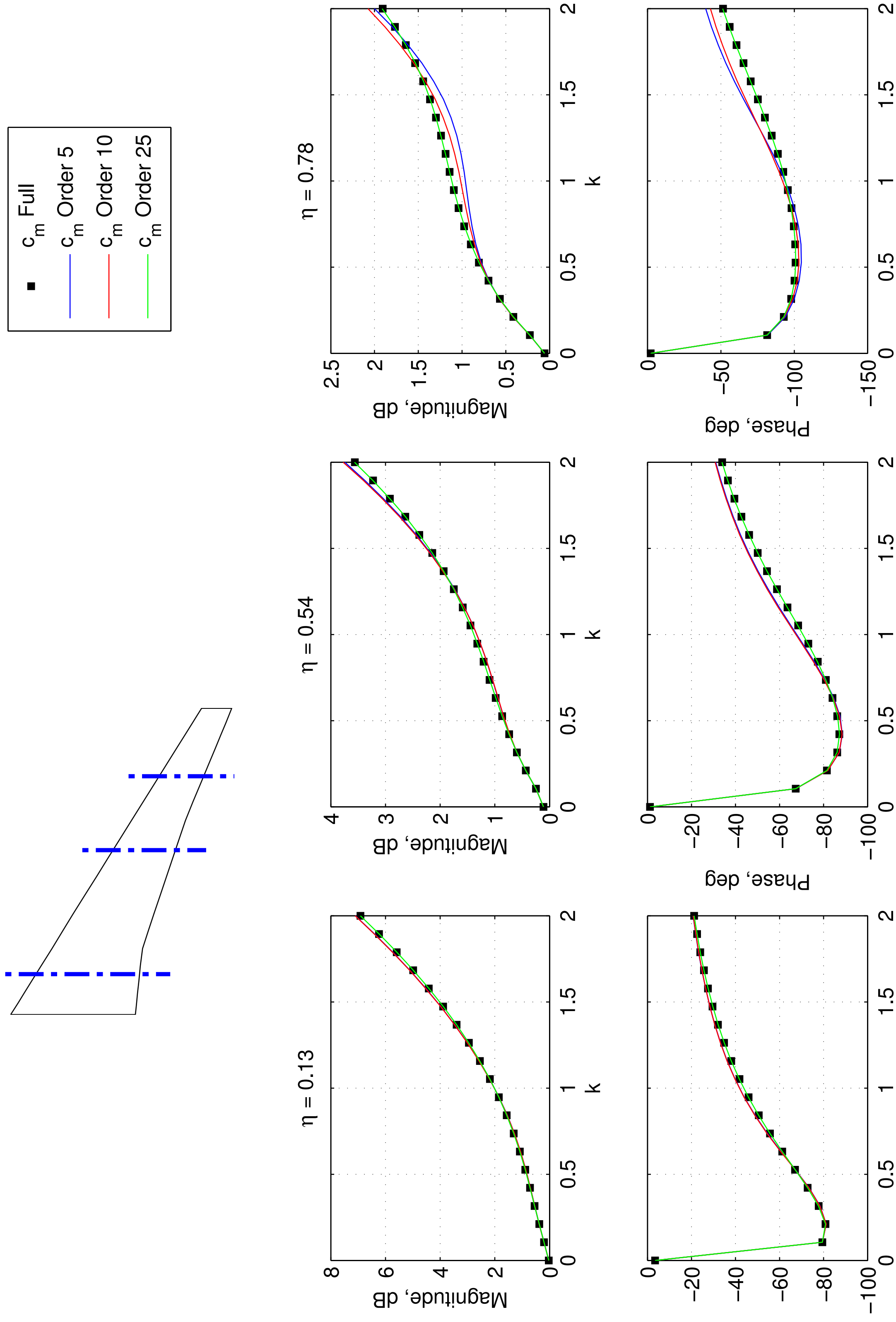

Figure 2.41: Reduced Order Models (Local Moment in Bending)

3 Structural Model

3.1 Stiffness and Mass Model

The stiffness and mass models are obtained from a detailed finite element representation of the aircraft structure as depicted in Fig. 3.1(a). Because the number of degrees of freedom of the full finite element model is too large for efficient aeroelastic analysis and only a subset of degrees of freedom is necessary to characterize the dynamic behavior of the aircraft in the lower frequency band, a static order reduction of the model according to Guyan is performed (see Link [80]). To this end, the matrix equation of the static problem is partitioned into two degrees of freedom sets. The first set (denoted by the subscript 'a') is the analysis set at which the external forces are applied, and the remaining degrees of freedom are collected in the omitted set (denoted by the subscript 'o'). The equation of static equilibrium can then be written as

$$\begin{bmatrix} K_{\mathrm{aa}} & K_{\mathrm{ao}} \\ K_{\mathrm{oa}} & K_{\mathrm{oo}} \end{bmatrix} \begin{Bmatrix} \boldsymbol{u}_{\mathrm{S,a}} \\ \boldsymbol{u}_{\mathrm{S,o}} \end{Bmatrix} = \begin{Bmatrix} \boldsymbol{P}_{\mathrm{a}} \\ \boldsymbol{0} \end{Bmatrix} \tag{3.1.1}$$

where K is the stiffness matrix, $\boldsymbol{u}_{\mathrm{S}}$ is the vector of nodal deformation and $\boldsymbol{P}$ is the vector of externally applied forces and moments. From Eq. (3.1.1), the reduced order static problem can be derived by substituting the lower partition of the equation into the upper partition, yielding

$$\left(K_{\mathrm{aa}} - K_{\mathrm{ao}} K_{\mathrm{oo}}^{-1} K_{\mathrm{oa}}\right) \boldsymbol{u}_{\mathrm{S,a}} = \boldsymbol{P}_{\mathrm{a}} \tag{3.1.2}$$

where the term in brackets is the statically reduced stiffness matrix. Only load-carrying structure is modelled in the full finite element model and therefore aircraft mass cannot be captured by material density and element volume only. Instead, mass distributions according to the aircraft configuration are obtained from a database and integrated to yield lumped sectional masses. As shown in Fig. 3.2, these point masses are connected to the finite element model via frameworks of rigid connectors, where the structural support points for the rigid connectors must be suitably selected so that the structure is able to sustain the inertia loads. Typically, the static reduction retains the degrees of freedom of the lumped masses, and this set will be denoted by the subscript 'g'. Consequently, M_{gg} and K_{gg} denote the reduced mass and stiffness matrices, respectively, and are square matrices of size n_{g}. Defining a general vector of external nodal loads $\boldsymbol{P}_{\mathrm{g}}$ and the vector of nodal degrees of freedom $\boldsymbol{u}_{\mathrm{g}}$, the dynamic equation of motion of the reduced order model can be written as

$$M_{\mathrm{gg}}\, \ddot{\boldsymbol{u}}_{\mathrm{g}} + K_{\mathrm{gg}}\, \boldsymbol{u}_{\mathrm{g}} = \boldsymbol{P}_{\mathrm{g}} \tag{3.1.3}$$

where structural damping has been neglected. Due to the static condensation, K_{gg} is a fully populated matrix whereas M_{gg} is a block-diagonal matrix containing the inertia tensors of the lumped masses. In Fig. 3.1(b), the reduced order stiffness and mass models derived from the full finite element model are depicted, where the size of the plotted spheres is proportional to the attached lumped masses.

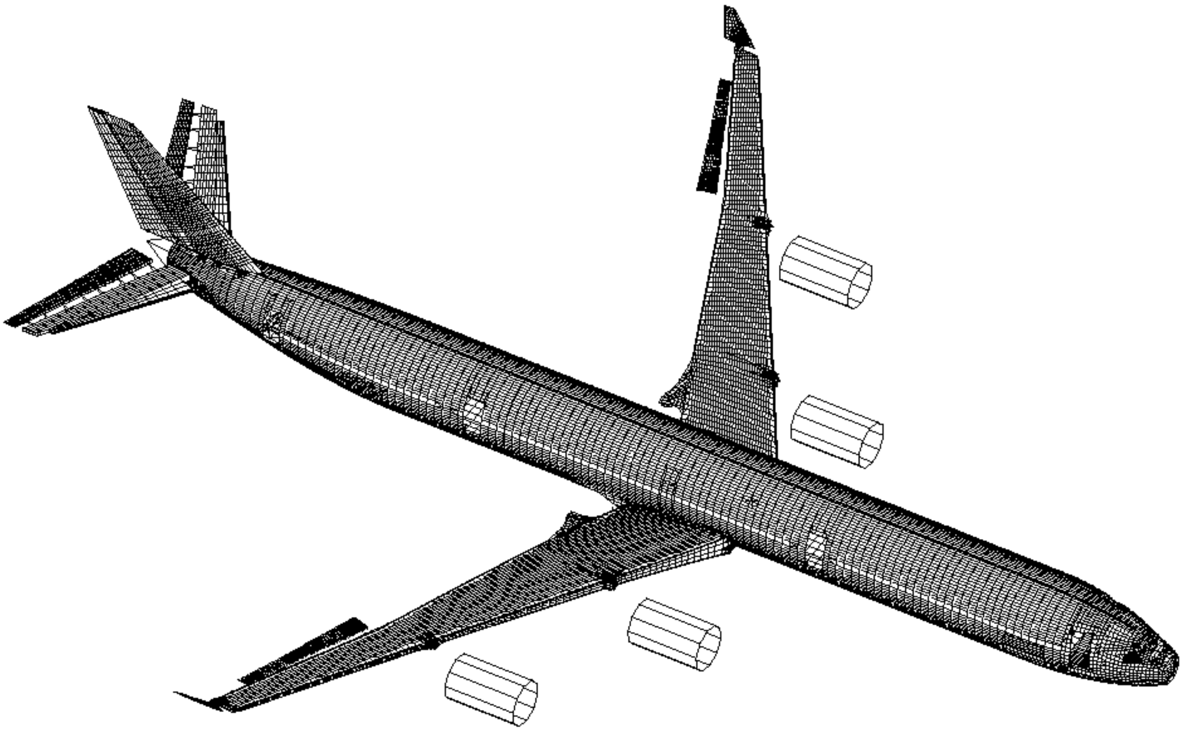

(a) Finite Element Model

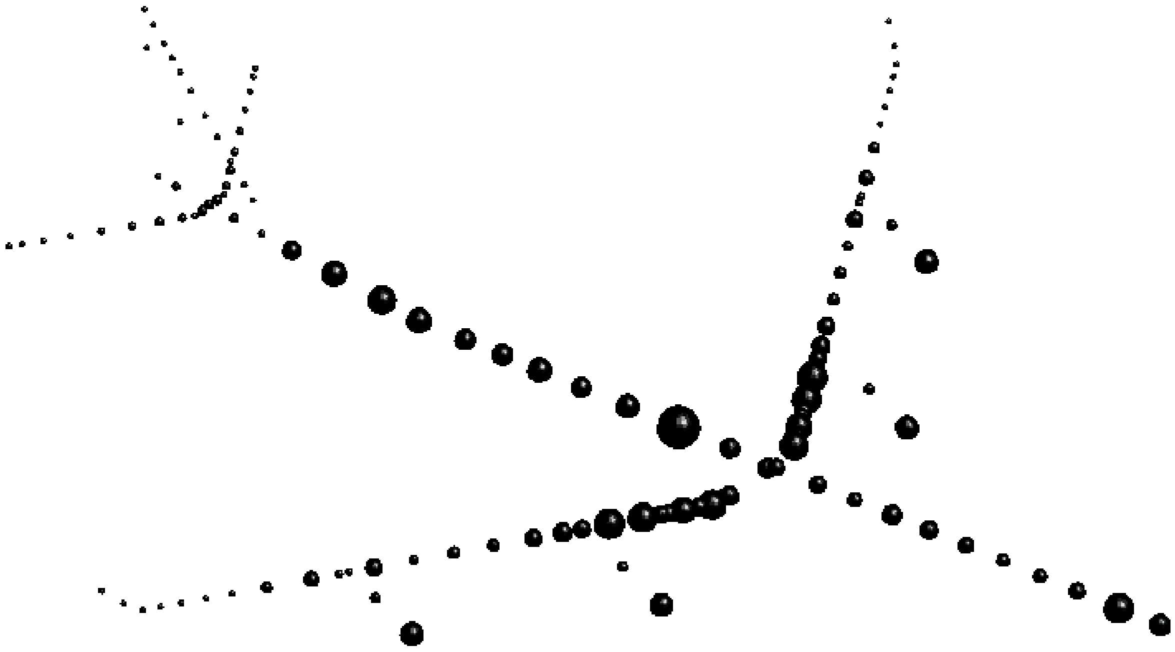

(b) Reduced Order Model

Figure 3.1: Structural Models

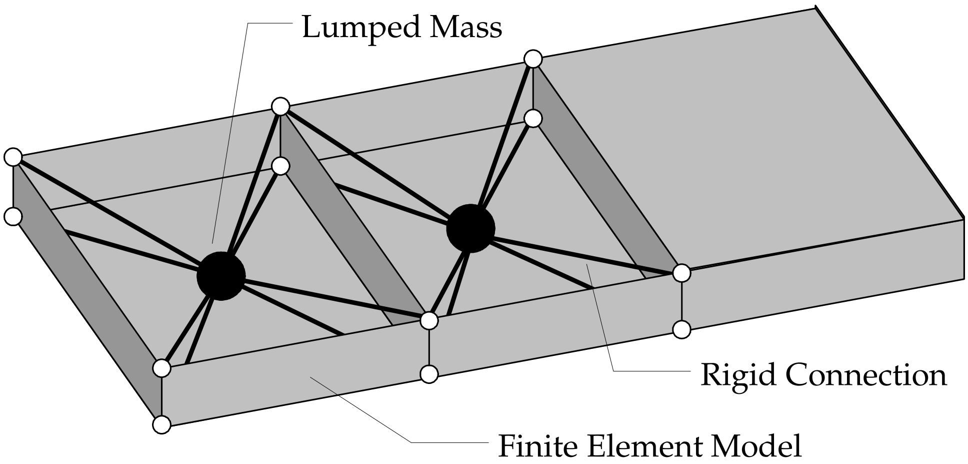

Figure 3.2: Lumped Mass Model

3.2 Modal Decomposition

The normal modes and Eigenfrequencies of the structural model are obtained by solving the generalized Eigenvalue problem

$$\left(\lambda^2 M_{\mathrm{gg}} + K_{\mathrm{gg}}\right) \mathbf{\Phi} = \mathbf{0}$$

where λ^2 and $\mathbf{\Phi}$ are the squared Eigenvalue and the Eigenvector, respectively. Because the structure is unconstrained (free-free), there exist six Eigenvalues of zero frequency for the rigid body modes and $n_{\mathrm{g}} - 6$ Eigenvalues of non-zero frequency for the elastic modes. The resulting mode shape matrix, partitioned into rigid body and elastic modes, is

$$\Phi_{\mathrm{gh}} = \left[\Phi^*_{\mathrm{gR}} \quad \Phi_{\mathrm{gE}}.\right]$$

where the subscript 'h' has been introduced to designate the modal space and the asterisk indicates that the rigid body shapes are defined about the principal axes of the aircraft. The deformation at the nodal degrees of freedom can now be approximated by a linear combination of time-independent Eigenvectors weighted by time-dependent generalized modal coordinates

$$\boldsymbol{u}_{\mathrm{g}} \approx \Phi_{\mathrm{gh}}\, \boldsymbol{\eta} \tag{3.2.1}$$

which becomes an exact relation once the complete set of rigid and elastic Eigenvectors is considered. Substitution of Eq. (3.2.1) into the nodal equation of motion Eq. (3.1.3) and pre-multiplication with the mode shape matrix yields the modal equation of motion

$$M_{\mathrm{hh}}\ddot{\boldsymbol{\eta}} + K_{\mathrm{hh}}\boldsymbol{\eta} = \boldsymbol{Q} \tag{3.2.2}$$

Here the generalized mass and stiffness matrix and vector of generalized loads are

$$\begin{aligned}
M_{\mathrm{hh}} &= \Phi^{\mathrm{T}}_{\mathrm{gh}} M_{\mathrm{gg}}\, \Phi_{\mathrm{gh}} = \begin{bmatrix} M_{\mathrm{RR}} & 0 \\ 0 & M_{\mathrm{EE}} \end{bmatrix} \\
K_{\mathrm{hh}} &= \Phi^{\mathrm{T}}_{\mathrm{gh}} K_{\mathrm{gg}}\, \Phi_{\mathrm{gh}} = \begin{bmatrix} 0 & 0 \\ 0 & K_{\mathrm{EE}} \end{bmatrix} \\
\boldsymbol{Q} &= \Phi^{\mathrm{T}}_{\mathrm{gh}} \boldsymbol{P}_{\mathrm{g}} = \begin{Bmatrix} \boldsymbol{Q}_{\mathrm{R}} \\ \boldsymbol{Q}_{\mathrm{E}} \end{Bmatrix}
\end{aligned}$$

respectively, where the partitioning into rigid and elastic modal contributions has already been performed. The rigid body modes about the principal axis Φ^{*}_{gR} are replaced by rigid body modes Φ_{gR} in the direction of the body axis $(x_{\mathrm{B}}, y_{\mathrm{B}}, z_{\mathrm{B}})$ and fixed to the center of gravity as depicted in Fig. 3.3, in order to facilitate the further development of the equations of motion. This leads to a non-diagonal rigid body part of the generalized mass matrix

$$M_{\mathrm{RR}} = \Phi^{\mathrm{T}}_{\mathrm{gR}}\, M_{\mathrm{gg}}\, \Phi_{\mathrm{gR}} = \begin{bmatrix} m\, I_3 & 0 \\ 0 & J_{\mathrm{B}} \end{bmatrix}$$

where m is the aircraft total mass, I_3 is the identity matrix of size 3 and J_{B} is the inertia tensor in the body axis system, in particular

$$J_{\mathrm{B}} = \begin{bmatrix} J_{\mathrm{x}} & 0 & -J_{\mathrm{xz}} \\ 0 & J_{\mathrm{y}} & 0 \\ -J_{\mathrm{zx}} & 0 & J_{\mathrm{z}} \end{bmatrix}$$

for a symmetric aircraft.

Typically the elastic mode shapes are mass-normalized and therefore

$$\begin{aligned} M_{\mathrm{EE}}(i,j) &= \begin{cases} 1 & \text{for} \quad i = j \\ 0 & \text{for} \quad i \neq j \end{cases} \\ K_{\mathrm{EE}}(i,j) &= \begin{cases} \lambda_i^2 & \text{for} \quad i = j \\ 0 & \text{for} \quad i \neq j \end{cases} \end{aligned}$$

where λ_i is the eigenvalue of the ith mode. To approximate damping effects of the structure, a generalized damping matrix

$$B_{\mathrm{hh}} = \begin{bmatrix} 0 & 0 \\ 0 & B_{\mathrm{EE}} \end{bmatrix}$$

with modal damping is introduced, e.g.

$$B_{\mathrm{EE}}(i,j) = \begin{cases} \zeta_i \lambda_i & \text{for} \quad i = j \\ 0 & \text{for} \quad i \neq j \end{cases}$$

where ζ_i is the modal damping factor in percentage of critical damping, typically a value of 1% for low frequency modes and 2% for higher frequency modes. In summary, the modal equations of motion

$$\begin{bmatrix} M_{\mathrm{RR}} & 0 \\ 0 & M_{\mathrm{EE}} \end{bmatrix} \begin{Bmatrix} \ddot{\eta}_{\mathrm{R}} \\ \ddot{\eta}_{\mathrm{E}} \end{Bmatrix} + \begin{bmatrix} 0 & 0 \\ 0 & B_{\mathrm{EE}} \end{bmatrix} \begin{Bmatrix} \dot{\eta}_{\mathrm{R}} \\ \dot{\eta}_{\mathrm{E}} \end{Bmatrix} + \begin{bmatrix} 0 & 0 \\ 0 & K_{\mathrm{EE}} \end{bmatrix} \begin{Bmatrix} \eta_{\mathrm{R}} \\ \eta_{\mathrm{E}} \end{Bmatrix} = \begin{Bmatrix} \boldsymbol{Q}_{\mathrm{R}} \\ \boldsymbol{Q}_{\mathrm{E}} \end{Bmatrix} \tag{3.2.3}$$

describe the linear dynamic behavior of the flexible aircraft with modal damping in an inertial frame of reference allowing small disturbances in rigid body motion.

3.3 Non-Linear Equations of Motion

The modal equations of motion presented in the previous section are extremely useful for the analysis of dynamic response and stability phenomena. Owing to their linearity, both time domain and frequency domain approaches can be employed. However, the restriction to only small scale rigid body motion renders these equations unsuitable for the simulation of freely maneuvering flexible aircraft. The set of equations of motion governing both large-amplitude rigid body motion and small-amplitude structural dynamic motion was derived by Waszak and Schmidt [133], making the following assumptions:

1. The aircraft is maneuvering over a flat Earth with constant gravitational acceleration.
2. Structural deformation is assumed sufficiently small and therefore linear elastic theory is valid.
3. A set of normal vibration modes from a free-free analysis of the structure is available.
4. The mass of the aircraft is concentrated in a collection of point masses with constant density and negligible rotational inertia.
5. Displacement and displacement rate are co-linear or displacement rate is very small and therefore their cross product is negligible.
6. The inertia tensor is constant.

These assumptions lead to a set of inertially uncoupled equations, e.g. the coupling of the rigid body and elastic motion occurs via the external applied loads only. A more general set of equations of motion also taking into account inertia coupling and rotational inertia of the lumped masses was derived by Reschke [102], where the equations presented here can be found as a special case.

The frames of reference required for the derivation are shown in Fig. 3.3. Attached to the center of gravity of the aircraft is the body fixed frame of reference B, with the x-axis forward, y-axis port and z-axis down. Also attached to the center of gravity is

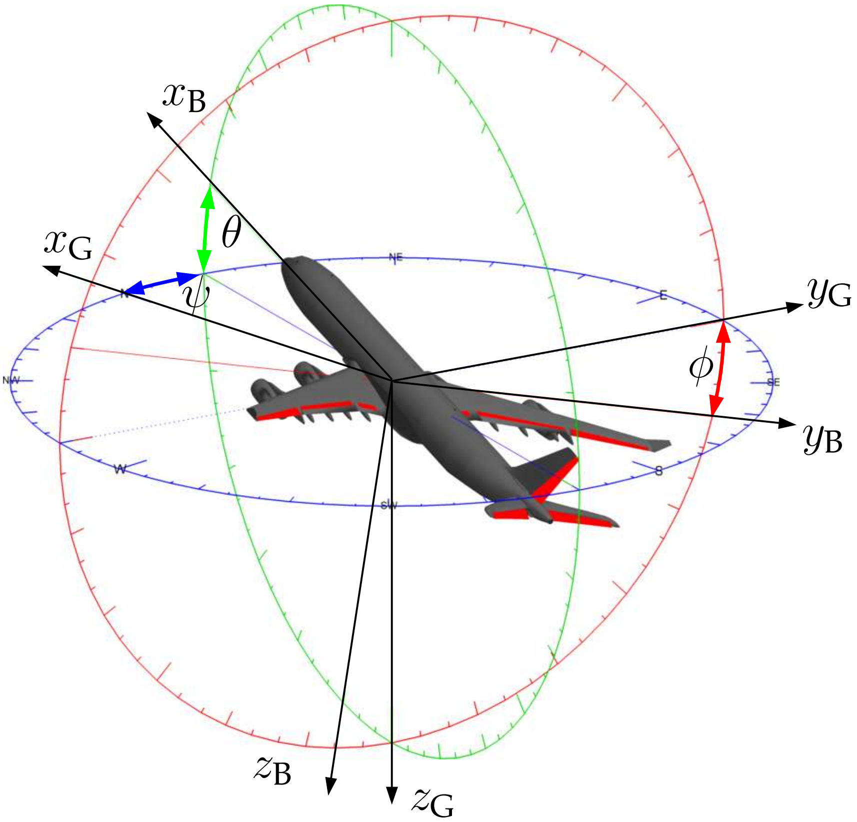

Figure 3.3: Geodetic and Body Fixed Frame of Reference

the geodesic frame of reference G, with the x-axis pointing North, y-axis pointing East and z-axis pointing down. Frame G is an inertial frame of reference because it does not rotate with the aircraft. The coordinate transformation from frame G to frame B is described by three consecutive rotations with the Euler angles $\boldsymbol{\Theta}^{\mathrm{T}} = \{\phi\ \theta\ \psi\}$. The first rotation is about the z_{G} axis by yaw angle ψ, taking x_{G} to axis k_1 and y_{G} to axis k_2. The next rotation is about k_2 by pitch angle θ, taking k_1 to x_{B} and z_{G} to k_3. The final rotation by bank angle ϕ about x_{B} takes k_2 to y_{B} and k_3 to z_{B}. The complete transformation matrix reads (see for instance Stevens and Lewis [115])

$$T_{\mathrm{BG}} = \begin{bmatrix} \cos\theta\cos\psi & \cos\theta\sin\psi & -\sin\theta \\ -\cos\phi\sin\psi + \sin\phi\sin\theta\cos\psi & \cos\phi\cos\psi + \sin\phi\sin\theta\sin\psi & \sin\phi\cos\theta \\ \sin\phi\sin\psi + \cos\phi\sin\theta\cos\psi & -\sin\phi\cos\psi + \cos\phi\sin\theta\sin\psi & \cos\phi\cos\theta \end{bmatrix} \tag{3.3.1}$$

In order to determine the propagation of the Euler angles, an additional transformation matrix is required that transforms the angular rates about the body axis $\boldsymbol{\omega}_{\mathrm{B}}^{\mathrm{T}} = \{p\ q\ r\}$ into rates of the Euler angles $\dot{\boldsymbol{\Theta}}^{\mathrm{T}} = \left\{\dot\phi\ \dot\theta\ \dot\psi\right\}$. This matrix is found to be (see for instance Stevens and Lewis [115])

$$R_{\mathrm{GB}} = \begin{bmatrix} 1 & \tan\theta\sin\phi & \tan\theta\cos\phi \\ 0 & \cos\phi & -\sin\phi \\ 0 & \frac{\sin\phi}{\cos\theta} & \frac{\cos\phi}{\cos\theta} \end{bmatrix} \tag{3.3.2}$$

Due to the cosine terms in the denominators of Eq. (3.3.2), the rate transformation matrix is not defined for pitch angles of $\pm 90^\circ$ and therefore attitude propagation by quaternions is preferable in case these angular values are attainable by the aircraft. For transport category aircraft, this magnitude of pitch attitude is not relevant and the more intuitive Euler angles can be used.

Using Lagrange's Principle, the well known non-linear force and moment equations for rigid body motion are obtained

$$m\left(\dot{\boldsymbol{V}}_{\mathrm{B}} + \boldsymbol{\omega}_{\mathrm{B}} \times \boldsymbol{V}_{\mathrm{B}} - T_{\mathrm{BG}}(\phi,\theta,\psi)\,\boldsymbol{g}_0\right) = \boldsymbol{F}_{\mathrm{B}} \tag{3.3.3}$$

$$J_{\mathrm{B}}\,\dot{\boldsymbol{\omega}}_{\mathrm{B}} + \boldsymbol{\omega}_{\mathrm{B}} \times J_{\mathrm{B}}\,\boldsymbol{\omega}_{\mathrm{B}} = \boldsymbol{M}_{\mathrm{B}} \tag{3.3.4}$$

and relate the body axis velocities $\boldsymbol{V}_{\mathrm{B}}^{\mathrm{T}} = \{u\ v\ w\}$ and the angular rates about the body axis $\boldsymbol{\omega}_{\mathrm{B}}^{\mathrm{T}} = \{p\ q\ r\}$ to the external applied rigid body forces $\boldsymbol{F}_{\mathrm{B}}$ and moments $\boldsymbol{M}_{\mathrm{B}}$ and the constant vector of gravitational acceleration $\boldsymbol{g}_0^{\mathrm{T}} = \{0\ 0\ g_0\}$ resolved in the geodetic system. Denoted by m and J_{B} are the aircraft total mass and constant inertia tensor about the body axis, respectively. The total rigid body load is obtained from

$$\boldsymbol{Q}_{\mathrm{R}} = \begin{Bmatrix} \boldsymbol{F}_{\mathrm{B}} \\ \boldsymbol{M}_{\mathrm{B}} \end{Bmatrix} = \boldsymbol{\Phi}_{\mathrm{gR}}^{\mathrm{T}}\,\boldsymbol{P}_{\mathrm{g}}$$

where $\boldsymbol{\Phi}_{\mathrm{gR}}$ is the matrix of rigid body mode shapes with respect to the body axis and $\boldsymbol{P}_{\mathrm{g}}$ is the vector of external applied loads also resolved in the body axis system. To close the problem of rigid body motion, the differential equations governing attitude and position of the aircraft are

$$\dot{\boldsymbol{\Theta}} = R_{\mathrm{GB}}(\phi,\theta)\,\boldsymbol{\omega}_{\mathrm{B}} \tag{3.3.5}$$

$$\dot{\boldsymbol{r}}_{\mathrm{G}} = T_{\mathrm{BG}}^{\mathrm{T}}(\phi,\theta,\psi)\,\boldsymbol{V}_{\mathrm{B}} \tag{3.3.6}$$

with the aircraft position vector $\boldsymbol{r}_{\mathrm{G}}^{\mathrm{T}} = \{r_{\mathrm{N}}\ r_{\mathrm{E}}\ -h\}$. Equations (3.3.3-3.3.6) are the classical non-linear flight dynamic equations formulated in body axis for a rigid aircraft with constant mass.

The additional equations governing the structural dynamics behavior are the modal equations of motion for n_e elastic modes

$$M_{\mathrm{EE}}\,\ddot{\boldsymbol{\eta}}_{\mathrm{E}} + B_{\mathrm{EE}}\,\dot{\boldsymbol{\eta}}_{\mathrm{E}} + K_{\mathrm{EE}}\,\boldsymbol{\eta}_{\mathrm{E}} = \boldsymbol{Q}_{\mathrm{E}} \tag{3.3.7}$$

where $M_{\mathrm{EE}}, B_{\mathrm{EE}}, K_{\mathrm{EE}}$ are the modal mass, damping and stiffness matrices, respectively, $\boldsymbol{\eta}_{\mathrm{E}}$ is the vector of generalized elastic modal coordinates and $\boldsymbol{Q}_{\mathrm{E}}$ is the vector of generalized elastic modal forces. It is obtained from

$$\boldsymbol{Q}_{\mathrm{E}} = \Phi_{\mathrm{gE}}^{\mathrm{T}}\,\boldsymbol{P}_{\mathrm{g}}$$

where Φ_{gE} is the matrix of elastic mode shapes. Even though it seems intuitive to simply combine the linear elastic modal equations of motion and the non-linear equations of rigid body motion, it is the orthogonality of the rigid body modes and elastic modes that leads to this simple result (the identical finding was reported by De Veubeke [26] and Canavin and Likins [16]).

3.4 Equation of Loads

To determine the internal structural loads experienced by the airframe, either a deformation (*mode displacement*) or momentum (*force summation*) approach is possible. If the structural deformation of the aircraft $\boldsymbol{u}_{\mathrm{g}}$ is known, the internal structural loads $\boldsymbol{L}_{\mathrm{g}}$ can be determined by

$$\boldsymbol{L}_{\mathrm{g}} = K_{\mathrm{gg}}\boldsymbol{u}_{\mathrm{g}}. \tag{3.4.1}$$

Using Eq. (3.2.1) and noticing that rigid body motion does not induce internal structural loads, this can be expressed in terms of the elastic modal coordinates

$$\boldsymbol{L}_{\mathrm{g}} = K_{\mathrm{gg}}\,\Phi_{\mathrm{gE}}\,\boldsymbol{\eta}_{\mathrm{E}}. \tag{3.4.2}$$

Unfortunately, as demonstrated for instance by Reschke [101], this easily applicable approach requires a large number of elastic mode shapes in order to obtain good convergence of the internal loads. Therefore, Reschke [102] derived the equations of structural loads accompanying the inertially uncoupled equations of motion using a momentum approach. By Newton's Second Law, the time rate of change of linear and angular momentum of a mass point equals the total applied forces and moments at the mass point (see for instance Meirovitch [89])

$$\dot{\boldsymbol{H}}_{\mathrm{g}} = \boldsymbol{P}_{\mathrm{g,total}}$$

where $\dot{\boldsymbol{H}}_{\mathrm{g}}$ is the vector of linear and angular rate of momentum of the mass points and $\boldsymbol{P}_{\mathrm{g,total}}$ is the vector of total forces and moments. The latter can be split up into the contributions

$$\boldsymbol{P}_{\mathrm{g,total}} = \boldsymbol{L}_{\mathrm{g}} + \boldsymbol{P}_{\mathrm{g}}$$

where $\boldsymbol{L}_{\mathrm{g}}$ and $\boldsymbol{P}_{\mathrm{g}}$ are the internal elastic nodal load and the external applied load, respectively. Formulating the rate of momentum vector $\dot{\boldsymbol{H}}_{\mathrm{g}}$ for a moving coordinate system and rearranging yields the desired internal elastic nodal loads

$$\boldsymbol{L}_{\mathrm{g}} = \boldsymbol{P}_{\mathrm{g}} - M_{\mathrm{gR}} \left\{ \begin{array}{c} \dot{\boldsymbol{V}}_{\mathrm{B}} + \boldsymbol{\omega}_{\mathrm{B}} \times \boldsymbol{V}_{\mathrm{B}} - T_{\mathrm{BG}}\,\boldsymbol{g}_0 \\ \dot{\boldsymbol{\omega}}_{\mathrm{B}} \end{array} \right\} - M_{\mathrm{gE}}\,\ddot{\boldsymbol{\eta}}_{\mathrm{E}} \tag{3.4.3}$$

where M_{gR} and M_{gE} are the right-generalized mass matrices of the rigid body modes and of the elastic modes, respectively, obtained from

$$\begin{aligned} M_{\mathrm{gR}} &= M_{\mathrm{gg}}\, \Phi_{\mathrm{gR}} \\ M_{\mathrm{gE}} &= M_{\mathrm{gg}}\, \Phi_{\mathrm{gE}}. \end{aligned}$$

When the linear modal equations of motion given in Eq. (3.2.2) are used, the equation of loads simplifies to

$$\boldsymbol{L}_{\mathrm{g}} = \boldsymbol{P}_{\mathrm{g}} - M_{\mathrm{gR}}\, \ddot{\boldsymbol{\eta}}_{\mathrm{R}} - M_{\mathrm{gE}}\, \ddot{\boldsymbol{\eta}}_{\mathrm{E}} \tag{3.4.4}$$

due to the fact that an inertial frame of reference is used.

3.5 Small Disturbance Equations

For stability and small-disturbance analysis, the non-linear equations of motion can be linearized. A steady, symmetric and trimmed flight condition, denoted by the subscript 0, is described by the parameters

$$\begin{aligned} \boldsymbol{V}_{\mathrm{B},0}^{\mathrm{T}} &= \{u_0\, 0\, w_0\} \\ V_0 &= \sqrt{u_0^2 + w_0^2} \\ \boldsymbol{\omega}_{\mathrm{B},0}^{\mathrm{T}} &= \{0\,0\,0\} \\ \boldsymbol{\Theta}_0^{\mathrm{T}} &= \{0\, \theta_0\, 0\} \\ \boldsymbol{r}_{\mathrm{G},0}^{\mathrm{T}} &= \{r_{\mathrm{N},0}\; r_{\mathrm{E},0}\; -h_0\} \end{aligned}$$

and perturbation of the reference condition will be denoted by primed quantities, e.g. u', v', w' etc.. The linearized force equation becomes

$$m\left(\dot{\boldsymbol{V}}_{\mathrm{B}}' - V_{\mathrm{B},0}\, \boldsymbol{\omega}_{\mathrm{B}}' - G_0\, \boldsymbol{\Theta}'\right) = \boldsymbol{F}_{\mathrm{B}}' \tag{3.5.1}$$

with the cross product matrix of the steady state velocity

$$V_{\mathrm{B},0} = \begin{bmatrix} 0 & -w_0 & 0 \\ w_0 & 0 & -u_0 \\ 0 & u_0 & 0 \end{bmatrix}$$

and the gravitation matrix obtained from linearization of the third column of matrix T_{BG} in Eq. (3.3.1)

$$G_0 = \begin{bmatrix} 0 & g_0 \cos\theta_0 & 0 \\ g_0 \cos\theta_0 & 0 & 0 \\ 0 & -g_0 \sin\theta_0 & 0 \end{bmatrix}. \tag{3.5.2}$$

The linearized moment equation and attitude equations are

$$J_{\mathrm{B}}\, \dot{\boldsymbol{\omega}}_{\mathrm{B}}' = \boldsymbol{M}_{\mathrm{B}}' \tag{3.5.3}$$

$$\dot{\boldsymbol{\Theta}}' = R_{\mathrm{GB},0}\, \boldsymbol{\omega}_{\mathrm{B}}' \tag{3.5.4}$$

where the linearized rate matrix

$$R_{\mathrm{GB},0} = \begin{bmatrix} 1 & 0 & \tan\theta_0 \\ 0 & 1 & 0 \\ 0 & 0 & \frac{1}{\cos\theta_0} \end{bmatrix} \tag{3.5.5}$$

is the non-linear rate matrix of Eq. (3.3.2) evaluated for $\boldsymbol{\Theta}_0$. Finally, the linearized position equation becomes

$$\dot{\boldsymbol{r}}'_{\mathrm{G}} = T^{V}_{\mathrm{BG},0}\, \boldsymbol{V}'_{\mathrm{B}} + T^{\Theta}_{\mathrm{BG},0}\, \boldsymbol{\Theta}' \tag{3.5.6}$$

and requires the lengthy linearization of the full T_{BG} matrix of Eq. (3.3.1) to obtain the velocity and attitude transformation matrices (see for instance Gupta et al. [47])

$$\begin{aligned} T^{V}_{\mathrm{BG},0} &= \begin{bmatrix} \cos\theta_0 & 0 & \sin\theta_0 \\ 0 & 1 & 0 \\ -\sin\theta_0 & 0 & \cos\theta_0 \end{bmatrix} \\ T^{\Theta}_{\mathrm{BG},0} &= \begin{bmatrix} 0 & 0 & 0 \\ -V_0\sin\theta_0 & 0 & V_0 \\ 0 & -V_0 & 0 \end{bmatrix} \end{aligned} \tag{3.5.7}$$

Owing to their linearity, the modal elastic equations of motion in Eq. (3.3.7) remain unchanged

$$M_{\mathrm{EE}}\, \ddot{\boldsymbol{\eta}}'_{\mathrm{E}} + B_{\mathrm{EE}}\, \dot{\boldsymbol{\eta}}'_{\mathrm{E}} + K_{\mathrm{EE}}\, \boldsymbol{\eta}'_{\mathrm{E}} = \boldsymbol{Q}'_{\mathrm{E}} \tag{3.5.8}$$

3.6 Transformation from Inertial to Body-Fixed Coordinates

It will now be shown, how the modal equations of motion Eq. (3.2.2), that are valid for rigid body motion in an inertial frame of reference can be transformed into the small disturbance equations of motion derived in the previous section. The modal rigid body velocity and position vectors

$$\dot{\boldsymbol{\eta}}_{\mathrm{R}} = \begin{Bmatrix} \dot{T}_x \\ \dot{T}_y \\ \dot{T}_z \\ \dot{R}_x \\ \dot{R}_y \\ \dot{R}_z \end{Bmatrix}, \quad \boldsymbol{\eta}_{\mathrm{R}} = \begin{Bmatrix} T_x \\ T_y \\ T_z \\ R_x \\ R_y \\ R_z \end{Bmatrix},$$

are related to the rigid body states in body fixed coordinates

$$\dot{\boldsymbol{x}}_{\mathrm{R}} = \begin{Bmatrix} u \\ v \\ w \\ p \\ q \\ r \end{Bmatrix}', \quad \boldsymbol{x}_{\mathrm{R}} = \begin{Bmatrix} r_{\mathrm{N}} \\ r_{\mathrm{E}} \\ -h \\ \phi \\ \theta \\ \psi \end{Bmatrix}'$$

via the linear transformation

$$\begin{Bmatrix} \dot{\boldsymbol{\eta}}_{\mathrm{R}} \\ \boldsymbol{\eta}_{\mathrm{R}} \end{Bmatrix} = T_{\mathrm{IB},0} \begin{Bmatrix} \dot{\boldsymbol{x}}_{\mathrm{R}} \\ \boldsymbol{x}_{\mathrm{R}} \end{Bmatrix} \tag{3.6.1}$$

with the transformation matrix

$$T_{\mathrm{IB},0} = \begin{bmatrix} T^{V}_{\mathrm{BG},0} & 0 & 0 & T^{\Theta}_{\mathrm{BG},0} \\ 0 & R_{\mathrm{GB},0} & 0 & 0 \\ 0 & 0 & I_3 & 0 \\ 0 & 0 & 0 & I_3 \end{bmatrix}$$

whose sub-matrices have been defined in Eqn. (3.3.2) and (3.5.7). In state space form, the modal equations of motion Eq. (3.2.3) can be written as

$$\begin{Bmatrix} \ddot{\eta}_\mathrm{R} \\ \dot{\eta}_\mathrm{R} \\ \ddot{\eta}_\mathrm{E} \\ \dot{\eta}_\mathrm{E} \end{Bmatrix} = E^{-1}\,A \begin{Bmatrix} \dot{\eta}_\mathrm{R} \\ \eta_\mathrm{R} \\ \dot{\eta}_\mathrm{E} \\ \eta_\mathrm{E} \end{Bmatrix} + E^{-1} \begin{Bmatrix} \boldsymbol{Q}_\mathrm{R} \\ 0 \\ \boldsymbol{Q}_\mathrm{E} \\ 0 \end{Bmatrix} \tag{3.6.2}$$

with the state matrices

$$\begin{aligned} E &= \begin{bmatrix} M_\mathrm{RR} & 0 & 0 & 0 \\ 0 & I_{n_\mathrm{R}} & 0 & 0 \\ 0 & 0 & M_\mathrm{EE} & 0 \\ 0 & 0 & 0 & I_{n_\mathrm{E}} \end{bmatrix} \\ A &= \begin{bmatrix} 0 & 0 & 0 & 0 \\ I_{n_\mathrm{R}} & 0 & 0 & 0 \\ 0 & 0 & -B_\mathrm{EE} & -K_\mathrm{EE} \\ 0 & 0 & I_{n_\mathrm{E}} & 0 \end{bmatrix} . \end{aligned}$$

The linear transformation between modal and body fixed rigid body coordinates can then be applied as a similarity transformation and yields the transformed equation of motion in terms of the typical flight dynamics parameters

$$\begin{Bmatrix} \ddot{\boldsymbol{x}}_\mathrm{R} \\ \dot{\boldsymbol{x}}_\mathrm{R} \\ \ddot{\eta}_\mathrm{E} \\ \dot{\eta}_\mathrm{E} \end{Bmatrix} = T^{-1}E^{-1}\,AT \begin{Bmatrix} \dot{\boldsymbol{x}}_\mathrm{R} \\ \boldsymbol{x}_\mathrm{R} \\ \dot{\eta}_\mathrm{E} \\ \eta_\mathrm{E} \end{Bmatrix} + T^{-1}E^{-1} \begin{Bmatrix} \boldsymbol{Q}_\mathrm{R} \\ 0 \\ \boldsymbol{Q}_\mathrm{E} \\ 0 \end{Bmatrix} \tag{3.6.3}$$

with the transformation matrix for the complete state vector

$$T = \begin{bmatrix} T_\mathrm{IB,0} & 0 \\ 0 & I_{2n_\mathrm{E}} \end{bmatrix} .$$

To complete the transformation, the gravitation term must be added to the equation

$$\begin{Bmatrix} \ddot{\boldsymbol{x}}_\mathrm{R} \\ \dot{\boldsymbol{x}}_\mathrm{R} \\ \ddot{\eta}_\mathrm{E} \\ \dot{\eta}_\mathrm{E} \end{Bmatrix} = \left(T^{-1}E^{-1}\,AT + \tilde{A} \right) \begin{Bmatrix} \dot{\boldsymbol{x}}_\mathrm{R} \\ \boldsymbol{x}_\mathrm{R} \\ \dot{\eta}_\mathrm{E} \\ \eta_\mathrm{E} \end{Bmatrix} + T^{-1}E^{-1} \begin{Bmatrix} \boldsymbol{Q}_\mathrm{R} \\ 0 \\ \boldsymbol{Q}_\mathrm{E} \\ 0 \end{Bmatrix} \tag{3.6.4}$$

with

$$\tilde{A} = \begin{bmatrix} 0 & \tilde{G}_0 & 0 & 0 \\ 0 & 0 & 0 & 0 \\ 0 & 0 & 0 & 0 \\ 0 & 0 & 0 & 0 \end{bmatrix} , \quad \tilde{G}_0 = \begin{bmatrix} 0 & m\,G_0 \\ 0 & 0 \end{bmatrix}$$

from Eq. (3.5.2).

In summary, three ways to obtain the small-disturbance equations of motion of the flexible aircraft relative to a trimmed, symmetrical flight condition are possible:

1. Numerical linearization of the non-linear equations of motion (Eqn.(3.3.3, 3.3.4, 3.3.5, 3.3.6)

2. Application of the symbolically linearized equations of motion (Eqn.(3.5.1, 3.5.3, 3.5.4, 3.5.6)

3. Transformation of the modal equations of motion and subsequent addition of the gravitation term (Eq. (3.6.4))

They are presented here in order to support the idea of an integral aircraft model from which special cases can be consistently derived.

4 Aeroelastic Model Integration

Subject of this chapter is the interaction of the aerodynamic, structural and mass models. In the first part, an interconnection method between the aerodynamic and structural model is developed, which governs the load transfer from the aerodynamic grid to the nodes of the finite element model and the mapping of the structural deformations back onto the boundary conditions of the aerodynamic model. The second part is concerned with the setup of the integral aircraft model, in particular the formation of the external forces acting on the aircraft. Depending on the choice of aerodynamic model, different formulations are presented that ensure that no double accounting of aeroelastic effects occurs.

4.1 Aero-Structural Coupling

In order to perform an aeroelastic analysis, it is necessary to combine structural and aerodynamic models. Defining the relationship between structural and aerodynamic variables permits the transfer of displacements and loads between the two domains. If the two models are geometrically identical, the transfer of displacement and loads reduces to equating the variables on both domains. However in practice, structural and aerodynamic models are frequently dissimilar and in the worst case do not have any geometrical definition points in common. This is due to the fact that structural analysis focusses on modelling the interior of a flexible body whereas aerodynamic analysis of the body rather investigates its properties on the surface and the exterior. In this case, a mathematical relationship must be established, which relates the degrees of freedom of both domains. It is customary to refer to this task as "splining"[1].

As a typical example, consider the aeroelastic model of the wing-tail combination from Section 2.2.7. The structure is represented by a reduced order model with a limited number of degrees of freedom defined at the bullet points in Fig. 4.1. The stiffness matrix relating these nodes is obtained by performing a static reduction on a detailed finite element model. No connection between neighboring nodes has been plotted to imply that the stiffness matrix is fully populated owing to the condensation procedure. The structural nodes are located along an axis equivalent to the elastic axis of the wing. The aerodynamic model consists of control points distributed over the lifting surface and is to be connected with the structural nodes. One way to achieve this is by augmentation of the structural model with rigid elements from the structural nodes to the leading and trailing edges, fitting of a surface spline to the deformation values and evaluation of the spline at the aerodynamic control points. In the following, an alternative method to establish the model interconnection is presented based on beam interpolation elements and rigid connectors. This method will be referred to as *FEM-*

---

[1] Actual spline interpolation is only one of several mathematical options.

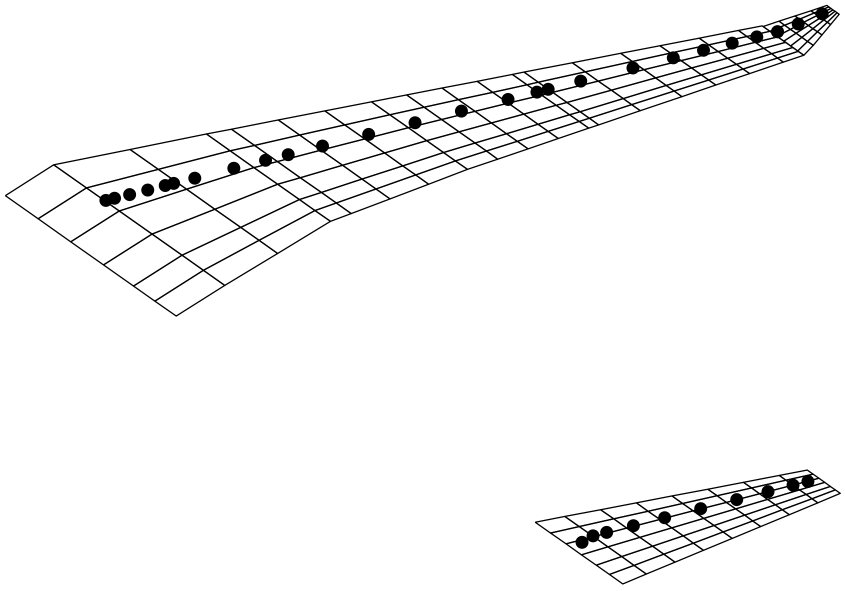

Figure 4.1: Aeroelastic Model of the Wing-Tail Configuration.

SPLINE-method.

4.1.1 Methodology

The *FEMSPLINE*-method requires three steps to determine the displacement of a node P on the aerodynamic model in accordance to the given distortion field of the structural model. First, the point F on the structural model with minimum distance to P is determined by orthogonal projection on the polygon line connecting the nodes of a component of the reduced order finite model. Second, the deformation at the projection point F is obtained by interpolation from the structural deformation field. Finally, the aerodynamic node P is displaced as if rigidly connected to F. When interpolating the deformation at the projection point F, the nodes of the reduced order model are assumed to be connected by virtual finite elements rather than fitting mathematical functions to the given scattered deformation data. These interpolation elements can be thought of as finite elements that contain shape functions but neither have mass nor stiffness. The physical rationale behind using orthogonal projection in conjunction with rigid lever arms becomes apparent when comparing the interconnection model with the real aircraft structure. In Fig. 4.2, the structural model of a vertical tail is depicted next to an aeroelastic model of the fin employing the *FEMSPLINE*. It is apparent that the rigid connectors of the model have a similar orientation as the structural ribs, thus capturing the high degree of rigidity in that direction and ensuring a physical load path. In the following, the three procedural steps will be outlined in detail.

Projection on Interpolation Elements

The aerodynamic node P is projected on the polygon line connecting a set of structural nodes $S_1, S_2, ..., S_n$ by means of vector analysis. First, the unit vector $\boldsymbol{a}_i$ pointing from S_i to S_{i+1}, the distance l_i from S_i to S_{i+1} and the vector $\boldsymbol{b}_i$ pointing from S_i to P are

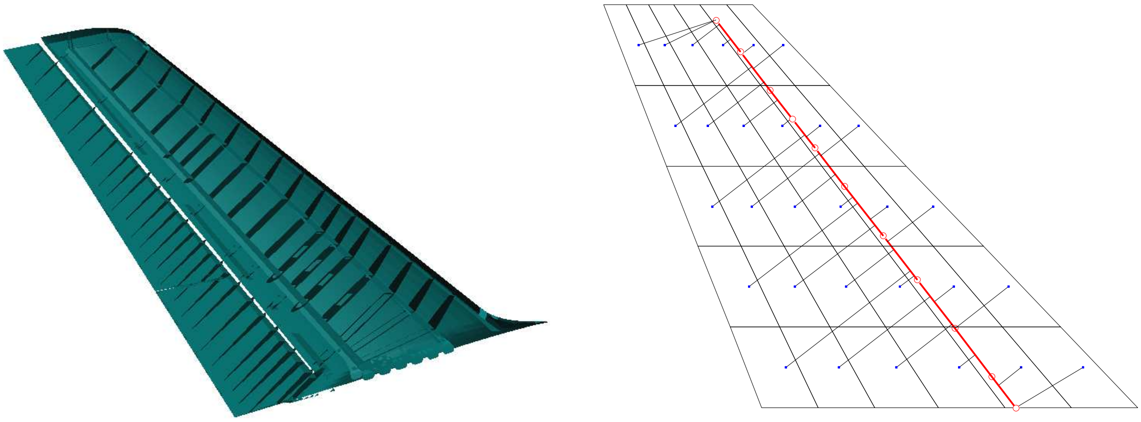

(a) Typical Vertical Tail Structure (b) *FEMSPLINE* Interconnection

Figure 4.2: Physical Rationale behind Orthogonal Projection

calculated

$$
\begin{aligned}
l_i &= |\boldsymbol{r}_{\mathrm{S},i+1} - \boldsymbol{r}_{\mathrm{S},i}| \\
\boldsymbol{a}_i &= \frac{1}{l_i}\left(\boldsymbol{r}_{\mathrm{S},i+1} - \boldsymbol{r}_{\mathrm{S},i}\right) \\
\boldsymbol{b}_i &= \frac{\boldsymbol{r}_{\mathrm{P}} - \boldsymbol{r}_{\mathrm{S},i}}{|\boldsymbol{r}_{\mathrm{P}} - \boldsymbol{r}_{\mathrm{S},i}|}
\end{aligned}
$$

Then, the scalar product $t_i = \boldsymbol{b}_i \cdot \boldsymbol{a}_i$ is computed and depending on the value of t_i it can be decided if the projection was successful:

$0 < t_i < l_i$: The projection was successful and the location of F is $\boldsymbol{r}_{\mathrm{F}} = \boldsymbol{r}_{\mathrm{S},i} + t_i\, \boldsymbol{a}_i$. The non-dimensional coordinate along the axis of the interpolation element i is $\xi = t_i/l_i$. This condition is true for node P_1 in Fig. 4.3.

$t_i > l_i$ for $(i = 1...n-1)$: The projection was unsuccessful and F is set to be the last node S_n. The dimensionless coordinate on the axis of interpolation element $n-1$ is consequently $\xi = 1$.

$t_i < 0$ for $(i = 1...n-1)$: The projection was unsuccessful and F is set to be the first node S_1. The dimensionless coordinate on the axis of interpolation element 1 is consequently $\xi = 0$. This condition is true for node P_2 in Fig. 4.3.

$t_{i-1} < 0$ and $t_i > l_i$: The projection was unsuccessful because interpolation elements i and $i-1$ form a convex corner. In that case F is set to be S_i. The dimensionless coordinate on the axis of interpolation element $i-1$ is $\xi = 1$ or alternatively $\xi = 0$ on element i. This condition is true for node P_3 in Fig. 4.3.

$0 < t_{i-1} < l_{i-1}$ and $0 < t_i < l_i$: The projection is ambiguous due to the concave corner formed by interpolation elements i and $i-1$. Either the first encountered solution is used or the solution yielding a point F closest to P is chosen (see Beckert [7]). The dimensionless coordinate on the axis of interpolation element $i-1$ is $\xi = t_{i-1}/l_{i-1}$ or $\xi = t_i/l_i$ on element i. This condition is true for node P_4 in Fig. 4.3.

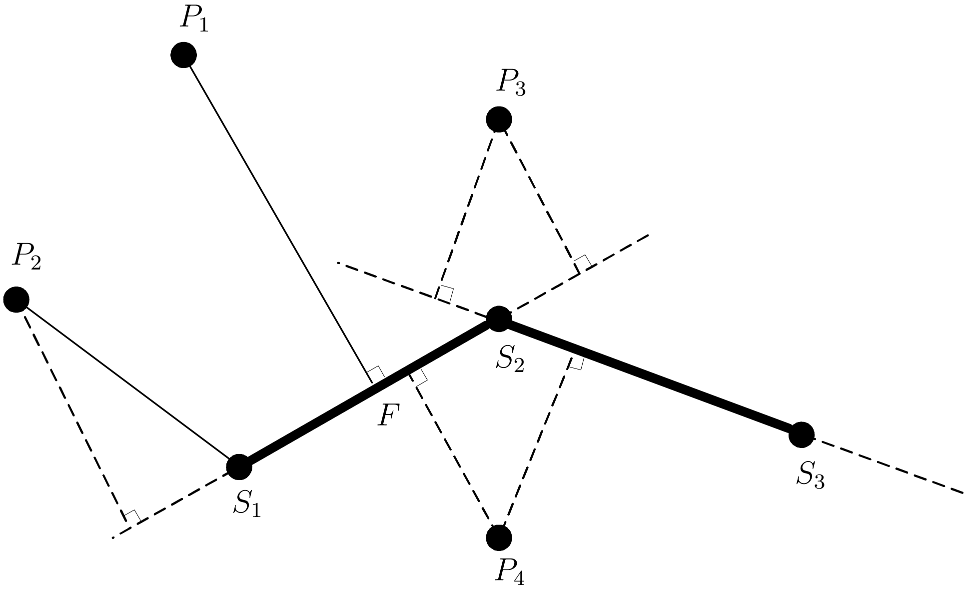

Figure 4.3: Projection of Aerodynamic Nodes onto the Structural Model

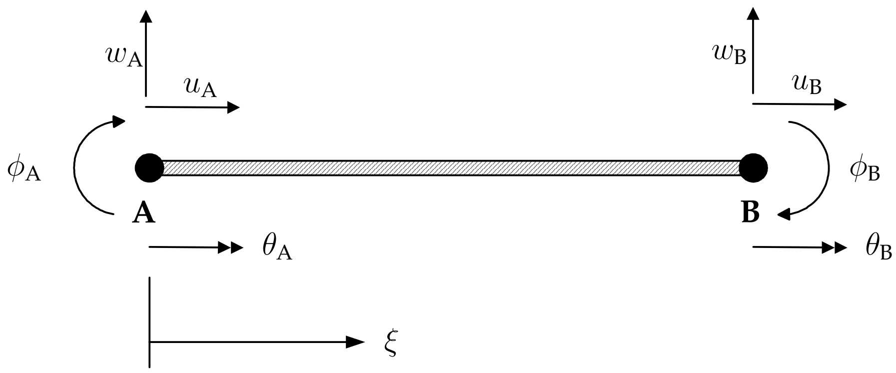

Figure 4.4: Beam Interpolation Element

Beam Interpolation Element

A general discussion of multi-dimensional interpolation elements can be found in the Ph.D. thesis by Beckert [7]. For the problem considered here, only one-dimensional, beam-like interpolation elements, similar to the approach outlined by Preidikman [98], are employed. In Fig. 4.4 a typical plain beam interpolation element is shown. It supports the interpolation of 4 parameters along the connection between node A and node B. The given degrees of freedom at the end points are displacement along the beam axis u, torsional angle about the beam axis θ, lateral displacement w and bending slope ϕ. The values of these freedoms at an arbitrary point between A and B are described by shape functions valid for a Bernoulli beam element with linear torsion and strain behavior. The derivation of these shape functions, also known as Hermite polynomials, can for instance be found in the textbook by Link [80]. Denoting the dimensionless coordinate along the beam as ξ and the length of the beam as l, the shape functions are found to be

$$\begin{array}{rclrcl} u_{u_\mathrm{A}} &=& 1-\xi & u_{u_\mathrm{B}} &=& \xi \\ w_{w_\mathrm{A}} &=& 1-3\,\xi^2+2\,\xi^3 & w_{w_\mathrm{B}} &=& 3\,\xi^2-2\,\xi^3 \\ w_{\phi_\mathrm{A}} &=& (\xi-2\,\xi^2+\xi^3)\,l & w_{\phi_\mathrm{B}} &=& (-\xi^2+\xi^3)\,l \\ \theta_{\theta_\mathrm{A}} &=& 1-\xi & \theta_{\theta_\mathrm{B}} &=& \xi \\ \phi_{w_\mathrm{A}} &=& (-6\,\xi+6\,\xi^2)/l & \phi_{w_\mathrm{B}} &=& (6\,\xi-6\,\xi^2)/l \\ \phi_{\phi_\mathrm{A}} &=& 1-4\,\xi+3\,\xi^2 & \phi_{\phi_\mathrm{B}} &=& -2\,\xi+3\,\xi^2 \end{array} \tag{4.1.1}$$

where for instance u_{u_A} is the shape function for displacement along the beam axis u due to displacement u_A at node A. Adopting matrix notation and introducing the variables v and ψ for lateral displacement and bending slope orthogonal to w and ϕ, we obtain the interpolation function for a three-dimensional beam interpolation element

$$\boldsymbol{u}(\xi) = C_\mathrm{A}(\xi)\,\boldsymbol{u}_\mathrm{A} + C_\mathrm{B}(\xi)\,\boldsymbol{u}_\mathrm{B} \tag{4.1.2}$$

with the interpolated and end point degrees of freedom vectors

$$\boldsymbol{u}(\xi) = \begin{bmatrix} u \\ v \\ w \\ \theta \\ \phi \\ \psi \end{bmatrix}_\xi , \quad \boldsymbol{u}_\mathrm{A} = \begin{bmatrix} u_\mathrm{A} \\ v_\mathrm{A} \\ w_\mathrm{A} \\ \theta_\mathrm{A} \\ \phi_\mathrm{A} \\ \psi_\mathrm{A} \end{bmatrix} , \quad \boldsymbol{u}_\mathrm{B} = \begin{bmatrix} u_\mathrm{B} \\ v_\mathrm{B} \\ w_\mathrm{B} \\ \theta_\mathrm{B} \\ \phi_\mathrm{B} \\ \psi_\mathrm{B} \end{bmatrix} \tag{4.1.3}$$

and the interpolation matrices for the left and right node evaluated at the target coordinate ξ along the beam axis

$$C_\mathrm{A}(\xi) = \begin{bmatrix} u_{u_\mathrm{A}} & 0 & 0 & 0 & 0 & 0 \\ 0 & w_{w_\mathrm{A}} & 0 & 0 & 0 & w_{\phi_\mathrm{A}} \\ 0 & 0 & w_{w_\mathrm{A}} & 0 & -w_{\phi_\mathrm{A}} & 0 \\ 0 & 0 & 0 & \theta_{\theta_\mathrm{A}} & 0 & 0 \\ 0 & 0 & -\phi_{w_\mathrm{A}} & 0 & \phi_{\phi_\mathrm{A}} & 0 \\ 0 & \phi_{w_\mathrm{A}} & 0 & 0 & 0 & \phi_{\phi_\mathrm{A}} \end{bmatrix}_\xi \tag{4.1.4}$$

$$C_\mathrm{B}(\xi) = \begin{bmatrix} u_{u_\mathrm{B}} & 0 & 0 & 0 & 0 & 0 \\ 0 & w_{w_\mathrm{B}} & 0 & 0 & 0 & w_{\phi_\mathrm{B}} \\ 0 & 0 & w_{w_\mathrm{B}} & 0 & -w_{\phi_\mathrm{B}} & 0 \\ 0 & 0 & 0 & \theta_{\theta_\mathrm{B}} & 0 & 0 \\ 0 & 0 & -\phi_{w_\mathrm{B}} & 0 & \phi_{\phi_\mathrm{B}} & 0 \\ 0 & \phi_{w_\mathrm{B}} & 0 & 0 & 0 & \phi_{\phi_\mathrm{B}} \end{bmatrix}_\xi .$$

This relation holds, if $\boldsymbol{u}_\mathrm{A}$ and $\boldsymbol{u}_\mathrm{B}$ are given in a cartesian coordinate system with the origin in point A, x-axis pointing from A to B and the y- and z-axis completing an arbitrarily oriented right hand system. For practical purposes it is more convenient to have the expression in global coordinates. If we denote with T the transformation matrix from the geometry coordinate system, in which nodes A and B are given, to the beam coordinate system, the modified beam interpolation equation with $\boldsymbol{u}_\mathrm{A}$, $\boldsymbol{u}_\mathrm{B}$ and $\boldsymbol{u}(\xi)$ now given in the geometric system becomes

$$\begin{aligned} \boldsymbol{u}(\xi) &= T^\mathrm{T} C_\mathrm{A}(\xi)\, T\, \boldsymbol{u}_\mathrm{A} + T^\mathrm{T} C_\mathrm{B}(\xi)\, T\, \boldsymbol{u}_\mathrm{B} \\ &= \tilde{C}_\mathrm{A}(\xi)\,\boldsymbol{u}_\mathrm{A} + \tilde{C}_\mathrm{B}(\xi)\,\boldsymbol{u}_\mathrm{B} \end{aligned} \tag{4.1.5}$$

The transformation matrix T is found by creating an auxiliary point offset by a fixed distance from the starting point of the interpolation element and using it to set up a right hand system according to the aforementioned convention.

Rigid Connectors

Once the projection point has been determined, the displacement of the aerodynamic node can readily be expressed in terms of the structural nodes. Assuming a rigid connection, the displacement of the aerodynamic node P in terms of the displacement of the projection node F is

$$\boldsymbol{u}_\mathrm{P} = \begin{bmatrix} 1 & 0 & 0 & 0 & r_3 & -r_2 \\ 0 & 1 & 0 & -r_3 & 0 & r_1 \\ 0 & 0 & 1 & r_2 & -r_1 & 0 \\ 0 & 0 & 0 & 1 & 0 & 0 \\ 0 & 0 & 0 & 0 & 1 & 0 \\ 0 & 0 & 0 & 0 & 0 & 1 \end{bmatrix} \boldsymbol{u}_\mathrm{F} = R\, \boldsymbol{u}_\mathrm{F} \tag{4.1.6}$$

with the rigid lever arm vector

$$\boldsymbol{r} = \begin{bmatrix} r_1 \\ r_2 \\ r_3 \end{bmatrix} = \boldsymbol{r}_\mathrm{P} - \boldsymbol{r}_\mathrm{F}.$$

Therefore, by combining Eqs. (4.1.5) and (4.1.6), we obtain the expression for the displacement transfer matrices G_A and G_B, that relate the displacement at the aerodynamic node P to the displacements of the structural nodes A and B forming the relevant interpolation element

$$\begin{aligned} \boldsymbol{u}_\mathrm{P} &= R\left(\tilde{C}_\mathrm{A}(\xi)\, \boldsymbol{u}_\mathrm{A} + \tilde{C}_\mathrm{B}(\xi)\, \boldsymbol{u}_\mathrm{B}\right) \\ &= G_\mathrm{A}(\xi)\, \boldsymbol{u}_\mathrm{A} + G_\mathrm{B}(\xi)\, \boldsymbol{u}_\mathrm{B} \end{aligned} \tag{4.1.7}$$

For a complete aircraft model, all connectivity relations between the structural and aerodynamic grid are sorted into a global interconnection matrix G_Ag such that

$$\boldsymbol{u}_\mathrm{A} = G_\mathrm{Ag} \boldsymbol{u}_\mathrm{g} \tag{4.1.8}$$

and therefore the aerodynamic panel degrees of freedom $\boldsymbol{u}_\mathrm{A}$ can be expressed as a function of the condensed structural model degrees of freedom $\boldsymbol{u}_\mathrm{g}$. In the next section it will be shown that these matrices are also applicable for the problem of load transfer from the aerodynamic grid to the structural nodes.

4.1.2 Principle of Virtual Work

For a given load on the structural nodes $\boldsymbol{P}_\mathrm{A}$ and $\boldsymbol{P}_\mathrm{B}$, the virtual work δW due to an arbitrary displacement of the nodes $\delta \boldsymbol{u}_\mathrm{A}$ and $\delta \boldsymbol{u}_\mathrm{B}$ must be equal to the virtual work performed on the aerodynamic node P by its corresponding load $\boldsymbol{f}_\mathrm{P}$ and virtual displacement $\delta \boldsymbol{u}_\mathrm{P}$ (see for instance Megson [88]):

$$\begin{aligned} \delta(W_\mathrm{A} + W_\mathrm{B}) &= \delta W_\mathrm{P} \\ \delta \boldsymbol{u}_\mathrm{A}^\mathrm{T} \boldsymbol{P}_\mathrm{A} + \delta \boldsymbol{u}_\mathrm{B}^\mathrm{T} \boldsymbol{P}_\mathrm{B} &= \delta \boldsymbol{u}_\mathrm{P}^\mathrm{T} \boldsymbol{P}_\mathrm{P} \end{aligned}$$

Expressing the virtual displacement of the aerodynamic node by the virtual displacement of the structural nodes, we obtain

$$\begin{aligned} \delta \boldsymbol{u}_\mathrm{A}^\mathrm{T} \boldsymbol{P}_\mathrm{A} + \delta \boldsymbol{u}_\mathrm{B}^\mathrm{T} \boldsymbol{P}_\mathrm{B} &= \left(G_\mathrm{A}\, \delta \boldsymbol{u}_\mathrm{A} + G_\mathrm{B}\, \delta \boldsymbol{u}_\mathrm{B}\right)^\mathrm{T} \boldsymbol{P}_\mathrm{P} \\ &= \delta \boldsymbol{u}_\mathrm{A}^\mathrm{T} G_\mathrm{A}^\mathrm{T} \boldsymbol{P}_\mathrm{P} + \delta \boldsymbol{u}_\mathrm{B}^\mathrm{T} G_\mathrm{B}^\mathrm{T} \boldsymbol{P}_\mathrm{P} \end{aligned}$$

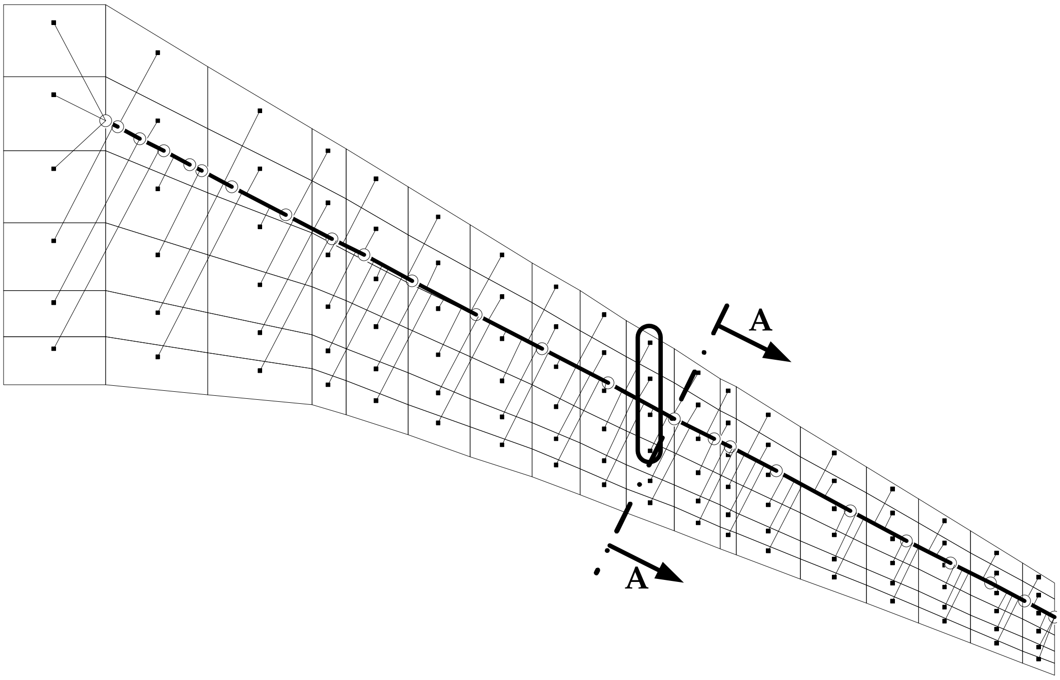

Figure 4.5: Wing Aeroelastic Model

and by comparison of the coefficients

$$\begin{aligned} \boldsymbol{P}_{\mathrm{A}} &= G_{\mathrm{A}}^{\mathrm{T}}\, \boldsymbol{P}_{\mathrm{P}} \\ \boldsymbol{P}_{\mathrm{B}} &= G_{\mathrm{B}}^{\mathrm{T}}\, \boldsymbol{P}_{\mathrm{P}}. \end{aligned} \tag{4.1.9}$$

Therefore, by using the transpose of the displacement transfer matrices G_{A} and G_{B} for the transfer of aerodynamic loads to the structural model, virtual work is conserved across the two domains. For the complete aircraft model, this can be written as

$$\boldsymbol{P}_{\mathrm{g}} = G_{\mathrm{Ag}}^{\mathrm{T}} \boldsymbol{P}_{\mathrm{A}} \tag{4.1.10}$$

This property is particularly important for dynamic aeroelastic analysis where any loss or accumulation of energy due to the coupling method of the models can lead to erroneous stability behavior and hence to false prediction of flutter or limit cycle oscillations.

4.1.3 Numerical Example

To demonstrate and validate the coupling method, the aerodynamic wing model of the wing-tail configuration from Chapter 2 is connected to a reduced order structural model of the wing. In Fig. 4.5, the top view of the resulting *FEMSPLINE*-model is shown with its rigid connectors linking the panel control points to the chain of interpolation elements. Notice that the first three panels of the most inboard and the two last panels of the most outboard aerodynamic strip of panels can not be projected and therefore are connected to the first and last structural node, respectively.

Deformation Transfer

The proper transfer of deformation from the structural model to the aerodynamic model is validated by mapping a generic deformation similar to a fundamental wing bending mode. In the upper part of Fig. 4.6(a), a perspective view of the deformed structural and aerodynamic nodes is given. Comparing vertical translation and twist angle at the structural nodes with the stripwise mean value of the mapped values on the aerodynamic model, excellent agreement is found and plotted in Fig. 4.6(b). The small deviations in twist are due to the streamwise direction used for computing the mean values of the aerodynamic deformation, which is not in line with the orientation of the rigid connectors.

Load Transfer

Using the transpose of the deformation transfer matrix, a uniform unit loading of the aerodynamic grid as depicted in Fig. 4.7(a) is mapped to the structural nodes. The local integrated shear force and torque along the axis formed by the structural nodes are compared in Fig. 4.7(b) and again show excellent agreement. The minor deviations observable in the shear force diagram can be explained as follows. When integrating the shear load for the wing section AA in Fig. 4.5 based on the structural grid point forces, the load will additionally include contributions from the forces applied at the circled aerodynamic control points outside of the intended domain of integration. The forces at these control points are transferred to the structural node on the cut AA via the connected interpolation element and cause a larger integral value compared to the direct integration of the aerodynamic forces. This shows that care must be taken when quantifying structural loads on the basis of mapped external forces because the splining method redistributes the external loading in a statically equivalent way. To obtain the true sectional shear/moment/torque values, the actual external load distribution should be integrated.

4.2 Model Integration

It will now be shown, how the integral aircraft model must be setup depending on the aerodynamic approach chosen. To recap, the flexible aircraft equations of motion are:

Equations of motion:

$$
\begin{array}{rcl}
\begin{array}{r} m\left(\dot{\boldsymbol{V}}_{\mathrm{B}} + \boldsymbol{\omega}_{\mathrm{B}} \times \boldsymbol{V}_{\mathrm{B}} - T_{\mathrm{BG}}(\phi,\theta,\psi)\,\boldsymbol{g}_0\right) \\ J_{\mathrm{B}}\,\dot{\boldsymbol{\omega}}_{\mathrm{B}} + \boldsymbol{\omega}_{\mathrm{B}} \times J_{\mathrm{B}}\,\boldsymbol{\omega}_{\mathrm{B}} \end{array} & = & \boldsymbol{Q}_{\mathrm{RR}} + \boldsymbol{Q}_{\mathrm{RE}} + \boldsymbol{Q}_{\mathrm{RG}} + \boldsymbol{Q}_{\mathrm{Radd}} \\
M_{ee}\ddot{\boldsymbol{\eta}}_e + B_{ee}\dot{\boldsymbol{\eta}}_e + K_{ee}\boldsymbol{\eta}_e & = & \boldsymbol{Q}_{\mathrm{ER}} + \boldsymbol{Q}_{\mathrm{EE}} + \boldsymbol{Q}_{\mathrm{EG}} + \boldsymbol{Q}_{\mathrm{Eadd}} \\
\dot{\boldsymbol{x}}_{\mathrm{A}} - R\boldsymbol{x}_{\mathrm{A}} & = & \boldsymbol{E}_{\mathrm{AR}} + \boldsymbol{E}_{\mathrm{AE}} + \boldsymbol{E}_{\mathrm{AG}}
\end{array}
$$

Attitude and Position:

$$
\begin{array}{rcl}
\dot{\boldsymbol{\Theta}} & = & R_{\mathrm{GB}}(\phi,\theta)\,\boldsymbol{\omega}_{\mathrm{B}} \\
\dot{\boldsymbol{r}}_{\mathrm{G}} & = & T_{\mathrm{BG}}^{\mathrm{T}}(\phi,\theta,\psi)\,\boldsymbol{V}_{\mathrm{B}}
\end{array}
$$

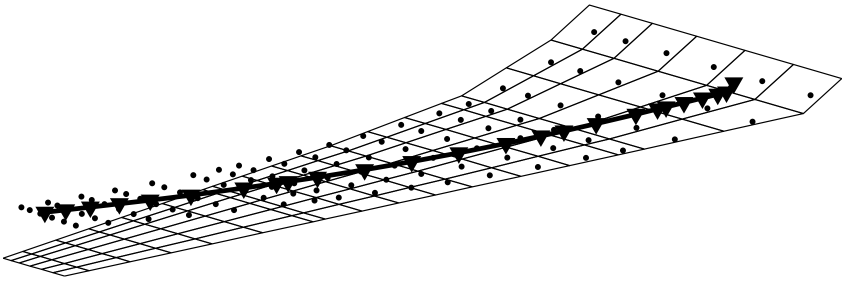

(a) Generic Wing Deformation

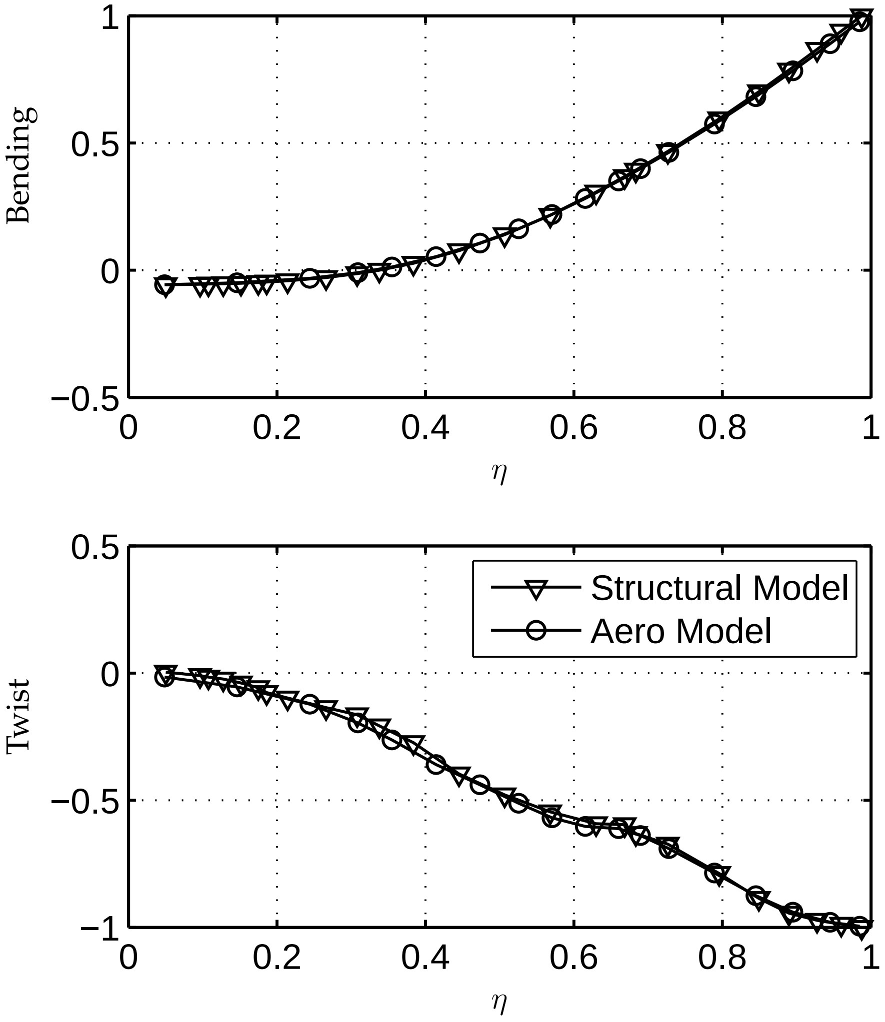

(b) Comparison of Wing Bending and Twist

Figure 4.6: Test Case for Deformation Transfer

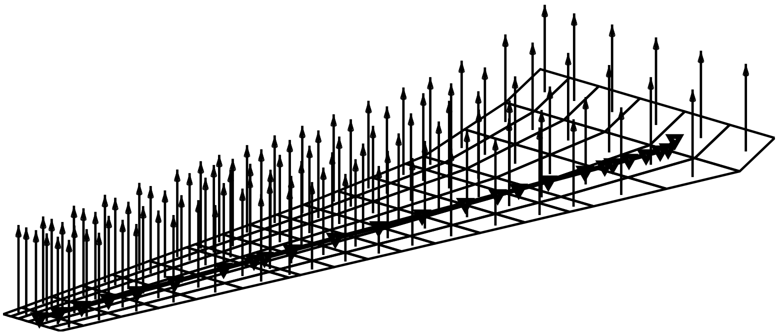

(a) Generic Wing Loading

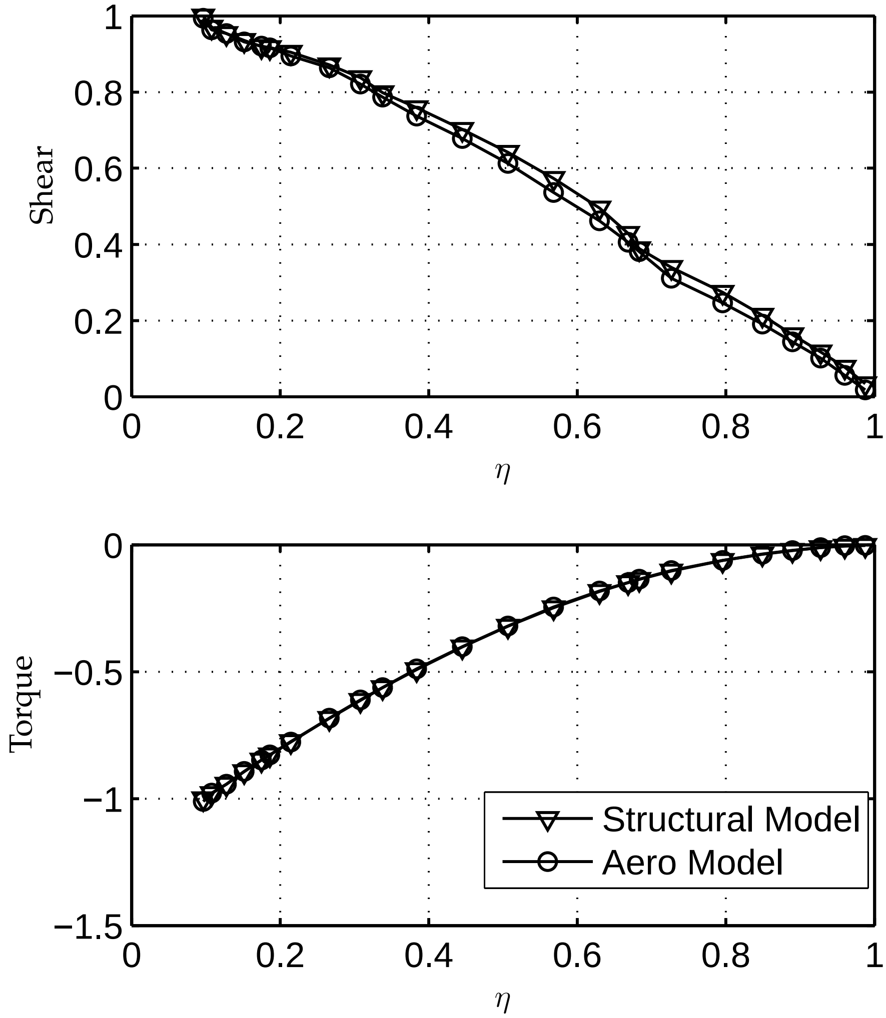

(b) Comparison of Integrated Shear and Torque

Figure 4.7: Test Case for Load Transfer

Without loss of generality, the linear rational function approximation (RFA) notation Eq. (2.2.55) for the unsteady aerodynamic model is used to allow for a more compact notation. The vectors Q_{Ri} and Q_{Ei} are the generalized external applied loads acting on the rigid body and elastic modes, due to rigid body motion, elastic deformation, gust and additional factors (engine thrust, landing gear etc.), respectively. E_{Ai} are the corresponding driving terms of the aerodynamic lag states. Depending on the intended use of the flexible aircraft model, many integration scenarios can be imagined. Three particularly interesting cases are described below.

4.2.1 Model Integration without Quasi-steady Aeroelastic Corrections

In this case, the database provides rigid non-linear aerodynamic loads including unsteady effects for rigid body motion and control surface deflection. The unsteady vortex lattice method (UVLM) model provides in addition to that the aerodynamic loads due to structural deformation and atmospheric gust:

$$\begin{aligned}
\begin{Bmatrix} \boldsymbol{Q}_{\mathrm{RR}} + \boldsymbol{Q}_{RC} \\ \boldsymbol{Q}_{\mathrm{ER}} + \boldsymbol{Q}_{EC} \end{Bmatrix} &= \begin{bmatrix} \Phi_{\mathrm{gR}}^{\mathrm{T}} \\ \Phi_{\mathrm{gE}}^{\mathrm{T}} \end{bmatrix} G_{Ag}^{\mathrm{T}} \boldsymbol{P}_{\mathrm{A}}^{\mathrm{NL(rigid)}} \\
\begin{Bmatrix} \boldsymbol{Q}_{\mathrm{RE}} \\ \boldsymbol{Q}_{\mathrm{EE}} \end{Bmatrix} &= \begin{bmatrix} \Phi_{\mathrm{gR}}^{\mathrm{T}} \\ \Phi_{\mathrm{gE}}^{\mathrm{T}} \end{bmatrix} G_{Ag}^{\mathrm{T}} q_{\infty} \left(A_0 \boldsymbol{\eta}_{\mathrm{E}} + A_1 \dot{\boldsymbol{\eta}}_{\mathrm{E}} + A_2 \ddot{\boldsymbol{\eta}}_{\mathrm{E}} + A_{1\mathrm{G}} \boldsymbol{u}_{\mathrm{G}} + A_{2\mathrm{G}} \dot{\boldsymbol{u}}_{\mathrm{G}} + D \boldsymbol{x}_{\mathrm{A}} \right) \\
\boldsymbol{E}_{\mathrm{AE}} &= E_1 \dot{\boldsymbol{\eta}}_{\mathrm{E}} + E_2 \ddot{\boldsymbol{\eta}}_{\mathrm{E}} \\
\boldsymbol{E}_{\mathrm{AG}} &= E_{2\mathrm{G}} \dot{\boldsymbol{u}}_{\mathrm{G}}
\end{aligned}$$

Because no unsteady rigid body aerodynamics need to be computed, the aerodynamic lag states are only driven by gust and elasticity and therefore $E_{\mathrm{AR}} = 0$.

4.2.2 Model Integration with Quasi-steady Aeroelastic Corrections

In this case, the database provides rigid non-linear aerodynamic data including unsteady effects for rigid body motion and control surface deflection, that have been corrected for quasi-steady aeroelastic effects. The unsteady vortex lattice model therefore must only provide the aerodynamic data for unsteady incremental elastic effects (residual model method (RMM)).

$$\begin{aligned}
\begin{Bmatrix} \boldsymbol{Q}_{\mathrm{RR}} + \boldsymbol{Q}_{RC} \\ \boldsymbol{Q}_{\mathrm{ER}} + \boldsymbol{Q}_{EC} \end{Bmatrix} &= \begin{bmatrix} \Phi_{\mathrm{gR}}^{\mathrm{T}} \\ \Phi_{\mathrm{gE}}^{\mathrm{T}} \end{bmatrix} G_{Ag}^{\mathrm{T}} \boldsymbol{P}_{\mathrm{A}}^{\mathrm{NL(qflex)}} \\
\begin{Bmatrix} \boldsymbol{Q}_{\mathrm{RE}} \\ \boldsymbol{Q}_{\mathrm{EE}} \end{Bmatrix} &= \begin{bmatrix} \Phi_{\mathrm{gR}}^{\mathrm{T}} \\ \Phi_{\mathrm{gE}}^{\mathrm{T}} \end{bmatrix} G_{Ag}^{\mathrm{T}} q_{\infty} \left(A_0 (\boldsymbol{\eta}_{\mathrm{E}} - \boldsymbol{\eta}_{\mathrm{E0}}) + A_1 \dot{\boldsymbol{\eta}}_{\mathrm{E}} + A_2 \ddot{\boldsymbol{\eta}}_{\mathrm{E}} + A_{1\mathrm{G}} \boldsymbol{u}_{\mathrm{G}} + A_{2\mathrm{G}} \dot{\boldsymbol{u}}_{\mathrm{G}} + D \boldsymbol{x}_{\mathrm{A}} \right) \\
\boldsymbol{E}_{\mathrm{AE}} &= E_1 \dot{\boldsymbol{\eta}}_{\mathrm{E}} + E_2 \ddot{\boldsymbol{\eta}}_{\mathrm{E}} \\
\boldsymbol{E}_{\mathrm{AG}} &= E_{2\mathrm{G}} \dot{\boldsymbol{u}}_{\mathrm{G}} \\
\text{with} & \\
\boldsymbol{\eta}_{\mathrm{E0}} &= K_{\mathrm{EE}}^{-1} \left(\boldsymbol{Q}_{\mathrm{ER}} + \boldsymbol{Q}_{EC} + \boldsymbol{Q}_{\mathrm{Eadd}} \right)
\end{aligned}$$

Again, notice that only lag states driven by the elastic modes and gust need to be taken into account. If the quasi-steady corrections do not include external force effects from e.g. thrust or landing gears, the term $\boldsymbol{Q}_{\mathrm{Eadd}}$ must be omitted from the computation of the quasi-steady deflection $\boldsymbol{\eta}_{\mathrm{E0}}$.

4.2.3 Model Integration with Dynamic Incremental Gust

In this case, the database provides the rigid non-linear aerodynamic loads including unsteady effects for rigid body motion and control surface deflection, corrected for static aeroelastic effects. Assuming that these forces do not excite significant structural vibrations, the unsteady vortex lattice model must only provide the aerodynamic data for the gust effect and the unsteady elastic deformation excited by it and therefore $\boldsymbol{Q}_{\mathrm{ER}} = \boldsymbol{Q}_{EC} = E_{\mathrm{AR}} = 0$.

$$\begin{aligned}
\boldsymbol{Q}_{\mathrm{RR}} + \boldsymbol{Q}_{RC} &= \Phi_{\mathrm{gR}}^{\mathrm{T}} G_{Ag}^{\mathrm{T}} \boldsymbol{P}_{\mathrm{A}}^{\mathrm{NL(qflex)}} \\
\begin{Bmatrix} \boldsymbol{Q}_{\mathrm{RE}} \\ \boldsymbol{Q}_{\mathrm{EE}} \end{Bmatrix} &= \begin{bmatrix} \Phi_{\mathrm{gR}}^{\mathrm{T}} \\ \Phi_{\mathrm{gE}}^{\mathrm{T}} \end{bmatrix} G_{Ag}^{\mathrm{T}} q_{\infty} \left(A_0 \boldsymbol{\eta}_{\mathrm{E}} + A_1 \dot{\boldsymbol{\eta}}_{\mathrm{E}} + A_2 \ddot{\boldsymbol{\eta}}_{\mathrm{E}} + A_{1\mathrm{G}} \boldsymbol{u}_{\mathrm{G}} + A_{2\mathrm{G}} \dot{\boldsymbol{u}}_{\mathrm{G}} + D \boldsymbol{x}_{\mathrm{A}} \right) \\
\boldsymbol{E}_{\mathrm{AE}} &= E_1 \dot{\boldsymbol{\eta}}_{\mathrm{E}} + E_2 \ddot{\boldsymbol{\eta}}_{\mathrm{E}} \\
\boldsymbol{E}_{\mathrm{AG}} &= E_{2\mathrm{G}} \dot{\boldsymbol{u}}_{\mathrm{G}}
\end{aligned}$$

The application of this type of model will be demonstrated in the following chapter, where the wake vortex encounter of a transport aircraft is studied.

5 Application to Wake Vortex Encounter

Wake vortex sheets created by large transport aircraft can become hazardous for other (lighter) aircraft following or traversing the flight path of the wake generating airplane. As sketched in Fig. 5.1, which has been reproduced according to [42], the follower aircraft can experience high structural loads when laterally traversing the pair of rolled up wake turbulence. In case of a more trailing flight path, the reaction on the aircraft can be a loss of altitude or rate of climb if the follower aircraft is flying between the tip vortices or an imposed rolling moment in case the flight path lies closer to one of the vortex cores. It is likely that a wake vortex encounter would cause the pilot to take corrective action and compensate for the disturbances of the flight path the aircraft experiences. In a less critical scenario, this could for instance lead to a go-around during final approach and consequently to a disruption to smooth airport operations and delays in the flight plan. With ever-growing air traffic it is therefore of vital economic interest to minimize the probability of wake vortex encounters, both from the perspective of an airport operator and a passengers' satisfaction minded airline. However, in the crash of American Airlines flight AA587 in the year 2001, wake vortex turbulence of a leading Boeing 747 and subsequent excessive control input of the pilot of the following Airbus A300 were deemed to be the root causes of the in-air structural disintegration of the Airbus and tragically recalled the flight safety aspects of wake vortex encounters [95].

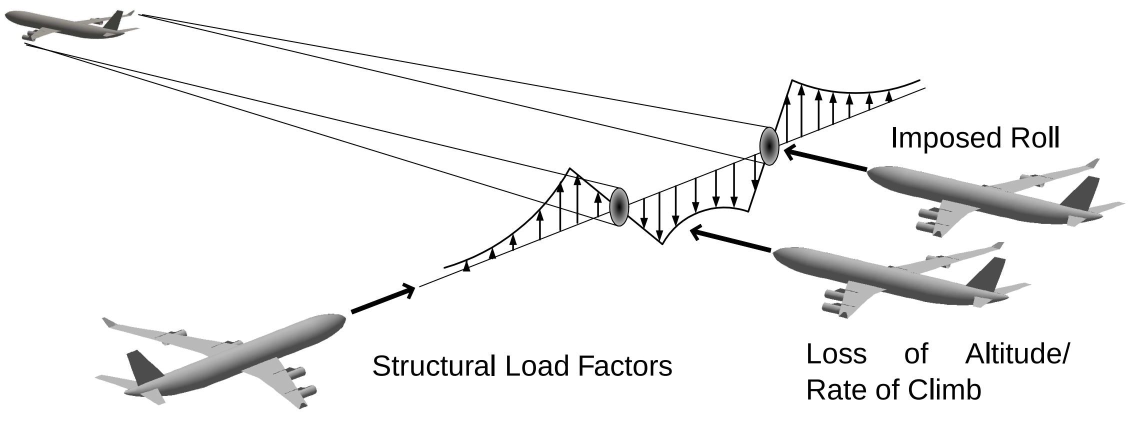

Figure 5.1: Hazards of Wake Vortex Encounters (according to [42])

To minimize the likelihood of an aircraft encountering significant wake turbulence, the air transport safety authorities have established separation minima in the approach and departure phase as a function of the weight categories of the leading and following aircraft. As shown in Fig. 5.2 which has been prepared on the basis of [20], the spacing can become as large as 8 Nautical Miles in the case of a light category aircraft (MTOW < 7 tons) following the super category Airbus A380-800 aircraft (MTOW > 560 tons). The separation is established to give the wake turbulence time to sink down and dissipate. This dissipation process is characterized by several phases, during which the pair of concentrated tip vortices experiences a sequence of instabilities (the first of which is the famous Crow instability [23]) and eventually forms a chain of decaying vortex rings as illustrated in Fig. 5.3.

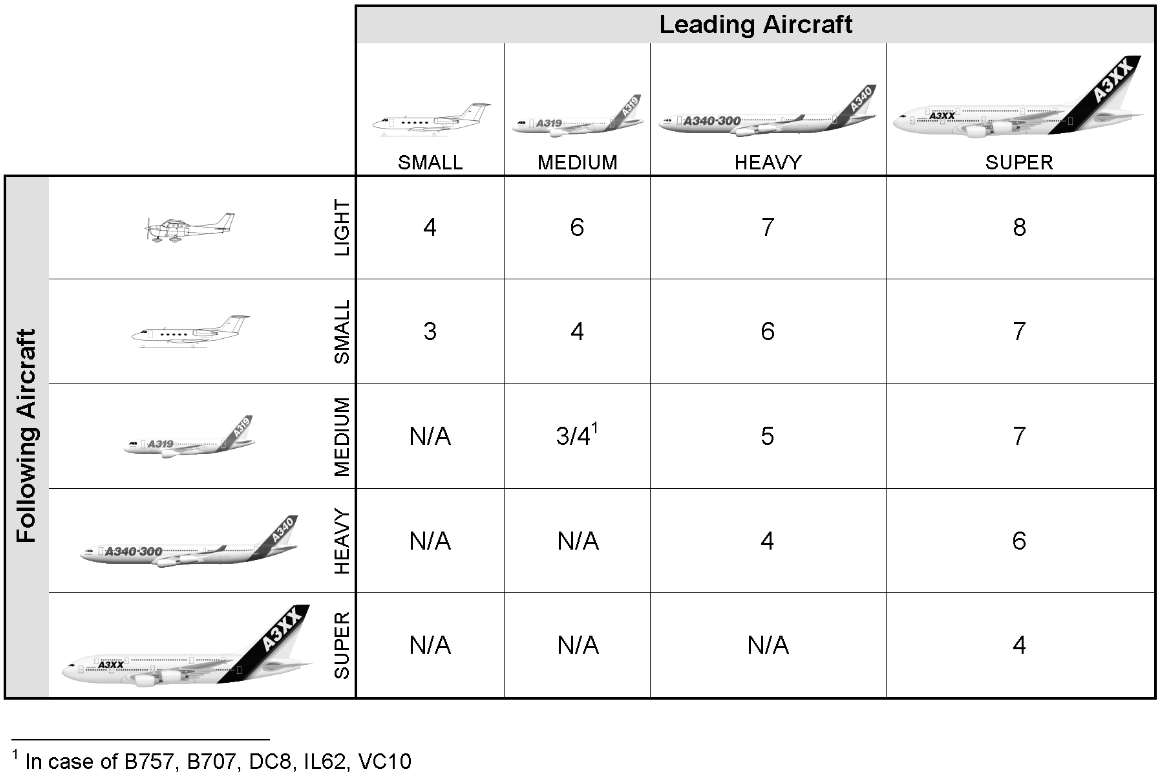

Following Aircraft	Leading Aircraft: SMALL	MEDIUM	HEAVY	SUPER
LIGHT	4	6	7	8
SMALL	3	4	6	7
MEDIUM	N/A	3/4[1]	5	7
HEAVY	N/A	N/A	4	6
SUPER	N/A	N/A	N/A	4

[1] In case of B757, B707, DC8, IL62, VC10

Figure 5.2: CAA Wake Turbulence Separation Minima in Nautical Miles – Final Approach [20]

In this chapter, the flexible aircraft modeling approach as outlined in the previous sections is applied to the flight loads analysis of a wake vortex encounter. The first objective is to quantify the resulting structural loads on a heavy category aircraft encountering wake turbulence of an Airbus A380-800. Second, the influence of the chosen aircraft modelling technique on the structural loads level is analyzed.

5.1 Wake Vortex Model

To study the basic characteristics of flight loads during a wake vortex encounter, a simple two dimensional analytical model of the wake vortex pair is chosen. An exact solution of the Navier-Stokes equation for laminar flow is the *Lamb-Oseen* vortex whose induced tangential velocity field can be described by

$$V_\theta(r,t) = \frac{\Gamma}{2\pi r}\left(1 - \mathrm{e}^{-\left(\frac{r}{r_c(t)}\right)^2}\right) \tag{5.1.1}$$

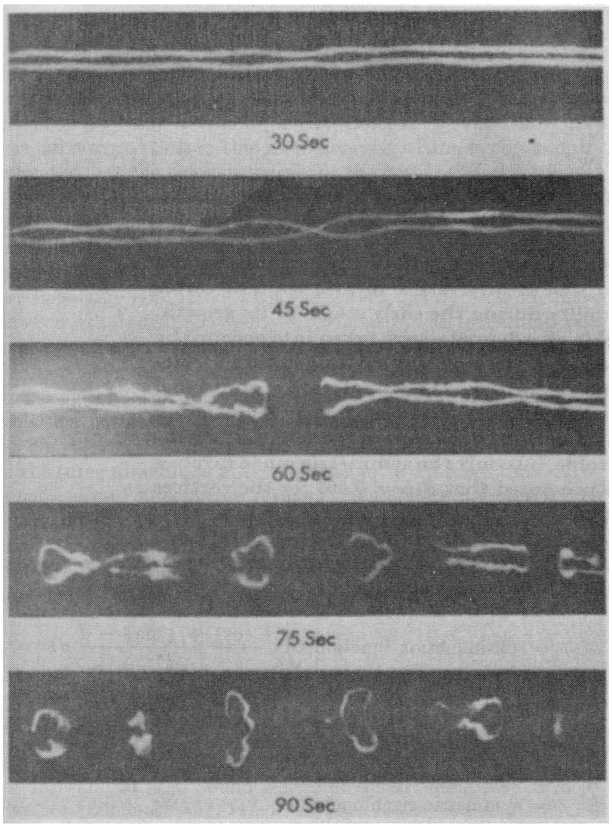

Figure 5.3: Phases of Wake Vortex Decay (from [23])

with Γ being the vortex circulation, r the distance of the sensing point to the vortex core, r_c is the vortex core radius and t is the time elapsed since the creation of the vortex. The *Lamb-Oseen* vortex differs from the potential vortex in that it exhibits a continuous, non-singular velocity profile for $t > 0$ and describes the dissipation of vorticity due to viscous effects. Inclusion of an additional vorticity aging effect and an improved vortex core radius model leads to the final expression used by Kloidt [69]:

$$V_\theta(r,t) = \frac{\Gamma_0}{2\pi r}\left(1 - \mathrm{e}^{-1.2564 \frac{r^2 \cos^2(\varphi_{25})}{1310\,\nu t}}\right) \tag{5.1.2}$$

where Γ_0 is the vortex circulation at the moment of generation, ν is the kinematic viscosity of air and φ_{25} is the sweep angle of the quarter chord line of the generator wing. This simple model has the following limitations

- the wake is space fixed and disturbance and deformation of the wake vortex pair by the encountering aircraft are neglected
- the wake topology is fixed and decay mechanisms as the *Crow* instability are neglected
- the wake age is constant along its length, i.e. Eq. (5.1.2) is applied along the vortex length for given $t = const.$

To determine the vortex strength, the *Kutta-Jukowski* theorem for vortex lift is applied to the balance of forces on the generator aircraft

$$\Gamma_0 = \frac{n_z W}{\rho V s b} \tag{5.1.3}$$

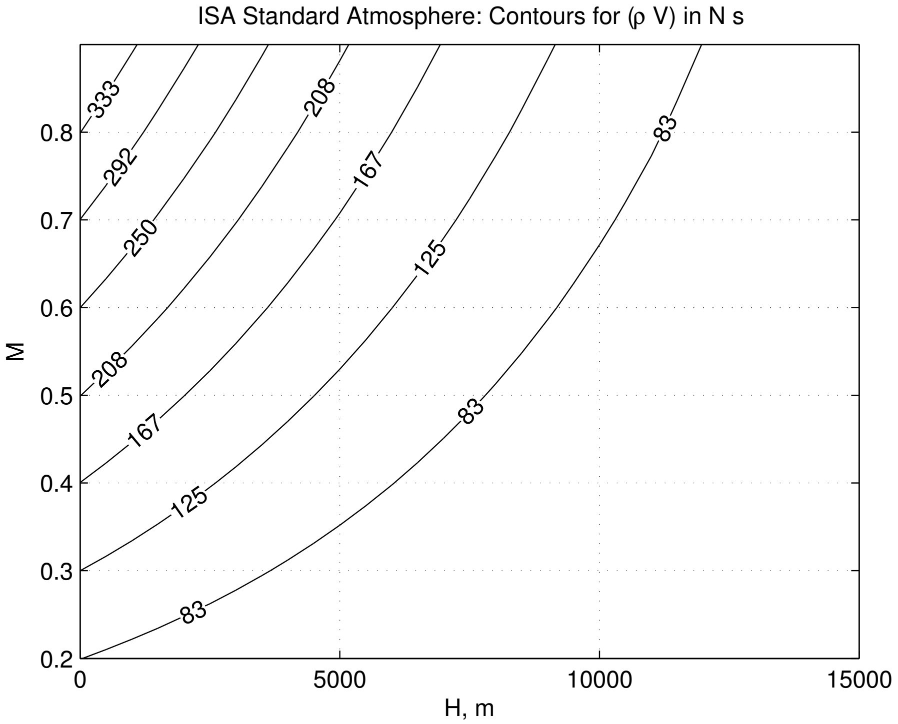

Figure 5.4: Contour Lines of Equal Wake Vortex Strength

with the load factor n_z, the aircraft weight W, air density ρ, flight speed V and effective lifting span sb. For wings with elliptical load distribution, the factor s assumes the value $\pi/4$ [10]. For fixed load factor, aircraft mass and span, Fig. 5.4 shows contour lines of equal vortex strength (or constant product ρV) as a function of flight altitude and Mach number based on the standard ISA atmosphere model. It can be inferred that an aircraft flying landing at typical $M = 0.2$ at sea level generates a wake vortex of equal circulatory strength as if cruising with $M = 0.68$ at 10000 meters altitude. Because the flight speed of a wake vortex encountering aircraft will be much slower at sea level (during take-off and approach) than at altitude (during cruise), the additional angle of attack caused by the wake vortex as the ratio of vortex induced velocity to flight speed will be higher at sea level. At the same time, the dynamic pressure will be much lower at sea level. The resulting proportionality for the forces experienced by an encountering aircraft can be derived as follows

$$F \propto \rho V^2 \alpha_{\text{ind}} \propto \rho V^2 \frac{V_{\text{ind}}}{V} \propto \rho V^2 \frac{\Gamma}{V} \propto \rho V^2 \frac{1}{\rho V^2} \approx const.$$

and suggests that if aerodynamic non-linearities and Mach number effects are neglected, an encounter at low Mach numbers at sea level is of comparable flight loads relevance as an encounter at cruising altitude.

5.2 Aircraft Models

Aircraft data required for the modeling of the wake generator, a super category Airbus A380-800, and the follower aircraft, a heavy category Airbus A340-300, can be found in Appendix C. The planforms or the two aircraft are compared in Fig. C.1.

The core model for the follower aircraft is the one typically used in the determination of maneuver flight loads: a rigid body moving with 6 degrees of freedom combined with a distributed mass and quasi-steady aerodynamic model corrected by static aeroelastic factors and increments. Several types of additional incremental models for the wake vortex effect are investigated to determine the influence of aerodynamic and structural modelling on the flight loads level derived from the wake vortex encounter. The list of chosen modelling options can be found in table 5.1. For aerodynamics, either steady or unsteady formulations of the vortex lattice method are applied. The structural behavior can be either rigid, quasi-flexible or fully dynamic. The reasoning for including unsteady aerodynamic and dynamic structural behavior, typically not considered for wake vortex encounters, can be derived from the induced velocity profile of a pair of *Lamb-Oseen* vortices. In the upper part of Fig. 5.5, the induced vertical velocity in a plane perpendicular to both vortices is plotted over the transverse non-dimensional coordinate x/c_{ref}. The strength and distance of the vortices correspond to the wake of a super category aircraft during approach at sea level. Velocity profiles are given for several points in time and diffusion of the vortex cores can be observed according to Eq. (5.1.2). Assuming an encounter speed V, the transverse coordinate can be interpreted as non-dimensional time and a Fast Fourier Analysis (FFT) of the velocity profiles as a function of reduced frequency $k = \omega c_{\text{ref}}/V$ can be used to compute the power spectral density (PSD) of the velocity field. The lower part of Fig. 5.5 compares the resulting PSDs to the spectra resulting from two sine-shaped velocity bursts fitted to the *Lamb-Oseen* field at $t = 84s$ and a harmonic velocity field of equal wave length. The harmonic velocity field exhibits the highest power spectral density confined to a narrow frequency band. The other spectra have a more broadband character and compared to the two sine-shaped bursts, the *Lamb-Oseen* vortices covers a wider range of frequencies that narrows with increasing diffusion of the vortex cores. From this comparison it is concluded that the *Lamb-Oseen* vortex pair is of comparable turbulent significance as a harmonic or discrete gust and therefore could be investigated with an unsteady, fully dynamic model as required for gust by the Airworthiness Authorities[1].

Model	Aerodynamics		Structure		
	Steady	Unsteady	Rigid	Quasi-Flex	Dynamic
1	×		×		
2	×			×	
3	×				×
4		×			×

Table 5.1: Incremental Aircraft Models

5.3 Loads Model

Integrated shear loads, bending and torsional moments are computed at monitor stations on all important aircraft components shown in Fig. 5.6. The direction of integration on all components is towards the wing center box, e.g. running from the aircraft nose towards the wing-fuselage joint and in the opposite direction coming from the empennage. The orientation of the loads coordinate systems on the left hand and right hand components has been chosen to ensure same sign for the bending and torsional

---

[1] see for instance CS 25 Subpart C - Structure § 25.341

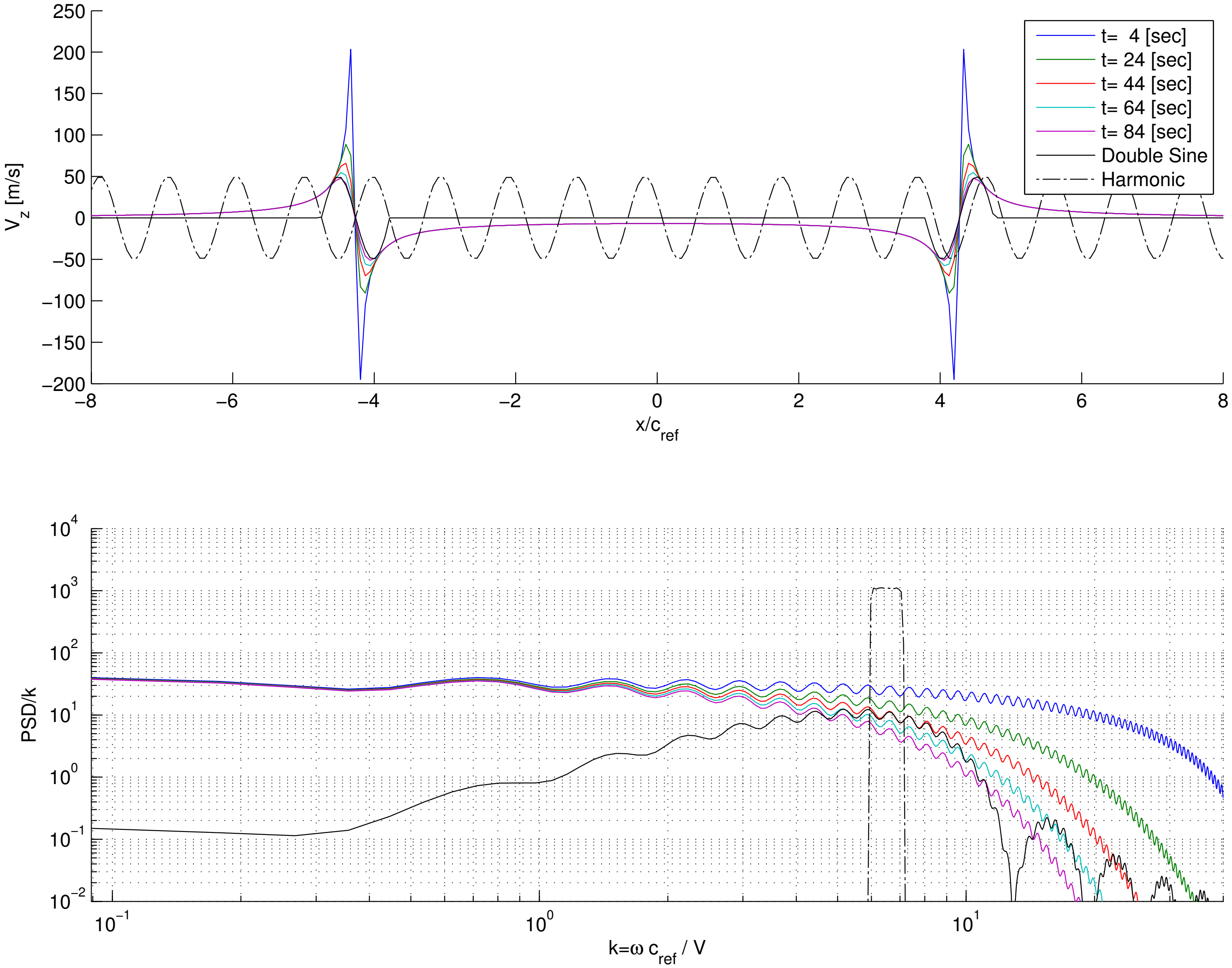

Figure 5.5: Velocity Spectra of a Pair of Lamb-Oseen Vortices

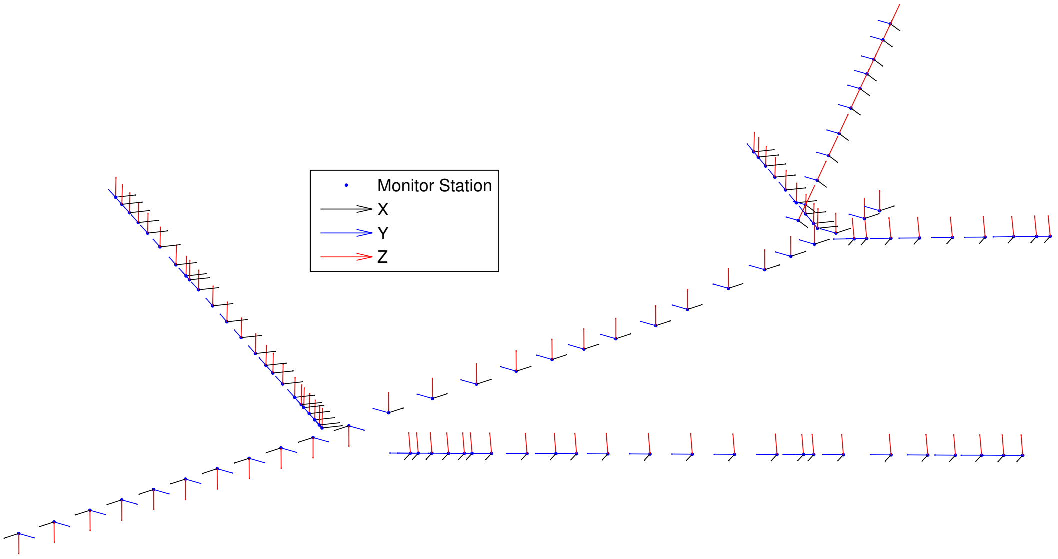

Figure 5.6: Load Monitor Stations and Coordinate Systems

moment in case of up bending of the respective component. Loads transfer from one component to the next is conducted in one step, i.e. no attachment definitions to redistribute the load over a wider area on the adjacent component are considered. Loads are computed according to the force summation method Eq. (3.4.3).

The assessment of loads levels is typically carried out by considering both envelopes of single load quantities over an entire aircraft component (*1D-envelopes*) and envelopes of pairs of load quantities at one monitor station of an aircraft component (*2D-envelopes*). The latter one is more relevant because structural design must be based on the extreme values of simultaneous multi-axial loading, for instance torque and bending moment.

5.4 Simplified Autopilot

In order to assess the effect of pilot input during the wake vortex encounter, simple feedback control loops for longitudinal and lateral aircraft motion were designed. Starting from the linearized flight mechanical model without structural dynamic degrees of freedom as outlined in Chapter 3.5, state space models with output feedback are formulated

$$\begin{aligned} \dot{\boldsymbol{x}} &= A\boldsymbol{x} + B\boldsymbol{u} \\ \boldsymbol{y} &= C\boldsymbol{x} \\ \boldsymbol{u} &= -K\boldsymbol{y} \end{aligned} \tag{5.4.1}$$

and a linear-quadratic-regulator (LQR) design process is applied to determine the feedback gain matrix K. Details of this time domain method can be found in any modern control theory textbook as for instance the one by Stevens and Lewis [115]. No particular effort was invested in the optimization of the feedback matrices as this aspect is an area of research for itself, see for instance the wake vortex controller design by

Kloidt [69] or the wake vortex encounter pilot model developed by Höhne et al. [54]. The use of LQR design in conjunction with a control surface actuator model featuring time delay, rate and travel limitation was still expected to give a relevant tendency in terms of flight loads.

5.5 Definition of Encounter

As introduced at the beginning of this chapter, the spatial attitude of the wake vortex pair relative to the flight path of the encountering aircraft is of great of importance to the classification of the wake vortex encounter. To describe the position of the wake vortex pair, four parameters have been chosen as illustrated in Fig.5.7. The first parameter is the lateral distance d_V of the center of gravity of the encountering aircraft to the flight path of the wake generating aircraft. The second parameter is the vertical offset Δz_V of the wake reference point relative to the flight path of the encountering aircraft. Two angular parameters, heading Ψ_V and flight path γ_V, describe the rotation of the vortex pair relative to the flight path of the encountering aircraft. The wake reference point location was computed under the constraint that at the start of the simulation $d_V = 250m$ was ensured, a value where the wake vortex is not significantly affecting the encountering aircraft yet. The other parameters were varied over the ranges tabulated in Tab. 5.2. They describe a pass-by below, directly through and above the wake vortex pair, with flight directions leading to both symmetric and asymmetric encounters with the wake of a climbing, descending and level flying aircraft.

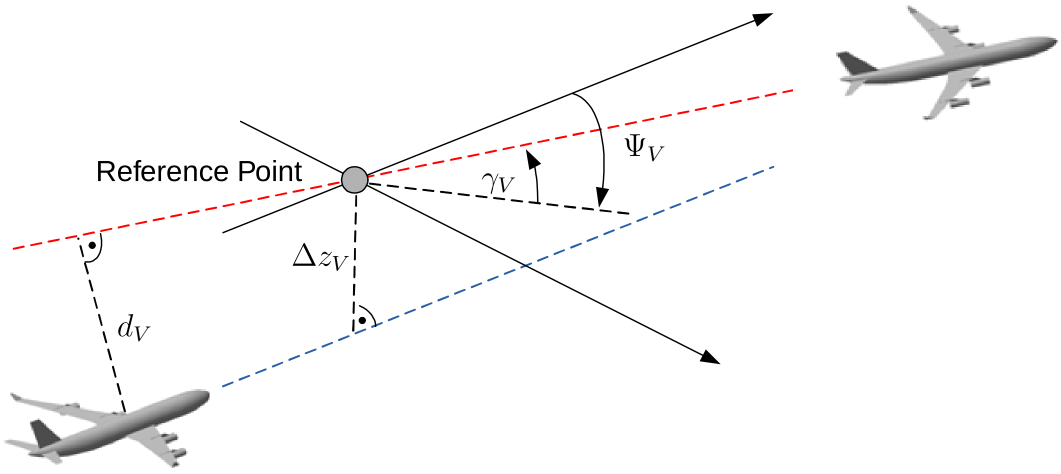

Figure 5.7: Parameters for Wake Vortex Encounter

Ψ_V [°]	30	40	50	60	70	80	90
γ_V [°]	-5	0	5				
Δz_V [m]	-5	0	5				

Table 5.2: Parameter Ranges for Wake Vortex Encounter

5.6 Simulation and Data Processing

The models as outlined here and in the previous chapters are implemented in the scientific computing environment MATLAB$^{\text{TM}}$& SIMULINK$^{\text{TM}}$. To determine the initial conditions for the time integration, trim solutions for level flight are computed using the freeware *TrimMod* toolbox by Buchholz [14] and subsequently a state space description of the model is obtained by linearization about the equilibrium point. The integration of the equations of motion is performed using the *Dormant-Prince*-method with adaptive stepsize, a member of the *Runge-Kutta*-family of solvers for ordinary differential equations.

The use of the unsteady vortex lattice method as outlined in Section 2.2 in conjunction with a prescribed wake model leads to a discrete time representation with variable time step size. It is the fixed spatial wake discretization Δx that in combination with changing flight speed V leads to the variable time step $\Delta t = \Delta x / V$ at which SIMULINK$^{\text{TM}}$ will automatically update the output of the UVLM model.

5.7 Results and Discussion

5.7.1 Anatomy of the Symmetrical and Asymmetrical Encounter

To develop an understanding of the sequence of loads acting on the aircraft during pass-through of a wake vortex pair, time histories of the incremental total aircraft aerodynamic forces and moments are examined for both symmetric and asymmetric encounters. In Fig. 5.8, the lift coefficient C_L and pitching moment coefficient C_M are plotted versus simulation time t. The time traces were obtained from a simulation with *Model 1* at Mach $M = 0.3$, altitude $h = 0$ and encounter parameters $\Psi_V = 90°$, $\gamma_V = 0°$ and $\Delta z_V = 0$. Looking at the fixed path trajectory, the aircraft experiences increasing positive lift and negligible pitching moment when approaching the first wake vortex. Lift reaches its first maximum when the wing root crosses the first vortex core and then steeply drops to negative lift until the wing tip also crosses the first core. During penetration of the first vortex, the aircraft experiences an increasing nose down pitching moment reaching a minimum at the point when the center of gravity of the aircraft passes the first vortex core. It follows a steep increase in pitching moment with a nose up maximum when the wing tip crosses the first vortex core. While the horizontal tail plane is approaching the first vortex core, the negative lift is decreasing and the pitching moment changes to a nose down direction. Vortex-traversal of the horizontal tail plane increases the negative lift and leads to strong maximum in pitch-up moment. Lift continues to decrease when the wing starts traversing the second vortex core, accompanied by a rise of the nose-up pitching moment. The absolute maximum of nose-up pitching moment is reached when the center of gravity passes the second vortex. At about the same time, lift is steeply jumping from negative to positive values. After the wing has crossed the second vortex, lift is dropping to small negative values until the traversal of the horizontal tail causes a brief increase. The pitching moment drops to zero during the traversal of the wing, then again rises until the tail plane traversal causes a steep nose down effect, eventually followed by a decay of the vortex induced effect.

Time traces for an asymmetric encounter with parameter $\Psi_V = 30°$ are shown in Fig. 5.9. In addition to the coefficients presented for the symmetric encounter, also

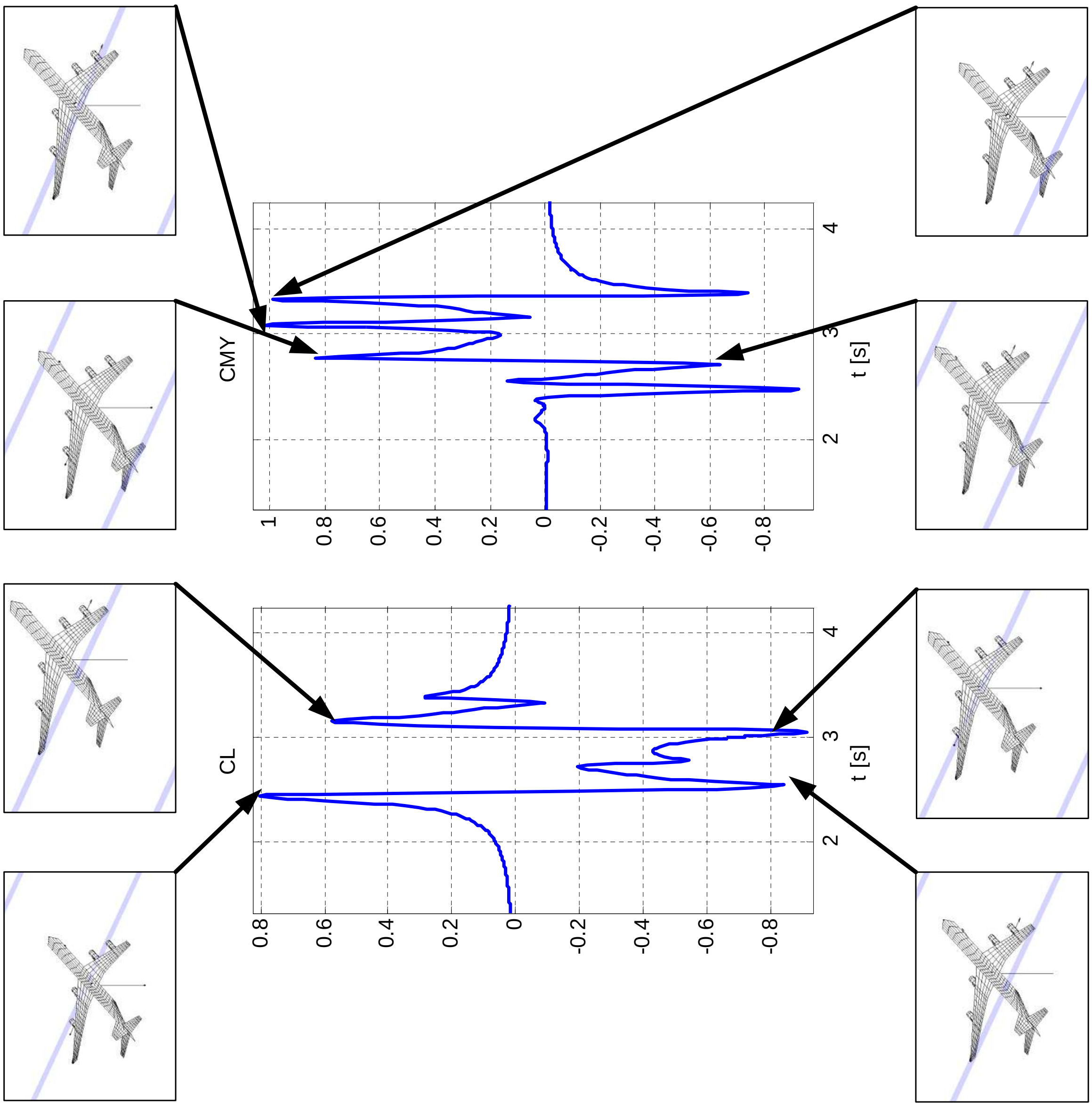

Figure 5.8: Total Aircraft Incremental Aerodynamic Forces during Symmetrical Encounter

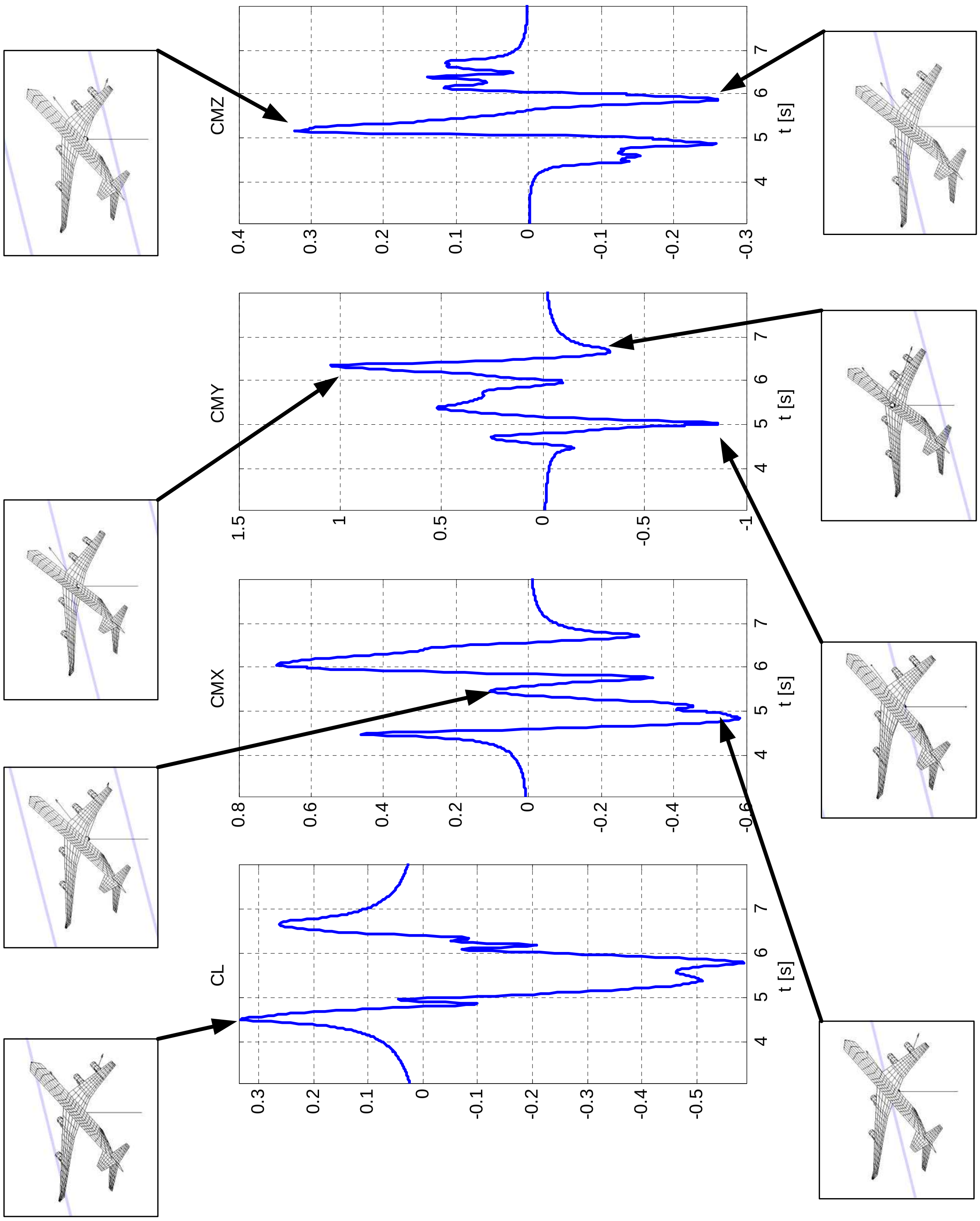

Figure 5.9: Total Aircraft Incremental Aerodynamic Forces during Asymmetrical Encounter

rolling moment C_l and yawing moment coefficient C_n are plotted versus simulation time t. Here the lift experienced by the aircraft is significantly smaller than in the symmetric case (around 30-60%) whereas pitching moment is of comparable magnitude. Rolling and yawing moments are 30-60% smaller than the pitching moment. Rolling and yawing moment both exhibit strong doublets with a peak to peak amplitude between 0.6 and 1.1 attained in less than 0.5 seconds.

5.7.2 Influence of Encounter Type on Flight Loads

In a first step, the sensitivity of component integrated loads and translational acceleration to the type of encounter is studied. Single-quantity loads envelopes for all 63 combinations of parameters given in Tab. 5.2 are computed with *Model 1* at Mach $M = 0.3$ and altitude $h = 0$. Both, simulations with autopilot switched on and off are considered. The lead time for the vortex decay is set to 120 seconds, corresponding to a separation distance of roughly 5 nautical miles, a value below the recommended minimum spacing of 6 nautical miles given in Fig. 5.2. The time histories of shear, moment and torque over the entire aircraft are then processed to obtain ensemble maximum and minimum values at each monitor station together with the corresponding encounter type and simulation time. The results for open loop and closed loop simulations can be found in tables D.1-D.18 in Appendix D.1. For the axis convention of the loads quantities, the reader is referred to Fig. 5.6.

Inspection of the tables reveals that no uniquely critical encounter for all load quantities on all aircraft components can be determined. Instead, the wing and the front vertical fuselage are for example most stressed during encounters with high azimuth angle Ψ_V whereas the most severe loads on horizontal and vertical tail and lateral fuselage can be found for low Ψ_V. Maximum wing shear and bending moment are found for a not inclined wake ($\theta_V = 0°$), whereas on the other components a tilted wake is more significant. Direct pass through of the wake with $\Delta z_V = 0$ generates the highest loads on all components except on the vertical tail where flying under the wake puts the surface closer to the concentrated vorticity. Use of the autopilot which forces the aircraft to pursue its undisturbed flight path has a different effect depending on the component. On the wing, the overall loads bandwidth is shifted to more negative values, e.g. the maximum values are decreased and the minimum values become more negative, in particular at the outer wing due to aileron deflection. On the horizontal tail, the autopilot increases the loads bandwidth due to the strong elevator commands in both directions. On the vertical tail, use of the rudder lowers the maximum torque values significantly and the minimum values are bigger in magnitude. On the rear fuselage, the loads are consistently larger in magnitude due to the autopilot.

In tables D.19-D.28 of Appendix D.2, envelope values for maximum and minimum translational acceleration are presented. These quantities are of interest for the installation of equipment and on the fuselage can also serve as an indication of passenger strain during the wake vortex encounter.

Two dimensional envelopes of shear and bending moment plotted against torque, respectively, can be found in Figs. 5.11 and 5.12 and illustrate the influence of azimuth angle Ψ_V on the combination of loads while wake elevation and offset are kept zero.

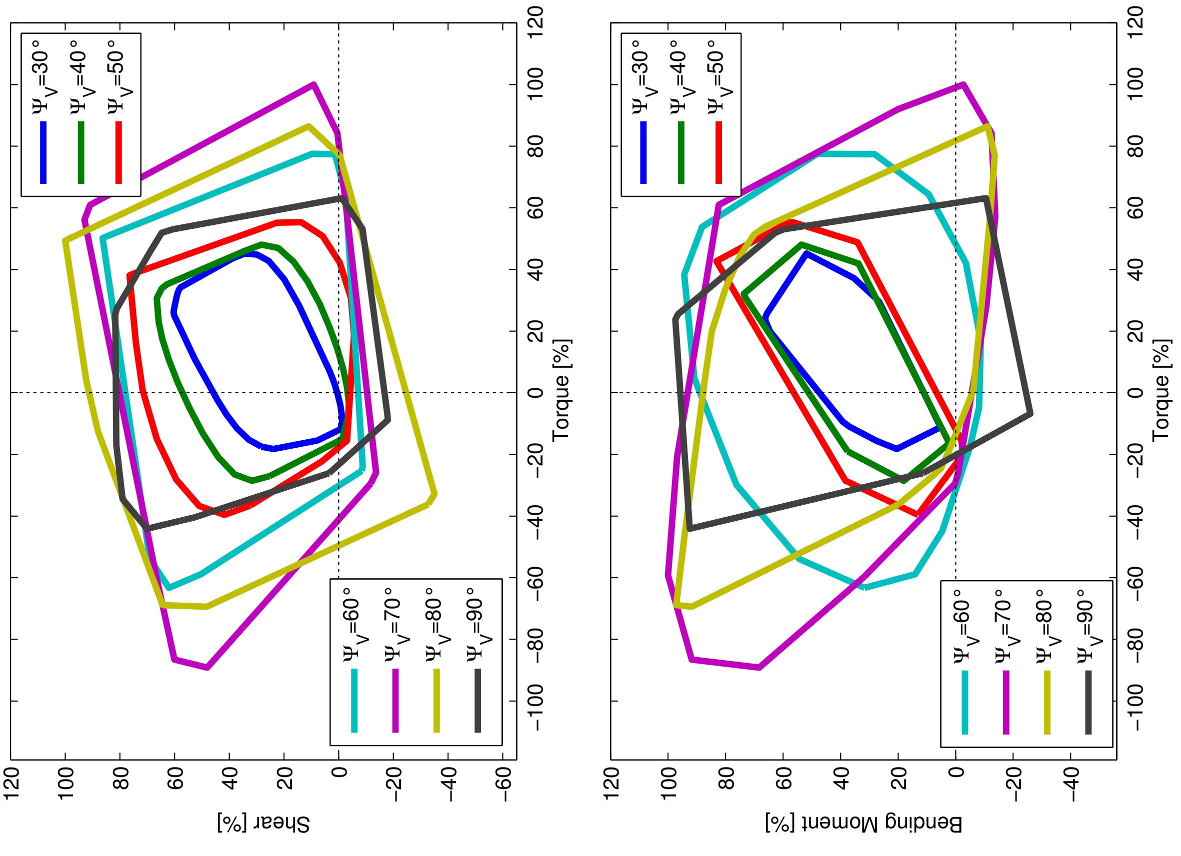

(a) Wing Root: F_z vs. M_x

(b) Wing Root: M_y vs. M_x

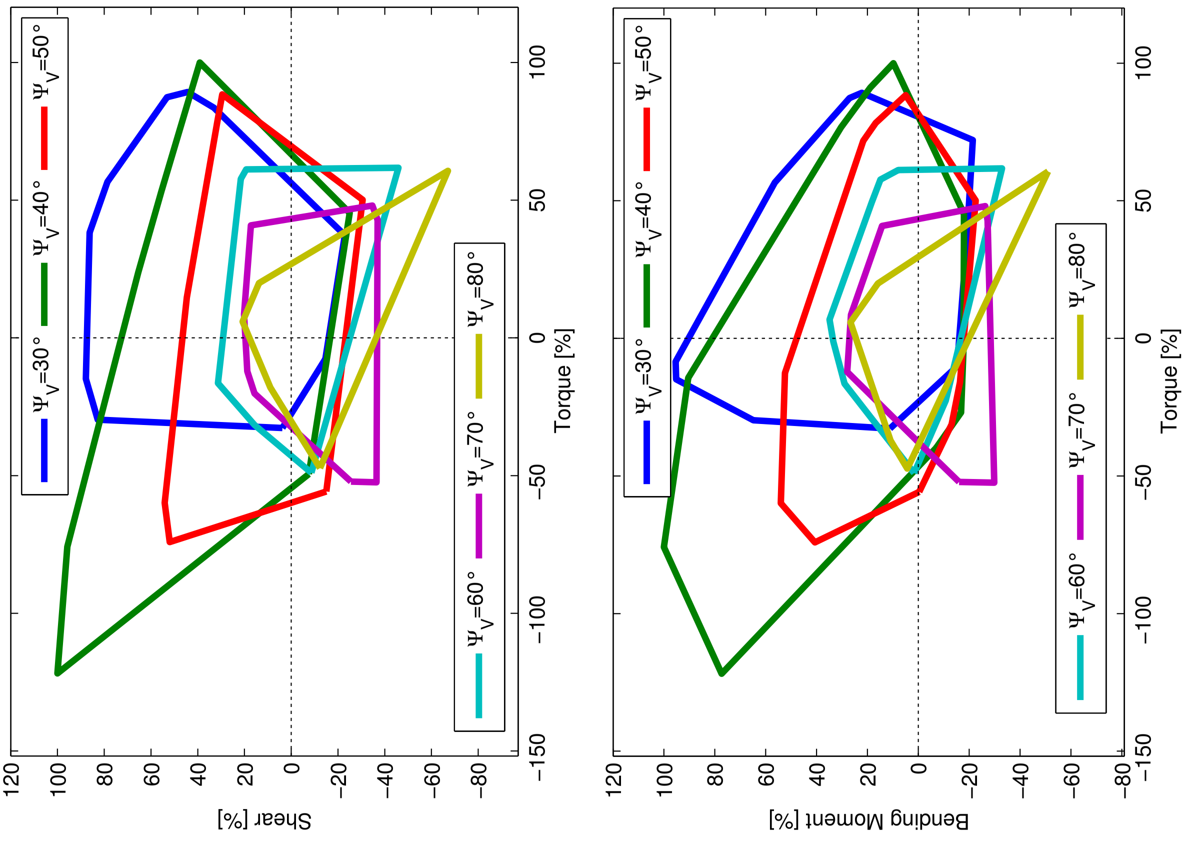

(c) Fin Root: F_x vs. M_z

(d) Fin Root: M_y vs. M_z

Figure 5.10: 2D Envelopes for Azimuth Ψ_V (Wing and Vertical Tail Plane)

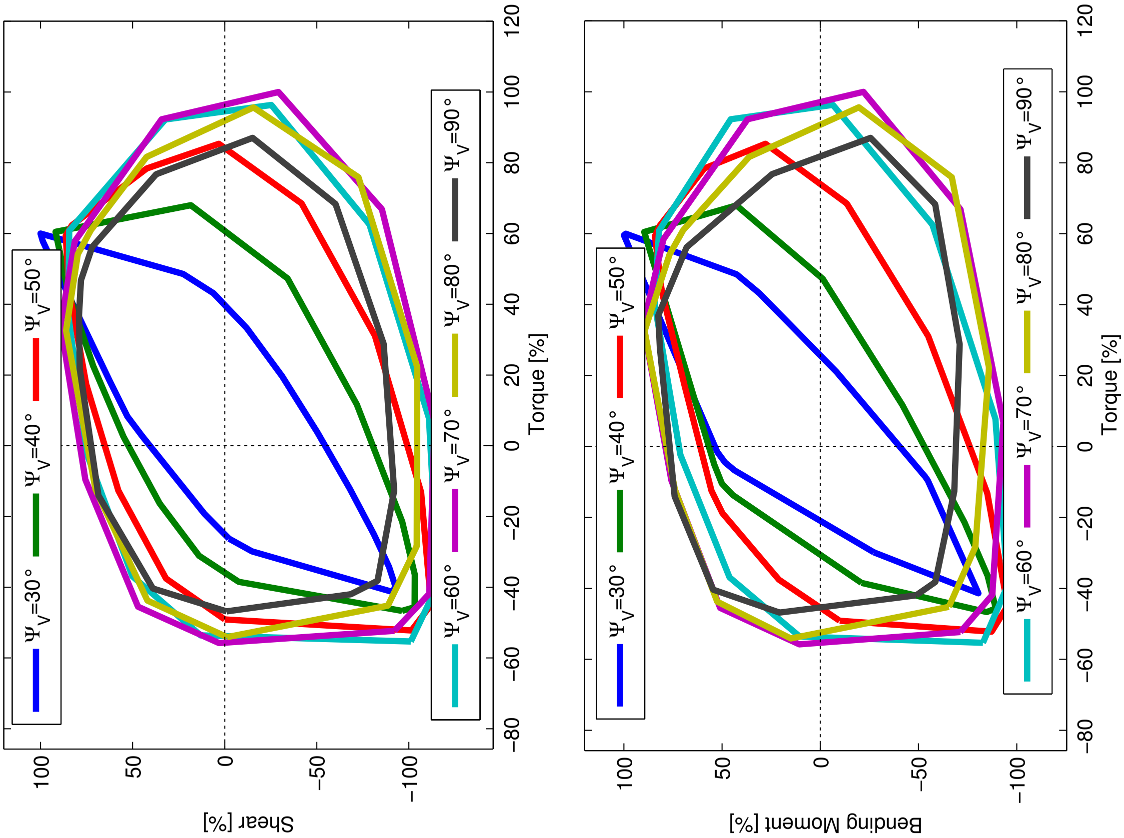

(a) HTP Root: F_z vs. M_x

(b) HTP Root: M_y vs. M_x

Figure 5.11: 2D Envelopes for Azimuth Ψ_V (Horizontal Tail Plane)

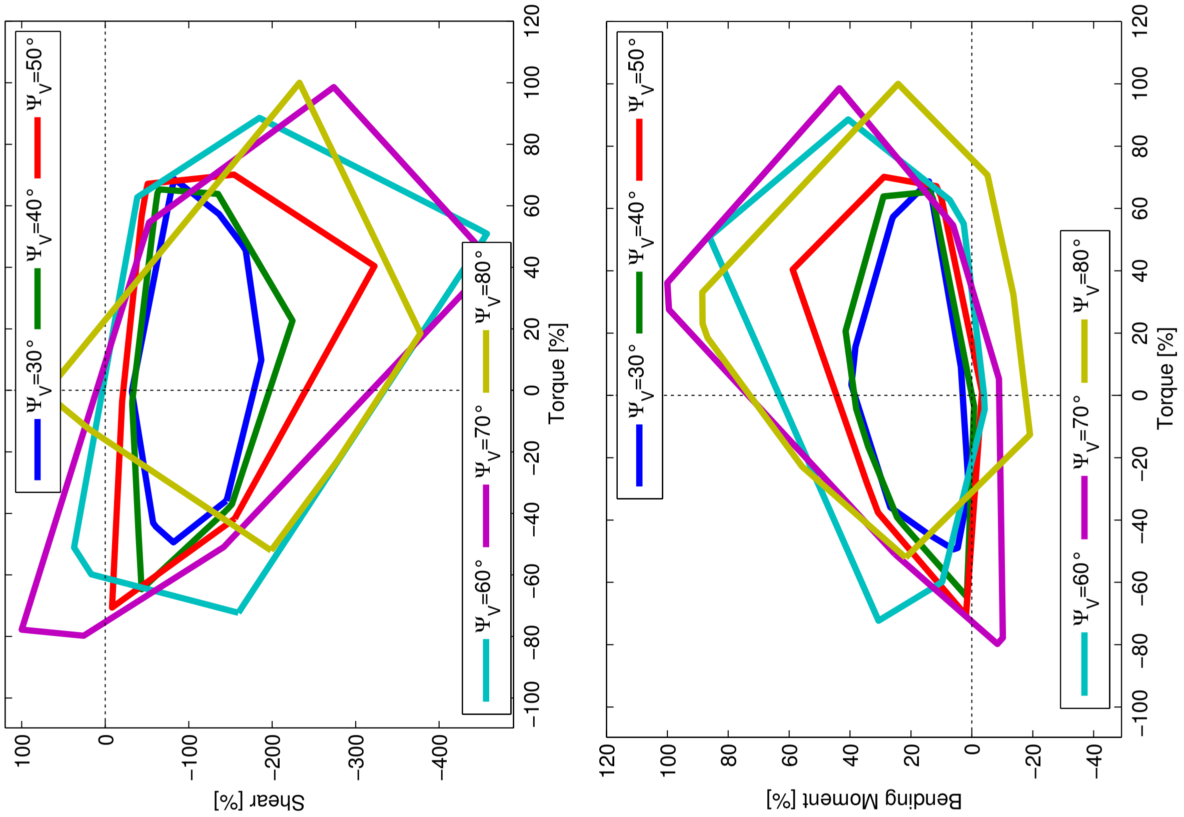

(a) Rear Fuselage (Vertical): F_z vs. M_x

(b) Rear Fuselage (Vertical): M_y vs. M_x

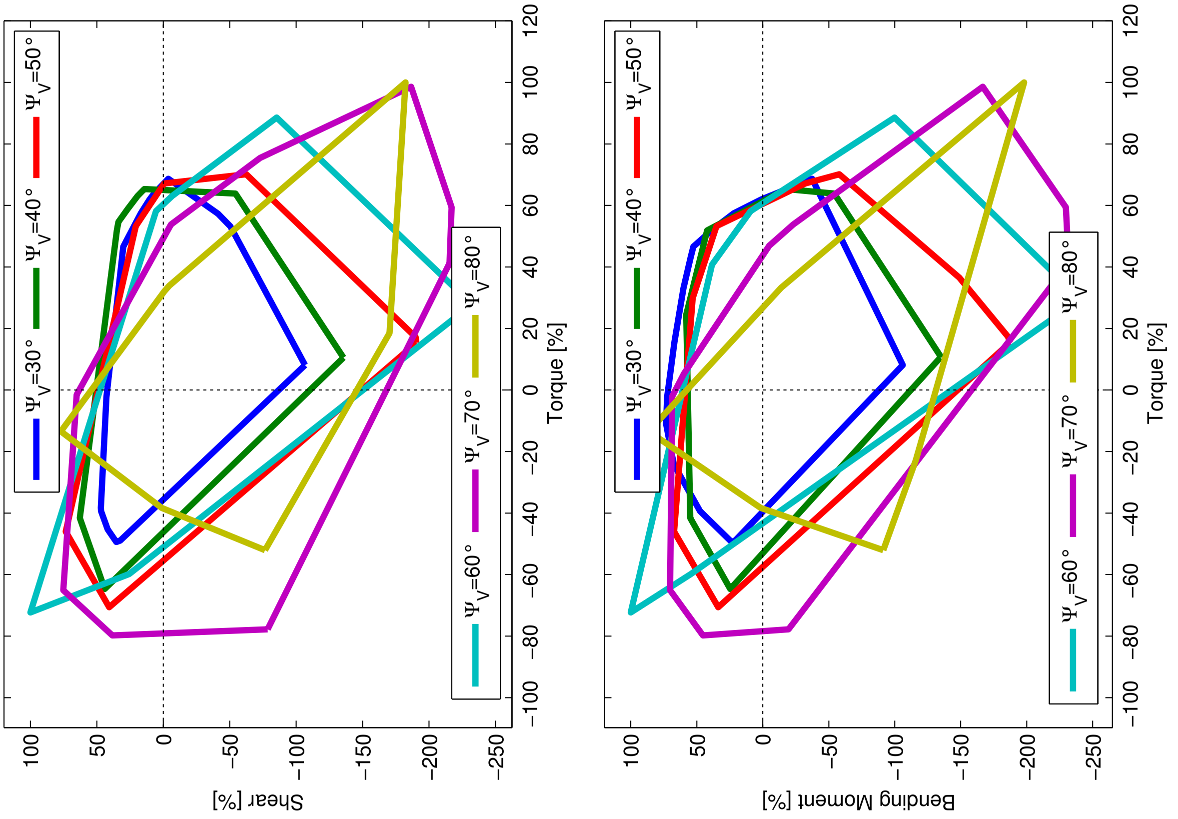

(c) Rear Fuselage (Lateral): F_y vs. M_x

(d) Rear Fuselage (Lateral): M_z vs. M_x

Figure 5.12: 2D Envelopes for Azimuth Ψ_V (Fuselage)

The monitor stations chosen are the root sections of the lifting surfaces and the fuselage station behind the wing center section. On the wing, increasing the azimuth angle enlarges both types of envelopes up to the point where dominantly only torque continues to rise. Torque reaches the maximum at $\Psi_V = 70^\circ$ and then drops off. The upper left quadrant of the bending moment against torque envelope at $\Psi_V = 70^\circ$ illustrates a typical situation during the encounter where neither bending moment nor torque assume extremal values but appear in extreme combination. On the horizontal tail, the azimuth sensitivity is not pronounced beyond $\Psi_V = 50^\circ$ and the maxima in shear and bending are very closely spaced. The situation is different on the vertical tail, where the envelopes significantly change their shape and area with azimuth angle. On the fuselage it is noticeable that all envelopes are bounded in one direction of shear or bending moment, i.e. changing the azimuth only widens the envelope along the torque axis and stretches it along one direction of the other axis.

5.7.3 Influence of Aircraft Modeling on Flight Loads

After this general assessment of the encounter type and its impact on flight loads and accelerations of the aircraft components, selected encounters are simulated using all four types of incremental aircraft models given in Table 5.1. Time histories of the integrated shear, bending moment and torque for the monitor stations described in the previous section can be found in Figs. 5.13 - 5.17. For the symmetric components wing and horizontal tail, curves for both the left and right hand side component are given as dotted and solid lines, respectively. All loads values are normalized with the maximum positive value obtained with *Model 1*. Compared to *Model 1*, including quasi-static structural flexibility in *Model 2* leads to a light alleviation of shear and bending moment levels on all components whereas torque is hardly affected. An exception is the vertical tail where increased torque peak values can be found. If instead structural dynamic behavior is assumed in *Model 3*, the transient loads become dominated by the component vibrational response with amplitudes significantly exceeding the levels of the quasi-static and rigid models. On the vertical tail where the dominant vibrational frequency is higher than the time scales of the wake vortex induced loads, the expected oscillatory behavior about a mean value approximately described by the quasi-static model solution can be observed. Also interesting to note is that dynamic torque on the fin closely follows the quasi-static values before passage of the first wake vortex filament excites a torsional vibration. When in addition to the structural dynamics also unsteady aerodynamics are included in *Model 4*, the dynamic effect on loads is diminished compared to *Model 3* with quasi-steady aerodynamic assumption. Besides the reduced amplitude, also slightly different phasing and frequency of vibration are visible (see for instance shear on the horizontal tail).

Exemplarily, vertical and lateral load factors at the aircraft center of gravity and at the cockpit derived with the different models are given in Figs. 5.18 - 5.19. Again all load factors are normalized with the maximum positive value obtained with *Model 1*. At the center of gravity, acceleration levels of all models are comparable. The models containing structural dynamics induce small amplitude vibrations longitudinally and laterally, signifying that the elastic behavior couples into the rigid body motion. At the cockpit, the structural dynamic effect of the flexible fuselage is felt dramatically with steady aerodynamics where peak load factors differ from the quasi-static and rigid approach by factors of 2 and more. Including unsteady aerodynamics reduces the effect of dynamic amplification of accelerations.

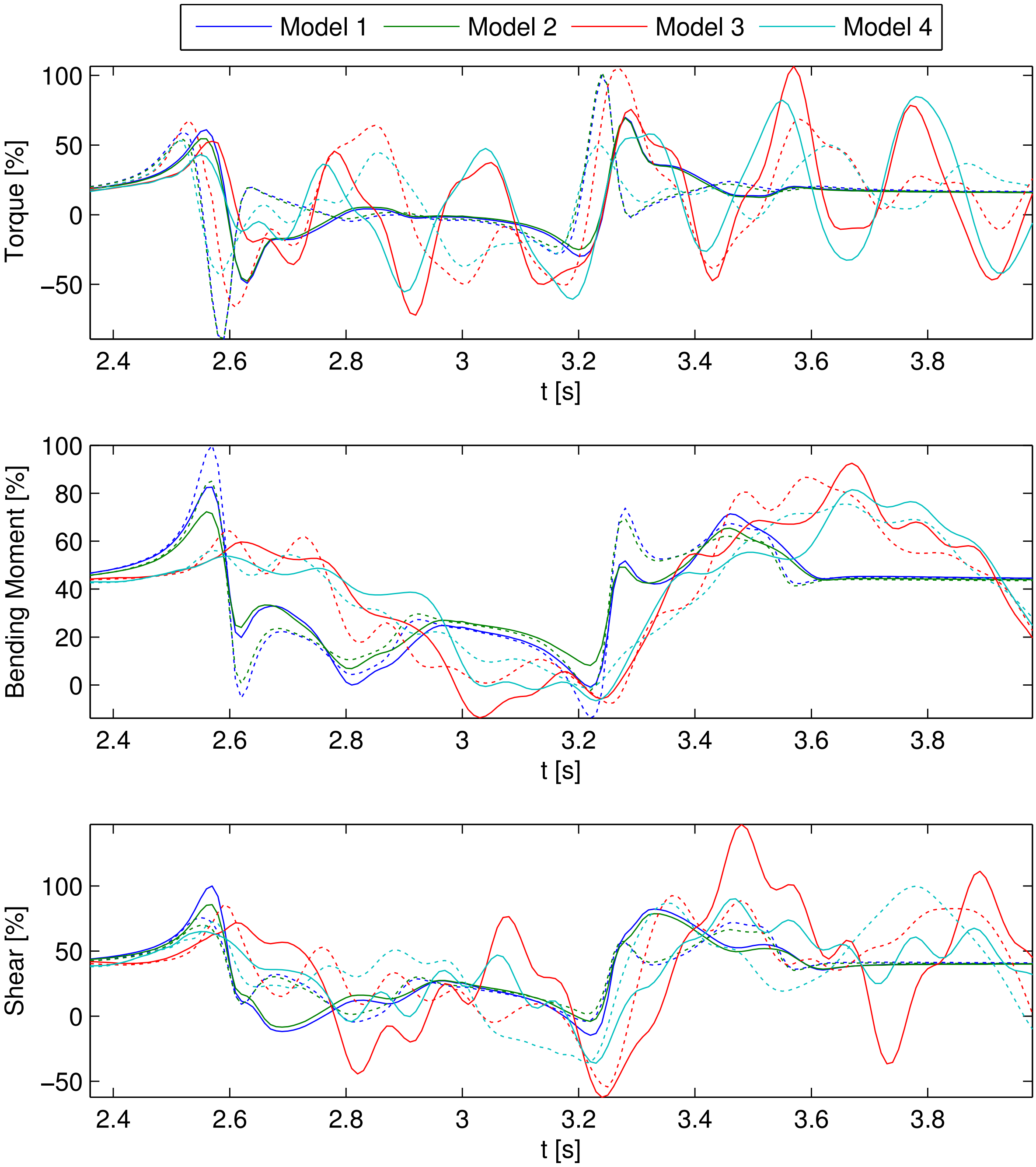

Figure 5.13: Effect of Aircraft Model on Wing Loads for a $\Psi_V = 70°$ Encounter

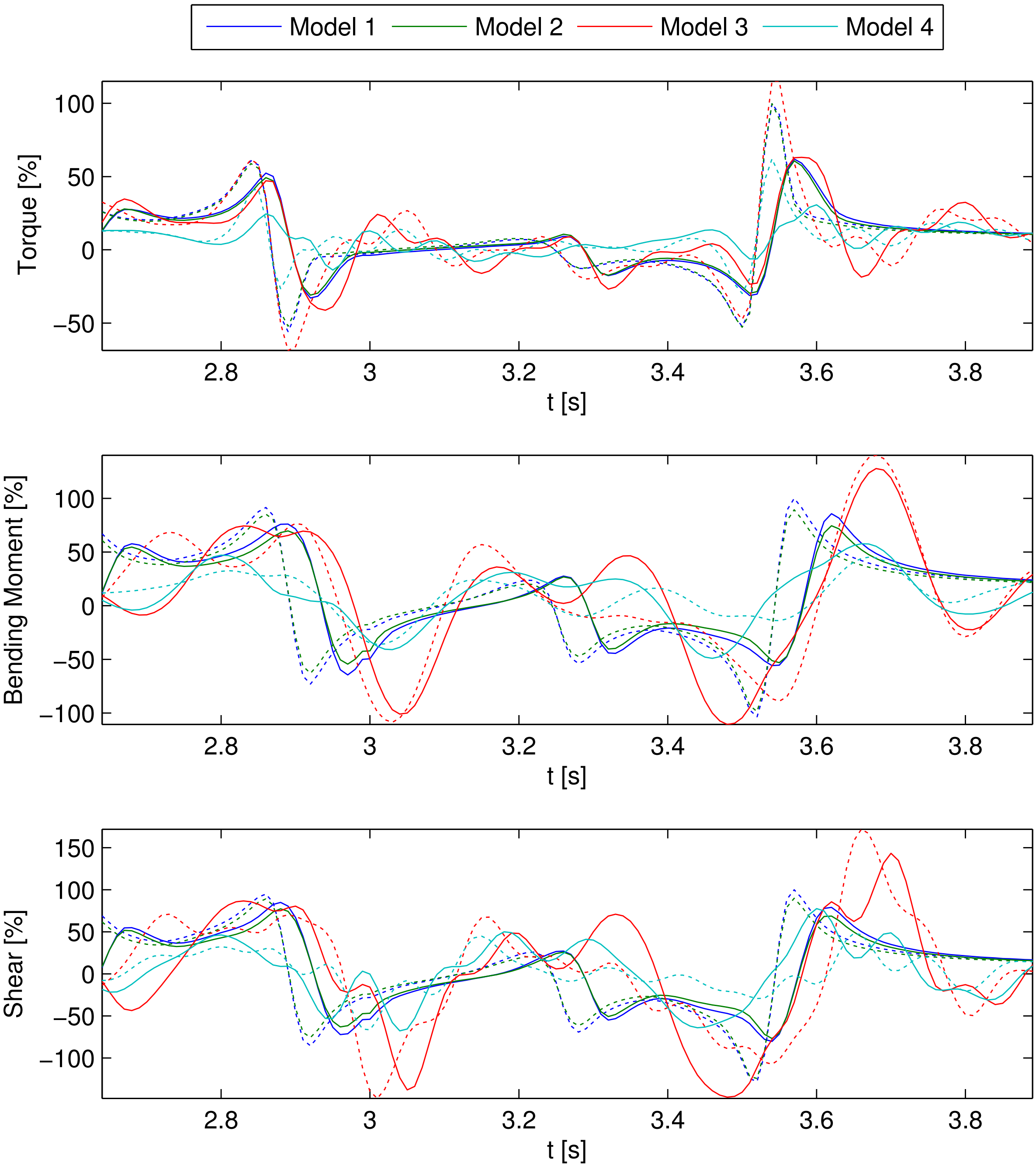

Figure 5.14: Effect of Aircraft Model on Horizontal Tail Loads for a $\Psi_V = 70^\circ$ Encounter

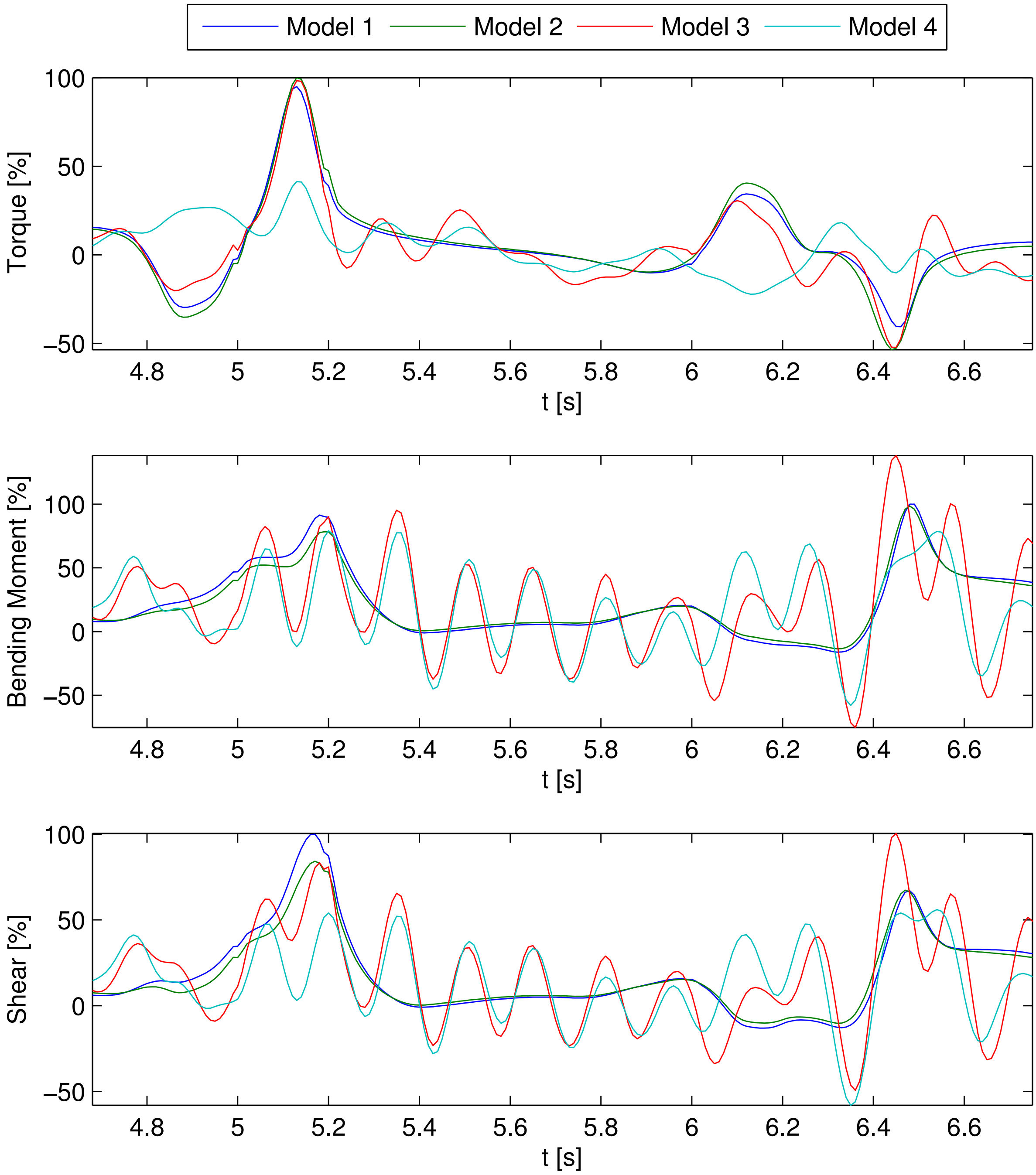

Figure 5.15: Effect of Aircraft Model on Vertical Tail Loads for a $\Psi_V = 30°$ Encounter

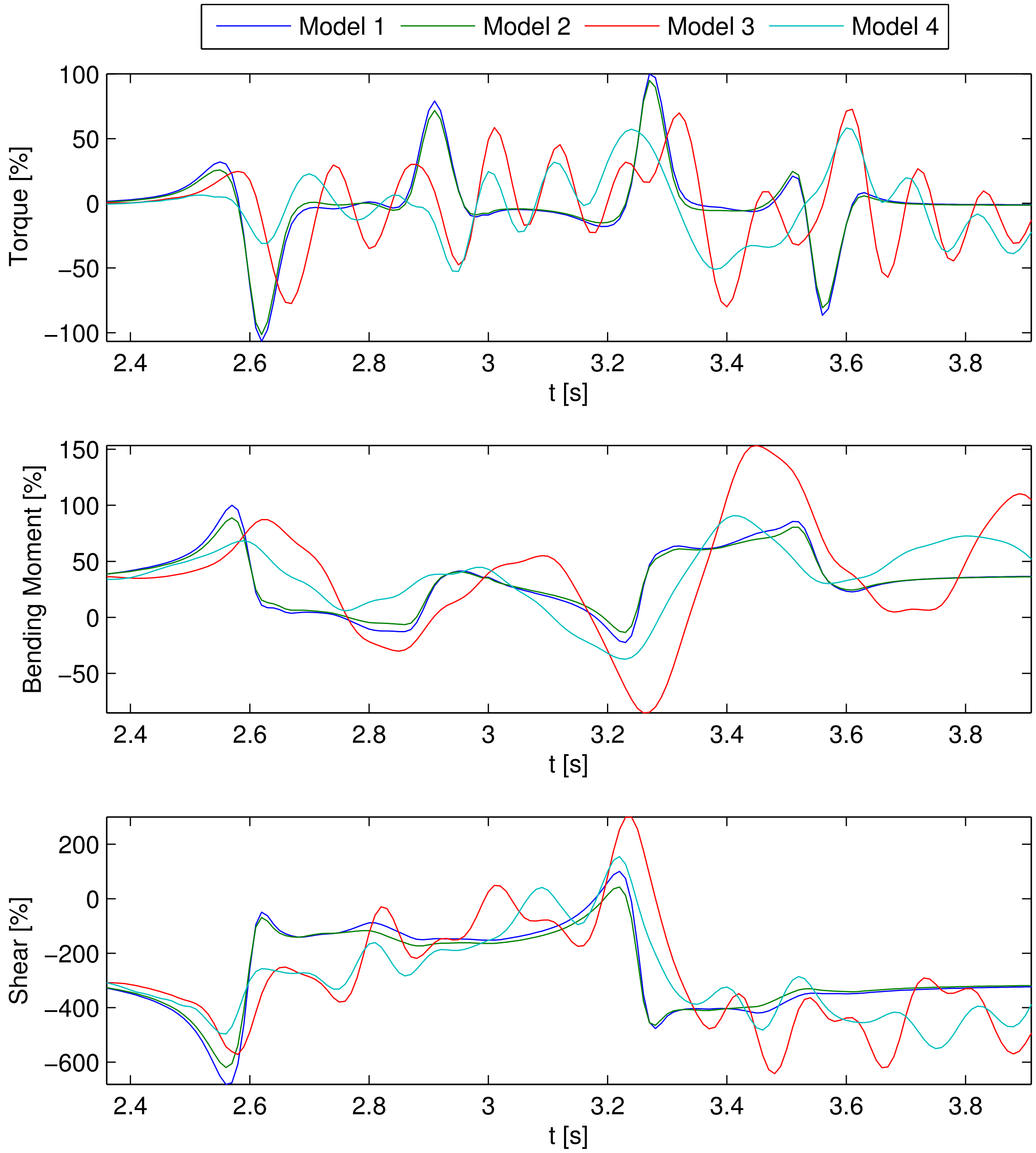

Figure 5.16: Effect of Aircraft Model on Vertical Fuselage Loads for a $\Psi_V = 70°$ Encounter

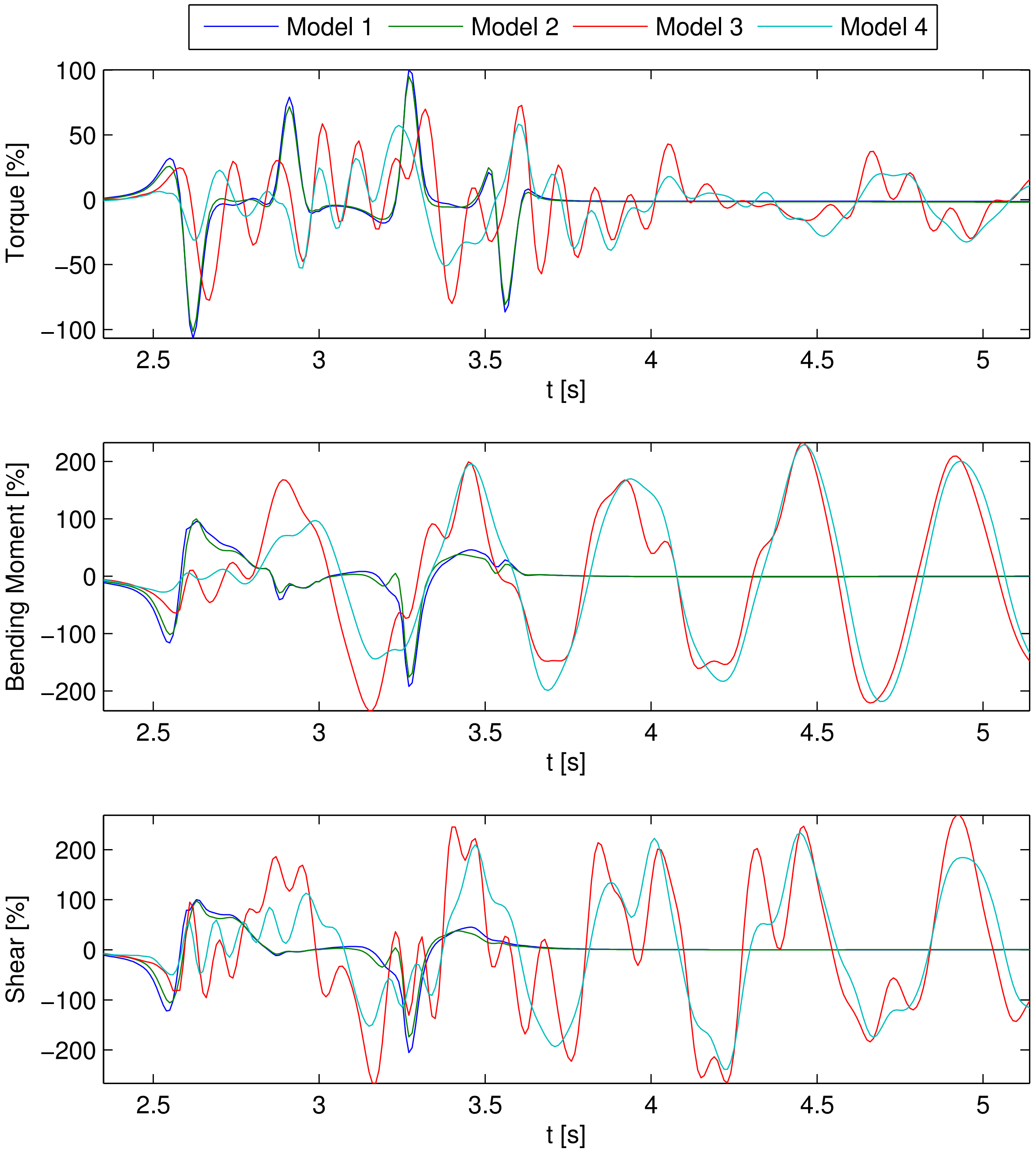

Figure 5.17: Effect of Aircraft Model on Lateral Fuselage Loads for a $\Psi_V = 70^\circ$ Encounter

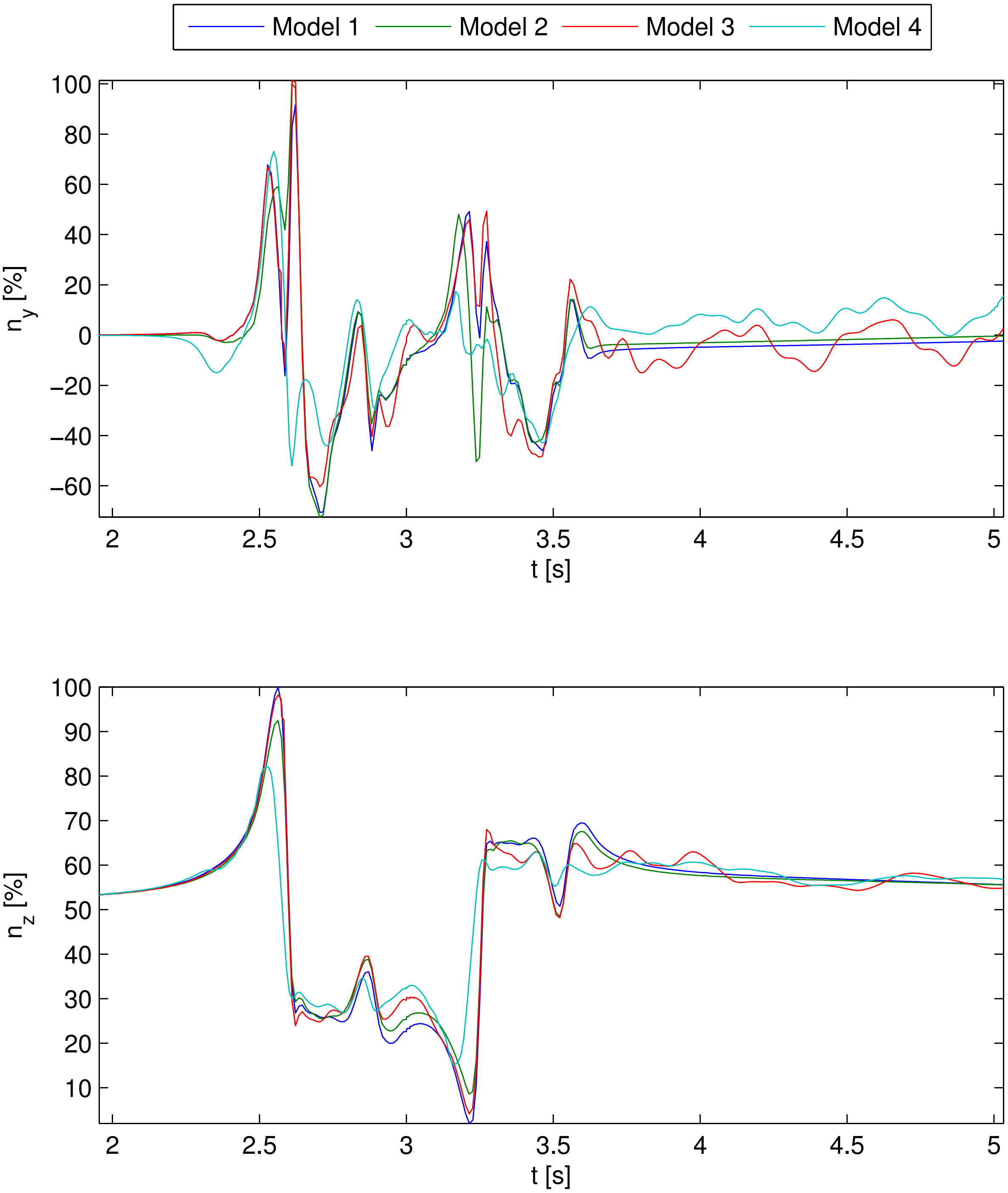

Figure 5.18: Effect of Aircraft Model on CG Load Factor for $\Psi = 70^\circ$ Encounter

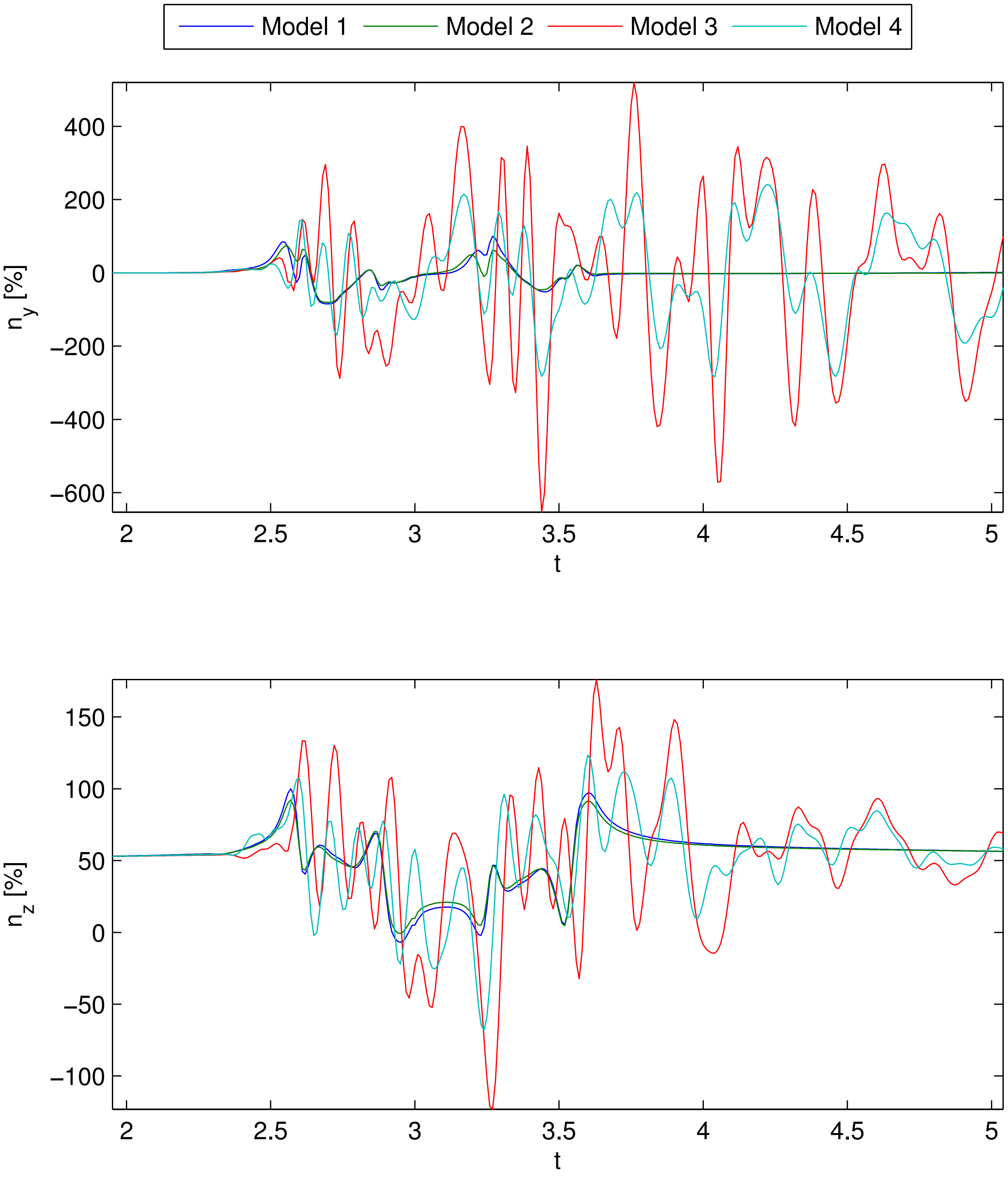

Figure 5.19: Effect of Aircraft Model on Load Factor at the Cockpit for $\Psi = 70^\circ$ Encounter

6 Conclusion and Outlook

The purpose of integral modeling of flexible aircraft is to provide a model simultaneously satisfying the requirements coming from the fields of static and dynamic flight loads analysis and aeroelasticity. It enables a multidisciplinary approach to aircraft design and analysis tasks that customarily are carried out in a segregated manner, for instance combined design of control laws for both trajectory and structural vibration control or analysis of flight loads during maneuvers in combination with atmospheric disturbances.

Aim of this thesis is the provision of a new approach to integral modeling. Starting points are industry standard models for maneuver loads and gust loads. The focus is put on the development of the aerodynamic model, which combines a database approach for steady non-linear aerodynamic loading with the steady and unsteady potential based vortex lattice method.

The reason for including the aerodynamic database in the model rather than opting for a purely numerical aerodynamic approach is the advantage of having non-linear, compressible, viscous aerodynamic data validated by flight test accessible at very low computational cost. By means of a mapping procedure, the aerodynamic strip loads retrieved from the database are distributed onto a reference surface grid that at the same time serves as the discretized representation of the aircraft for the numerical aerodynamic method. The mapping procedure uses force shape functions borrowed from incompressible airfoil theory to translate sectional loads into a chordwise distribution of discrete forces in the plane and normal to the lifting surfaces. Compared to an approach where an equivalent downwash distribution for the vortex lattice method leading to matched sectional loads is sought for, the method presented here is also able to resolve the in-plane forces and is independent of the numerical aerodynamic method.

The idea of a common reference surface grid facilitates the use of a single interconnection method between aerodynamic grid and structural grid for both database and numerical part of the aerodynamic model. This ensures consistent load paths in the structure and from a process point of view removes the need to maintain and verify two different approaches. Because the industry standard interconnection method contained in the finite element package *MSC.Nastran* only supports two degrees of freedom (lift and pitching moment), a new method based on finite interpolation elements with rigid orthogonal connectors is applied. It supports all 6 nodal degrees of freedom for the aero-structural coupling and is ideally suited for the application with condensed finite element models. From a process point of view, it allows a highly automatized build up of the aircraft component interconnections without the need for coordinate system or spline axis definitions.

For the unsteady aerodynamic part of the model, a different route compared to typical aeroelastic time domain analysis is taken. Instead of starting out with frequency domain aerodynamic forces coming from the industry standard doublet lattice method and subsequently transforming these into the time domain by rational function approximation (RFA), a direct time domain approach is chosen. The reason for that decision is the frequently tedious RFA process, the better accessibility of a time domain model to physical interpretation and the ability to include geometrical non-linear effects. The unsteady vortex lattice method constitutes a good trade-off between numerical accuracy and computational performance and despite of its limitation to potential, incompressible flow is a good means to introduce aerodynamic unsteadiness into an aircraft simulation model. This thesis contributes in several aspects to the established unsteady vortex lattice method:

1. A comprehensive presentation of the non-linear and linearized mathematical formulation in the time domain for both lifting surfaces and non-lifting bodies is given. This includes the treatment of different wake types and the interaction of wakes and bodies.
2. Consistent quasi-steady and steady formulations are derived from the full unsteady method including different rate of incident approximations.
3. A correction method for the unsteady method based on steady aerodynamic reference data is proposed and verified with computational fluid dynamics (CFD).
4. The linearized formulation is cast in discrete time state space form and consistently transformed to continuous time using the z-transform.
5. An incremental formulation of the method is derived where the wake only contains the unsteady part of the solution. This formulation is then cast into the notation typically used for RFA which simplifies the introduction of the method into existing software as replacement to the RFA.
6. To answer the need for fast and compact models, balanced truncation is applied to the state space formulation. The new element is the application of the balanced order reduction to each wake column rather than to the entire model which permits the application of dense matrix methods despite of the large original model size.
7. In order to obtain a truly integral model for both time and frequency domain, the consistent harmonic formulation of the unsteady vortex lattice method is derived and a new approach to solving the resulting equation system with inversion of only frequency dependent partitions of the system matrix is presented.

The time and frequency domain implementation of the method is validated using a combination of analytical and numerical reference results on lifting surfaces and bodies.

To complete the flexible aircraft model, the equations of motion for the fully flexible aircraft with non-linear rigid body formulation are presented and means to obtain linearized representations for small disturbance analysis are discussed.

As a typical field of application for the integral model, a flight loads study of wake vortex encounters is performed in which the sensitivity of aircraft component loads to the way the encountering aircraft traverses the wake is determined. No encounter is equally critical for all aircraft components and loads quantities, but the comparison of results obtained with different types of incremental aerodynamic models shows a wide variance of loads and acceleration levels.

6.1 Outlook

Future recommended work in continuation of this thesis can be divided into modeling and application aspects. In terms of modeling, the following enhancements could be pursued:

1. Introduction of compressibility would expand the applicability of the UVLM to moderate subcritical Mach numbers. Relevant publications however, for instance the paper by Hernandes and Soviero [53], suggest a significant increase of complexity of the method.
2. The correction of the UVLM with steady aerodynamic data could be performed continuously during the simulation based on output of the aerodynamic database.
3. The number of required wake elements in the UVLM could be reduced by introducing higher order wake elements. This would decrease the model size and increase the permissible time step.
4. The influence of steady-state wake shape on the harmonic airloads could be studied by first performing a free-wake steady state computation and subsequently derive the influence coefficients for the harmonic problem from the deformed wake.
5. The UVLM could be integrated into a geometrical non-linear analysis where the aerodynamic influence coefficients are continuously updated according the shape of the aircraft.
6. Balanced truncation using sparse matrix methods could be applied to the entire UVLM state space formulation rather than to the wake columns only. This should lead to a further decrease in model size.

The following applications based on the presented model are proposed for studies:

1. A more detailed wake vortex encounter analysis with respect to flight loads should be performed using a realistic flight control system and a pilot reaction model. The wake vortex effect could be enhanced by either
    - including the deformation of the *Lamb-Oseen* vortex due to the velocity induced by the encountering aircraft
    - introduction of a higher fidelity wake model
    - use of a database velocity field obtained by LIDAR measurement or CFD
2. Multi-objective design optimization with flight loads and aeroelastic constraints could be performed using the model.

Bibliography

[1] E. Albano and W. P. Rodden. A doublet-lattice method for calculating lift distributions on oscillating surfaces in subsonic flows. *AIAA Journal*, 7(2):279–285, 1969.

[2] John D. Anderson. *Fundamentals of Aerodynamics*. Aerospace Science Series. McGraw-Hill International Editions, 2nd edition, 1991.

[3] A. C. Antoulas, D. C. Sorensen, and S. Gugercin. A survey of model reduction methods for large scale systems. *Contemporary Mathematics*, (280):193–219, 2001.

[4] Myles L. Baker, D. Lewis Mingori, and Patrick J. Goggin. Approximate subspace iteration for constructing internally balanced reduced order models of unsteady aerodynamic systems. In *37th AIAA Structures, Structural Dynamics and Materials Conference, Salt Lake City*, number AIAA-96-1441-CP. AIAA, 1996.

[5] W. F. Ballhaus and P. M. Goorjian. Implicit finite-difference computations of unsteady transonic flows about airfoils. *AIAA Journal*, 15(12):1728–1735, 1977.

[6] B. C. Basu and G. J. Hancock. The unsteady motion of a two-dimensional aerofoil in incompressible inviscid flow. *Journal of Fluid Mechanics*, 87(1):159–178, 1978.

[7] Armin Beckert. *Ein Beitrag zur Strömungs-Struktur-Kopplung für die Berechnung des aeroelastischen Gleichgewichtszustandes*. Doktorarbeit, German Aerospace Center (DLR), Institute of Aeroelasticity, Göttingen, Germany, 1997.

[8] R. L. Bisplinghoff, H. Ashley, and R. L. Halfman. *Aeroelasticity*. Addison-Wesley Publishing Co., 1955.

[9] P. S. Brar, R. Raul, and R. H. Scanlan. Numerical calculation of flutter derivatives via indicial functions. *Journal of Fluids and Structures*, 10:337–351, 1996.

[10] Christian Breitsamter. Nachlaufwirbelsysteme großer Transportflugzeuge - Experimentelle Charakterisierung und Beeinflussung. Habilitationsschrift, Lehrstuhl für Aerodynamik, Technische Universität München, 2007.

[11] J. Brink-Spalink and J. M. Bruns. Correction of unsteady aerodynamic influence coefficients using experimental or CFD data. In *Proceedings of the AIAA/ASME/ASCE/AHS Structures, Structural Dynamics and Materials Conference, Atlanta, GA (USA)*, 2000.

[12] Rudolf Brockhaus. *Flugregelung*. Springer-Verlag, 2nd edition, 2001.

[13] A. P. Brown. An engineering study of the unsteady response of a jet transport during a wake encounter in a transitional state of potential crow instability. In *AIAA Atmospheric Flight Mechanics Conference and Exhibit*, Aug 2002.

[14] Jörg Buchholz. TrimMod for Simulink. Matlab File Exchange, 2001. URL `http://www.mathworks.com/matlabcentral/fileexchange/268`.

[15] Carey S. Buttrill, Thomas A. Zeiler, and Douglas P. Arbuckle. Nonlinear simulation of a flexible aircraft in maneuvering flight. In *Proceedings of the 1987 Flight Simulation Technologies Conference, Monterey, California, August 17-19, 1987.*, number AIAA-87-2501, 1987.

[16] J. R. Canavin and P. W. Likins. Floating reference frames for flexible spacecraft. *AIAA Journal of Spacecraft*, 14:724–732, 1977.

[17] Jens Cattarius. *Numerical Wing/Store Interaction Analysis of a Parametric F-16 Wing*. PhD thesis, Virginia Polytechnic Institute and State University, VA, USA, 1999.

[18] Tuncer Cebeci, Max Platzer, Hsun Chen, Kue-Cheng Chang, and Jian P. Shao. *Analysis of low-speed unsteady airfoil flows*. Springer-Verlag, 1 edition, 2005.

[19] P. Cicala. Present state of development in nonsteady motion of lifting surface. NACA Technical Memorandum NACA-TM-1277, NACA, 1951.

[20] Civil Aviation Authority. Wake turbulence. Aeronautical Information Circular AIC P 18/2009, Civil Aviation Authority (CAA), Mar 2009.

[21] Henry A. Cole and Euclid C. Holleman. Measured and predicted dynamic response characteristics of a flexible airplane to elevator control over a frequency range including three structural modes. NACA Technical Note NACA TN-4147, Ames Aeronautical Laboratory, Moffett Field, CA, USA, Feb 1958.

[22] Henry A. Cole, Stuart C. Brown, and Euclid C. Holleman. The effects of flexibility on the longitudinal and lateral-directional response of a large airplane. NACA Research Memorandum NACA-RM-A55D14, Ames Aeronautical Laboratory, Moffett Field, CA, USA, May 1955.

[23] S. C. Crow. Stability theory for a pair of trailing vortices. *AIAA Journal*, 8(12): 2172–2179, 1970.

[24] H. J. Damveld. Determination of instationary aeroelastic stability derivatives for real-time simulation. In *Proceedings of the AIAA Atmospheric Flight Mechanics Conference and Exhibit, Providence, Rhode Island*, number AIAA 2004-5365, 2004.

[25] H. Daughaday and R. A. Piziali. An improved computational model for predicting the unsteady aerodynamic loads of rotor blades. *Journal of The American Helicopter Society*, 11(4):3–10, 1966.

[26] D. Fraeijs De Veubeke. The dynamics of flexible bodies. *International Journal of Engineering Science*, 14(10):895–913, 1976.

[27] Alin Dorian Dinu, Ruxandra Mihaela Botez, and Iulian Cotoi. Chebyshev polynomials for unsteady aerodynamic calculations in aeroservoelasticity. *AIAA Journal of Aircraft*, 43(1):165–171, 2006.

[28] DLR. *Technical Documentation of the DLR TAU-Code*. DLR Institute of Aerodynamics and Flow Technology, Göttingen and Brunswick, Germany, 2005.

[29] Mark Drela. Integrated simulation model for preliminary aerodynamic, structural, and control-law design of aircraft. In *40th AIAA SDM Conference*, number AIAA Paper 99-1394, St. Louis, USA, April 1999. vortex lattice.

[30] J. R. Dykman and W. P. Rodden. Structural dynamics and quasistatic aeroelastic equations of motion. *AIAA Journal of Aircraft*, 37(3):538–542, 2000.

[31] John W. Edwards, Holt Ashley, and John V. Breakwell. Unsteady aerodynamic modeling for arbitrary motions. *AIAA Journal*, 17(4):365–374, Apr 1979.

[32] G. Einarsson and J. Neumann. Multidisciplinary simulation of a generic delta wing: aerodynamic, flight-dynamic, and structure-mechanic coupling. In *Proceedings of the Int. Conf. on Computational Methods for Coupled Problems in Science and Engineering, Barcelona*, 2005.

[33] David Eller. *On an Efficient Method for Time-Domain Computational Aeroelasticity*. PhD thesis, Stockholm Royal Institute of Technology, 2005.

[34] B. Etkin. Aerodynamic transfer functions: an improvement on stability derivatives for unsteady flight. UTIA Report 42, Institue of Aerophysics, University of Toronto, Canada, Oct 1956.

[35] Bernard Etkin and LLoyd D. Reid. *Dynamics of Flight*. John Wiley & Sons, Inc., 3rd edition, 1993.

[36] C. Farhat, K. Pierson, and C. Degand. Multidisciplinary simulation of the maneuvering of an aircraft. *Engineering with Computers*, 17(17):16–27, 2001.

[37] G. F. Franklin, J. D. Powell, and M. L. Workman. *Digital Control of Dynamic Systems*. Addison-Wesley Publishing Co., 2nd edition, 1990.

[38] Tracy E. Fritz and Lyle N. Long. A parallel, object-oriented unsteady vortex lattice method for flapping flight. In *AIAA Aerospace Sciences Meeting*, number AIAA Paper 2004-0039, Reno, USA, January 2004. vortex lattice.

[39] I. E. Garrick. On some reciprocal relations in the theory of nonstationary flows. NACA Technical Report NACA-TR-629, NACA, 1938.

[40] Wolfgang Geissler. Berechnung der Druckverteilung an harmonisch oszillierenden dicken Rümpfen in inkompressibler Strömung. DLR Forschungsbericht 76-48, German Aerospace Center (DLR), Institute of Aerodynamics, Göttingen, Germany, 1976.

[41] Wolfgang Geissler. Verfahren in der instationären Aerodynamik. DLR Forschungsbericht 93-21, German Aerospace Center (DLR), Institute of Aerodynamics, Göttingen, Germany, 1993.

[42] Alfred Gessow. Introduction. In *Symposium on Wake Vortex Minimization*, number SP-409. NASA, Feb. 1976.

[43] Philippe Geuzaine, G. Brown, C. Harris, and C. Farhat. Aeroelastic dynamic analysis of a full F-16 configuration for various fight conditions. *AIAA Journal*, 41(3):363–371, 2003.

[44] J. Giesing. Two-dimensional potential flow theory for multiple bodies in small amplitude motion. *AIAA Journal*, 8(11):1944–1953, 1970.

[45] C. Gologan and G. Schneider. New aerodynamic approach for maneoeuver simulation including dynamic loads. In *DGLR Deutscher Luft- und Raumfahrtkongress*, volume 3, Hamburg, Germany, September 2001. vortex lattice.

[46] Randal E. Guendel. Unsteady aerodynamics for aeroelastic applications using the impulse reponse method. Master's thesis, Massachusetts Institute of Technology, 2000.

[47] K. K. Gupta, M. J. Brenner, and L. S. Voelker. Development of an integrated aeroservoelastic analysis program and correlation with test data. Technical Report NASA/TP-3120, NASA Dryden Flight Research Facility, 1991.

[48] Benjamin D. Hall. Numerical simulations of the aeroelastic response of an actively controlled flexible wing. Master's thesis, Virginia Polytechnic Institute and State University, VA, USA, 1999. vortex lattice.

[49] Kennet C. Hall. Eigenanalysis of unsteady flows about airfoils, cascades and wings. *AIAA Journal*, 32(12):2426–2432, Dec 1994.

[50] M. Hanel. *Robust integrated flight and aeroelastic control system design for a large transport aircraft*. PhD thesis, University of Stuttgart, 2001.

[51] Moqin He, Brain Veitch, Neil Bose, Bruce Colbourne, and Pengfei Liu. A three-dimensional wake impingement model and applications on tandem oscillating foils. *Journal of Ocean Engineering*, 34:1197–1210, 2007.

[52] Horst H. Henke. Progress of the viscous-coupled 3d Euler method EUVISC and its aeroelastic application. In *International Forum on Aeroelasticity and Structural Dynamics, Munich, Germany*, 2003.

[53] Fabiano Hernandes and Paulo A. O. Soviero. Unsteady aerodynamic coefficients obtained by a compressible vortex lattice method. *AIAA Journal of Aircraft*, 46(4): 1291–1301, 2009.

[54] G. Höhne, M. Fuhrmann, and R. Luckner. Critical wake vortex encounter scenarios. In *Deutscher Luft- und Raumfahrt-Kongress, München*, Nov 2003.

[55] K. Isogai. Calculation of unsteady transonic flow over oscillating airfoils using the full potential equation. In *Structures, Structural Dynamics and Materials Conference, 18th; United States*, pages 245–256, 1977.

[56] Keiichi Ito. Optimization of flapping wing motion. In *International Counsil of the Aeronautical Sciences (ICAS)*, number 814, 2002.

[57] Richard M. James. On the remarkable accuracy of the vortex lattice method. *Computer methods in applied mechanics and engineering*, 1:59–79, 1972.

[58] Wayne Johnson. *Helicopter Theory*. Dover Publications Inc., New York, 1980.

[59] Robert T. Jones. The unsteady lift of a wing of finite aspect ratio. NACA Report NACA-TR-681, Langley Memorial Aeronautical Laboratory, Virginia, USA, 1939.

[60] R. Karkehabadi. *Numerical simulations of wings in unsteady flows*. PhD thesis, Virginia Polytechnic Institute and State University, 1995.

[61] Reza Karkehabadi. Thick wings in steady and unsteady flows. *AIAA Journal of Aircraft*, 41(4):964–967, 2004. vortex lattice.

[62] Reza Karkehabadi. Aerodynamic interference of a large and a small aircraft. *AIAA Journal of Aircraft*, 41(6):1424–1429, Nov 2004.

[63] Mordechay Karpel. Time-domain aeroservoelastic modeling using weighted unsteady aerodynamic forces. *AIAA Journal of Guidance*, 13(1):30–37, Jan 1988.

[64] Joseph Katz and Allen Plotkin. *Low speed aerodynamics*. Cambridge University Press, 2nd edition, 2001.

[65] B. E. Kinnaman. Flutter analysis of complex airplanes by experimental methods. *Journal of Aeronautical Science*, 19(9):577–584, Sep 1952.

[66] S. Kinnas, C. Y. Hsin, and D. Keenan. A potential based panel method for the unsteady flow around open and ducted propellers. In *Eighteenth Symposium on Naval Hydrodynamics*, 1991.

[67] Vladislav Klein. Modeling of longitudinal unsteady aerodynamics of a wing-tail combination. NASA Contractor Report NASA CR-99-209547, The George Washington University Joint Institute for Advancement of Flight Sciences (JIAFS) and NASA Langley Research Center, Hampton, VA, USA, 1999.

[68] Vladislav Klein and Keith D. Noderer. Modeling of aircraft unsteady aerodynamic characteristics. NASA Technical Memorandum 109120 NASA Technical Memorandum 109120, The George Washington University Joint Institute for Advancement of Flight Sciences (JIAFS) and NASA Langley Research Center, Hampton, VA, USA, 1994.

[69] Stephan Kloidt. *Beiträge zum Entwurf eines Flugregelungssystems zur Reduktion des Wirbelschleppeneinflusses*. Dissertation, Technische Universität Berlin, 2007.

[70] Klaus König and Jörg Schuler. Integral control of large flexible aircraft. In *Proceedings of the RTO AVT Specialists' Meeting on Structural Aspects of Flexible Aircraft Control*, number RTO MP-36, pages 19.1–19.12, Ottawa, Canada, October 1999.

[71] P. Konstadinopoulos, D. F. Thrasher, D. T. Mook, A. H. Nayfeh, and L. Watson. A vortex-lattice method for general, unsteady aerodynamics. *AIAA Journal of Aircraft*, 22(1):43–49, 1985.

[72] H. G. Küssner. Zusammenfassender Bericht über den instationären Auftrieb von Tragflügeln. *Luftfahrtforschung*, 13:410–424, 1936.

[73] H. G. Küssner. Theorie des schwingenden Streckenprofils bei kompressibler Unterschallströmung. Teil 1: Herleitung der geschlossenen analytischen Lösung für den Stördruck. Technical Report 67J03, AVA, 1967.

[74] H. G. Küssner and H. Göllnitz. Tabellen der aerodynamischen Derivativa des schwingende Streckenprofiles mit Knicken und Stufen. Technical Report 64J04, Aerodynamische Versuchsanstalt Göttingen, Abteilung Aeroelastizität, 1964. In German.

[75] H. G. Küssner and L. Schwarz. Der schwingende Flügel mit aerodynamisch ausgeglichenem Ruder. *Luftfahrtforschung*, 17:337–354, 1940.

[76] M. K. Laha. A vortex lattice method for thin wings oscillating in ideal flow. *Aeronautical Jounal*, (11):314–320, 1993.

[77] T. Lampe, Y. Sedin, and P. Weinerfelt. Flight test verification of a wake vortices model. In *Flight Test – Sharing Knowledge and Experience Meeting Proceedings*, number RTO–MP–SCI–162, pages 4.1–4.16. NATO Research and Technology Organisation, 2005.

[78] B. Laschka. Zur Theorie der harmonisch schwingenden tragenden Fläche bei Unterschallanströmung. *Zeitschrift für Flugwissenschaften*, 11(7):265–292, 1963.

[79] E. Lavretsky. High speed civil transport (HSCT) flight simulation and analysis software development. In *Proceedings of the 36th Aerospace Sciences Meeting and Exhibit, Reno, Nevada*, number AIAA-98-0173, 1998.

[80] Michael Link. *Finite Elemente in der Statik und Dynamik*. Teubner, Stuttgart, Germany, 3rd edition, 2002.

[81] H. Lomax, M. Heaslet, F. Fuller, and L. Sluder. Two and three-dimensional unsteady lift problems in high-speed flight. NACA technical report NACA TR 1077, Ames Aeronautical Laboratory, Moffett Field, CA, USA, 1952.

[82] Lyle N. Long and George A Watts. Arbitrary motion aerodynamics using an aeroacoustic approach. *AIAA Journal*, 25(11):1442–1448, 1987.

[83] Gertjan Looye. Integration of rigid and aeroelastic aircraft models using the residualised model method. In *Proceedings of International Forum on Aeroelasticity and Structural Dynamics, Munich, Germany*, 2004.

[84] S. Lu and R. Voss. TDLM-A transonic doublet lattice method for 3d potential unsteady transonic flow computation. Technical Report DLR-FB 92-25, DLR Institut für Aeroelastik, Göttingen, Germany, 1992.

[85] Wolfgang Luber. Wake penetration effects on dynamic loads and structural design of military and civil aircraft. In *International Forum on Aeroelasiticy and Structural Dynamics (IFASD), Seattle, USA*, number IFASD-2009-011, 2009.

[86] B. Maskew and B. M. Rao. Unsteady analysis of rotor blade tip flow. NASA Contractor Report NASA-CR-3868, NASA Langley Research Center, 1985.

[87] Bernard Mazelsky and Joseph A. Drischler. Numerical determination of indicial lift and moment functions for a two-dimensional sinking and pitching airfoil at Mach numbers 0.5 and 0.6. NACA Technical Note NACA-TN-2739, Langley Memorial Aeronautical Laboratory, Virginia, USA, 1952.

[88] T. H. G. Megson. *Aircraft structures for engineering students*. Arnold, 3rd edition, 1999.

[89] Leonard Meirovitch. *Principles and techniques of vibrations*. Prentice Hall, 1997.

[90] Leonard Meirovitch and Ilhan Tuzcu. Multidisciplinary approach to the modeling of flexible aircraft. In *Proceedings of the CEAS/AIAA/AIAE International Forum on Aeroelasticity and Structural Dynamics*, volume 3, pages 435–448, Madrid, Spain, June 2001.

[91] R. D. Milne. Dynamics of the deformable aeroplane. Reports and Memoranda 3345, Aeronautical Research Council, 1964.

[92] W. Mönnich. Zur Modellierung von Flügelabwind-Laufzeiteinflüssen in der Flugzeugslängsbewegung. In *DGLR Deutscher Luft- und Raumfahrtkongress*, number 86-165, pages 335–341, 1986.

[93] Luigi Morino. Boundary integral equations in aerodynamics. *Applied Mechanics Review*, 46(8):445–466, Aug 1993.

[94] J. A. Moulder, W. H. J. J. van Staveren, and J. C. van der Vaart. *Flight Dynamics (Lecture Notes)*. Delft University of Technology, Faculty of Aerospace Engineering, 2000.

[95] National Transportation and Safety Board (NTSB). In-flight separation of vertical stabilizer, American Airlines flight 587, Airbus Industrie A300-605r, n14053, Belle Harbor, New York, November 12, 2001. Aircraft Accident Report NTSB/AAR-04/04, National Transportation and Safety Board (NTSB), 2004.

[96] R.H. Ni and F. Sisto. Numerical computation of non-stationary flat plate cascade in compressible flow. *ASME Journal of Engineering for Power*, 98(2):165–170, Apr 1976.

[97] Thilo Penzl. LYAPACK - a Matlab toolbox for large lyapunov and riccati equations, model reduction problems, and linear-quadratic optimal control problems. User Guide 1.0, Technical University of Chemnitz, Germany, 1999.

[98] Sergio Preidikman. *Numerical simulations of the interactions among aerodynamics, structural dynamics, and control systems*. PhD thesis, Virginia Polytechnic Institute and State University, 1998.

[99] William D. Ramsey. *Boundary integral methods for lifting bodies with vortex wakes*. PhD thesis, Massachusetts Institute of Technology, 1996.

[100] D.E. Raveh, M. Karpel, and S. Yaniv. Nonlinear design loads for maneuvering elastic aircraft. *AIAA Journal of Aircraft*, 37(2):313–318, 2000.

[101] Christian Reschke. Berechnung dynamischer lasten bei elastischen strukturen. Master's thesis, University of Stuttgart, 2003. In German language.

[102] Christian Reschke. *Integrated flight loads modelling and analysis for flexible transport aircraft*. PhD thesis, University of Stuttgart, 2006.

[103] Kapseong Ro and Jewel B. Barlow. On the development of flexible aircraft equations of motion. In *20th Congress of the International Council of the Aeronautical Sciences (ICAS)*, volume 1, pages 569–584, Sep 1996.

[104] W. P. Rodden and J. P. Giesing. Application of oscillatory aerodynamic theory to estimation of dynamic stability derivatives. *AIAA Journal of Aircraft*, 7:272–275, 1970.

[105] Kenneth L. Roger. Airplane math modeling methods for active control design. In *Structural Aspects of Active Control*, number AGARD-CP-228, pages 4.1–4.11. AGARD Structures and Materials Panel, 1977.

[106] Vernon J. Rossow. Validation of vortex-lattice method for loads on wings in lift-generated wakes. *AIAA Journal of Aircraft*, 32(6):1254–1262, 1995. vortex lattice NASA TM-95-207379.

[107] Luis Pablo Ruiz-Calavera. A time-marching method for calculating unsteady airloads on three-dimensional wings. Part II: Full-potential formulation. DLR Forschungsbericht 89-59, German Aerospace Center (DLR), Institute of Aeroelasticity, Göttingen, Germany, 1989.

[108] John. A. Rule, David E. Cox, and Robert L. Clark. Aerodynamic model reduction through balanced realization. *AIAA Journal*, 42(5):1045–1048, May 2004. Technical Notes.

[109] Hermann Schlichting and Erich Truckenbrodt. *Aerodynamik des Flugzeugs*, volume 1. Springer-Verlag, 2nd edition, 1967.

[110] Hermann Schlichting and Erich Truckenbrodt. *Aerodynamik des Flugzeugs*, volume 2. Springer-Verlag, 2nd edition, 1967.

[111] Jörg Schuler. *Flugregelung und aktive Schwingungsdämpfung für flexible Grossraumflugzeuge*. Doktorarbeit, Universität Stuttgart, Germany, 1998.

[112] N. Siepenkötter and W. Alles. Stability analysis fo the nonlinear dynamics of flexible aircraft. In *DGLR Deutscher Luft- und Raumfahrtkongress*, number DGLR-2002-201, pages 301–310, Stuttgart, Germany, sep 2002.

[113] Timothy A. Smith, James W. Hakanson, and Satish S. Nair. State-space model generation for flexible aircraft. *AIAA Journal of Aircraft*, 41(6):1473–1481, 2004.

[114] H. Söhngen. Zur Frage der Lösung der flugmechanischen Bewegungsgleichungen bei instationären Luftkraftansätzen. Technical Report P-31-7, Deutsche Versuchsanstalt für Luftfahrt, Institut für Aerodynamik, Berlin-Adlershof, 1941.

[115] Brain L. Stevens and Frank L. Lewis. *Aircraft Control and Simulation*. John Wiley & Sons, Inc., 1992.

[116] Thomas William Strganac. *Numerical model of unsteady subsonic aeroelastic behavior*. PhD thesis, Virginia Polytechnic Institute and State University, VA, USA, 1987. vortex lattice.

[117] Christopher Szymendera. Computational free wake analysis of a helicopter rotor. Master's thesis, The Pennsylvania State University, 2002. vortex lattice.

[118] Deman Tang, Earl H. Dowell, and Kenneth C. Hall. Limit cycle oscillations of a cantilevered wing in low subsonic flow. *AIAA Journal*, 37(3):364–371, Mar 1999.

[119] John C. Tannehill, Dale A. Anderson, and Richard H. Pletcher. *Computational fluid mechanics and heat transfer*. Series in computational and physical processes in mechanics and thermal sciences. Taylor & Francis, 2nd edition, 1997.

[120] The Mathworks. *MATLAB External Interfaces*, 6th edition, 2003.

[121] The Mathworks. *Writing S-Functions*, 5th edition, 2004.

[122] H. Tijedeman. Investigation of the transonic flow around oscillating airfoils. Technical Report TR77U90, Nationaal Lucht- en Ruimtevaartlaboratorium (NLR), 1977.

[123] Murray Tobak. On the use of the indicial function concept in the analysis of unsteady motions of wings and wing-tail combinations. NACA Technical Report NACA-TR-1188, Ames Aeronautical Laboratory, Moffett Field, CA, USA, 1954.

[124] P.A. van Gelder et al. F-16 wing loads under heavy load conditions. In *Proceedings of the International Forum on Aeroelasticity and Structural Dynamics*, Amsterdam, The Netherlands, June 2003.

[125] Willem H. J. J. van Staveren. *Analyses of aircraft responses to atmospheric turbulence*. PhD thesis, Delft University of Technology, NL, 2003.

[126] D. Vasilyev and J. White. A more reliable reduction algorithm for behavioral model extraction. In *Proceedings of the International Conference on Computer Aided Design, San Jose, CA (USA)*, 2005.

[127] R. Vepa. *Finite state modelling of aeroelastic systems*. PhD thesis, Department of Applied Mechanics, Stanford University, Jun 1975.

[128] Dan D. Vicroy and Truc Nguyen. A numerical simulation study to develop an acceptable wake encounter boundary for a b737-100 airplane. In *AIAA Atmospheric Flight Mechanics Conference, San Diego, CA, USA*, number AIAA-1996-3372, Jul 1996.

[129] Th. von Kármán and W. R. Sears. Airfoil theory for non-uniform motion. *Journal of the Aeronautical Sciences*, 5(10):379–390, Aug 1938.

[130] Herbert Wagner. Über die Entstehung des dynamischen Auftriebs von Tragflügeln. *Z.F.A.M.M.*, 5(1):17–35, 1925.

[131] A. B. Walden and C. P. van Dam. Study of the mutual interaction between a wing wake and an encountering airplane. Nasa cr-97-206493, Department of Mechanical and Aeronautical Engineering, University of California, Davis, CA, USA, 1997. wake vortex with PMARC.

[132] Zhicun Wang. *Time-domain simulations of aerodynamic forces on three-dimensional configurations, unstable aeroelastic responses, and control by neural network systems*. PhD thesis, Virginia Polytechnic Institute and State University, VA, USA, 2004.

[133] Martin R. Waszak and David K. Schmidt. Flight dynamics of aeroelastic vehicles. *AIAA Journal of Aircraft*, 25(6):563–571, 1988.

[134] F. Wille. Theorie des schwingenden Streckenprofils bei kompressibler Unterschallströmung. Teil 2: Berechnung der Küssnerschen Wirbelschleppenfunktion (T-Funktion). Technical Report DLR-FB 68-60, DLR, 1968.

[135] David J. Willis, Jaime Peraire, and Jacob K. White. A combined pFFT-multipole tree code, unsteady panel method with vortex particle wakes. In *43rd AIAA Aerospace Scineces Meeting and Exhibit, Reno, N.V.*, number 2005-0854, 2005.

[136] B.A. Winther, P.J. Goggin, and J.R. Dykman. Reduced-order dynamic aeroelastic model development and integration with nonlinear simulation. *AIAA Journal of Aircraft*, 37(5):833–839, 2000.

[137] Zheng-Yin Ye. A nonlinear vortex lattice method for unsteady flow with separated vortex. Forschungsbericht 94-32, Institute of Aeroelasticity, German Aerospace Center (DLR), Göttingen, Germany, 1994.

[138] H. M. Youssef, A. P. Nayak, and K. G. Gousman. Integrated total and flexible body dynamics of fixed wing aircraft. In *Proceedings of the AIAA/ASME/ASCE/AHS Structures, Structural Dynamics and Materials Conference*, number 3, pages 1230–1236, 1988.

[139] Yunkai Zhou and D.C. Sorensen. Approximate implicit subspace iteration with alternating directions for LTI system model reduction. *Numerical Linear Algebra with Applications*, 2007. URL `http://faculty.smu.edu/yzhou/publications.htm`. Unpublished.

[140] H. Zingel. Measurement of steady and unsteady airloads on a stiffness scaled model of a modern transport aircraft wing. In *International Forum on Aeroelasticity and Structural Dynamics*, number 91-069, Aachen, Germany, June 1991.

[141] Gabriel Zrenner. Approximation instationärer luftkräfte eines Tragflügels für die Echtzeit-Flugsimulation. [approximation of unsteady aerodynamic loads on a wing for real-time flight simulation]. Diplomarbeit, Technical University of Berlin, Germany, 1996.

A Validation of the Vortex Lattice Method

A.1 Lifting Surfaces

The validation of the VLM for finite lifting surfaces is carried out on a typical transport aircraft wing (AMP wing, see Zingel [140]) by comparison with the Doublet Lattice Method (DLM) as developed by Albano and Rodden [1], the industry's standard tool for frequency domain aerodynamics. In Fig. A.1, the wing discretization used for both methods with 14 chordwise and 37 spanwise panels is shown together with the wake discretization for the VLM. The wake step size is set to 25% chord length of the largest wing panel and the wake extends 3 wing semi-spans in the downstream direction.

For the validation of the VLM for 2D thin airfoils, two different approaches can be chosen. Either a rectangular wing with very high aspect ratio is modelled and the lift and moment of a strip at midspan where the 3D effect is small are compared to the analytical results. Or a rectangular wing with very high aspect ratio is modelled with only one spanwise vortex element and the velocity induced by the streamwise vortex filaments is omitted. Both approaches yield similar results and subsequently a panel grid with 10 chordwise vortex loops and a wake extending more than 70 chord lengths is employed.

A.1.1 Steady 3D Solution

Steady state results of the AMP wing are shown in Fig. A.2 together with results of the DLM, which for zero reduced frequency is equivalent to the VLM. The plots show the spanwise local load $k_z l/l_g$ and moment distributions $k_m l/l_g$ versus the non-dimensional spanwise coordinate $\eta = 2y/b$ for an angle of attack $\alpha = 1^\circ$ and a Mach number $M = 0.5$. The agreement is perfect and validates the steady state implementation including the Prandtl-Glauert compressibility correction.

A.1.2 Unsteady 2D Solutions

Analytical solutions for the unsteady aerodynamic loading of a thin airfoil in incompressible potential flow are well known and can be found for instance in Bisplinghoff et al. [8]. In the following, these analytical solutions are used to validate the unsteady VLM in both frequency and time domain. For the frequency domain validation, the HVLM as described in 2.2.6 is used and for the time domain validation, the normal time stepping procedure is applied.

Analytically, a thin airfoil undergoing harmonic vertical translation with amplitude

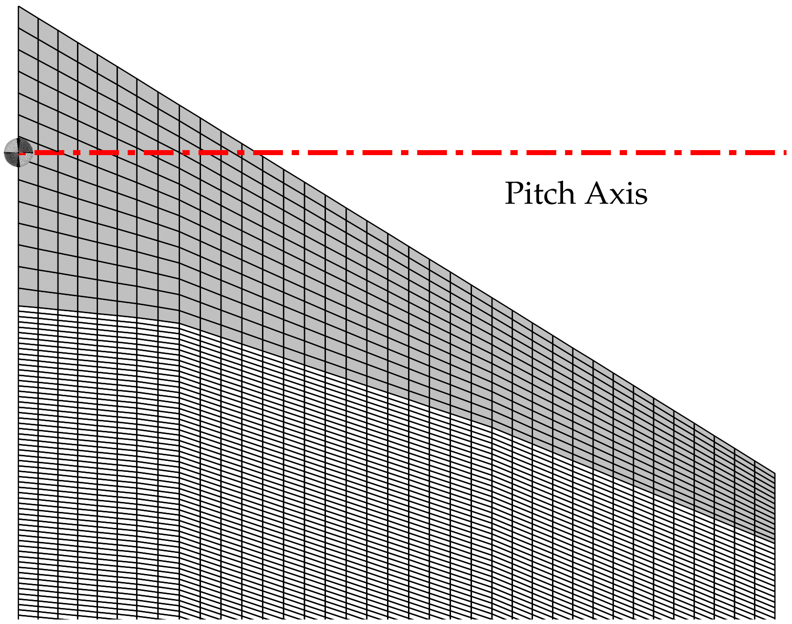

Figure A.1: Surface Grid of Typical Transport Aircraft Wing

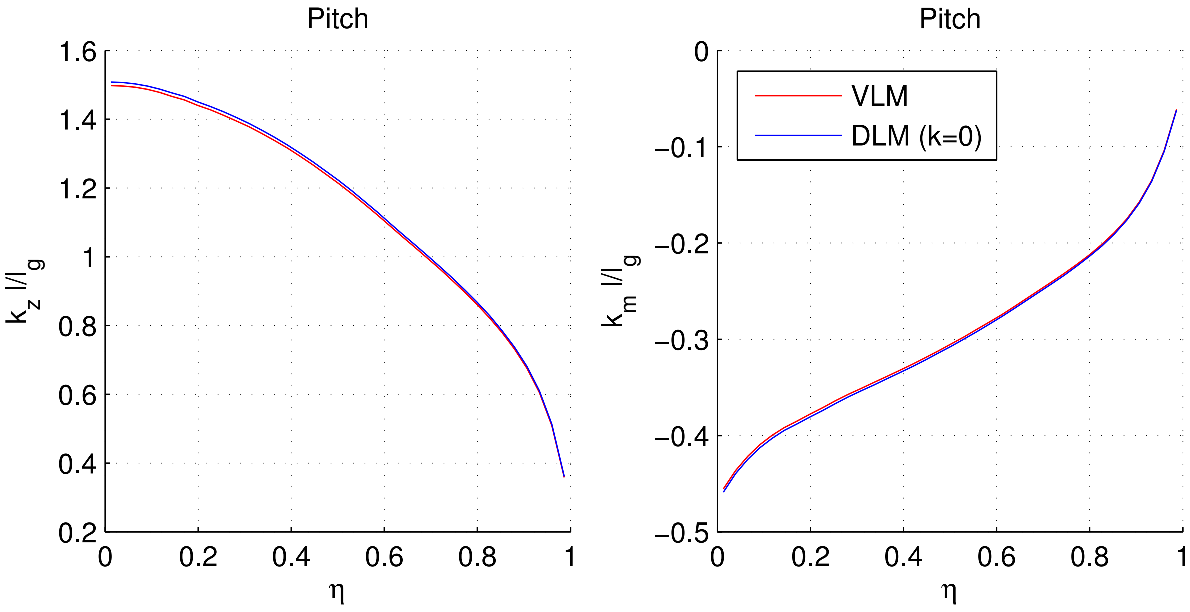

Figure A.2: Validation of VLM with Doublet Lattice Method (AMP Wing Distributions for $k = 0$,$M = 0.5$, $\alpha = 1°$)

h and pitching motion about midchord with amplitude α experiences the complex lift coefficient $c_l = l/(q_\infty c)$ and complex moment coefficient about midchord $c_m = m/(q_\infty c^2)$

$$\begin{aligned} h &= \bar{h}\,\mathrm{e}^{\mathrm{i}k\tau} & \alpha &= \bar{\alpha}\,\mathrm{e}^{\mathrm{i}k\tau} \\ \frac{c_l}{2\bar{h}/c} &= 2\pi \mathrm{i}kC(k) - \pi k^2 & \frac{c_l}{\bar{\alpha}} &= \pi \mathrm{i}k + \pi C(k)(\mathrm{i}k + 2) \\ \frac{c_m}{2\bar{h}/c} &= \pi \mathrm{i}kC(k) & \frac{c_m}{\bar{\alpha}} &= \frac{1}{8}k^2\pi - \frac{1}{2}\mathrm{i}k\pi + \pi C(k)(\frac{1}{2}\mathrm{i}k + 1) \end{aligned}$$

Here $k = \omega c/2V$ is the reduced frequency with respect to semichord, $\tau = tc/2V$ is the nondimensional time and $C(k)$ is the complex unsteady lift deficiency function, also known as Theodorsen function.

A thin airfoil travelling in a harmonic vertical gust field with amplitude w_G experiences the complex lift and moment coefficient about mid chord

$$\begin{aligned} w_G &= \bar{w}_G \mathrm{e}^{\mathrm{i}k(\tau-\xi)} \\ \frac{c_l}{\bar{w}_G/V} &= 2\pi S(k) \\ \frac{c_m}{\bar{w}_G/V} &= \pi S(k) \end{aligned}$$

Here $\xi = 2x/c$ is the nondimensional position on the airfoil ($-1 < \xi < 1$) and $S(k)$ is the complex gust load function, also known as Sears function.

Comparison plots for these three harmonic cases are depicted in Fig. A.3. The numerical results agree very well with the analytical solutions up to reduced frequencies of $k = 5$, both for rigid body motion and gust. There is a slight trend of increased disagreement towards the higher reduced frequencies, but no effort has been made to optimize the number of chordwise panels, wake step size or wake trailing edge offset.

In the time domain, two important analytical solutions are given for a thin airfoil undergoing a step change of angle of attack and entering a sharp-edged gust. For the angle of attack step, the transient lift coefficient was derived by Wagner [130] and can be approximated as (see Bisplinghoff et al. [8])

$$\begin{aligned} \frac{c_l(\tau)}{c_l(\tau \to \infty)} &= \phi(\tau) \\ \phi(\tau) &\approx 1 - 0.165\,\mathrm{e}^{-0.0455\tau} - 0.335\,\mathrm{e}^{-0.3\tau} \end{aligned}$$

in terms of Wagner's function $\phi(\tau)$. In addition, Jones [59] provided approximations for elliptical wings with finite aspect ratio, for $\Lambda = 6$ the result is

$$\phi(\tau)_{\Lambda=6} \approx 1 - 0.3694\,\mathrm{e}^{-0.324\tau}$$

The lift transient due to airfoil entering a sharp edged gust was derived by Küssner [72] and can be approximated as (see Bisplinghoff et al. [8])

$$\begin{aligned} \frac{c_l(\tau)}{c_l(\tau \to \infty)} &= \psi(\tau) \\ \psi(\tau) &\approx 1 - 0.5\,\mathrm{e}^{-0.130\tau} - 0.5\,\mathrm{e}^{-\tau} \end{aligned}$$

in terms of Küssner's function $\psi(\tau)$.

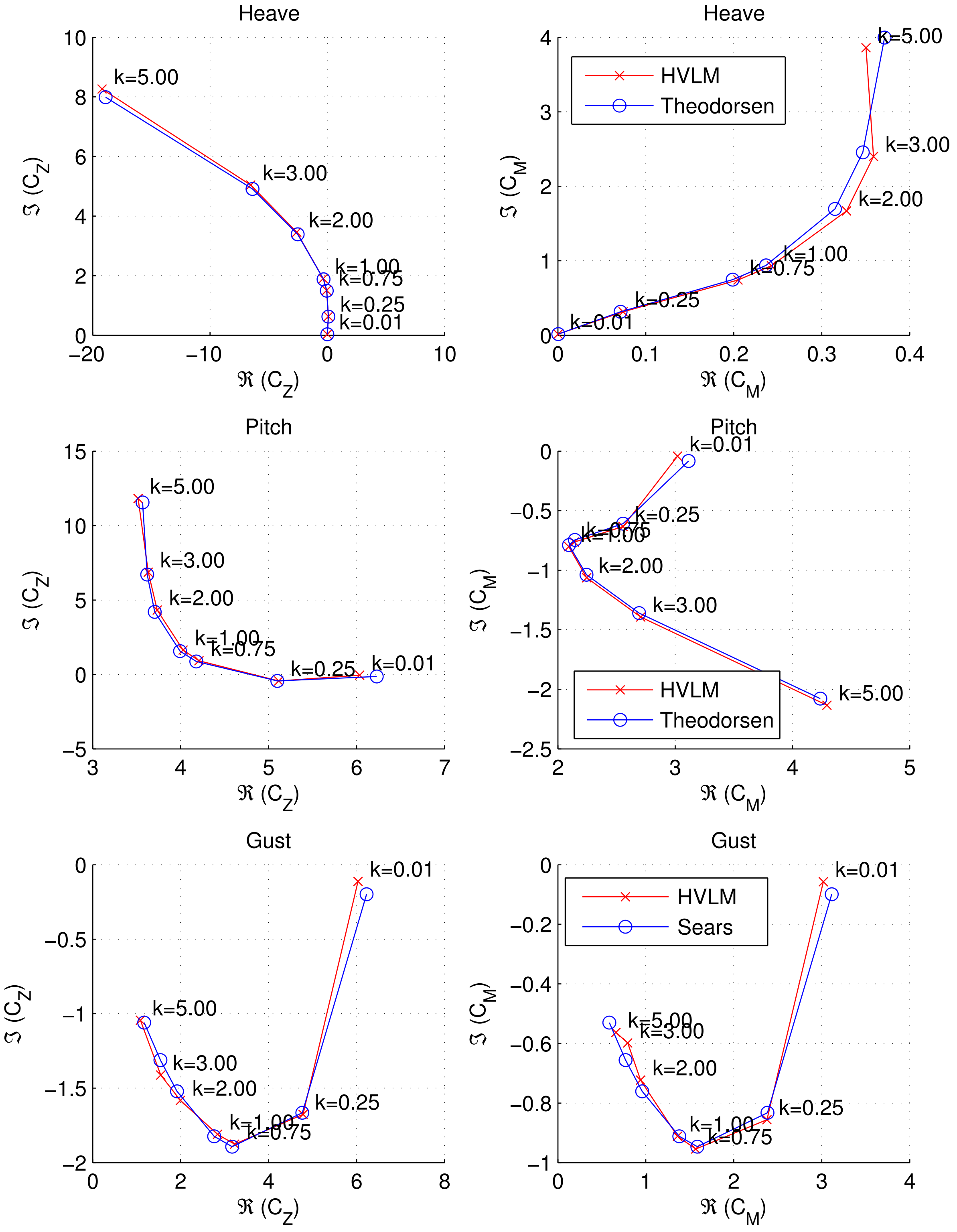

Figure A.3: Validation of HVLM with Analytical Solutions

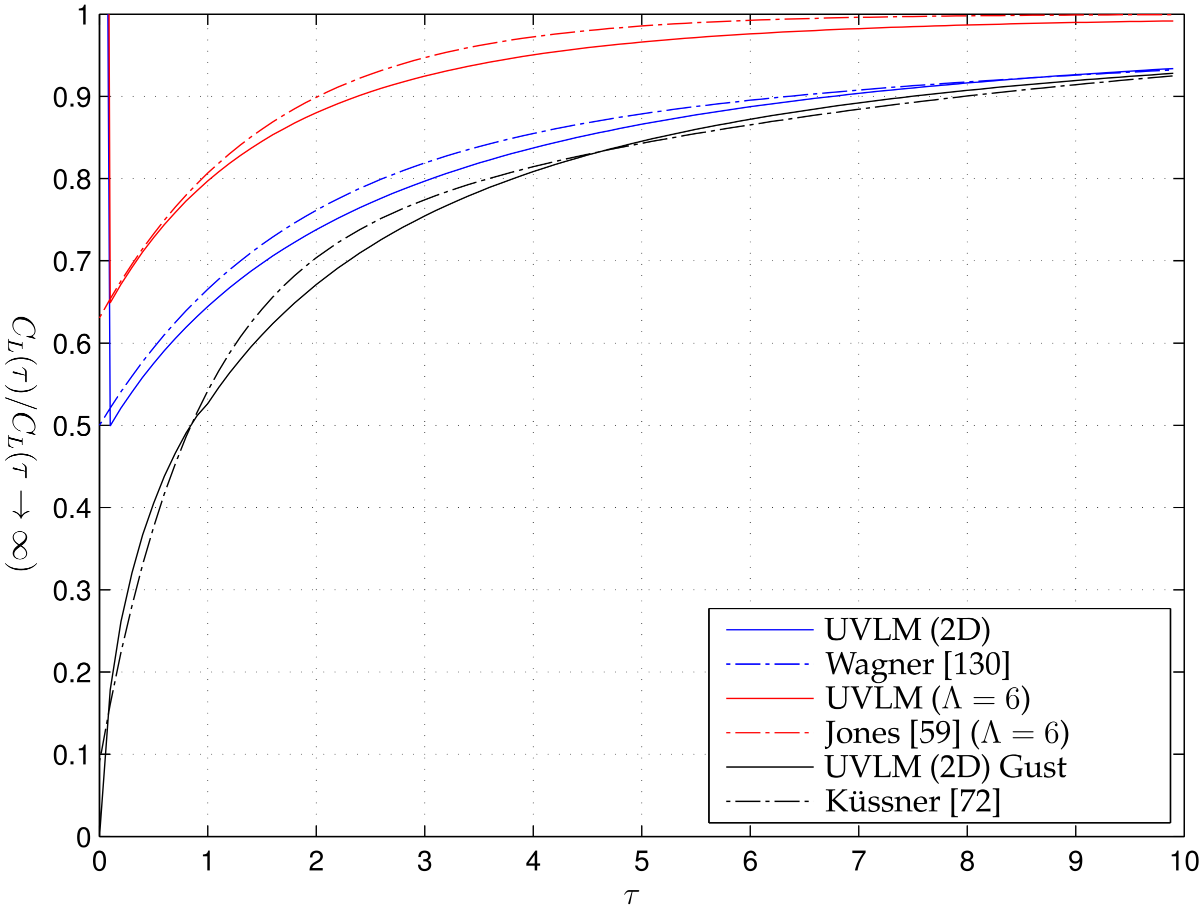

Figure A.4: Validation of UVLM with Analytical Solutions

In Fig. A.4, the time domain results of the VLM are compared to the analytical solutions. For the angle of attack step case with finite aspect ratio, a rectangular wing with $\Lambda = 6$ was simulated and not an elliptical wing as assumed by Jones. The simulation results agree very well with the analytical results for small values of τ. In the intermediate time frame ($\tau < 5$), small discrepancies can be perceived in the sense that the UVLM lift grows slower than analytically predicted. For larger time values the curves converge.

A.1.3 Unsteady 3D Solutions

Analogously to the 2D case, total wing lift and moment coefficients for heaving and pitching motion as well as harmonic vertical gust are shown for the AMP wing in Fig. A.5. The lateral axis used for pitching motion running through the moment reference point at 50% of the wing root chord is shown in Fig. A.1. The HVLM results are comparted to DLM results and again show very good agreement for reduced frequencies based on the aerodynamic mean chord of the wing $k = \omega l_A/V$ up to 2. To illustrate the small magnitude of discrepancy, the spanwise local load $k_z l/l_g$ and moment distributions $k_m l/l_g$ for a reduced frequency $k = 2$ are plotted versus the non-dimensional spanwise coordinate $\eta = 2y/b$ in Fig. A.6. The agreement with DLM is less favorable on the inboard part of the wing, where HVLM overpredicts lift and moment. To ensure that this discrepancy is not due to wrong implementation of the method of images for the left half of the wing, results are recomputed with a full model but only confirm the previous findings.

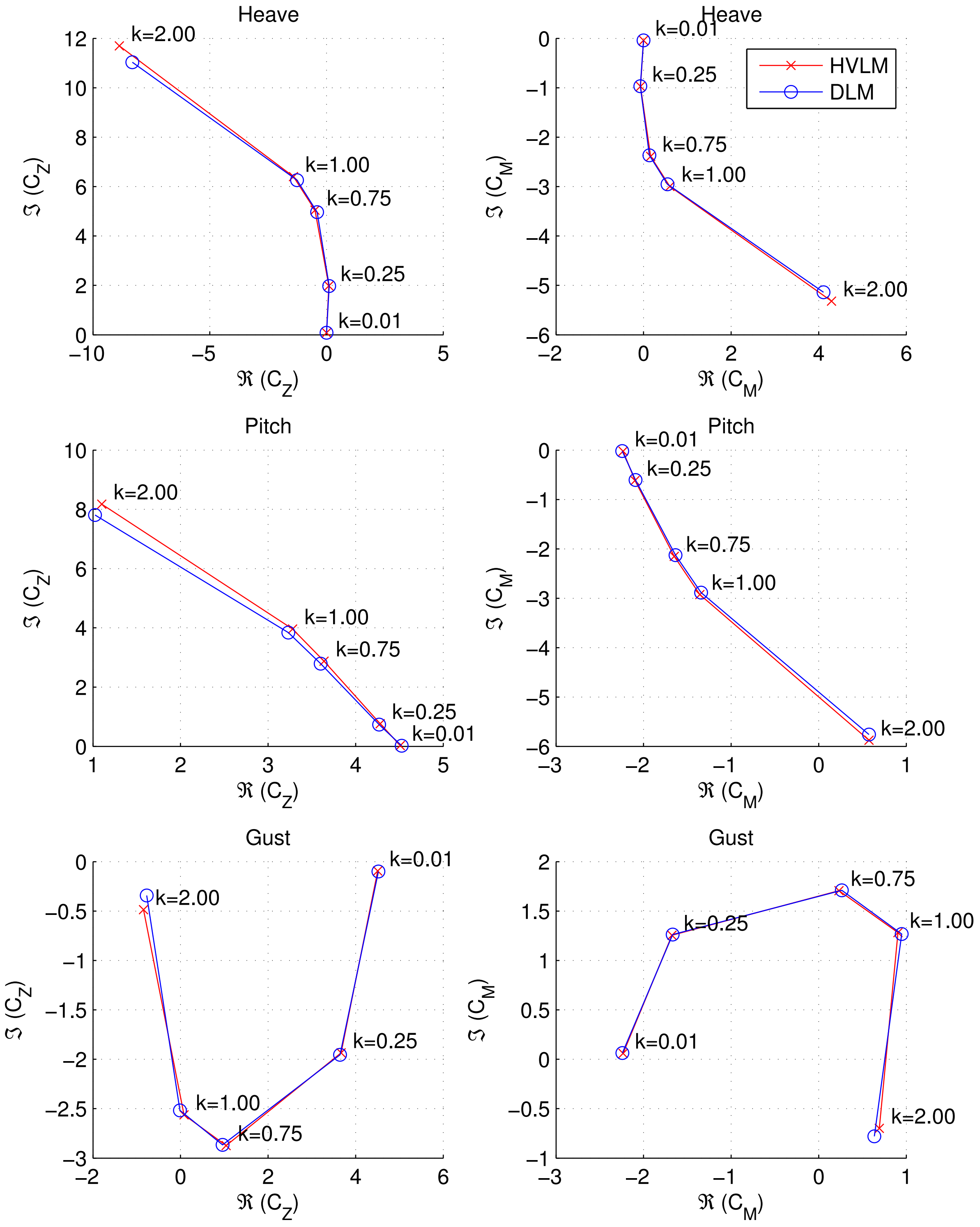

Figure A.5: Validation of HVLM with Doublet Lattice Method (AMP Wing Totals)

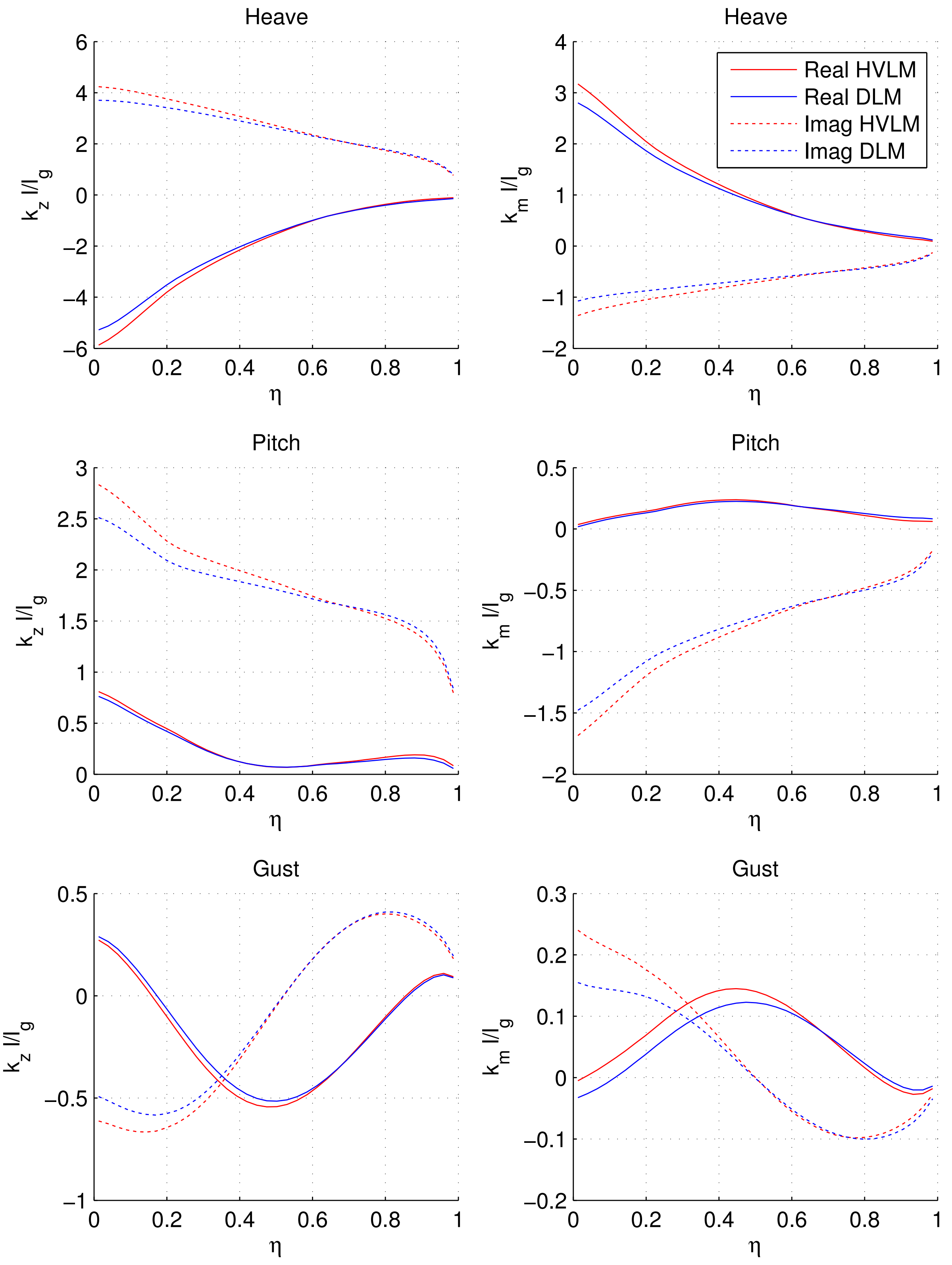

Figure A.6: Validation of HVLM with Doublet Lattice Method (AMP Wing Distributions for $k = 2$)

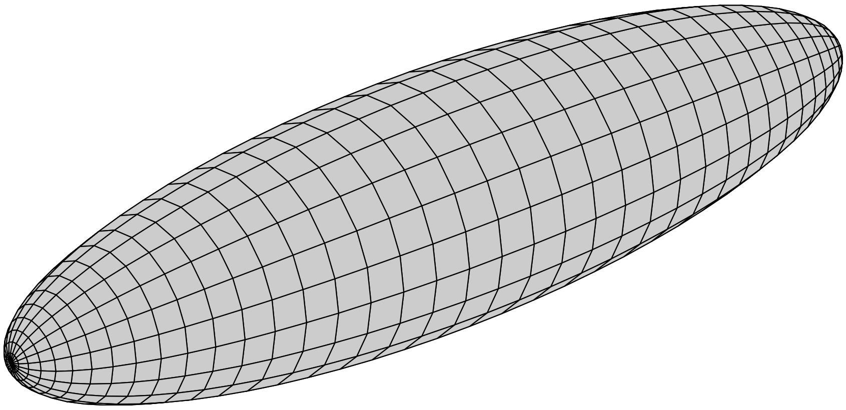

Figure A.7: Surface Grid of Ellipsoid with Aspect Ratio 4

A.2 Validation of Bodies

The validation of the VLM for bodies is carried out on a ellipsoid with aspect ratio $a/b = 4$. The surface panel discretization with 40 panels in the longitudinal and 20 panels in the circumferential direction is shown in Fig. A.7. Because the body is assumed to be non-lifting, no wake modelling is required.

A.2.1 Steady 3D Solution

Exact solutions for ellipsoids in steady, axial, incompressible potential flow can be found in for instance Schlichting and Truckenbrodt [110]. The pressure distribution in the streamwise direction is given by the relation

$$c_p(\xi) = 1 - A^2 \frac{1-\xi^2}{1-\left[1-\left(\frac{b}{a}\right)^2\right]\xi^2}$$

where a and b are the major and minor equatorial radius, respectively, A is a tabulated function with $A \approx 1.08$ for $a/b = 4$, and $\xi = \frac{x}{a}$ is the non-dimensional coordinate along the longitudinal body axis. The VLM pressure results for $\alpha = 0°$ are plotted together with the analytical results in Fig. A.8(a).

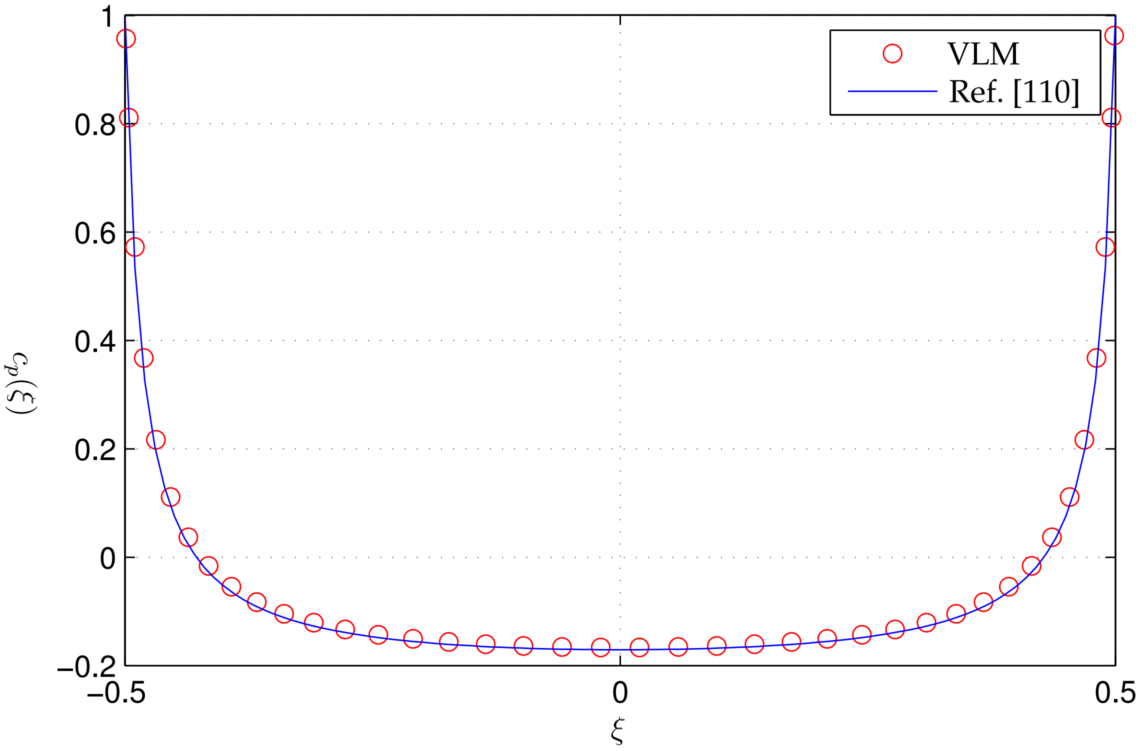

(a) $\alpha = 0°$

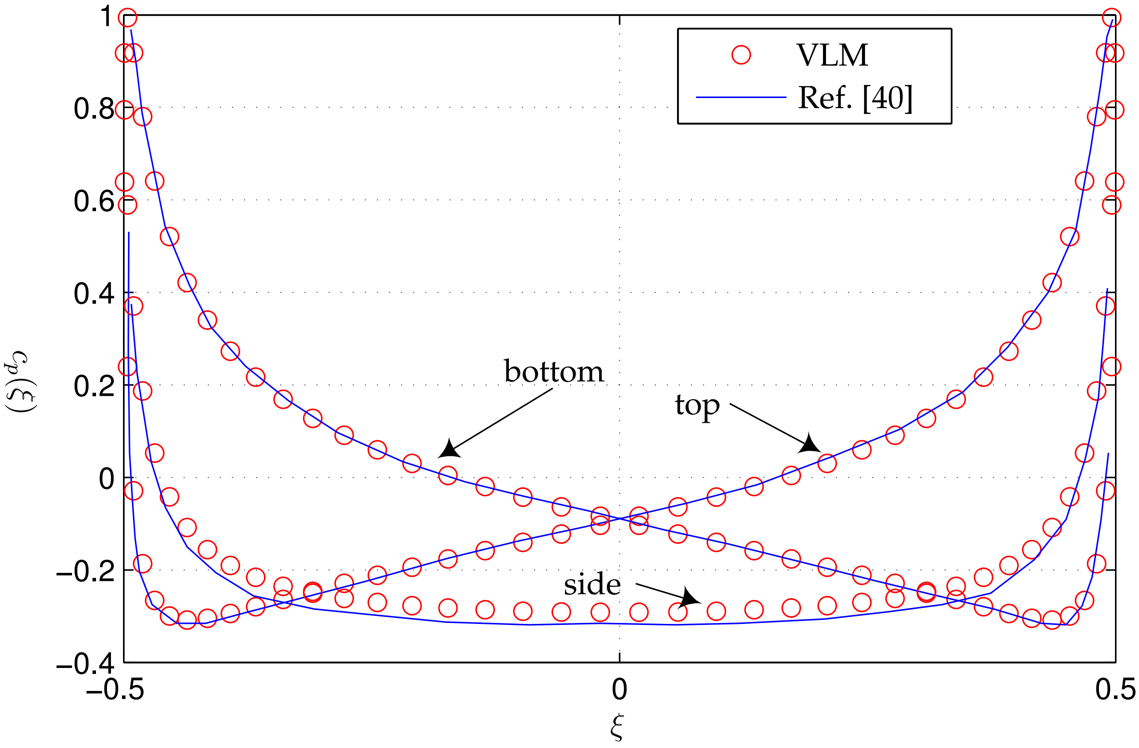

(b) $\alpha = 15°$

Figure A.8: Validation of VLM (Ellipsoid with Aspect Ratio 4)

Again, the agreement with exact theory is very good. Steady and unsteady numerical solutions for ellipsoids in incompressible potential flow were published by Geissler [40]. He employed a boundary element method with sources in the shape of truncated cones to represent body of revolutions and derived the solution for non-slender bodies at incidence and undergoing finite amplitude motion. In Fig. A.8(b), the VLM results for the ellipsoid at an angle of attack of $\alpha = 15^\circ$ are compared to Geissler's results on the upper, lower and side of body. The agreement on the upper and lower body is excellent, on the side of the body a small discrepancy is visible. This could be due to the required interpolation of pressures of the VLM on the horizontal cut as the cut is also a panel boundary.

A.2.2 Unsteady 3D Solution

Geissler's [40] unsteady results for the heave and pitch motion of the ellipsoid are compared to the HVLM results in Fig. A.9. The steady angle of attack is $\alpha_0 = 0^\circ$, the reduced frequency based on the body length is $k = 2\omega a/V = 1$ and the pitching axis is located at the center of the body. Heave and pitch amplitude were both set to unity. Shown are the real and imaginary parts of the pressure distribution on the top of the body. The overall agreement is very good with the HVLM slightly underpredicting the suction peaks at the tips of the body compared to Geissler's method.

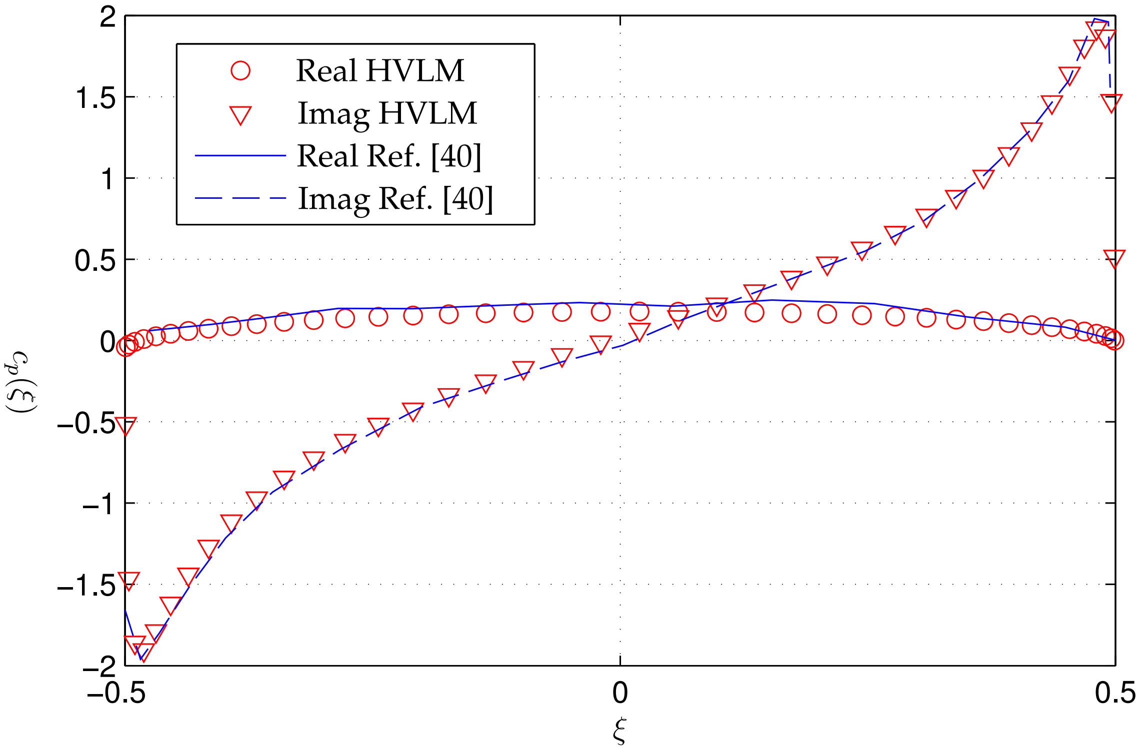

(a) Heave $k = 1$

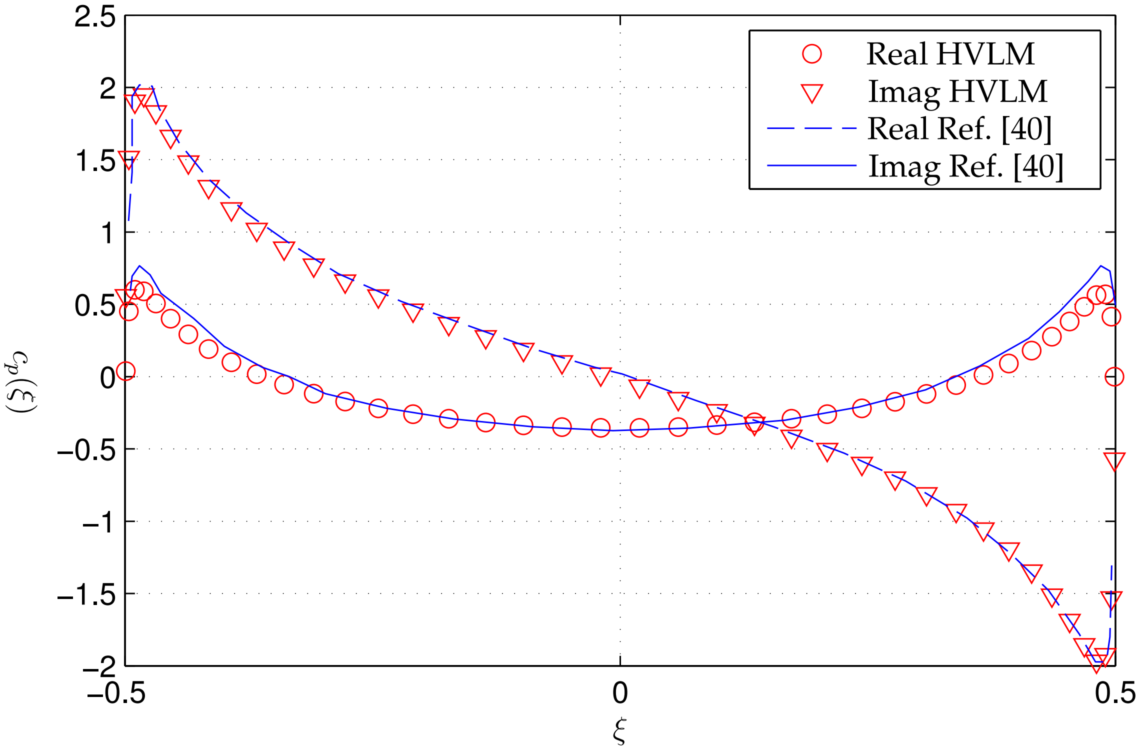

(b) Pitch $k = 1$

Figure A.9: Validation of HVLM (Ellipsoid with Aspect Ratio 4)

B Linearized Formulation of the Unsteady Vortex Lattice Method

The linearized formulation of the unsteady vortex lattice method as introduced in Chapter 2.2.3 requires the construction of several matrices and vectors, which will be described in detail below.

B.1 Linearized Downwash

The linearized downwash equation Eq. (2.2.36)

$$\delta \boldsymbol{d} = D_1 \boldsymbol{u}_\mathrm{A} + D_2 \dot{\boldsymbol{u}}_\mathrm{A} + D_3 \boldsymbol{u}_\mathrm{G}$$

contains the normalwash matrix D_1 due to panel displacement

$$D_1 = \begin{bmatrix} \boldsymbol{d}_{1,1} & \boldsymbol{0} & \dots & \boldsymbol{0} \\ \boldsymbol{0} & \boldsymbol{d}_{1,2} & \dots & \boldsymbol{0} \\ \vdots & \vdots & \ddots & \vdots \\ \boldsymbol{0} & \boldsymbol{0} & \dots & \boldsymbol{d}_{1,N_\mathrm{P}} \end{bmatrix} \quad \text{with} \quad \boldsymbol{d}_{1,k}^\mathrm{T} = \begin{Bmatrix} 0 \\ 0 \\ 0 \\ \boldsymbol{n} \times \boldsymbol{v}_\mathrm{R} \end{Bmatrix}_k ,$$

the normalwash matrix D_2 due to panel velocity

$$D_2 = \begin{bmatrix} \boldsymbol{d}_{2,1} & \boldsymbol{0} & \dots & \boldsymbol{0} \\ \boldsymbol{0} & \boldsymbol{d}_{2,2} & \dots & \boldsymbol{0} \\ \vdots & \vdots & \ddots & \vdots \\ \boldsymbol{0} & \boldsymbol{0} & \dots & \boldsymbol{d}_{2,N_\mathrm{P}} \end{bmatrix} \quad \text{with} \quad \boldsymbol{d}_{2,k}^\mathrm{T} = \begin{Bmatrix} \boldsymbol{n} \\ \Delta \boldsymbol{c}_{75} \times \boldsymbol{n} \end{Bmatrix}_k .$$

and the normalwash matrix D_3 due to atmospheric gust

$$D_3 = \begin{bmatrix} \boldsymbol{d}_{3,1} & \boldsymbol{0} & \dots & \boldsymbol{0} \\ \boldsymbol{0} & \boldsymbol{d}_{3,2} & \dots & \boldsymbol{0} \\ \vdots & \vdots & \ddots & \vdots \\ \boldsymbol{0} & \boldsymbol{0} & \dots & \boldsymbol{d}_{3,N_\mathrm{P}} \end{bmatrix} \quad \text{with} \quad \boldsymbol{d}_{3,k}^\mathrm{T} = -\boldsymbol{n}_k .$$

For body panels, the last three elements of $\boldsymbol{d}_{2,k}$ are set to zero as the collocation point is the panel centroid. Panel displacements and velocities at the panel centroid are collected in the vectors $\boldsymbol{u}_\mathrm{A}$ and $\dot{\boldsymbol{u}}_\mathrm{A}$, respectively:

$$\boldsymbol{u}_\mathrm{A} = \begin{Bmatrix} \boldsymbol{u}_1 \\ \boldsymbol{\varphi}_1 \\ \vdots \\ \boldsymbol{u}_{N_\mathrm{P}} \\ \boldsymbol{\varphi}_{N_\mathrm{P}} \end{Bmatrix} \quad \text{with} \quad \boldsymbol{u}_k = \begin{Bmatrix} u_x \\ u_y \\ u_z \end{Bmatrix}_k , \quad \boldsymbol{\varphi}_k = \begin{Bmatrix} \varphi_x \\ \varphi_y \\ \varphi_z \end{Bmatrix}_k$$

$$\dot{\boldsymbol{u}}_\mathrm{A} = \begin{Bmatrix} \dot{\boldsymbol{u}}_1 \\ \dot{\boldsymbol{\varphi}}_1 \\ \vdots \\ \dot{\boldsymbol{u}}_{N_\mathrm{P}} \\ \dot{\boldsymbol{\varphi}}_{N_\mathrm{P}} \end{Bmatrix} \quad \text{with} \quad \dot{\boldsymbol{u}}_k = \begin{Bmatrix} \dot{u}_x \\ \dot{u}_y \\ \dot{u}_z \end{Bmatrix}_k , \quad \dot{\boldsymbol{\varphi}}_k = \begin{Bmatrix} \dot{\varphi}_x \\ \dot{\varphi}_y \\ \dot{\varphi}_z \end{Bmatrix}_k$$

and the panel gust disturbances are assembled in the gust vector $\boldsymbol{u}_\mathrm{G}$

$$\boldsymbol{u}_\mathrm{G} = \begin{Bmatrix} \boldsymbol{u}_{\mathrm{G},1} \\ \vdots \\ \boldsymbol{u}_{\mathrm{G},N_\mathrm{P}} \end{Bmatrix} \quad \text{with} \quad \boldsymbol{u}_{\mathrm{G},k} = \begin{Bmatrix} u_{\mathrm{G},x} \\ u_{\mathrm{G},y} \\ u_{\mathrm{G},z} \end{Bmatrix}_k$$

where the gust velocities must be specified at the panel collocation point and resolved in the directions of the body axis system.

B.2 Linearized Loads of Lifting Surface Panels

The linearized load of lifting surface panels given in Eq. (2.2.37)

$$\boldsymbol{f}_\mathrm{A}/q_\infty = S_1 P\, \boldsymbol{\Gamma}_\mathrm{P} + S_2\, \dot{\boldsymbol{\Gamma}}_\mathrm{P}$$

contains the load matrix S_1 from linearization of the *Kutta-Joukowski* theorem

$$S_1 \;=\; \frac{2}{V_\infty^2} \begin{bmatrix} \boldsymbol{s}_{1,1} & \mathbf{0} & \dots & \mathbf{0} \\ \mathbf{0} & \boldsymbol{s}_{1,2} & \dots & \mathbf{0} \\ \vdots & \vdots & \ddots & \vdots \\ \mathbf{0} & \mathbf{0} & \dots & \boldsymbol{s}_{1,N_\mathrm{P}} \end{bmatrix} \quad \text{with} \quad \boldsymbol{s}_{1,k} = \begin{Bmatrix} \boldsymbol{v}_\mathrm{R} \times \boldsymbol{r} \\ (\boldsymbol{v}_\mathrm{R} \times \boldsymbol{r}) \times \Delta \boldsymbol{c}_{25} \end{Bmatrix}_k$$

the load matrix S_2 for the total derivative of the potential

$$S_2 = -\frac{2}{V_\infty^2} \begin{bmatrix} \boldsymbol{s}_{2,1} & \mathbf{0} & \dots & \mathbf{0} \\ \mathbf{0} & \boldsymbol{s}_{2,2} & \dots & \mathbf{0} \\ \vdots & \vdots & \ddots & \vdots \\ \mathbf{0} & \mathbf{0} & \dots & \boldsymbol{s}_{2,N_\mathrm{P}} \end{bmatrix} \quad \text{with} \quad \boldsymbol{s}_{2,k} = \begin{Bmatrix} A\,\boldsymbol{n} \\ 0 \\ 0 \\ 0 \end{Bmatrix}_k .$$

and the permutation matrix P to obtain the effective panel circulation where

$$P_{i,j} = \begin{cases} 1 & \text{if } i{=}j \\ -1 & \text{if panel } j \text{ is the upstream neighbor of panel } i. \end{cases}$$

The panel forces and moments with respect to the panel centroid are collected in the total panel load vector $\boldsymbol{f}_\mathrm{A}$

$$\boldsymbol{f}_\mathrm{A} = \begin{Bmatrix} \boldsymbol{f}_1 \\ \boldsymbol{m}_1 \\ \vdots \\ \boldsymbol{f}_{N_\mathrm{P}} \\ \boldsymbol{m}_{N_\mathrm{P}} \end{Bmatrix} \quad \text{with} \quad \boldsymbol{f}_k = \begin{Bmatrix} f_x \\ f_y \\ f_z \end{Bmatrix}_k , \quad \boldsymbol{m}_k = \begin{Bmatrix} m_x \\ m_y \\ m_z \end{Bmatrix}_k$$

B.3 Linearized Loads of Body Panels

The linearized steady load of body panels given in Eq. (2.2.38)

$$\boldsymbol{f}_\mathrm{A}/q_\infty = S_2 S_\mathrm{V} \left(\delta \boldsymbol{d}_\tau + (G + A_\tau) \boldsymbol{\Gamma}_\mathrm{P} + B_\tau \boldsymbol{\Gamma}_\mathrm{W} \right)$$

contains the panel velocity matrix S_V of the steady state

$$S_\mathrm{V} \;=\; \begin{bmatrix} \boldsymbol{s}_{\mathrm{V},1} & \mathbf{0} & \dots & \mathbf{0} \\ \mathbf{0} & \boldsymbol{s}_{\mathrm{V},2} & \dots & \mathbf{0} \\ \vdots & \vdots & \ddots & \vdots \\ \mathbf{0} & \mathbf{0} & \dots & \boldsymbol{s}_{\mathrm{V},N_\mathrm{P}} \end{bmatrix} \quad \text{with} \quad \boldsymbol{s}_{\mathrm{V}k}^\mathrm{T} = \begin{Bmatrix} (\boldsymbol{v}_\mathrm{R} + \boldsymbol{v}_\mathrm{ind} + \bar{\boldsymbol{v}})_0 \cdot \boldsymbol{\tau}_1 \\ (\boldsymbol{v}_\mathrm{R} + \boldsymbol{v}_\mathrm{ind} + \bar{\boldsymbol{v}})_0 \cdot \boldsymbol{\tau}_2 \end{Bmatrix}_k$$

and $\delta \boldsymbol{d}_\tau$ is the vector of tangential disturbance velocities on the body panels derived from

$$\delta \boldsymbol{d}_\tau = D_{1\tau} \boldsymbol{u}_\mathrm{A} + D_{2\tau} \dot{\boldsymbol{u}}_\mathrm{A} + D_{3\tau} \boldsymbol{u}_\mathrm{G}$$

with the tangential disturbance matrix $D_{1\tau}$ due to panel displacement

$$D_{1\tau} = \begin{bmatrix} D_{1\tau,1} & \mathbf{0} & \dots & \mathbf{0} \\ \mathbf{0} & D_{1\tau,2} & \dots & \mathbf{0} \\ \vdots & \vdots & \ddots & \vdots \\ \mathbf{0} & \mathbf{0} & \dots & D_{1\tau,N_\mathrm{P}} \end{bmatrix} \quad \text{with} \quad D_{1\tau,k} = \begin{bmatrix} 0 & 0 & 0 & (\boldsymbol{\tau}_1 \times \boldsymbol{v}_\mathrm{R})^\mathrm{T} \\ 0 & 0 & 0 & (\boldsymbol{\tau}_2 \times \boldsymbol{v}_\mathrm{R})^\mathrm{T} \end{bmatrix}_k$$

the tangential disturbance matrix $D_{2\tau}$ due to panel velocity

$$D_{2\tau} = \begin{bmatrix} D_{2\tau,1} & \mathbf{0} & \dots & \mathbf{0} \\ \mathbf{0} & D_{2\tau,2} & \dots & \mathbf{0} \\ \vdots & \vdots & \ddots & \vdots \\ \mathbf{0} & \mathbf{0} & \dots & D_{2\tau,N_\mathrm{P}} \end{bmatrix} \quad \text{with} \quad D_{2\tau,k} = \begin{bmatrix} -\boldsymbol{\tau}_1^\mathrm{T} & 0 & 0 & 0 \\ -\boldsymbol{\tau}_2^\mathrm{T} & 0 & 0 & 0 \end{bmatrix}_k$$

and the tangential disturbance matrices $D_{3\tau}$ due atmospheric velocity

$$D_{3\tau} = \begin{bmatrix} D_{3\tau,1} & \mathbf{0} & \dots & \mathbf{0} \\ \mathbf{0} & D_{3\tau,2} & \dots & \mathbf{0} \\ \vdots & \vdots & \ddots & \vdots \\ \mathbf{0} & \mathbf{0} & \dots & D_{3\tau,N_\mathrm{P}} \end{bmatrix} \quad \text{with} \quad D_{3\tau,k} = \begin{bmatrix} \boldsymbol{\tau}_1^\mathrm{T} \\ \boldsymbol{\tau}_2^\mathrm{T} \end{bmatrix}_k$$

Further on, G is the circulation differentiation matrix containing the derivative coefficients in the two tangential directions multiplied by 0.5. To illustrate its construction, assume the application of a standard central difference scheme. Denoting the target panel by (i,j) and placing the origin of the arc length at the target panel centroid, the coefficients of the second order polynomial for the circulation in the direction of $\boldsymbol{\tau}_1$ (the i-direction) is determined by the equation system:

$$\begin{Bmatrix} \Gamma_{i-1,j} \\ \Gamma_{i,j} \\ \Gamma_{i+1,j} \end{Bmatrix} = \begin{bmatrix} ||\boldsymbol{r}_{50i,j} - \boldsymbol{r}_{50i-1,j}||^2 & -||\boldsymbol{r}_{50i,j} - \boldsymbol{r}_{50i-1,j}|| & 1 \\ 0 & 0 & 1 \\ ||\boldsymbol{r}_{50i+1,j} - \boldsymbol{r}_{50i,j}||^2 & ||\boldsymbol{r}_{50i+1,j} - \boldsymbol{r}_{50i,j}|| & 1 \end{bmatrix} \begin{Bmatrix} a_{i,j} \\ b_{i,j} \\ c_{i,j} \end{Bmatrix}$$

where the distance between the panel centroids has been chosen as an approximate arc length. If a higher degree of accuracy is required, the arc length should be determined along line segments from the first panel centroid to the mid point of the common panel edge of the two panels and from there to the panel centroid of the second panel. The desired vortex sheet strength at the target panel is the first derivative of the second order polynomial evaluated at the arc length origin, therefore

$$\gamma_{\tau_1,i} = \begin{Bmatrix} 0 & 0 & 1 \end{Bmatrix} \begin{bmatrix} ||\boldsymbol{r}_{50i,j} - \boldsymbol{r}_{50i-1,j}||^2 & -||\boldsymbol{r}_{50i,j} - \boldsymbol{r}_{50i-1,j}|| & 1 \\ 0 & 0 & 1 \\ ||\boldsymbol{r}_{50i+1,j} - \boldsymbol{r}_{50i,j}||^2 & ||\boldsymbol{r}_{50i+1,j} - \boldsymbol{r}_{50i,j}|| & 1 \end{bmatrix}^{-1} \begin{Bmatrix} \Gamma_{i-1,j} \\ \Gamma_{i,j} \\ \Gamma_{i+1,j} \end{Bmatrix}$$

The derivative in the $\boldsymbol{\tau}_2$ (the j-direction) is formed analogously and both gradient vectors are sorted into the overall gradient matrix G such that

$$\boldsymbol{\gamma} = 2\mathsf{G}\boldsymbol{\Gamma}_\mathrm{P} \qquad \text{with} \quad \boldsymbol{\gamma} = \begin{Bmatrix} \gamma_{\tau_1,1} \\ \gamma_{\tau_2,1} \\ \vdots \\ \gamma_{\tau_1,N_\mathrm{P}} \\ \gamma_{\tau_2,N_\mathrm{P}} \end{Bmatrix}.$$

The tangential aerodynamic influence matrices A_τ and B_τ provide the induced tangential velocity of the bound vortex loops and wake, respectively:

$$\boldsymbol{v}_{\mathrm{ind},\tau} = \mathsf{A}_\tau\boldsymbol{\Gamma}_\mathrm{P} + \mathsf{B}_\tau\boldsymbol{\Gamma}_\mathrm{W} \qquad \text{with} \quad \boldsymbol{v}_{\mathrm{ind},\tau} = \begin{Bmatrix} v_{\mathrm{ind},\tau_1,1} \\ v_{\mathrm{ind},\tau_2,1} \\ \vdots \\ v_{\mathrm{ind},\tau_1,N_\mathrm{P}} \\ v_{\mathrm{ind},\tau_2,N_\mathrm{P}} \end{Bmatrix}.$$

The unsteady panel load due to the time derivative of the potential is given in Eq. (2.2.40)

$$\boldsymbol{f}_\mathrm{A}/q_\infty = \mathsf{S}_2\left(\left(\mathsf{I}_{0\mathrm{P}} + \mathsf{I}_\mathrm{P}\left(\mathsf{G} + \mathsf{A}_\tau\right)\right)\dot{\boldsymbol{\Gamma}}_\mathrm{P} + \left(\mathsf{I}_{0\mathrm{W}} + \mathsf{I}_\mathrm{P}\mathsf{B}_\tau\right)\dot{\boldsymbol{\Gamma}}_\mathrm{W}\right)$$

and contains the upstream potential matrix $\mathsf{I}_{0\mathrm{P}}$ and $\mathsf{I}_{0\mathrm{W}}$ for bound and wake panels, which can be determined from

$$\mathsf{I}_{0\mathrm{P}} = \boldsymbol{IT}_\infty\mathsf{A}_x$$
$$\mathsf{I}_{0\mathrm{W}} = \boldsymbol{IT}_\infty\mathsf{B}_x$$

Here we have introduced the trapezoidal integration vector for the induced velocity along the straight line extending upstream from the body apex

$$\boldsymbol{T}_\infty^\mathrm{T} = \frac{1}{2}\begin{Bmatrix} ||\boldsymbol{r}_{\mathrm{S},2} - \boldsymbol{r}_{\mathrm{S},1}|| \\ ||\boldsymbol{r}_{\mathrm{S},2} - \boldsymbol{r}_{\mathrm{S},1}|| \\ \vdots \\ ||\boldsymbol{r}_{\mathrm{S},N-1} - \boldsymbol{r}_{\mathrm{S},N-3}|| \\ ||\boldsymbol{r}_{\mathrm{S},N} - \boldsymbol{r}_{\mathrm{S},N-1}|| \end{Bmatrix}$$

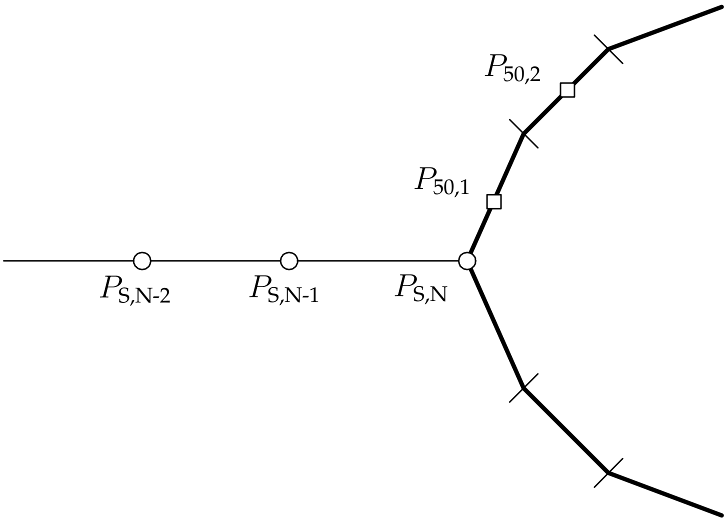

Figure B.1: Upstream Integration for the Potential

which applies trapezoidal integration to scalar values given at N control points $P_{\mathrm{S},i}$ distributed on a straight line extending upstream from the body apex as depicted in Fig. B.1. The two aerodynamic influence matrices A_x and B_x provide the induced velocities at these control points in the direction of the straight line and the unit vector $\boldsymbol{I}$ contains as many elements as there are body panels.

Finally, I_{P} is the body contour integration matrix

$$I_{\mathrm{P}} = \frac{1}{2}\begin{bmatrix} \boldsymbol{I}_{\mathrm{P},11} & \mathbf{0} & \dots & \mathbf{0} \\ \boldsymbol{I}_{\mathrm{P},21} & \boldsymbol{I}_{\mathrm{P},22} & \cdots & \mathbf{0} \\ \vdots & \vdots & \ddots & \vdots \\ \boldsymbol{I}_{\mathrm{P},N1} & \boldsymbol{I}_{\mathrm{P},N2} & \dots & \boldsymbol{I}_{\mathrm{P},NN} \end{bmatrix}$$

where the first row element $\boldsymbol{I}_{\mathrm{P},11}$ contains the trapezoidal integration coefficients from the apex to the first body panel centroid and subsequent rows are a copy of the preceding row plus the integration coefficients describing the integration from the previous panel centroid to the next one.

B.4 Discrete to Continuous Time Conversions of the Wake State Equation

In Section 2.2.3, the state space equation for the wake circulation was introduced as

$$\dot{\boldsymbol{\Gamma}}_{\mathrm{W}} = \bar{A}\boldsymbol{\Gamma}_{\mathrm{W}} + \bar{B}_1\boldsymbol{d} + \bar{B}_2\dot{\boldsymbol{d}}$$

and depending on the choice of approximation for the continuous time *Laplace* variable s, the coefficients of the state space equation assume different values. In the following tables, the continuous time coefficients resulting from three different types of numerical time integration are given in terms of the discrete time coefficients.

	Forward Rectangular: $s \approx \frac{z-1}{\Delta t}$
$\bar{A}$	$\frac{1}{\Delta t}\left(T_{\mathrm{W}} - T_{\mathrm{P}}A^{-1}B - I\right)$
$\bar{B}_1$	$-\frac{1}{\Delta t}T_{\mathrm{P}}A^{-1}$
$\bar{B}_2$	–

	Backward Rectangular: $s \approx \frac{1}{\Delta t}\frac{z-1}{z}$
$\bar{A}$	$\frac{1}{\Delta t}\left(T_{\mathrm{W}} - T_{\mathrm{P}}A^{-1}B\right)^{-1}\left(T_{\mathrm{W}} - T_{\mathrm{P}}A^{-1}B - I\right)$
$\bar{B}_1$	$-\frac{1}{\Delta t}\left(T_{\mathrm{W}} - T_{\mathrm{P}}A^{-1}B\right)^{-1}T_{\mathrm{P}}A^{-1}$
$\bar{B}_2$	$\left(T_{\mathrm{W}} - T_{\mathrm{P}}A^{-1}B\right)^{-1}T_{\mathrm{P}}A^{-1}$

	Bilinear: $s \approx \frac{2}{\Delta t}\frac{z-1}{z+1}$
$\bar{A}$	$\frac{2}{\Delta t}\left(T_{\mathrm{W}} - T_{\mathrm{P}}A^{-1}B + I\right)^{-1}\left(T_{\mathrm{W}} - T_{\mathrm{P}}A^{-1}B - I\right)$
$\bar{B}_1$	$-\frac{2}{\Delta t}\left(T_{\mathrm{W}} - T_{\mathrm{P}}A^{-1}B + I\right)^{-1}T_{\mathrm{P}}A^{-1}$
$\bar{B}_2$	$\left(T_{\mathrm{W}} - T_{\mathrm{P}}A^{-1}B + I\right)^{-1}T_{\mathrm{P}}A^{-1}$

As mentioned before, only the forward rectangular integration (*Euler*-integration) preserves the sparse structure of the state matrix $\bar{A}$ and from a computer memory point of view is the most feasible solution. To illustrate the low impact of this choice on the unsteady aerodynamic loading, the transfer function from heaving motion onto lift and pitching moment about the leading edge of a rectangular wing of aspect ratio 6 is shown in Fig. B.2. With increasing reduced frequency, the forward rectangular approximation yields a higher magnitude and phase angle than the bilinear approximation. At the highest reduced frequency examined here, the error in magnitude is less than 3% and the difference in phase angle is lower than 4%. In terms of model size, the forward rectangular approximation in this example requires only 1% of computer memory compared to the bilinear model.

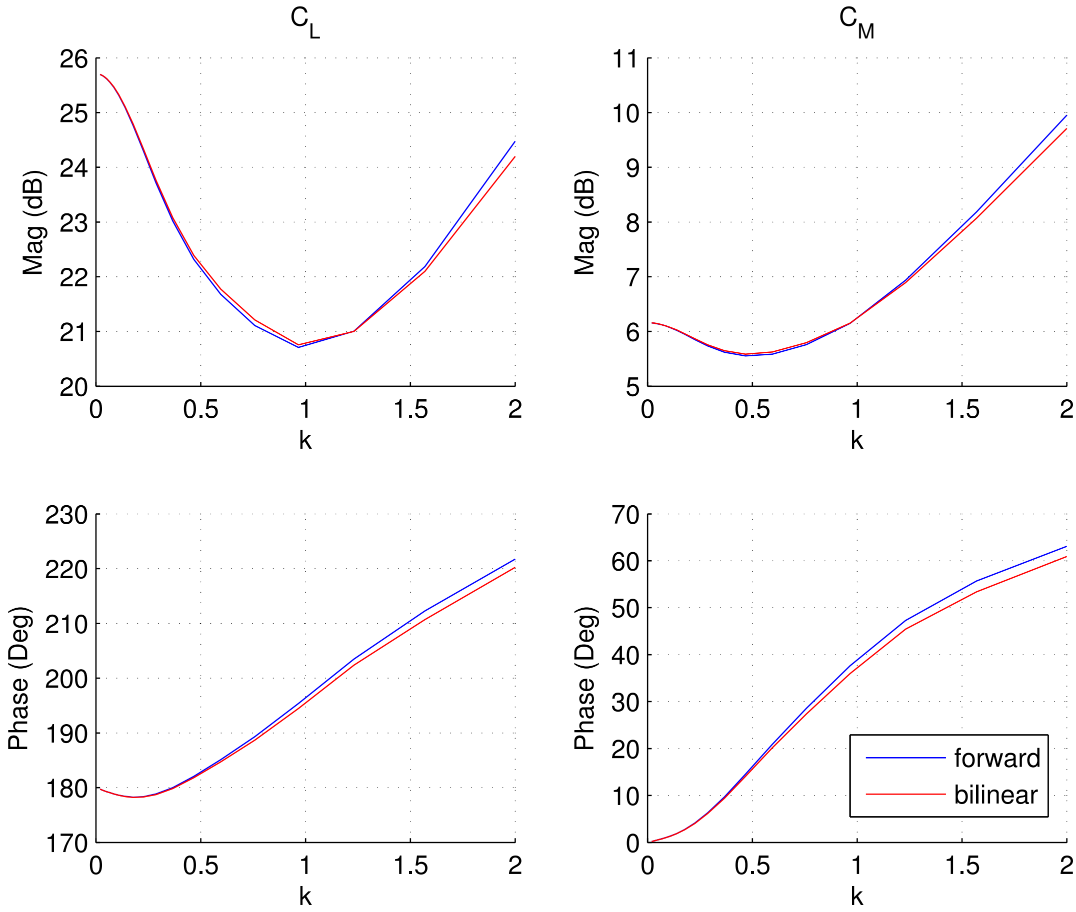

Figure B.2: Impact of Discrete to Continuous Time Transformations on the Transfer Function of a Rectangular Wing (AR=6) in Heaving Motion

C Aircraft Data

Length	73 m
Wing Span	79 m
Height	24 m
Mass	386 t
Approach Speed	146 kt (75 m/s)
Approach Mach	0.22
Wing Sweep (25% chord)	34°

Table C.1: Leading Aircraft: Airbus A380-800

Length	73 m
Wing Span	60 m
Height	17 m
Mass	209 t
Wing Sweep (25% chord)	30°

Table C.2: Follower Aircraft: Airbus A340-300

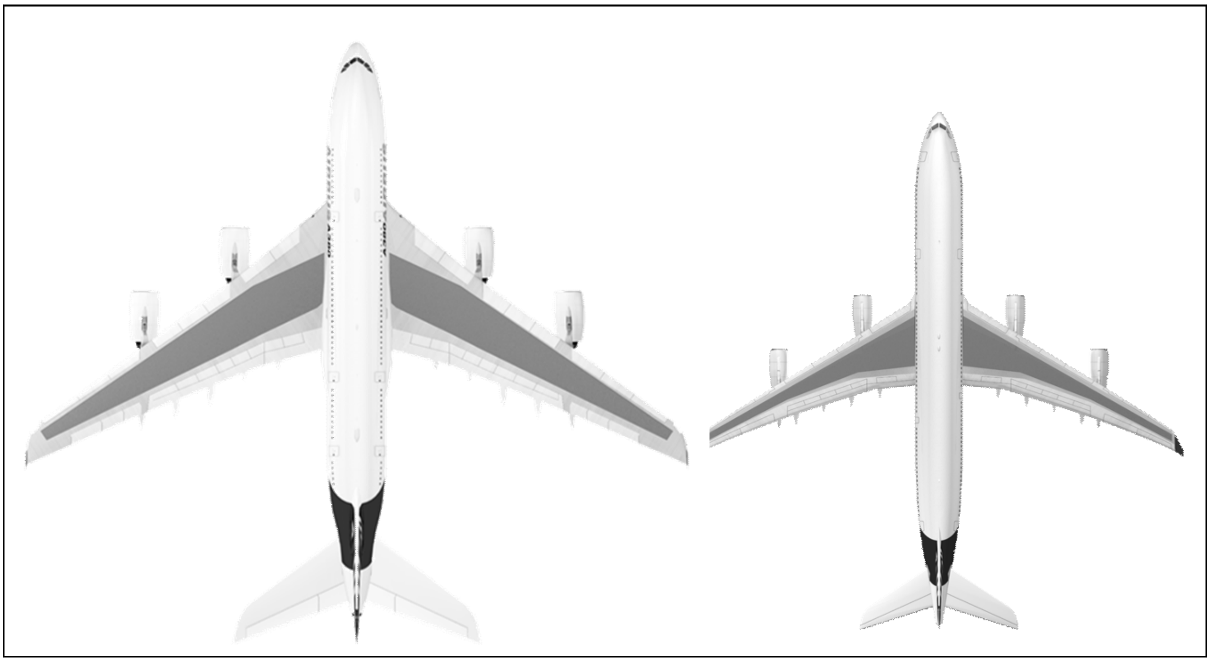

Figure C.1: Planform View of Airbus Aircraft

D Envelopes for Wake Vortex Encounter

This appendix contains the tabulated results from the parametric wake vortex encounter study using *Model 1* from Chapter 5. Given are flight loads and acceleration envelopes of all main structural components for simulations with and without autopilot. All values are normalized by the maximum positive value obtained on the respective components for simulations without autopilot. For every envelope point, a case key using the convention `AxxEyyHzzz` is given where `xx` is the wake azimuth angle ψ_V [DEG], `yy` is the elevation angle γ_V [DEG] and `zzz` is the vertical wake offset Δz_V [m].

D.1 Integrated Loads

D.1.1 Wing Envelopes

STN	Y [m]	T_Z [%]	Case	M_X [%]	Case	M_Y [%]	Case
1	2.79	92.91	A80E00H000	100.00	A70E00H000	100.00	A70E-5H000
2	3.12	86.45	A80E00H000	98.66	A70E00H000	94.57	A70E-5H000
3	3.70	95.25	A80E00H000	95.96	A70E00H000	90.07	A70E-5H000
4	4.40	97.28	A80E00H000	92.48	A70E00H000	88.03	A70E-5H000
5	5.07	100.00	A80E00H000	88.94	A70E00H000	88.12	A70E-5H000
6	5.40	97.63	A80E00H000	87.14	A70E00H000	85.51	A70E-5H000
7	6.22	94.98	A80E00H000	82.85	A70E00H000	76.84	A70E-5H000
8	7.71	93.88	A90E00H000	74.43	A70E00H000	63.05	A70E-5H000
9	8.94	92.38	A90E00H000	67.52	A70E00H000	54.42	A70E-5H000
10	9.80	98.76	A80E00H000	60.32	A70E00H000	42.19	A70E-5H000
11	11.13	95.15	A80E00H000	51.75	A70E00H000	38.20	A70E-5H000
12	12.91	86.19	A80E00H000	41.49	A70E00H000	30.25	A70E-5H000
13	14.69	71.89	A80E00H000	33.05	A70E00H000	24.49	A60E-5H000
14	16.47	61.18	A80E00H000	26.36	A70E00H000	20.28	A60E-5H000
15	18.27	50.70	A80E00H000	21.84	A60E00H000	16.63	A60E-5H000
16	19.38	45.42	A80E00H000	19.56	A60E00H000	14.85	A60E-5H000
17	19.82	50.26	A60E00H000	16.25	A60E00H000	10.26	A80E05H000
18	21.07	44.85	A70E00H000	12.38	A60E00H000	8.51	A80E05H000
19	23.08	38.84	A60E00H000	6.95	A60E00H000	6.63	A80E05H000
20	24.63	29.58	A60E00H000	3.91	A60E00H000	4.48	A80E05H000
21	25.79	21.48	A60E00H000	2.27	A60E00H000	2.94	A80E05H000
22	26.90	15.57	A60E00H000	1.17	A60E00H000	1.89	A80E05H000
23	27.84	9.45	A60E00H000	0.60	A60E00H000	0.79	A80E05H000
24	28.64	5.69	A60E00H000	0.30	A60E00H000	0.42	A30E00H000

Table D.1: Wing Maximum Envelope

STN	Y [m]	T_Z [%]	Case	M_X [%]	Case	M_Y [%]	Case
1	2.79	97.07	A80E00H000	99.99	A90E00H000	96.00	A70E-5H000
2	3.12	90.74	A80E00H000	98.36	A90E00H000	90.83	A70E-5H000
3	3.70	95.50	A80E00H000	95.37	A90E00H000	86.71	A70E-5H000
4	4.40	93.69	A80E00H000	91.67	A90E00H000	84.88	A70E-5H000
5	5.07	96.45	A80E00H000	87.83	A90E00H000	85.06	A70E-5H000
6	5.40	94.81	A80E00H000	85.88	A90E00H000	82.54	A70E-5H000
7	6.22	91.63	A80E00H000	81.12	A90E00H000	74.31	A70E-5H000
8	7.71	91.04	A90E00H000	72.57	A90E00H000	61.31	A70E-5H000
9	8.94	89.72	A90E00H000	65.53	A70E00H000	53.06	A70E-5H000
10	9.80	96.16	A80E00H000	59.08	A90E00H000	41.58	A70E-5H000
11	11.13	93.07	A90E00H000	50.90	A90E00H000	37.71	A70E-5H000
12	12.91	84.80	A90E00H000	40.91	A90E00H000	29.99	A70E-5H000
13	14.69	72.73	A90E00H000	32.29	A90E00H000	23.38	A60E-5H000
14	16.47	61.42	A90E00H000	25.49	A60E00H000	19.53	A60E-5H000
15	18.27	50.07	A90E00H000	21.16	A60E00H000	16.12	A60E-5H000
16	19.38	43.77	A80E00H000	18.97	A60E00H000	14.28	A60E-5H000
17	19.82	48.43	A60E00H000	15.78	A60E00H000	10.15	A80E05H000
18	21.07	43.18	A70E00H000	12.05	A60E00H000	8.45	A80E05H000
19	23.08	37.51	A60E00H000	6.80	A60E00H000	6.66	A80E05H000
20	24.63	28.73	A60E00H000	3.85	A60E00H000	4.38	A80E05H000
21	25.79	20.98	A60E00H000	2.25	A60E00H000	2.90	A80E05H000
22	26.90	15.32	A60E00H000	1.16	A60E00H000	1.87	A80E05H000
23	27.84	9.36	A60E00H000	0.60	A60E00H000	0.78	A80E05H000
24	28.64	5.66	A60E00H000	0.30	A60E00H000	0.39	A30E00H000

Table D.2: Wing Maximum Envelope (Closed Loop)

STN	Y [m]	T_Z [%]	Case	M_X [%]	Case	M_Y [%]	Case
1	2.79	-32.54	A80E00H000	-26.32	A90E00H000	-84.30	A70E00H000
2	3.12	-32.04	A80E00H000	-25.94	A90E00H000	-85.08	A70E00H000
3	3.70	-28.85	A80E00H000	-25.25	A90E00H000	-86.36	A70E00H000
4	4.40	-27.23	A80E00H000	-24.37	A90E00H000	-87.54	A70E00H000
5	5.07	-23.44	A80E00H000	-23.50	A90E00H000	-87.58	A70E00H000
6	5.40	-21.08	A80E00H000	-23.08	A90E00H000	-83.97	A70E00H000
7	6.22	-19.46	A90E00H000	-22.01	A90E00H000	-79.18	A70E00H000
8	7.71	-20.39	A90E00H000	-19.96	A90E00H000	-73.42	A70E00H000
9	8.94	-20.84	A90E00H000	-18.24	A90E00H000	-66.38	A70E00H000
10	9.80	-19.85	A90E00H000	-17.04	A90E00H000	-44.31	A70E00H000
11	11.13	-20.37	A90E00H000	-15.39	A90E00H000	-41.11	A70E00H000
12	12.91	-20.53	A90E00H000	-13.32	A90E00H000	-35.08	A70E00H000
13	14.69	-20.56	A90E00H000	-11.14	A90E00H000	-29.27	A70E00H000
14	16.47	-20.07	A90E00H000	-8.92	A90E00H000	-26.56	A60E00H000
15	18.27	-19.06	A90E00H000	-6.71	A90E00H000	-26.26	A60E00H000
16	19.38	-17.44	A90E00H000	-6.81	A70E00H000	-26.22	A60E00H000
17	19.82	-15.50	A90E00H000	-5.28	A70E00H000	-10.47	A70E00H000
18	21.07	-14.26	A90E00H000	-4.35	A70E00H000	-8.64	A70E00H000
19	23.08	-12.43	A90E00H000	-2.62	A70E00H000	-6.60	A80E00H000
20	24.63	-10.48	A70E00H000	-1.51	A70E00H000	-4.41	A80E00H000
21	25.79	-7.81	A70E00H000	-0.91	A70E00H000	-2.82	A80E00H000
22	26.90	-6.08	A70E00H000	-0.48	A70E00H000	-1.73	A80E00H000
23	27.84	-3.70	A70E00H000	-0.27	A70E00H000	-0.86	A80E00H000
24	28.64	-2.37	A70E00H000	-0.14	A70E00H000	-0.51	A60E00H000

Table D.3: Wing Minimum Envelope

STN	Y [m]	T_Z [%]	Case	M_X [%]	Case	M_Y [%]	Case
1	2.79	-36.83	A80E00H000	-29.31	A90E00H000	-83.87	A70E00H000
2	3.12	-36.20	A80E00H000	-28.87	A90E00H000	-84.55	A70E00H000
3	3.70	-33.07	A80E00H000	-28.05	A90E00H000	-85.82	A70E00H000
4	4.40	-31.38	A80E00H000	-27.03	A90E00H000	-86.99	A70E00H000
5	5.07	-27.58	A80E00H000	-26.02	A90E00H000	-87.07	A70E00H000
6	5.40	-25.21	A80E00H000	-25.53	A90E00H000	-83.51	A70E00H000
7	6.22	-22.60	A90E00H000	-24.30	A90E00H000	-78.72	A70E00H000
8	7.71	-23.22	A90E00H000	-21.96	A90E00H000	-72.34	A70E00H000
9	8.94	-23.54	A90E00H000	-20.01	A90E00H000	-65.35	A70E00H000
10	9.80	-22.62	A90E00H000	-18.62	A90E00H000	-44.45	A70E00H000
11	11.13	-23.04	A90E00H000	-16.67	A90E00H000	-41.24	A70E00H000
12	12.91	-22.93	A90E00H000	-14.31	A90E00H000	-35.19	A70E00H000
13	14.69	-22.63	A90E00H000	-11.90	A90E00H000	-29.34	A70E00H000
14	16.47	-21.83	A90E00H000	-9.48	A90E00H000	-26.07	A60E00H000
15	18.27	-20.52	A90E00H000	-7.56	A70E00H000	-25.83	A60E00H000
16	19.38	-18.60	A90E00H000	-7.59	A70E00H000	-25.84	A60E00H000
17	19.82	-16.51	A90E00H000	-5.94	A70E00H000	-10.77	A70E00H000
18	21.07	-15.16	A90E00H000	-4.82	A70E00H000	-8.88	A70E00H000
19	23.08	-13.80	A70E00H000	-2.83	A70E00H000	-6.78	A80E00H000
20	24.63	-11.67	A70E00H000	-1.60	A70E00H000	-4.52	A80E00H000
21	25.79	-8.53	A70E00H000	-0.94	A70E00H000	-2.89	A80E00H000
22	26.90	-6.48	A70E00H000	-0.49	A70E00H000	-1.76	A80E00H000
23	27.84	-3.83	A70E00H000	-0.27	A70E00H000	-0.87	A80E00H000
24	28.64	-2.39	A70E00H000	-0.14	A70E00H000	-0.50	A60E00H000

Table D.4: Wing Minimum Envelope (Closed Loop)

D.1.2 Horizontal Tail Envelopes

STN	Y [m]	T_Z [%]	Case	M_X [%]	Case	M_Y [%]	Case
1	1.16	100.00	A40E-5H000	100.00	A40E-5H000	100.00	A80E05H000
2	1.68	99.76	A40E-5H000	88.97	A40E-5H000	99.02	A80E05H000
3	2.70	96.67	A40E-5H000	67.93	A40E-5H000	93.23	A80E05H000
4	3.89	83.97	A30E-5H000	46.59	A40E-5H000	68.69	A80E05H000
5	5.26	67.93	A30E-5H000	26.38	A40E-5H000	45.08	A90E-5H000
6	6.64	50.04	A40E-5H000	11.55	A40E-5H000	28.67	A90E-5H000
7	7.83	31.41	A40E-5H000	3.62	A40E-5H000	14.96	A90E-5H000
8	8.79	13.99	A40E-5H000	0.71	A40E-5H000	5.63	A90E-5H000
9	9.35	6.06	A40E-5H000	0.09	A80E-5H000	1.98	A90E05H000

Table D.5: Horizontal Tail Maximum Envelope

STN	Y [m]	T_Z [%]	Case	M_X [%]	Case	M_Y [%]	Case
1	0.00	104.98	A40E-5H000	103.90	A50E-5H000	123.38	A70E05H000
2	0.52	104.70	A40E-5H000	92.01	A50E-5H000	123.04	A70E05H000
3	1.54	101.16	A40E-5H000	69.65	A50E-5H000	115.34	A70E05H000
4	2.73	106.06	A30E00H-10	47.29	A50E-5H000	85.81	A70E05H000
5	4.10	69.72	A40E-5H000	26.47	A50E-5H000	297.15	A30E00H-10
6	5.48	50.37	A50E-5H000	11.50	A50E-5H000	43.32	A70E05H000
7	6.67	31.05	A50E-5H000	3.62	A50E-5H000	16.78	A90E05H000
8	7.63	14.06	A50E-5H000	0.70	A50E-5H000	8.83	A30E00H010
9	8.20	6.13	A50E-5H000	0.10	A80E-5H000	2.17	A70E05H000

Table D.6: Horizontal Tail Maximum Envelope (Closed Loop)

STN	Y [m]	T_Z [%]	Case	M_X [%]	Case	M_Y [%]	Case
1	1.16	-100.22	A60E00H000	-83.47	A50E00H000	-61.22	A70E-5H000
2	1.68	-97.68	A60E00H000	-72.60	A50E00H000	-61.00	A70E-5H000
3	2.70	-88.70	A60E00H000	-52.98	A50E00H000	-57.06	A70E-5H000
4	3.89	-71.47	A50E00H000	-34.56	A50E00H000	-42.72	A70E-5H000
5	5.26	-53.45	A50E00H000	-18.58	A50E00H000	-29.32	A80E-5H000
6	6.64	-36.25	A50E00H000	-7.84	A50E00H000	-18.12	A70E-5H000
7	7.83	-21.49	A50E00H000	-2.43	A50E00H000	-10.33	A70E-5H000
8	8.79	-9.71	A50E00H000	-0.43	A50E00H000	-5.58	A50E-5H000
9	9.35	-3.80	A50E00H000	-0.11	A90E-5H000	-2.30	A60E-5H000

Table D.7: Horizontal Tail Minimum Envelope

STN	Y [m]	T_Z [%]	Case	M_X [%]	Case	M_Y [%]	Case
1	0.00	-116.80	A60E00H000	-97.91	A60E00H000	-69.33	A70E-5H000
2	0.52	-114.36	A60E00H000	-84.83	A60E00H000	-69.10	A60E-5H000
3	1.54	-104.16	A60E00H000	-61.58	A60E00H000	-64.58	A70E-5H000
4	2.73	-84.56	A60E00H000	-39.60	A60E00H000	-48.21	A60E-5H000
5	4.10	-176.11	A30E00H-10	-20.78	A60E00H000	-56.86	A70E00H-10
6	5.48	-41.42	A60E00H000	-8.48	A60E00H000	-19.83	A70E-5H000
7	6.67	-23.66	A60E00H000	-2.50	A60E00H000	-11.13	A70E-5H000
8	7.63	-10.46	A60E00H000	-0.39	A70E-5H000	-5.73	A50E-5H000
9	8.20	-3.72	A50E00H000	-0.11	A90E05H000	-2.36	A50E-5H000

Table D.8: Horizontal Tail Minimum Envelope (Closed Loop)

D.1.3 Vertical Tail Envelopes

STN	Z [m]	T_Y [%]	Case	M_X [%]	Case	M_Z [%]	Case
1	0.00	100.00	A30E00H000	100.00	A30E-5H-10	100.00	A30E05H000
2	0.64	93.45	A30E-5H-10	87.30	A30E-5H-10	76.52	A30E05H000
3	1.64	87.66	A30E-5H-10	67.82	A30E-5H-10	71.05	A30E05H000
4	2.64	79.08	A30E-5H-10	50.44	A30E-5H-10	47.03	A40E05H000
5	3.54	71.31	A30E-5H-10	35.58	A30E-5H-10	31.15	A40E05H000
6	4.57	60.17	A30E-5H-10	21.91	A30E-5H-10	15.49	A40E05H000
7	5.37	51.02	A30E-5H-10	12.82	A30E-5H-10	13.46	A40E-5H000
8	5.96	37.59	A30E-5H-10	8.17	A30E-5H-10	5.04	A40E00H-10
9	6.55	32.29	A30E-5H-10	4.11	A30E-5H-10	5.60	A40E00H-10
10	7.35	18.35	A30E-5H-10	0.71	A30E05H-10	3.15	A40E00H-10
11	8.00	5.55	A30E-5H-10	0.14	A80E05H000	2.07	A30E05H-10

Table D.9: Vertical Tail Maximum Envelope

STN	Z [m]	T_Y [%]	Case	M_X [%]	Case	M_Z [%]	Case
1	0.00	99.17	A30E-5H010	90.23	A30E-5H-10	70.22	A30E05H000
2	0.64	89.81	A30E-5H010	79.06	A30E-5H-10	51.64	A40E05H000
3	1.64	79.39	A30E-5H-10	61.77	A30E-5H-10	46.89	A40E05H000
4	2.64	71.65	A30E-5H-10	46.19	A30E-5H-10	28.20	A40E05H000
5	3.54	65.47	A30E-5H-10	32.97	A30E-5H-10	18.26	A50E05H000
6	4.57	55.82	A30E-5H-10	20.40	A30E-5H-10	12.24	A40E-5H000
7	5.37	47.64	A30E-5H-10	12.11	A30E-5H-10	12.41	A40E-5H000
8	5.96	35.35	A30E-5H-10	7.74	A30E-5H-10	5.48	A40E-5H000
9	6.55	30.54	A30E-5H-10	3.80	A30E-5H-10	6.64	A40E-5H000
10	7.35	17.62	A30E-5H-10	0.69	A30E-5H010	4.03	A40E-5H000
11	8.00	5.18	A30E05H-10	0.16	A90E00H000	1.98	A30E05H-10

Table D.10: Vertical Tail Maximum Envelope (Closed Loop)

STN	Z [m]	T_Y [%]	Case	M_X [%]	Case	M_Z [%]	Case
1	0.00	-20.78	A80E00H000	-15.13	A90E00H000	-55.24	A40E-5H010
2	0.64	-18.22	A90E00H000	-12.58	A90E00H000	-59.57	A30E05H-10
3	1.64	-14.82	A80E00H000	-9.10	A90E00H000	-59.17	A30E05H-10
4	2.64	-11.80	A80E00H000	-6.27	A90E00H000	-45.02	A30E05H-10
5	3.54	-8.64	A80E00H000	-3.82	A90E00H000	-30.00	A40E05H-10
6	4.57	-5.91	A80E00H000	-2.31	A90E00H000	-23.30	A40E05H-10
7	5.37	-4.48	A80E00H000	-1.46	A90E00H000	-15.35	A40E05H-10
8	5.96	-3.26	A90E00H000	-0.96	A90E00H000	-10.03	A50E05H-10
9	6.55	-2.46	A90E00H000	-0.57	A90E00H000	-8.17	A50E05H-10
10	7.35	-1.87	A50E05H-10	-0.23	A90E00H000	-4.12	A30E-5H-10
11	8.00	-1.27	A40E05H-10	-0.05	A90E00H000	-3.34	A40E-5H000

Table D.11: Vertical Tail Minimum Envelope

STN	Z [m]	T_Y [%]	Case	M_X [%]	Case	M_Z [%]	Case
1	0.00	-30.95	A80E00H000	-23.73	A90E00H000	-56.11	A50E00H000
2	0.64	-28.64	A90E00H000	-19.73	A90E00H000	-48.11	A40E00H000
3	1.64	-22.21	A80E00H000	-14.24	A90E00H000	-48.47	A40E00H000
4	2.64	-18.08	A90E00H000	-9.83	A90E00H000	-41.21	A30E05H-10
5	3.54	-12.73	A80E00H000	-5.89	A90E00H000	-32.24	A30E05H-10
6	4.57	-8.73	A80E00H000	-3.55	A90E00H000	-29.43	A30E05H-10
7	5.37	-6.62	A30E05H-10	-2.24	A90E00H000	-20.20	A30E05H-10
8	5.96	-4.87	A90E00H000	-1.47	A90E00H000	-13.28	A40E05H-10
9	6.55	-3.67	A90E00H000	-0.89	A90E00H000	-10.73	A40E05H-10
10	7.35	-3.77	A40E05H-10	-0.36	A90E00H000	-4.50	A40E05H-10
11	8.00	-2.63	A30E05H-10	-0.09	A90E00H000	-4.15	A50E05H-10

Table D.12: Vertical Tail Minimum Envelope (Closed Loop)

D.1.4 Fuselage Envelopes

STN	X [m]	T_Z [%]	Case	M_Y [%]	Case
1	3.34	16.75	A90E00H000	0.35	A50E-5H000
2	5.69	53.05	A90E00H000	1.36	A50E-5H000
3	8.08	62.49	A90E00H000	4.46	A90E00H000
4	10.20	69.42	A90E00H000	8.08	A90E00H000
5	12.32	74.74	A90E00H000	12.11	A90E00H000
6	14.44	82.37	A90E00H000	16.40	A90E00H000
7	16.56	90.49	A90E00H000	21.23	A90E00H000
8	18.68	100.00	A90E00H000	26.48	A90E00H000
9	20.80	95.09	A90E00H000	32.21	A90E00H000
10	22.93	91.17	A90E00H000	37.80	A90E00H000
11	25.32	81.42	A90E00H000	43.60	A90E00H000
12	27.97	37.36	A90E00H000	100.00	A80E00H000
13	30.89	36.75	A90E00H000	84.51	A80E00H000
14	33.81	41.13	A90E00H000	69.82	A80E00H000
15	36.46	46.82	A90E00H000	57.61	A60E00H000
16	38.85	44.26	A90E00H000	51.23	A60E00H000
17	40.98	39.49	A90E00H000	46.04	A80E05H000
18	43.10	36.41	A90E00H000	41.34	A80E05H000
19	45.75	34.32	A90E00H000	35.28	A80E05H000
20	47.87	32.44	A90E00H000	30.61	A80E05H000
21	50.60	43.06	A60E-5H000	24.59	A80E05H000
22	53.02	58.12	A60E-5H000	19.12	A80E05H000
23	54.76	65.87	A60E-5H000	14.99	A80E05H000
24	56.34	70.07	A60E-5H000	11.04	A80E05H000
25	57.76	-1.38	A90E00H000	2.92	A30E00H000
26	59.66	-5.21	A30E-5H000	1.01	A30E00H000
27	60.68	-2.73	A30E-5H000	0.51	A30E00H000

Table D.13: Fuselage Maximum Vertical Envelope

STN	X [m]	T_Z [%]	Case	M_Y [%]	Case
1	3.34	19.95	A90E00H000	0.36	A50E-5H000
2	5.69	61.02	A90E00H000	1.46	A50E-5H000
3	8.08	71.84	A90E00H000	5.23	A90E00H000
4	10.20	79.67	A90E00H000	9.39	A90E00H000
5	12.32	85.65	A90E00H000	14.02	A90E00H000
6	14.44	94.04	A90E00H000	18.94	A90E00H000
7	16.56	102.96	A90E00H000	24.45	A90E00H000
8	18.68	113.07	A90E00H000	30.42	A90E00H000
9	20.80	108.54	A90E00H000	36.92	A90E00H000
10	22.93	102.64	A90E00H000	43.29	A90E00H000
11	25.32	88.09	A90E00H000	49.98	A90E00H000
12	27.97	41.91	A90E00H000	103.38	A90E00H000
13	30.89	41.56	A90E00H000	87.35	A90E00H000
14	33.81	43.74	A90E00H000	73.20	A90E00H000
15	36.46	47.94	A90E00H000	62.95	A60E00H000
16	38.85	50.03	A90E00H000	56.20	A60E00H000
17	40.98	45.71	A90E00H000	50.31	A60E00H000
18	43.10	38.78	A90E00H000	45.09	A80E05H000
19	45.75	32.39	A90E00H000	38.44	A80E05H000
20	47.87	36.64	A90E00H000	33.20	A80E05H000
21	50.60	46.41	A60E-5H000	26.33	A80E05H000
22	53.02	61.17	A60E-5H000	19.95	A80E05H000
23	54.76	69.06	A60E-5H000	15.19	A80E05H000
24	56.34	74.07	A60E-5H000	10.91	A80E05H000
25	57.76	33.58	A30E00H000	6.66	A30E00H000
26	59.66	53.79	A30E00H000	2.29	A30E00H000
27	60.68	26.06	A30E00H000	1.19	A30E00H000

Table D.14: Fuselage Maximum Vertical Envelope (Closed Loop)

STN	X [m]	T_Z [%]	Case	M_Y [%]	Case
1	3.34	-11.48	A40E05H-10	-0.18	A40E05H-10
2	5.69	-25.79	A90E00H000	-0.97	A40E05H-10
3	8.08	-31.41	A90E00H000	-2.45	A90E00H000
4	10.20	-34.82	A90E00H000	-4.29	A90E00H000
5	12.32	-37.32	A90E00H000	-6.31	A90E00H000
6	14.44	-40.83	A90E00H000	-8.46	A90E00H000
7	16.56	-43.58	A90E00H000	-10.83	A90E00H000
8	18.68	-48.39	A90E00H000	-13.36	A90E00H000
9	20.80	-50.09	A90E00H000	-16.12	A90E00H000
10	22.93	-47.59	A90E00H000	-19.10	A90E00H000
11	25.32	-44.55	A90E00H000	-22.19	A90E00H000
12	27.97	-207.35	A60E00H000	-29.28	A90E00H000
13	30.89	-217.91	A70E00H000	-26.37	A90E00H000
14	33.81	-183.41	A80E00H000	-23.42	A90E00H000
15	36.46	-176.11	A90E00H000	-20.38	A90E00H000
16	38.85	-165.19	A90E00H000	-18.23	A60E-5H000
17	40.98	-148.06	A90E00H000	-18.62	A60E-5H000
18	43.10	-133.34	A90E00H000	-18.55	A60E-5H000
19	45.75	-116.00	A80E00H000	-17.58	A60E-5H000
20	47.87	-95.62	A80E00H000	-16.24	A60E-5H000
21	50.60	-82.53	A60E00H000	-13.67	A70E-5H000
22	53.02	-81.14	A60E00H000	-10.24	A70E-5H000
23	54.76	-84.02	A80E05H000	-7.47	A70E-5H000
24	56.34	-95.23	A80E05H000	-5.49	A70E-5H000
25	57.76	-23.49	A30E00H000	0.45	A30E-5H000
26	59.66	-35.23	A30E00H000	0.16	A30E-5H000
27	60.68	-17.43	A30E00H000	0.08	A30E-5H000

Table D.15: Fuselage Minimum Vertical Envelope

STN	X [m]	T_Z [%]	Case	M_Y [%]	Case
1	3.34	-11.38	A90E00H000	-0.16	A40E05H-10
2	5.69	-30.30	A90E00H000	-0.85	A90E00H000
3	8.08	-36.70	A90E00H000	-2.87	A90E00H000
4	10.20	-40.66	A90E00H000	-5.01	A90E00H000
5	12.32	-43.58	A90E00H000	-7.38	A90E00H000
6	14.44	-47.61	A90E00H000	-9.88	A90E00H000
7	16.56	-50.95	A90E00H000	-12.65	A90E00H000
8	18.68	-56.28	A90E00H000	-15.61	A90E00H000
9	20.80	-58.13	A90E00H000	-18.82	A90E00H000
10	22.93	-55.63	A90E00H000	-22.27	A90E00H000
11	25.32	-49.98	A90E00H000	-25.88	A90E00H000
12	27.97	-203.57	A60E00H000	-34.63	A90E00H000
13	30.89	-213.54	A70E00H000	-31.35	A90E00H000
14	33.81	-178.59	A80E00H000	-28.02	A90E00H000
15	36.46	-170.76	A90E00H000	-24.59	A90E00H000
16	38.85	-166.72	A90E00H000	-21.35	A90E00H000
17	40.98	-153.79	A90E00H000	-20.47	A60E-5H000
18	43.10	-131.54	A90E00H000	-20.16	A60E-5H000
19	45.75	-108.67	A80E00H000	-18.95	A60E-5H000
20	47.87	-96.21	A60E00H000	-17.46	A60E-5H000
21	50.60	-96.10	A60E00H000	-14.85	A70E-5H000
22	53.02	-96.92	A60E00H000	-11.26	A70E-5H000
23	54.76	-98.79	A70E00H000	-8.36	A70E-5H000
24	56.34	-103.74	A80E05H000	-6.18	A70E-5H000
25	57.76	-50.92	A30E00H000	-4.45	A30E00H000
26	59.66	-80.31	A30E00H000	-1.52	A30E00H000
27	60.68	-38.64	A30E00H000	-0.80	A30E00H000

Table D.16: Fuselage Minimum Vertical Envelope (Closed Loop)

STN	X [m]	T_Y [%]	Case	M_Z [%]	Case	M_X [%]	Case
1	3.34	15.97	A30E05H000	0.59	A40E-5H000	3.04	A40E-5H000
2	5.69	25.07	A30E05H000	2.17	A30E05H000	4.17	A40E-5H000
3	8.08	28.17	A30E05H000	4.72	A30E05H000	4.54	A50E-5H000
4	10.20	29.27	A30E05H000	7.21	A30E05H000	5.09	A30E05H000
5	12.32	28.86	A30E05H000	9.76	A30E05H000	5.55	A30E05H000
6	14.44	30.63	A30E05H000	12.19	A30E05H000	7.23	A30E05H000
7	16.56	29.02	A40E00H000	14.48	A30E05H000	7.70	A30E00H000
8	18.68	30.02	A50E00H000	16.29	A30E05H000	8.28	A30E00H000
9	20.80	26.85	A50E00H000	17.94	A30E05H000	8.90	A30E00H000
10	22.93	25.32	A50E00H000	19.25	A30E05H000	9.70	A30E00H000
11	25.32	26.95	A40E05H-10	20.51	A30E05H000	10.35	A30E00H000
12	27.97	96.92	A70E05H000	100.00	A70E05H000	97.97	A70E00H000
13	30.89	95.96	A70E05H000	88.29	A70E00H000	98.37	A70E00H000
14	33.81	100.00	A70E05H000	75.77	A70E00H000	98.50	A30E00H000
15	36.46	93.15	A70E05H000	65.55	A70E00H000	98.73	A30E00H000
16	38.85	89.04	A70E05H000	56.39	A70E00H000	99.14	A30E00H000
17	40.98	85.32	A70E00H000	48.56	A70E00H000	99.69	A30E00H000
18	43.10	82.15	A70E00H000	41.00	A70E00H000	100.00	A30E00H000
19	45.75	78.30	A70E00H000	31.37	A70E00H000	99.51	A30E00H000
20	47.87	74.58	A70E00H000	24.65	A70E00H000	99.37	A30E00H000
21	50.60	69.85	A70E00H000	16.41	A70E00H000	97.97	A30E00H000
22	53.02	64.48	A70E00H000	11.68	A60E05H000	96.59	A30E00H000
23	54.76	59.52	A70E00H000	10.35	A40E00H000	95.43	A30E00H000
24	56.34	28.55	A40E-5H000	10.22	A40E00H000	72.26	A70E05H000
25	57.76	8.44	A30E00H000	0.42	A30E05H000	0.35	A30E05H-10
26	59.66	3.71	A30E05H000	0.13	A30E05H000	0.13	A40E00H000
27	60.68	2.51	A30E05H000	0.01	A60E00H000	0.08	A40E00H000

Table D.17: Fuselage Maximum Lateral Envelope

STN	X [m]	T_Y [%]	Case	M_Z [%]	Case	M_X [%]	Case
1	3.34	17.24	A30E05H000	0.58	A40E-5H000	2.59	A50E05H-10
2	5.69	28.88	A30E00H000	2.33	A30E05H000	4.09	A40E05H-10
3	8.08	30.42	A30E05H000	5.12	A30E00H000	4.52	A40E05H-10
4	10.20	31.60	A30E05H000	7.80	A30E05H000	5.61	A30E05H000
5	12.32	30.87	A30E05H000	10.53	A30E05H000	6.20	A30E00H000
6	14.44	33.12	A30E05H000	13.10	A30E05H000	8.01	A30E00H000
7	16.56	30.91	A40E00H000	15.47	A30E05H000	8.51	A30E00H000
8	18.68	31.44	A50E00H000	17.36	A30E05H000	9.15	A30E00H000
9	20.80	25.99	A50E00H000	19.05	A30E05H000	9.72	A30E00H000
10	22.93	26.16	A30E00H000	20.39	A30E05H000	10.58	A30E00H000
11	25.32	29.26	A40E05H-10	21.75	A30E05H000	11.27	A30E00H000
12	27.97	102.48	A70E05H000	105.43	A70E05H000	109.37	A30E00H000
13	30.89	101.39	A70E05H000	92.76	A70E05H000	109.57	A30E00H000
14	33.81	105.90	A70E05H000	79.51	A70E05H000	109.47	A30E00H000
15	36.46	97.34	A70E05H000	68.20	A70E05H000	109.47	A30E00H000
16	38.85	93.64	A70E05H000	58.58	A70E05H000	109.63	A30E00H000
17	40.98	89.04	A70E05H000	50.39	A70E05H000	109.88	A30E00H000
18	43.10	85.13	A70E05H000	42.58	A70E05H000	110.07	A30E00H000
19	45.75	80.63	A70E05H000	32.72	A70E05H000	109.32	A30E00H000
20	47.87	76.13	A70E05H000	25.90	A70E05H000	108.60	A30E00H000
21	50.60	71.12	A70E00H000	17.73	A40E-5H010	106.43	A30E00H000
22	53.02	65.60	A70E00H000	12.83	A40E-5H010	104.20	A30E00H000
23	54.76	60.51	A70E00H000	9.48	A60E05H000	102.61	A30E00H000
24	56.34	31.09	A40E00H000	10.63	A40E00H000	78.73	A70E05H000
25	57.76	9.08	A30E00H000	0.43	A30E05H000	0.38	A30E05H000
26	59.66	3.80	A30E05H000	0.14	A30E05H000	0.13	A30E05H000
27	60.68	2.62	A30E05H000	0.02	A60E00H000	0.08	A30E05H000

Table D.18: Fuselage Maximum Lateral Envelope (Closed Loop)

D.2 Accelerations

D.2.1 Wing Envelopes

STN	Y [m]	Max. N_Z [%]	Case	Min. N_Z [%]	Case
1	1.46	36.63	A60E00H000	-2.46	A80E00H000
2	2.79	39.07	A60E00H000	-5.87	A80E00H000
3	3.12	39.64	A60E00H000	-6.49	A80E00H000
4	3.7	40.63	A60E00H000	-7.64	A80E00H000
5	4.4	41.85	A60E00H000	-9.00	A80E00H000
6	5.07	43.01	A60E00H000	-10.31	A80E00H000
7	5.4	43.57	A60E00H000	-10.96	A80E00H000
8	6.22	44.99	A60E00H000	-12.56	A80E00H000
9	7.71	47.59	A60E00H000	-15.50	A80E00H000
10	8.94	49.69	A60E00H000	-17.88	A80E00H000
11	9.8	51.19	A60E00H000	-19.59	A80E00H000
12	11.13	54.04	A70E00H000	-22.65	A70E00H000
13	12.91	58.71	A70E00H000	-27.59	A70E00H000
14	14.69	63.39	A70E00H000	-32.54	A70E00H000
15	16.47	68.07	A70E00H000	-37.47	A70E00H000
16	18.27	72.77	A70E00H000	-42.44	A70E00H000
17	19.38	75.71	A70E00H000	-45.54	A70E00H000
18	19.82	76.84	A70E00H000	-46.74	A70E00H000
19	21.07	80.13	A70E00H000	-50.21	A70E00H000
20	23.08	85.40	A70E00H000	-55.77	A70E00H000
21	24.63	89.47	A70E00H000	-60.07	A70E00H000
22	25.79	92.54	A70E00H000	-63.30	A70E00H000
23	26.9	95.44	A70E00H000	-66.37	A70E00H000
24	27.84	97.92	A70E00H000	-68.97	A70E00H000
25	28.64	100.00	A70E00H000	-71.19	A70E00H000

Table D.19: Wing Acceleration Envelope

STN	Y [m]	Max. N_Z [%]	Case	Min. N_Z [%]	Case
1	1.46	36.02	A60E00H000	-3.05	A80E00H000
2	2.79	38.30	A60E00H000	-6.58	A80E00H000
3	3.12	38.85	A60E00H000	-7.21	A80E00H000
4	3.7	39.84	A60E00H000	-8.32	A80E00H000
5	4.4	41.02	A60E00H000	-9.67	A80E00H000
6	5.07	42.15	A60E00H000	-10.96	A80E00H000
7	5.4	42.71	A60E00H000	-11.59	A80E00H000
8	6.22	44.11	A60E00H000	-13.17	A80E00H000
9	7.71	46.65	A60E00H000	-16.05	A80E00H000
10	8.94	48.72	A60E00H000	-18.40	A80E00H000
11	9.8	50.19	A60E00H000	-20.07	A80E00H000
12	11.13	52.66	A70E00H000	-23.59	A70E00H000
13	12.91	57.24	A70E00H000	-28.56	A70E00H000
14	14.69	61.83	A70E00H000	-33.52	A70E00H000
15	16.47	66.40	A70E00H000	-38.49	A70E00H000
16	18.27	71.01	A70E00H000	-43.50	A70E00H000
17	19.38	73.88	A70E00H000	-46.60	A70E00H000
18	19.82	75.00	A70E00H000	-47.82	A70E00H000
19	21.07	78.21	A70E00H000	-51.30	A70E00H000
20	23.08	83.37	A70E00H000	-56.90	A70E00H000
21	24.63	87.35	A70E00H000	-61.22	A70E00H000
22	25.79	90.35	A70E00H000	-64.48	A70E00H000
23	26.9	93.58	A70E00H000	-67.55	A70E00H000
24	27.84	96.59	A70E00H000	-70.17	A70E00H000
25	28.64	99.14	A70E00H000	-72.39	A70E00H000

Table D.20: Wing Acceleration Envelope (Closed Loop)

D.2.2 Horizontal Tail Envelopes

STN	Y [m]	Max. N_Z [%]	Case	Min. N_Z [%]	Case
1	0.55	88.33	A80E05H000	-26.12	A90E00H000
2	1.11	88.36	A80E05H000	-26.12	A90E00H000
3	1.16	88.43	A80E05H000	-26.15	A90E00H000
4	1.68	88.90	A80E05H000	-26.62	A90E00H000
5	2.7	89.80	A80E05H000	-27.53	A90E00H000
6	3.89	90.90	A80E05H000	-28.56	A90E00H000
7	5.26	92.14	A80E05H000	-29.77	A90E00H000
8	6.64	93.98	A30E-5H000	-31.10	A90E05H000
9	7.83	96.62	A30E-5H000	-33.08	A30E-5H010
10	8.79	98.73	A30E-5H000	-35.65	A80E00H000
11	9.35	100.00	A30E-5H000	-37.79	A80E00H000

Table D.21: Horizontal Tail Acceleration Envelope

STN	Y [m]	Max. N_Z [%]	Case	Min. N_Z [%]	Case
1	0.55	93.14	A90E00H000	-46.79	A90E00H000
2	1.11	93.14	A90E00H000	-46.79	A90E00H000
3	1.16	93.21	A90E00H000	-46.86	A90E00H000
4	1.68	93.75	A90E00H000	-47.46	A90E00H000
5	2.7	95.25	A30E05H-10	-48.66	A90E00H000
6	3.89	98.66	A30E05H-10	-50.10	A90E00H000
7	5.26	102.58	A30E05H-10	-51.74	A90E00H000
8	6.64	106.49	A30E05H-10	-53.38	A90E00H000
9	7.83	109.90	A30E05H-10	-56.12	A80E00H000
10	8.79	112.61	A30E05H-10	-60.10	A80E00H000
11	9.35	114.25	A30E05H-10	-62.47	A80E00H000

Table D.22: Horizontal Tail Acceleration Envelope (Closed Loop)

D.2.3 Vertical Tail Envelopes

STN	Z [m]	Max. N_Y [%]	Case	Min. N_Y [%]	Case
1	0	40.05	A60E00H000	-32.68	A30E00H000
2	0.64	44.31	A60E00H000	-34.29	A30E00H000
3	1.64	50.98	A60E00H000	-36.79	A30E00H000
4	2.64	58.40	A70E05H000	-39.35	A30E00H000
5	3.54	65.11	A70E05H000	-44.26	A80E00H000
6	4.57	72.78	A70E05H000	-50.88	A80E00H000
7	5.37	78.70	A70E05H000	-55.99	A80E00H000
8	5.96	83.46	A70E00H000	-59.80	A80E00H000
9	6.55	88.32	A70E00H000	-63.61	A80E00H000
10	7.35	94.74	A70E00H000	-68.72	A80E00H000
11	8	100.00	A70E00H000	-72.93	A80E00H000

Table D.23: Vertical Tail Acceleration Envelope

STN	Z [m]	Max. N_Y [%]	Case	Min. N_Y [%]	Case
1	0	42.16	A60E00H000	-30.88	A30E00H000
2	0.64	46.67	A60E00H000	-31.98	A30E00H000
3	1.64	53.73	A60E00H000	-34.04	A70E00H000
4	2.64	60.80	A60E00H000	-39.80	A80E00H000
5	3.54	67.72	A60E00H000	-45.76	A80E00H000
6	4.57	75.69	A60E00H000	-52.53	A80E00H000
7	5.37	81.95	A70E00H000	-57.74	A80E00H000
8	5.96	86.97	A70E00H000	-61.65	A80E00H000
9	6.55	92.03	A70E00H000	-65.56	A80E00H000
10	7.35	98.70	A70E00H000	-70.78	A80E00H000
11	8	104.21	A70E00H000	-75.04	A80E00H000

Table D.24: Vertical Tail Acceleration Envelope (Closed Loop)

D.2.4 Fuselage Envelopes

STN	X [m]	Max. N_Z [%]	Case	Min. N_Z [%]	Case
1	3.34	100.00	A90E00H000	-38.69	A90E00H000
2	5.69	95.51	A90E00H000	-34.47	A90E00H000
3	8.08	90.95	A90E00H000	-30.21	A90E00H000
4	10.2	86.93	A90E00H000	-26.41	A90E00H000
5	12.32	82.87	A90E00H000	-22.61	A90E00H000
6	14.44	78.84	A90E00H000	-18.82	A90E00H000
7	16.56	74.78	A90E00H000	-15.02	A90E00H000
8	18.68	70.75	A90E00H000	-11.39	A90E00H000
9	20.8	67.32	A90E00H000	-8.25	A90E00H000
10	22.93	64.08	A70E00H000	-5.32	A90E00H000
11	25.32	63.75	A70E00H000	-3.00	A90E00H000
12	27.97	63.49	A70E00H000	-0.99	A90E00H000
13	30.89	63.19	A70E00H000	-0.03	A70E-5H000
14	33.81	62.89	A70E00H000	-0.36	A90E00H000
15	36.46	62.86	A80E00H000	-1.75	A90E00H000
16	38.85	63.59	A90E00H000	-3.20	A90E00H000
17	40.98	64.87	A90E00H000	-4.49	A90E00H000
18	43.1	66.13	A90E00H000	-6.04	A90E00H000
19	45.75	68.80	A80E05H000	-8.91	A90E00H000
20	47.87	72.04	A80E05H000	-11.19	A90E00H000
21	50.6	76.23	A80E05H000	-14.46	A90E00H000
22	53.02	79.93	A80E05H000	-18.19	A90E00H000
23	54.76	82.60	A80E05H000	-21.00	A90E00H000
24	56.34	85.01	A80E05H000	-23.54	A90E00H000
25	57.76	87.19	A80E05H000	-25.85	A90E00H000
26	59.66	90.10	A80E05H000	-28.89	A90E00H000
27	60.68	91.65	A80E05H000	-30.54	A90E00H000

Table D.25: Fuselage Vertical Acceleration Envelope

STN	X [m]	Max. N_Z [%]	Case	Min. N_Z [%]	Case
1	3.34	112.18	A90E00H000	-46.15	A90E00H000
2	5.69	106.27	A90E00H000	-41.27	A90E00H000
3	8.08	100.26	A90E00H000	-36.32	A90E00H000
4	10.2	94.92	A90E00H000	-31.96	A90E00H000
5	12.32	89.60	A90E00H000	-27.57	A90E00H000
6	14.44	84.25	A90E00H000	-23.18	A90E00H000
7	16.56	78.94	A90E00H000	-18.79	A90E00H000
8	18.68	73.75	A90E00H000	-14.56	A90E00H000
9	20.8	69.07	A90E00H000	-10.83	A90E00H000
10	22.93	64.38	A90E00H000	-7.33	A90E00H000
11	25.32	62.46	A70E00H000	-4.39	A90E00H000
12	27.97	62.73	A70E00H000	-2.08	A90E00H000
13	30.89	62.99	A70E00H000	-4.49	A90E00H000
14	33.81	63.29	A70E00H000	-6.93	A90E00H000
15	36.46	64.15	A30E05H-10	-9.87	A90E00H000
16	38.85	66.72	A30E05H-10	-12.61	A90E00H000
17	40.98	69.03	A30E05H-10	-15.09	A90E00H000
18	43.1	71.34	A30E05H-10	-17.99	A90E00H000
19	45.75	74.22	A30E05H-10	-22.35	A90E00H000
20	47.87	76.49	A30E05H-10	-25.82	A90E00H000
21	50.6	79.43	A30E05H-10	-30.60	A90E00H000
22	53.02	82.93	A90E00H000	-35.89	A90E00H000
23	54.76	86.23	A90E00H000	-39.68	A90E00H000
24	56.34	89.27	A90E00H000	-43.12	A90E00H000
25	57.76	92.01	A90E00H000	-46.25	A90E00H000
26	59.66	95.64	A90E00H000	-50.41	A90E00H000
27	60.68	97.59	A90E00H000	-52.62	A90E00H000

Table D.26: Fuselage Vertical Acceleration Envelope (Closed Loop)

STN	X [m]	Max. N_Y [%]	Case	Min. N_Y [%]	Case
1	3.34	90.15	A30E05H000	-53.97	A70E00H000
2	5.69	90.15	A30E05H000	-49.71	A70E00H000
3	8.08	90.00	A30E05H000	-45.44	A70E00H000
4	10.2	89.85	A30E05H000	-41.47	A70E00H000
5	12.32	89.85	A30E05H000	-38.68	A40E-5H010
6	14.44	89.71	A30E05H000	-38.68	A40E-5H010
7	16.56	89.56	A30E05H000	-38.68	A40E-5H010
8	18.68	89.56	A30E05H000	-38.68	A40E-5H010
9	20.8	89.41	A30E05H000	-38.82	A40E-5H010
10	22.93	89.26	A30E05H000	-38.82	A40E-5H010
11	25.32	89.12	A30E05H000	-38.82	A40E-5H010
12	27.97	89.12	A30E05H000	-38.82	A40E-5H010
13	30.89	88.97	A30E05H000	-38.82	A40E-5H010
14	33.81	88.82	A30E05H000	-38.82	A40E-5H010
15	36.46	88.68	A30E05H000	-38.82	A40E-5H010
16	38.85	88.53	A30E05H000	-42.35	A30E00H000
17	40.98	88.38	A30E05H000	-47.21	A30E00H000
18	43.1	88.38	A30E05H000	-52.06	A30E00H000
19	45.75	88.24	A30E05H000	-58.24	A30E00H000
20	47.87	88.24	A30E05H000	-64.71	A30E00H000
21	50.6	88.09	A30E05H000	-73.09	A30E00H000
22	53.02	88.09	A30E05H000	-80.44	A30E00H000
23	54.76	87.94	A30E05H000	-85.74	A30E00H000
24	56.34	93.97	A60E00H000	-90.59	A30E00H000
25	57.76	100.00	A60E00H000	-95.00	A30E00H000
26	59.66	107.94	A60E00H000	-100.74	A30E00H000
27	60.68	112.21	A60E00H000	-103.82	A30E00H000

Table D.27: Fuselage Lateral Acceleration Envelope

STN	X [m]	Max. N_Y [%]	Case	Min. N_Y [%]	Case
1	3.34	63.53	A30E00H000	-52.65	A70E00H000
2	5.69	57.79	A30E00H000	-48.53	A70E00H000
3	8.08	52.06	A30E00H000	-44.26	A70E00H000
4	10.2	47.06	A30E00H000	-40.59	A70E00H000
5	12.32	42.06	A30E00H000	-36.91	A70E00H000
6	14.44	37.21	A30E00H000	-33.09	A70E00H000
7	16.56	32.65	A30E00H000	-29.41	A70E00H000
8	18.68	30.59	A30E00H000	-25.74	A70E00H000
9	20.8	32.06	A30E00H000	-25.59	A30E-5H010
10	22.93	33.68	A30E00H000	-26.32	A30E-5H010
11	25.32	35.59	A30E00H000	-27.21	A30E-5H010
12	27.97	38.38	A30E00H000	-28.09	A30E-5H010
13	30.89	41.62	A30E00H000	-28.97	A30E-5H010
14	33.81	45.74	A30E00H000	-30.00	A30E-5H010
15	36.46	50.15	A30E00H000	-32.65	A30E05H-10
16	38.85	53.97	A30E00H000	-36.62	A30E00H000
17	40.98	57.50	A30E00H000	-42.50	A30E00H000
18	43.1	61.03	A30E00H000	-48.38	A30E00H000
19	45.75	65.44	A30E00H000	-55.74	A30E00H000
20	47.87	71.03	A30E00H000	-62.35	A30E00H000
21	50.6	78.38	A30E00H000	-71.03	A30E00H000
22	53.02	84.85	A30E00H000	-78.68	A30E00H000
23	54.76	91.62	A60E00H000	-84.26	A30E00H000
24	56.34	98.68	A60E00H000	-89.26	A30E00H000
25	57.76	105.00	A60E00H000	-93.82	A30E00H000
26	59.66	113.38	A60E00H000	-99.85	A30E00H000
27	60.68	117.94	A60E00H000	-103.09	A30E00H000

Table D.28: Fuselage Lateral Acceleration Envelope (Closed Loop)

ISSN 1434-8454

ISRN DLR-FB-2010-37